



HAL
open science

Large-area Nanosensors Based on Self-assembled Ag/Au Bimetallic Nanostructures

Abeer Fahes

► **To cite this version:**

Abeer Fahes. Large-area Nanosensors Based on Self-assembled Ag/Au Bimetallic Nanostructures. Theoretical and/or physical chemistry. Université de Lorraine, 2022. English. NNT: 2022LORR0034 . tel-03774868

HAL Id: tel-03774868

<https://hal.univ-lorraine.fr/tel-03774868v1>

Submitted on 12 Sep 2022

HAL is a multi-disciplinary open access archive for the deposit and dissemination of scientific research documents, whether they are published or not. The documents may come from teaching and research institutions in France or abroad, or from public or private research centers.

L'archive ouverte pluridisciplinaire **HAL**, est destinée au dépôt et à la diffusion de documents scientifiques de niveau recherche, publiés ou non, émanant des établissements d'enseignement et de recherche français ou étrangers, des laboratoires publics ou privés.



AVERTISSEMENT

Ce document est le fruit d'un long travail approuvé par le jury de soutenance et mis à disposition de l'ensemble de la communauté universitaire élargie.

Il est soumis à la propriété intellectuelle de l'auteur. Ceci implique une obligation de citation et de référencement lors de l'utilisation de ce document.

D'autre part, toute contrefaçon, plagiat, reproduction illicite encourt une poursuite pénale.

Contact bibliothèque : ddoc-theses-contact@univ-lorraine.fr

LIENS

Code de la Propriété Intellectuelle. articles L 122. 4

Code de la Propriété Intellectuelle. articles L 335.2- L 335.10

http://www.cfcopies.com/V2/leg/leg_droi.php

<http://www.culture.gouv.fr/culture/infos-pratiques/droits/protection.htm>



**UNIVERSITÉ
DE LORRAINE**



Laboratoire de Chimie et Physique
Approche Multi-échelles des Milieux Complexes

ECOLE DOCTORALE C2MP : Chimie - Mécanique - Matériaux- Physique

THESE

Pour obtenir le grade de

Docteur

De

L'UNIVERSITE DE LORRAINE

Spécialité : Chimie-physique

Présentée et soutenue publiquement par

Abeer FAHES

Le 10 Mars 2022

Large-area Nanosensors Based on Self-assembled Ag/Au Bimetallic Nanostructures

Jury

Prof. Gregory Barbillon

EPF- Ecole d'Ingénieurs

Rapporteur

Prof. Michel Voué

Université de Mons

Rapporteur

Prof. Elena Ionescu

Université de Technologie de Troyes

Examinatrice

Dr. Solenne Fleutot

Université de Lorraine

Examinatrice

Président de Jury

Directeur de thèse

Co-Directeur de thèse

Prof. Michel Voué

Prof. Aotmane EN-NACIRI

Dr. Suzanna AKIL

Acknowledgments

It is my honor to express gratitude to the people who have been instrumental in the successful completion of this thesis.

First and foremost, I am thankful to God for giving me life, granting me strength, and keeping me upright.

The supervision, encouragement, and support provided by Prof. Aotmane EN NACIRI and Dr. Suzanna AKIL were crucial to the completion of this dissertation. My warmest thanks go first to my thesis director, Prof. Aotmane EN NACIRI, for his constant counseling and proper guidance throughout my thesis work. Thank you for trusting me, guiding me, and leaving so much autonomy when discussing and introducing my ideas.

I would like to acknowledge my approbation and humility to my co-director Dr. Suzanna AKIL. Her multidisciplinary knowledge gave rise to long discussion sessions which nourished both this manuscript and my scientific culture. As a result of her mentorship, I became an experienced and independent chemist. Her prompt inspiration, timely suggestions with kindness, enthusiasm, and dynamism allowed me to fulfill this project with improved skills in scientific work. Your insightful feedback pushed me to sharpen my thinking and brought my work to a higher level. Thank you!

I am indebted to the support that was given by the C2MP Doctoral School, which funded this work in all its stages. I thank L2n “Light, Nanomaterials, Nanotechnologies Laboratory” for their ongoing collaboration with our department team in conducting SEM characterizations especially my colleague Mohammad NAVVABPOUR. The FEDER “Fond Européen de Développement Regional” and “Région Grand-Est” are also acknowledged for their financial support (Pronano project).

My warmest thanks go to the Jury members and the president Prof. Michel Voué. I would like to thank the reviewers of this thesis, Prof. Gregory Barbillon and Prof. Michel Voué, for their careful reading and their avenues for reflection, as well as the examiners, Prof. Elena Ionescu and Dr. Solenne Fleutot, for the enriching discussion during the defense. I would like to acknowledge the valuable comments and suggestions of the Jury members, which have improved the quality of this work.

Additionally, I would like to thank Prof. Olivier PAGES, director of the LCP-A2MC laboratory, for hosting me in the laboratory and providing me access to research facilities. Without his support, this research would not have been accomplished.

I would like to express my very great appreciation to Prof. Yann BATTIE and Prof. Safi JRADI, committee members for the three years of the thesis, for their valuable and constructive suggestions during the planning and development of this research work.

I am particularly grateful for the technical assistance given by Pascal Franchetti, Montassar Billeh Bouzouraa, and Mohammad Baker Choker.

I offer my special thanks to Prof. Nazir FAZEL who was always ready to help at any time without any hesitation. It was a pleasure to know him, he was supportive, kind, and humorous.

I credit my drive and ambition to my dad Imad FAHES, who taught me to push myself to explore just how far I could go, and to take pride in my accomplishments along the way. I also appreciate all the support I received from my mom and brothers. No amount of words will be enough to tell how grateful I am to you. Thank you for everything you've done for me. Everything I have and everything I am, I owe it all to you.

I am heartily grateful to my fiancé Ibrahim, who gave me moral support, and self-giving care love. Since the day I started my thesis, his continuous support is the one thing I can always count on. His patience, guidance, and motivation helped me whenever I faced difficult circumstances. You always made me a priority. Thank you for dedicating your time to helping me fulfill my dreams and expectations. Thanks for supporting me wholeheartedly.

I would like to thank my friends, lab mates, colleagues, and research team for a cherished time spent together in the lab. Thank you to everyone who made this experience an unforgettable moment, especially my precious friend Malak who was always by my side.

To my parents

To Ibrahim

“Keep your dreams alive. Understand to achieve anything requires faith and belief in yourself, vision, hard work, determination, and dedication. Remember all things are possible for those who believe.”

Gail Devers

Abstract

The hybrid bimetallic systems, composed of two incorporated metallic nanostructures, have been considered a sustainable technology due to their ability to enhance, renovate, and enrich the properties of their integrated components. The solution-based chemical synthesis of plasmonic bimetallic nanoparticles (BNPs) with different morphologies has received considerable attention and has been the most widely used. However, in order to stabilize these BNPs at nanoscale, they must be treated with several steps and several chemical compounds, such as surfactants to compensate their surface energy. Even though these BNPs have been widely applied in many applications, there is still a need for a low-cost, scalable, and straightforward alternative. To date, no approach has been developed for directly synthesizing BNPs substrates on surfaces by self-assembly of polymers with a precise control over particle sizes and morphologies.

In this context, we have developed in this thesis a reproducible and well-controlled strategy which is polymer-mediated self-assembly based. The nanofabrication method is called vapor-induced phase separation (VIPS), to self-assemble silver nanoparticles (AgNPs) and gold nanoparticles (AuNPs) in a poly(methyl methacrylate, PMMA) thin layer. The M^{n+} /PMMA dispersion combined to the silicon (N-doped) substrate, used as a support for nanostructures, exhibit multifunctional properties, serving as reducing agent, surfactant and structure directing agent. For the purpose of achieving the desired materials, the experimental parameters of the synthetic approach were precisely optimized, despite the fact that it is difficult to mechanistically study the process of particle growth since this synthetic approach includes many components (Si substrate, PMMA, counter ions, Ag^+ and Au^{3+}) that could cooperatively work or compete with one another. Accordingly, we performed an in-depth study to understand to some extent the physico-chemical mechanism of synthesis. This was achieved through optical measurements by micro-extinction setup. Surface-enhanced Raman scattering (SERS) measurements were then performed to assess the sensitivity of the samples as sensors. Ultimately, the present thesis offers novel possibilities for creating rationally designed hybrid nanomaterials of controllable dimensions and geometries over a large-area for applications in detection and particularly for SERS, and for photocatalysis.

Résumé en français

Les systèmes bimétalliques hybrides, composés de deux nanostructures métalliques, sont considérés comme une technologie durable en raison de leur capacité à améliorer, rénover et enrichir les propriétés de leurs composants intégrés. La synthèse chimique en solution de nanoparticules bimétalliques plasmoniques (BNPs) avec différentes morphologies a suscité une attention considérable et a été la plus utilisée. Cependant, afin de stabiliser ces BNPs à l'échelle nanométrique, l'étape de fabrication nécessite l'utilisation de plusieurs étapes et de plusieurs composés chimiques tels que les tensioactifs pour compenser l'énergie de surface. Même si ces BNPs ont été largement impliquées dans de nombreuses applications, il existe toujours un besoin d'alternatif d'élaboration à faible coût, évolutif et applicable directement. Jusqu'à présent, aucune étude n'a permis la synthèse par auto-assemblage de polymère de substrats de BNPs directement en surface avec un contrôle précis des tailles et morphologies des nanoparticules.

Dans ce contexte, nous avons développé dans cette thèse une technique reproductible et bien contrôlée, appelée séparation de phase induite par la vaporisation (VIPS), pour auto-assembler des nanoparticules d'or (AuNPs) et d'argent (AgNPs) dans une fine couche de poly(méthacrylate de méthyle, PMMA). Les substrats de Silicium (dopés N) utilisés comme support des nanostructures combinés à la dispersion de $M^{n+}/PMMA$, présentent des propriétés multifonctionnelles, servant de réducteurs, de tensioactifs et d'agents de direction de structure. Dans le but d'obtenir les plateformes souhaitées, les paramètres expérimentaux de l'approche synthétique ont été optimisés avec précision malgré le fait qu'il est difficile d'étudier mécaniquement le processus de croissance des NPs car cette approche de synthèse est constituée d'un grand nombre de composants (substrat de Silicium, PMMA, contre-ions, Ag^+ et Au^{3+}) qui pourraient coopérer ou entrer en compétition les uns avec les autres. En conséquence, nous avons effectué une étude approfondie pour comprendre dans une certaine mesure le mécanisme physico-chimique de synthèse. Ceci a été réalisé à travers des mesures optiques par micro-extinction. Des mesures SERS ont été ensuite effectuées pour évaluer la sensibilité des échantillons en tant que capteurs. Enfin, la présente thèse offre de nouvelles possibilités pour créer des nanomatériaux hybrides de dimensions et géométries contrôlables sur une grande surface pour des applications en détection et particulièrement pour le SERS, et pour la photocatalyse.

Publications

Fahes, A., En Naciri, A., Navvabpour, M., Jradi, S., & Akil, S. (2021). Self-Assembled Ag Nanocomposites into Ultra-Sensitive and Reproducible Large-Area SERS-Active Opaque Substrates. **Nanomaterials**, 11(8), 2055.

Omar, R., Naciri, A. E., **Fahes, A.**, Jradi, S., Issa, A., Kuznetsov, D., ... & Akil, S. (2020). Precise control of the size and gap between gold nanocubes by surface-based synthesis for high SERS performance. **Soft matter**, 16(7), 1857-1865.

Fahes, A., Naciri, A. E., Navvabpour, M., Shoker, M.B., Jradi, S., & Akil, S. A Novel Surface-Based Strategy for selective overgrowth of Ag nanoparticles on Au nanocrystals. **Submitted to Journal of Materials Chemistry C** – Submission number: **TC-ART-04-2022-001531**.

Fahes, A., Naciri, A. E., Navvabpour, M., Shoker, M.B., Jradi, S., & Akil, S. Synthetic Design of shape-controlled Ag/Au oligomers via silver-assisted growth strategy. **Submitted to Soft matter journal**.

Contributions at National and International Conferences

“Large-area Nanosensors Based on Self-Assembled Bimetallic Nanostructures” Fahes, A., En Naciri, A., Navvabpour, M., Jradi, S., & Akil, S. Rencontres jeunes du C’Nano Est, June 21, 2021. **(Oral Presentation)**

“Large-area Nanosensors Based on Self-Assembled Bimetallic Nanostructures” Fahes, A., En Naciri, A., Navvabpour, M., Jradi, S., & Akil, S. 17ème journée de la matière condensée (JMC 17), August 24-27, 2021. **(Oral Presentation)**

“Large-area Nanosensors Based on Self-Assembled Bimetallic Nanostructures” Fahes, A., En Naciri, A., Navvabpour, M., Jradi, S., & Akil, S. European Materials Research Society (E-MRS) Fall Meeting, September 20-23, 2021. **(Oral Presentation)**

“Large-area Nanosensors Based on Self-Assembled Bimetallic Nanostructures” Fahes, A., En Naciri, A., Navvabpour, M., Jradi, S., & Akil, S. Journée des Jeunes Chercheurs du laboratoire LCP-A2MC, July 8, 2021. **(Oral Presentation)**

Table of Contents

Acknowledgments.....	3
Abstract.....	6
Résumé en français.....	7
Publications.....	8
Contributions at National and International Conferences.....	8
Table of Contents.....	9
List of Figures.....	12
List of Tables.....	17
List of Abbreviations.....	18
List of Symbols.....	19
List of Chemicals.....	20
General Introduction.....	21
Chapter 1: Bibliographic Study.....	24
1.1 Introduction.....	24
.....	25
1.2 New/Enhanced features of bimetallic against monometallic nanostructures.....	25
1.2.1 Optical properties.....	26
1.2.2 Catalytic properties.....	27
1.2.3 LSPR sensing properties.....	29
1.2.4 SERS Enhancement features.....	31
1.2.5 Solar photothermal conversion properties.....	33
1.3 Significant properties of monometals influencing the final bimetallic nanostructures (alloy or core-shell or heterostructure).....	34
1.4 Synthetic Approaches for controlled morphologies of bimetallic nanostructures.....	37
1.4.1 Lithographic Fabrication (EBL, NSL, NIL).....	38
1.4.2 DNA-mediated synthesis.....	41
1.4.3 Seed-mediated Growth (SMG).....	43
1.4.4 Copolymer-mediated self-assembly.....	47
1.4.5 Other Synthetic Approaches.....	51
1.5 Conclusion.....	51
1.6 References.....	53

Chapter 2: Self-Assembled Ag Nanocomposites into Ultra-Sensitive and Reproducible Large-Area SERS-Active Opaque Substrates	71
2.1 Introduction	71
2.1.1 Fabrication of AgNPs By Different Self-Assembly Approaches (Copolymer/Polymer/DNA-templated synthesis)	72
2.2 Experimental Part	74
2.2.1 Synthetic Approach	74
2.2.2 Polymer/Silver Solutions Preparation	76
2.3 Results and Discussions	76
2.3.1 Adjusting the Optical and Structural Properties of AgNPs	76
2.3.1.1 Impact of Spin-Coating Speed	77
2.3.1.2 Impact of Concentration of Ag Precursor	82
2.3.2 SERS Analysis	91
2.4 Conclusion	94
2.5 References	95
Chapter 3: A Novel Surface-Based Strategy For selective overgrowth of Ag nanostructures on Au nanocrystals	100
3.1 Introduction	100
3.2 Experimental Part	102
3.2.1 Fabrication of bimetallic substrates	102
3.3 Results and Discussions	104
3.3.1 Influence of Ag/Au molar ratio	104
3.3.1.1 Structural properties	104
3.3.1.2 Optical vs chemical characterizations	107
3.3.1.3 Sensing properties (SERS) :	109
3.3.2 Speed Effect Study on the bimetallic sample at $R_{Ag/Au} = 0.6$	111
3.3.3 Optical monitoring on $R_{Ag/Au} = 0.6$ at 7000 rpm	114
3.3.4 Proposed Mechanism at different Ag/Au ratios	117
3.4 Conclusion	120
3.5 References	121
Chapter 4: Synthetic design of shape-controlled Ag/Au oligomers via silver-assisted growth strategy	129
4.1 Introduction	129

4.2 Results and Discussions	133
4.2.1 SEM Images & Optical Characteristics:.....	133
4.2.2 Optical Monitoring and Proposed Mechanism.....	136
4.2.3 SERS features	139
4.3 Conclusion.....	141
4.4 References	142
Summary, Conclusions, Perspectives, and Supplementary Information	146
Conclusions	146
Perspectives.....	148
Appendix-A (related to Chapters 3 and 4)	150
Preliminary Studies to fabricate BNPs	150
Mixing two metallic precursors in solution	150
Removing PMMA from first Ag ⁺ /PMMA layer followed by subsequent deposition of Au ³⁺ /PMMA as second layer	151
Disjunctive Deposition of two metallic layers.....	152
Successive Deposition of two metallic layers.....	153
Appendix-B (related to Chapter 2).....	154
Principle of Ellipsometry.....	154
Ellipsometric Data Analysis	155
Ellipsometry Technique.....	156
Modelling.....	156
Fitting the Experimental Measurements & Extraction of Optical Constants	159
Size Distributions Histograms	162
Speed Effect Study.....	162
Concentration Effect Study	163
Appendix-C	164
Characterization techniques.....	164
References	167

List of Figures

- Figure 1.** Representative TEM and SEM images for different controlled shapes of BNPs synthesized using different synthetic routes. (a-b) Pt/Pd alloy nanocubes and nanotetrahedrons respectively; (c) Pt/Pd alloy icosahedra; (d) Au/Pd alloy octapodal; (e) Pt/Pd alloy nanocages; (f) Pt/Pd alloy hollow nanocubes; (g) Au/Pd alloy hexaoctahedrons; (h) Pt/Cu alloy concave nanocubes; (i-j) Au/Pd core-shell tetrahedra, and concave octahedral respectively; (k) Au/Pd core-shell tetrahedra; (l) Au/Pd core-shell trisoctahedra; (m) Au/Pd core-shell concave nanocubes; (n) Au/Pd core-shell convex polyhedra. The insets of each image shows the corresponding high-resolution images. Adapted from [9,10] 25
- Figure 2.** SEM images of (A) Ag nanocubes acting as sacrificial templates; (B-D) Ag/Au nanoboxes and nanocages obtained from sequential stages of galvanic replacement reaction; (E) Corresponding UV-Vis spectra of Ag nanocubes and Ag/Au nanoboxes/nanocages showing that LSPR peak of different compositions of Ag/Au alloy NPs was red-shifted in a predictable manner by controlling the mole ratio of HAuCl_4 to AgNO_3 . Adapted from [20,21] 26
- Figure 3.** The relationship between $\ln(C/C_0)$ and reaction time (t) indicating the rate of catalytic reduction of p-nitrophenol to p-aminophenol by NaBH_4 using MCA-Pd; MCA-Au; and MCA-Pd/Au (Ratio 1/1) as catalysts. The ratios of 4-nitrophenol concentration (C) at time t using the above MCA-based catalysts to its initial value C_0 were directly given by the relative intensity of the respective absorbance A/A_0 . Adapted from [26] 27
- Figure 4.** Graph showing the conversion of toluene as a function of the reaction temperature for Pd/TiO₂; Au/TiO₂; Pd(shell)-Au(core)/TiO₂; Au(shell)-Pd(core)/TiO₂; and Pd-Au(alloy)/TiO₂ catalysts. Mesoporous TiO₂ was used as support due to its high surface area. Adapted from [33] 29
- Figure 5.** SERS spectra of R6G adsorbed onto (a) Au monolayer; (b) Ag@Au monolayer; (c) Ag monolayer; and (d) Au@Ag monolayer. Adapted from [53] 32
- Figure 6.** Schematic representation of the controllable synthesis of nanomushrooms and their application in multiplex DNA detection. AuNPs modified with Raman-labeled DNA were used for the oriented growth of silver on their surfaces. Nano-mushrooms with interior gaps were formed in the absence of NaCl; these nanomushrooms generated strong SERS signals. Interestingly, anisotropic Au/Ag nanostructures without interior gaps that showed very weak SERS signals were synthesized in the same reaction solutions if the NaCl in the AuNP-DNA solution was not removed. Adapted from [55] 33
- Figure 7.** Illustration of a possible mixing pattern in a bimetallic alloy system. (a) the core-shell structure; and (b) heterostructure belong to a phase-separated alloy. Solid-solution alloys include (c) an ordered alloy with long-range order; and (d) random alloys with short-range order. Adapted from [62] 34
- Figure 8.** Optical spectra of colloidal solutions of bimetallic NPs of alloy type with different metal molar ratios (a); and core-shell type with different topology (b). Adapted from [80] 37
- Figure 9.** Synthetic approaches for bimetallic nanostructures with controlled shapes. (A) Co-reduction method to form dendritic core-shells or alloyed nanocrystals with polyhedral shapes. (B) Galvanic replacement reaction method to form porous hollow bimetallic nanostructures. (C) Seeded growth for the formation of core-shell nanostructures. Depending on the amount of the

precursor and the deposition mode of the second metal, it may form a conformal thin layer coating, thick shell, or nanoparticle array on the surface of the first metal. Adapted from [5]..... 38

Figure 10. Schematic view showing the formation of periodic arrays of Au nanostructures using NIL followed by templated dewetting, and transformation of Au seed arrays into different structures of BNPs using solution-based syntheses adapted from one of the many seed-mediated protocols that have been devised to generate colloidal nanostructures. Adapted from [120] 41

Figure 11. Proposed Mechanism of Growth of different morphological features of Pd/Au Bimetallic Nanostructures Influenced by Different Sequences of DNA. Adapted from [124] 42

Figure 12. Schematic illustration of the evolution of morphology associated with the Au/Pd core-shell nanocrystals as a function of reaction rate. Adapted from [138] 44

Figure 13. Schematic illustration of two typical growth modes of heterogeneous structure for binary metal core-shell nanoparticles. Adapted from [143] 47

Figure 14. Schematic illustration of the formation of AuAg NPs inside BCPs: (I) PS(145)-PVP(32); and (II) PS(854)-PVP(38). Adapted from [150]..... 48

Figure 15. Controlling the micelle morphology through the addition of a co-solvent (H₂O), which selectively swells the micelle's core (P4VP). The morphology is shifted from spherical micelles to rods (or cylinders) and rings as well as vesicles. The TEM micrographs show each of the morphologies separately, where the nanoparticles appear as dark spots in the polymer matrix. The scale bar in the micrographs is 50 nm. Adapted from [145]..... 49

Figure 16. Schematic illustration for the preparation of multifunctional core-shell nanofibers functionalized with two different types of nanoparticles loaded in the core and in the shell from self-assembled block copolymer template via selective solvent approach. Adapted from [151]. 50

Figure 17. (a) Schematic representation of the VIPS approach, showing the growth of two different diameters of AgNPs into PMMA nanoholes attached with; (b) an AFM image; and (c) its corresponding line-scan profile..... 75

Figure 18. Schematic view showing steps for formation of Ag⁺/PMMA solutions 76

Figure 19. SEM images of 40 mM Ag/PMMA samples fabricated at different spin-coating speeds: (a) 3000; (b) 5000; and (c) 7000 rpm. All insets are the corresponding magnified SEM images at 300 nm. 78

Figure 20. Average diameters (D1 and D2) of AgNPs with their correlated error bars versus spin-coating speed..... 79

Figure 21. Reflection spectrum of AgNPs/PMMA nanocomposites prepared with different spin-coating speeds. The spectra were extracted using a bright-field optical microscope. 81

Figure 22. The influence of spin-coating speeds on the thickness of deposited PMMA layers when metal is introduced. Error bars are also displayed in this plot. Measurements of thickness values are extracted using an AFM technique via a line-scratching method. 82

Figure 23. SEM images of Ag samples obtained by varying the concentration of Ag precursor. The scale bar is 100 nm. The insets show the absorption coefficient (α) of AgNPs/PMMA pre-synthesized substrates at each concentration. 83

Figure 24. Two-dimensional tapping mode AFM images (500 × 500 nm) for Ag samples prepared at different concentrations..... 84

Figure 25. Spectral evolution of reflection of AgNPs/PMMA nanocomposites upon varying the concentration of Ag precursor. 86

Figure 26. Variations of experimental ellipsometric angles (a) Ψ and (b) Δ in AgNPs/PMMA film/c-Si structures, as functions of the concentration of the Ag precursor.	88
Figure 27. Mie theory calculations for the extinction cross-sections of different sizes of AgNPs suspended in a highly porous PMMA.....	90
Figure 28. The Raman and SERS spectra of BPE at 10^{-5} M. Raman measurements were obtained with 10^{-2} M of BPE. Spectra were obtained at P = 5 mW over 5 s. Each curve is an average of 10 spectra collected from different positions on the substrate. All spectra were shifted vertically for the observation in all figures.....	91
Figure 29. The Raman and SERS spectra of BPE at 10^{-10} M for AgNPs prepared with different silver precursor concentrations. Raman measurements were obtained with 10^{-2} M of BPE. Spectra were obtained at P = 5 mW over 5 s. Each curve is an average of 10 spectra collected from different positions on the substrate.....	92
Figure 30. SEM images of bimetallic nanostructures synthesized by deposition of two M^+ /PMMA layers on Arsenide-doped silicon (Si-As) substrate. Different mixing patterns of BNPs obtained with different ratios of Ag/Au: (a) $R_{Ag/Au} = 2$; (b) $R_{Ag/Au} = 0.6$; (c) $R_{Ag/Au} = 0.5$; and (d) $R_{Ag/Au} = 0.4$. Scale bars of SEM images are: (a) 3; (b) 1; (c) 10; and (d) 20 μm . The insets correlate with the reflection optical results taken from BNPs substrates. The reflection spectra were collected by modifying the concentrations of NaAuCl ₄ /PMMA-acetone from 20 to 100 mM, whereas the concentration of AgNO ₃ /PMMA and the speed were kept constant at 40 mM and 7000 rpm respectively.....	106
Figure 31. EDX spectrum showing the characteristic X-rays originated from interacting a single core/shell nanoparticle with an electron beam. This spectrum refers to the sample prepared at ratio $R_{Ag/Au} = 0.6$	108
Figure 32. Raman and SERS spectra of BP-coated bimetallic substrates with different compositions recorded at λ excitation of: (a) 633 nm; and (b) 514 nm. Normalization of SERS intensities was performed by Origin software.	110
Figure 33. (a) SEM micrographs of Ag/Au core-shell structures obtained by varying spin-coating speed at constant ratio $R_{Ag/Au} = 0.6$; (b) The influence of spin-coating speed on the experimental reflection spectra of BNPs as it approaches a silicon surface; and (c) The variation of the maximum wavelength of the first plasmon band as a function of spin-coating speed.	113
Figure 34. Spectral evolution of reflected bands of Ag/Au/PMMA metallic layers on Si surface at ratio R= 0.6 and speed 7000 rpm from (a) fresh substrate to (b) 6h old substrate to (g) 1 week old substrate.	116
Figure 35. Schematic illustration of the mechanistic framework of BNPs at slow, moderate, and fast regimes of kinetics.	119
Figure 36. Representative SEM images of synthesized Ag/Au bimetallic nanostructures, demonstrating that diverse morphologies and configurations are made possible by deposition of different concentrations of Ag^+ /PMMA on Si-As substrates: (a) hetero-oligomers at low ratios of $R_{Ag/Au} = 0.3$; and (b) eccentric core-shell structures at high ratios of $R_{Ag/Au} = 0.6$. The scale bar of SEM images is 1 μm . The insets show the corresponding optical spectra changes and a cross-sectional SEM image of each bimetallic nanostructure, revealing its structure and profile. (c) Schematic illustration of the kinetically-controlled bimetallic nanostructures produced by simply altering the rate of reaction and concentration of Ag^+ /PMMA precursor.	134

Figure 37. EDX spectrum showing the characteristic X-rays originated from interacting a single hetero-oligomer nanoparticle with an electron beam. This spectrum refers to the sample prepared at ratio $R_{Ag/Au} = 0.3$.	135
Figure 38. The reflected plasmon band positions measured as a function of synthesis time for the sample prepared at low ratio $R_{Ag/Au} = 0.3$. Monitoring of spectral profiles identifies the mechanism involved in the formation of hetero-oligomers on substrate-based platforms.	138
Figure 39. Raman and SERS spectra on the hetero-oligomers and eccentric core-shell bimetallic nanostructures at different excitation wavelengths: (a) 633 nm; and (b) 514 nm. Each spectrum is an average of at least 3 regions which were acquired from randomly selected spots on the samples.	139
Figure 40. SERS spectra collected from 4 randomly selected points on (a) hetero-oligomers; and (b) eccentric core-shell substrate surfaces.	141
Figure 41. Reflection optical spectra of hetero-oligomers bimetallic sample before and after rinsing of second PMMA layer	149
Figure 42. SEM images showing a bimetallic system that could demonstrates an alloyed structure.	150
Figure 43. Photograph of the Au–Ag bimetallic nanofluids prepared using different molar ratios of Au to Ag precursors.	151
Figure 44. SEM images of (a) Ag(40)/PMMA without rinsing; and (b) Ag(40)/PMMA after rinsing with MIBK for 1 min	152
Figure 45. SEM images of Ag(40)-Au(60) bimetallic sample synthesized by disjunctive deposition of the two layers with a time delay of 1 week.	153
Figure 46. SEM image showing the arrangement of the two PMMA layers after a successive deposition with time delay of 10 min	154
Figure 47. Schematic illustration of spectroscopic ellipsometry principle. Adapted from [2].	155
Figure 48. Configuration of the UVISEL phase modulated ellipsometer used for measurements. Adapted from [6].	156
Figure 49. Physical model constructed for a thin MNPs/PMMA film formed on a substrate surface.	158
Figure 50. Flowchart of the data analysis procedure in spectroscopic ellipsometry. Adapted from [5].	159
Figure 51. Comparison between experimental and fitted pseudo-imaginary and real dielectric functions (ϵ_i , ϵ_r) of AgNPs/PMMA film/c-Si structures at different concentrations of Ag precursor: (a) 10; (b) 20; (c) 30; and (d) 40 mM.	160
Figure 52. Dielectric functions ((a) ϵ_r and (b) ϵ_i) of Ag/PMMA layers at different concentrations.	161
Figure 53. Refractive index ((a) n) and extinction coefficients ((b) k) of AgNPs/PMMA layers at different concentrations.	161
Figure 54. Size distribution histograms for the determination of average diameters (D1 and D2) of AgNPs prepared at different spin-coating speeds: (a,b) 3000; (c,d) 5000; and (e,f) 7000 rpm.	162

Figure 55. Size distribution histograms for the determination of average diameters (D1 and D2) of AgNPs prepared at different concentrations of Ag precursor: (a,b) 10; (c,d) 20; (e,f) 30; and (g,h) 40 mM. 164

List of Tables

Table 1. Solar photothermal conversion performance of different particles prepared using a sodium citrate thermal reduction method. Adapted from [61]	33
Table 2. List of other synthetic approaches for BNPs.....	51
Table 3. Average diameters of AgNPs (D1 and D2) at different concentrations.....	84
Table 4. A summary of (a) alloyed; (b) core-shell; and (c) heterostructures bimetallic systems with well-defined shapes synthesized by four colloidal routes, and lists of their geometric structures and key factors of shape control. Adapted from [15]	131

List of Abbreviations

μ_{ext} : Micro-extinction	MG: Maxwell-Garnet
0D, 1D, 2D, 3D: dimensional	MNPs: Metallic nanoparticles
AFM: Atomic force microscopy	NA: Numerical aperture
AgNPs: Silver nanoparticles	NIL: Nanoimprint lithography
AgNS: Silver nanospheres	NPs: Nanoparticles
AuNC: Gold nanocubes	NSL: nanosphere lithography
AuNH: Gold nanohexagons	OAP: Oriented attachment process
AuNPs: Gold nanoparticles	PdNPs: Palladium nanoparticles
AuNR: Gold nanorectangles	PtNPs: Platinum nanoparticles
AuNRs: Gold nanorods	RI: Refractive index
AuNS: Gold nanospheres	RIE: Reactive ion etch
BCPs: Block copolymers	RT: Room temperature
BEM: Boundary Elementary Method	SEM: Scanning electron microscope
BNPs: Bimetallic nanoparticles	SERS: Surface-enhanced Raman Scattering
DDA: Discrete dipole approximation	SK: Stranski – Krastanov
EBL: Electron beam lithography	SMG: Seed-mediated growth
EDX: Energy dispersive X-ray spectroscopy	SPR: Surface plasmon resonance
EF: Enhancement factor	TEM: Transmission electron microscope
EM: Electromagnetic enhancement	UPD: Underpotential deposition
EMT: effective medium theory	UV-Vis-NIR: Ultraviolet-Visible-Near Infrared
FCC: Face-centered cubic	VIPS: Vapor-induced phase separation
FM: Frank-van der Merwe	VOC: Volatile organic compounds
GRR: Galvanic replacement reaction	VW: Volmer-Weber
IgG: Immunoglobulin G protein	XPS: X-ray photoelectron spectroscopy
LDH: Layered double hydroxide	
LOD: Limit of detection	
LSPR: Localized surface plasmon resonance	

List of Symbols

Å: Angstrom	SCV: SERS confocal volume
C: Concentration	V: Volume of particle
c: Speed of light	α : Absorption coefficient
D_0 : Dissociation energy (kJ/mol)	Γ_i : Broadening coefficient
D1, D2: Average diameters	Δ : Phase difference
E^0 : Reduction potential	δ_p, δ_s : phases of r_p and r_s
f_i : Strength of oscillator	ϵ : Composite effective dielectric function.
h: Beam penetration depth	ϵ_∞ : contribution of optical transitions at higher energies
i: Number of optical transitions.	ϵ_m : Dielectric function of matrix
I_{SERS}, I_{normal} : intensities of the same band for SERS and normal Raman spectra	λ : Wavelength
k: Extinction coefficient	σ_{ext} : Extinction cross-sections
K: Kelvin	χ^2 : Mean squared error
M: Number of model parameters	Ψ : Amplitude ratio
min: Minutes	ω : Frequency
Mw: Molecular weight	ω_i : Resonance frequency
N: Number of data collected	ϵ_i : Imaginary dielectric function
n: Refractive index	ϵ_r : Real dielectric function
N_{normal} : number of molecules excited in Raman	
N_{SERS} : number of molecules probed in SERS	
r: Atomic sizes	
r: Beam radius	
R: Radius	
$R_{Ag/Au}$: Ratio	
r_p, r_s : Fresnel amplitude reflection coefficients	
rpm: Rounds per minute	
S: Excited surface	
s: Seconds	

List of Chemicals

4,4'-BP: Bipyridine	ITO: Indium tin oxide
4-AP: 4-Aminophenol	MCA: Melamine cyanurate
4-NP: 4-Nitrophenol	MIBK: Methyl isobutyl ketone
A10: Adenine	Na: Sodium
Ag: Silver	NaAuCl ₄ ·2H ₂ O: Sodium tetrachloroaurate dihydrate
AgBr: Silver bromide	NaBH ₄ : Sodium borohydride
AgCl: Silver chloride	NaCl: Sodium chloride
AgNO ₃ : Silver nitrate	Ni: Nickel
Ar : Argon	NO ₂ : Nitrogen dioxide
Au: Gold	NO ₃ ⁻ : Nitrate
BPE: Trans-1,2-4 (bipyridyl) ethylene	Pd: Palladium
C10: Cytosine	PDDA: Poly (diallyldimethylammonium chloride)
Cl ⁻ : Chloride	PdH: Palladium hydride
Cl: Chlorine	PMMA: Poly(methyl methacrylate)
CTAB: Cetyltrimonium bromide	PS-b-P4VP: Poly(styrene-block-4-vinylpyridine)
CTAC: Cetyltrimethylammonium chloride	Pt: Platinum
Cu: Copper	PVA: Poly (vinylalcohol)
CV: Crystal violet	R6G: Rhodamine 6G
Cy3: Cyanine dyes	Rh: Rhodium
DNA: Deoxyribonucleic Acid	RNA: Ribose nucleotides
G10: Guanine	Ru: Ruthenium
GR: Graphene	Si-As: Silicon arsenide
H ₂ : hydrogen	T10: Thymine
H ₂ O: Water	TAMRA: Tetramethylrhodamine
HAuCl ₄ ·3H ₂ O: Chloroauric acid	TiO ₂ : Titanium dioxide
Hg: mercury	TMAH: Tetramethylammonium hydroxide
InGaAs: Indium gallium arsenide	Xe: Xenon
Ir: Iridium	

General Introduction

The thesis is composed of **five chapters**, each of them dealing with different aspects of controlling structural properties of monometallic (AgNPs) and bimetallic nanoparticles (Ag/Au).

Chapter 1 is the introductory chapter and it is divided into two main parts. The first part highlighted the importance of incorporating two metallic nanoparticles (MNPs) into one system in several applications such as catalysis, SERS, localized surface plasmon resonance (LSPR) sensors, and photothermal conversion. These multifunctionalities arise from the synergistic effects that occur between the hybrid systems including electronic effects, bifunctional effects, and ensemble effects. The second part provided an overview for synthetic approaches mostly used for the synthesis of bimetallic nanostructures with well-controlled morphological features. A majority of the studies cited in the literature rely on solution-based protocols.

A process known as VIPS, used for the fabrication of monodisperse gold nanocubes embedded in a polymer layer, was accomplished recently. This simple, fast, and one-step synthetic approach showed its effectiveness in controlling the sizes and the shapes of obtained nanoparticles. Besides, there was no need for using a reducing agent or block copolymer; thus there was no requirement for either functionalizing the surface or etching of polymer film. Specifically, in **Chapter 2, 3, and 4**, we discussed extending the VIPS process to a large variety of monometallic (Ag) and bimetallic (Ag/Au) salts.

In **Chapter 2**, a brief review of methods for synthesizing AgNPs by means of polymers, block copolymers, and deoxyribonucleic acid (DNA) self-assembly is presented, as well as some of their severe shortcomings-such as lack of reproducibility and uniformity in SERS performances. Hence, if we want to go further, and use self-assembly to build functional nanomaterials that could be compatible with SERS applications, it is necessary to increase the stability and efficiency of self-assembled systems. This chapter described the synthesis of efficient Ag/PMMA nanocomposites in large quantities using a novel simple synthesis approach called VIPS to form large-scale, reproducible, and ultra-sensitive SERS substrates on opaque surfaces. Using VIPS technique, a thin-layer PMMA is self-assembled into nanoholes that are used as synthesis reactors for MNPs. This chapter also examined the different experimental parameters affecting the structural and optical properties of AgNPs. AgNPs as nanosensors, in particular, were optimized by adjusting a number of factors, including metal precursor concentration and spin-coating speed. Changing the

concentration of Ag precursor significantly influenced the particle quality and the self-assembly efficiency. Below a threshold critical concentration, a thermodynamic instability hindered the self-assembly at the beginning of the process due to a PMMA aggregation. In addition, a suitable speed was chosen for fabricating a thin and homogeneous substrate layer, and for producing a high reflection sensitivity from nanoparticles (NPs). The extraction of optical properties of AgNPs were required to adjust the Raman excitation wavelength to closely fit the band of surface plasmon resonance in SERS measurements. AgNPs were optically characterized by two complementary techniques: a direct micro-extinction technique, and an indirect ellipsometric technique that requires a construction of a physical model. A physical model revealing the PMMA and AgNPs as a one homogeneous layer is constructed based on three classical Lorentz oscillators (one for PMMA and two others for AgNPs). According to the Lorentz dispersion law, this model generates satisfactory quantitative data (Optical constants, thicknesses, and absorption coefficients) by involving a primary measurement of the raw experimental ellipsometric angles (amplitude ratio (Ψ) and phase difference (Δ)) followed by a correct fitting of these angles. Subsequently, the experimental and theoretical data sets were compared with Mie simulations to confirm the results. The relationship between structural dimensions and SERS enhancement properties was investigated in order to develop nanosensors that could detect weak traces of chemical and biological molecules. In this study, we showed that high yields of AgNPs localized within holes of PMMA can be employed as efficient and robust SERS substrates for detecting BPE molecules with high enhancement factors (EF) at a trace level, which is an extremely difficult task. PMMA's hydrophobic properties, which provide a mechanism for selective adsorption of BPE molecules on AgNPs, as well as increased densities of AgNPs on surface and close match between LSPR and Raman wavelengths, lead to an increase in SERS enhancement.

Bimetallic systems are effective in renovating and enriching the properties of their integrated components. VIPS approach would lend itself well for use in the synthesis of shape-controlled Ag/Au BNPs with different types. For this reason, **Chapter 3 and 4** were devoted to developing a more efficient VIPS approach to produce reproducible, large-scale, and architecture-controlled bimetallic nanomaterials on surfaces that are relevant for SERS and plasmon detection. **Chapter 3** demonstrated that the site-selective heterogeneous nucleation and growth of Ag on Au seeds occurred even if the synthesis is surfactant-free, and highly anisotropic growth modes were achieved on surfaces through a seed-mediated growth i.e. heterostructures and core/shell

configurations. In **Chapter 4**, this approach was also utilized to fabricate BNPs with hetero-oligomers configurations through a step-growth mode and an oriented attachment process (OAP). In both chapters, due to surface effects, the deposition of a second metal completely changes the resonance conditions and alter the optical and structural properties of NPs. BNPs cannot simply be controlled by the same rules established for controlling the shapes of MNPs. Additionally, we presented the different characterization techniques employed along these studies which aided in a complementary manner in the understanding of the nanoparticles' chemical composition, structural properties and morphology, optical and sensing properties. These include EDX, SEM, μ ext spectroscopy, and SERS spectroscopic technique. We also investigated how different synthetic reaction conditions such as spin-coating speed, concentrations of Ag and Au precursors, and molar ratios of Ag/Au modulated the structural, optical, and sensing properties of bimetallic nanostructures. The right ratio ($R_{Ag/Au}$) between two metals played a key role in the growth of bimetallic nanostructures to limit monometallic phase separation and allow composition control. The limited fundamental understanding of BNPs on surfaces still makes it difficult to understand the exact mechanism that causes hybrid interactions on surfaces despite the progress in this area. For this reason, efforts were dedicated to understand the role of each constituent in the nanostructure formation process on surface. The work throughout the chapters has revolved around the investigation of the underlying mechanisms of BNPs formation via a Thermodynamic/Physico-chemical study and a Real-time mechanistic study. The Au additives acted in two ways as an agent that accelerates the reduction of Ag and leads to the formation of BNPs, and as a seeding agent serving to provide preferred sites for Ag atom growth. The Ag additives acted as shape-directing agents due to an underpotential deposition (UPD), which is responsible for stabilizing the various surface facets that enclose the AuNPs. By assessing these sensors at different Raman excitation wavelengths, we then demonstrated that bimetallic substrates could serve as a wide-range SERS active substrate. The conclusions that emerged from the studies enabled an analysis of a number of parameters, whose influence on the structuring surface will be the subject of extensive investigation.

Chapter 5 summarizes the main conclusions derived from the previous four chapters and looks ahead to future possibilities (perspectives) of this work.

Chapter 1: Bibliographic Study

1.1 Introduction

The organization of BNPs with different atomic arrangements can be generally categorized into three main types: (a) Core-Shell Structures (intermetallic or solid solution) (b) Alloyed Structures (c) Heterostructures [1]. Adopting a specific type of arrangements does not only depend on the precise control over nucleation and growth processes but also on several factors such as bond energy, surface energy, atomic radius, charge transfer, surface-ligands bond strength, specific electronic/magnetic effects, and preparation methods and conditions, etc. [2,3]. The distribution of each metal within a particle and its organization is strongly linked to the synthetic approaches used in fabricating BNPs [4]. Also, a growing body of literature has investigated that the properties and application domains of BNPs depend on their structures. Therefore, to a greater extent, synthetic control is needed for these structures in order to perform robust plasmonic studies with greater amelioration for practical applications.

In contrast to monometallic nanoparticles, it is worth noting that the shape-controlled synthesis of bimetallic nanostructures is more complex and potentially much more attractive. Involving a second metal in the reaction can have unusual effects on the plasmonic and structural properties of NPs due to an alteration in: (i) the reaction kinetics of nucleation and growth processes, (ii) surface energy and lattice strain of nanocrystals, (iii) binding strength of the functional groups with the two metallic atoms [5]. Many attempts have been made in purpose of generalizing methods applicable for many particular bimetallic systems [6–8]. A large number of bimetallic nanostructures of different controlled shapes have rapidly emerged in the past decade. Figure 1 pinpoints the different possibilities in the shapes and structures organization of a series of bimetallic nanostructures synthesized using different synthetic approaches [9,10].

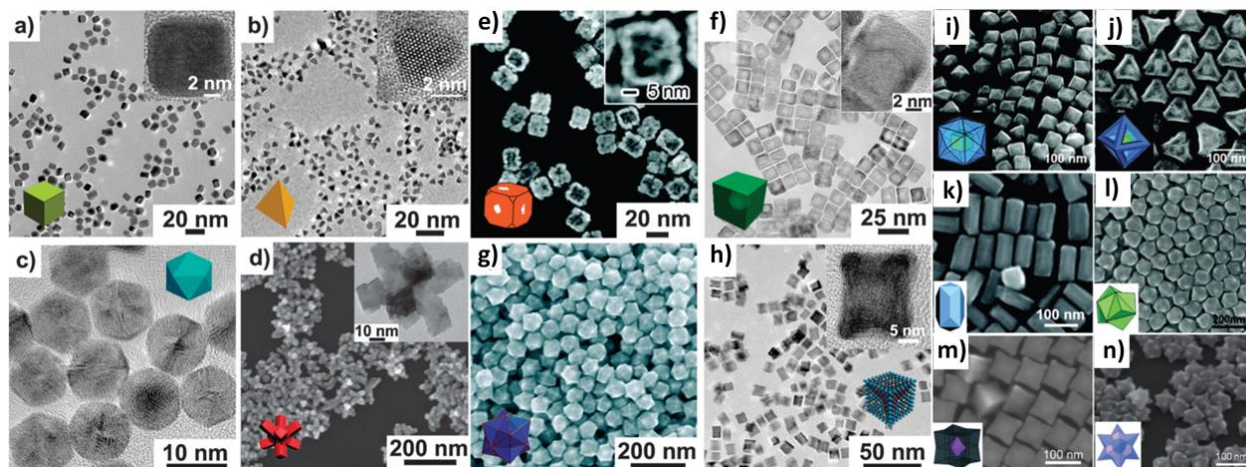


Figure 1. Representative TEM and SEM images for different controlled shapes of BNPs synthesized using different synthetic routes. (a-b) Pt/Pd alloy nanocubes and nanotetrahedrons respectively; (c) Pt/Pd alloy icosahedra; (d) Au/Pd alloy octapodal; (e) Pt/Pd alloy nanocages; (f) Pt/Pd alloy hollow nanocubes; (g) Au/Pd alloy hexa-octahedrons; (h) Pt/Cu alloy concave nanocubes; (i-j) Au/Pd core-shell tetrahexahedra, and concave octahedral respectively; (k) Au/Pd core-shell tetrahexahedra; (l) Au/Pd core-shell trisoctahedra; (m) Au/Pd core-shell concave nanocubes; (n) Au/Pd core-shell convex polyhedra. The insets of each image shows the corresponding high-resolution images. Adapted from [9,10]

1.2 New/Enhanced features of bimetallic against monometallic nanostructures

The construction of bimetallic architectures have revealed some exquisite features that can be dramatically different from their corresponding pure monometallic counterparts and physical mixings [11]. A better understanding of the new enhanced traits developed upon incorporating two MNPs into one system could have enormous benefits, as these architectures are ubiquitous in plasmonic research due to their utilization in diverse applications such as catalysis, SERS, LSPR sensors, and photothermal conversion [12–15].

1.2.1 Optical properties

NPs of different sizes or shapes can be coupled together for multiplexed detection, thus taking the advantage of extending the range of detection spectrum (Vis-NIR). Bimetallic nanostructures actually display the capability of optimizing the wavelength of Plasmon absorption band of metallic mixture; thus, offering a multipurpose tool for biosensing. Cui et al. indicated that the peak position of Au/Pt core-shell bimetallic system shifts from 550 to 650 nm when Pt shell thickness increases from 21 to 40 nm. Meanwhile, a broad absorption band was also observed in the UV region which was further red-shifted from 280 to 370 nm with the same increase in Pt shell thickness [16]. Another example on Ag-based alloy nanostructures, including Ag/Au [17], Ag/Pt [18], and Ag/Pd [19], revealed many interesting optical properties distinct from pure AgNPs. Galvanic replacement of Ag nanocubes (with an edge length of 45 nm and a strong dipole resonance at 440 nm) with an aqueous H_{Au}Cl₄ aqueous solution, produces Ag/Au nanocages with extinction peaks tunable across the NIR region as shown in Figure 2. Upon titrating the suspension of Ag nanocubes with different volumes of H_{Au}Cl₄ aqueous solution, the extinction peak showed a remarkable red-shift to 900 nm and beyond [20,21]. Such shifts into NIR regions are highly desirable, thus making this optical effect predominantly employed towards biosensing and SERS detection of biological and chemical analytes.

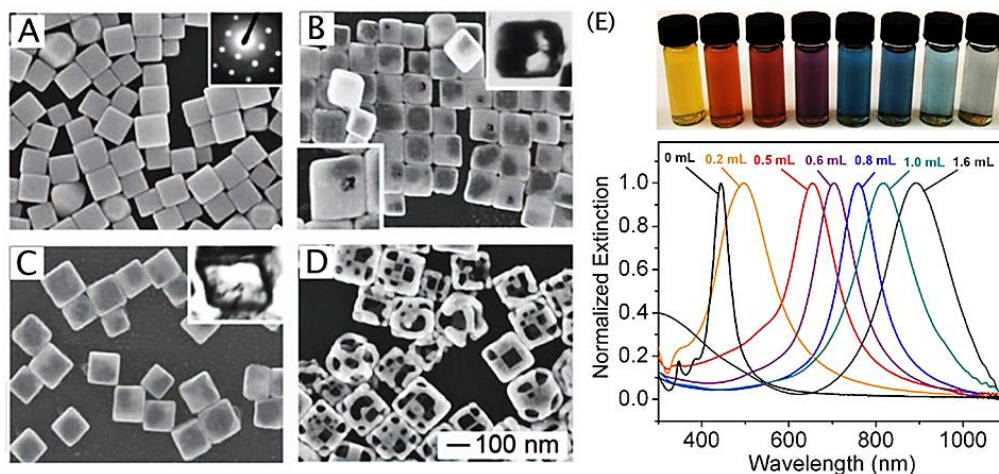


Figure 2. SEM images of (A) Ag nanocubes acting as sacrificial templates; (B-D) Ag/Au nanoboxes and nanocages obtained from sequential stages of galvanic replacement reaction; (E) Corresponding UV-Vis spectra of Ag nanocubes and Ag/Au nanoboxes/nanocages showing that LSPR peak of different compositions of Ag/Au alloy NPs was red-shifted in a predictable manner by controlling the mole ratio of H_{Au}Cl₄ to AgNO₃. Adapted from [20,21]

1.2.2 Catalytic properties

Several studies have highlighted the importance of BNPs in revealing improved catalytic properties over monometallic counterparts [22–25]. A comparison study between Pd/Au noble monometallic and bimetallic NPs, synthesized by simply embedding Pd and Au precursor with Melamine cyanurate (MCA) at room temperature (RT) without any additional reductant and stabilizer, has been conducted by Feng Jiang et al. to distinguish the differences in catalytic reduction of 4-nitrophenol (4-NP) into 4-aminophenol (4-AP) [26]. By referring to Figure 3, further analysis validated that Pd/Au bimetallic NPs exhibited superior catalytic activities than monometallic counterparts. Moreover, the adequate time required for the reduction of 4-NP into 4-AP follows the order where Pd/Au BNPs (10 minutes (min)) precede the noble monometallic PdNPs (18 min) and AuNPs (40 min) respectively. In this regard, the highest catalytic activity of BNPs was imputed to synergistic effects occurring between both AuNPs and PdNPs.

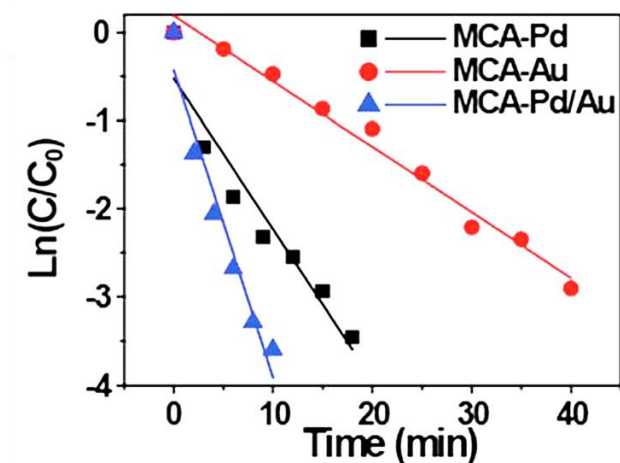


Figure 3. The relationship between $\ln(C/C_0)$ and reaction time (t) indicating the rate of catalytic reduction of p-nitrophenol to p-aminophenol by NaBH_4 using MCA-Pd; MCA-Au; and MCA-Pd/Au (Ratio 1/1) as catalysts. The ratios of 4-nitrophenol concentration (C) at time t using the above MCA-based catalysts to its initial value C_0 were directly given by the relative intensity of the respective absorbance A/A_0 . Adapted from [26]

Also, Nidhi's findings appear to support the fact that BNPs are qualified as effective catalysts with high improvement [27]. In summary, Layered double hydroxide (LDH) was used as a seed for deposition of Au and Ag to form BNPs following a simple wet chemical process. Au/Ag bimetallic nanoalloys with molar ratios 1:3, supported on LDH and used as catalysts for the reduction of 4-NP to 4-AP, revealed a higher catalytic activity with an enhanced potential for utilization in industrial applications owing it to their higher stability, efficiency, and recyclability in comparison to their monometallic counterparts.

Moreover, a dual-functional system for exploring catalytic reactions in situ through SERS fingerprinting can be developed by enriching the efficient catalytic Pd, Ni, and PtNPs with the SERS-active AgNPs [28–30].

As mentioned by Dan Xu et al., catalytic properties are sensitive to the intrinsic nature of the elemental compositions of the whole NPs and their surface elemental distributions [23]. A tiny change in composition could cause obvious changes in electrocatalytic activity and long-term stability [31]. Moreover, different ordering for deposition of metals can offer changes in the catalytic activity of the synthesized BNPs [32]. M. Hosseini et al. stated that the difference in catalytic activities of the prepared catalysts could be linked to the latter's surface structure (i.e. alloy or core-shell morphology) [33]. As clarified in Figure 4, a higher activity for the oxidation of toluene was achieved with Pd(shell)-Au(core)/TiO₂ compared to other catalysts Au(shell)-Pd(core)/TiO₂ and Pd-Au (alloy). The order of activity for catalysts was highly influenced by the preferential adsorption of oxygen molecules on the surface of catalysts where there is a competition for adsorption between the molecules of oxygen and volatile organic compounds (VOC). Experts confirmed that gold acts as an electronic promoter for Pd, that's why the higher catalytic activity was observed with Pd(shell)-Au(core)/TiO₂. In addition, the lower activity of Au(shell)-Pd(core)/TiO₂ could also be correlated to its lower affinity for adsorption of oxygen due to the lower ability of Au to polarize oxygen molecules.

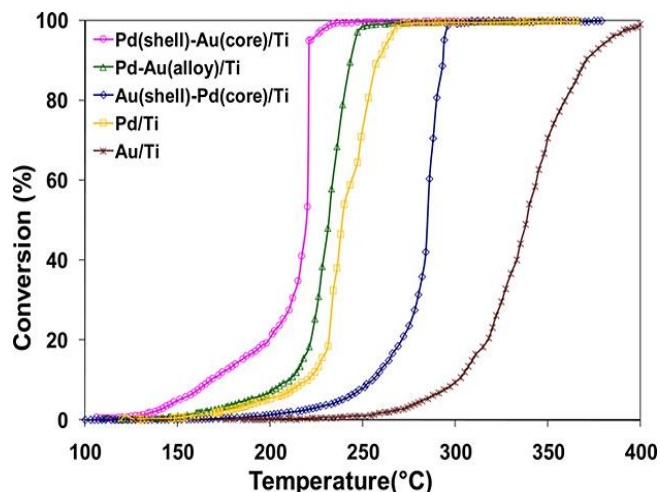


Figure 4. Graph showing the conversion of toluene as a function of the reaction temperature for Pd/TiO₂; Au/TiO₂; Pd(shell)–Au(core)/TiO₂; Au(shell)–Pd(core)/TiO₂; and Pd–Au(alloy)/TiO₂ catalysts. Mesoporous TiO₂ was used as support due to its high surface area. Adapted from [33]

1.2.3 LSPR sensing properties

The fundamental mechanism of the LSPR sensor is based on the monitoring of the refractive index (RI) variations of the medium on the surface of the sensor [34]. Surface of BNPs can be precisely functionalized by recognition groups, which can interact with target analytes. This method is generally useful with many systems, containing nucleic acid, peptides, proteins, DNA, ribose nucleotides (RNA), and carbohydrates, by modifying the sensors with the corresponding recognition element. When interacted with target analytes, the dielectric environment near the surface of BNPs will be altered. Consequently, such changes will be revealed as shifts in the resonance frequency of LSPR, which can be measured by either angular examination, wavelength investigation, or intensity measurements [1]. These strategies are usually done for highlighting the sensitivity of a given plasmonic sensor. Following this concept, a large number of sensors have been developed and used in diverse applications in fields of medical diagnostic, food safety, environmental protection and biotechnology [35,36].

For example, Jing Wang et al. draw our attention to the enhanced sensitivity of a wavelength modulator surface plasmons resonance (SPR) biosensor emerging from Au/Ag alloy nanocomposites immobilized on the surface of a gold substrate modified with sulfhydryl groups [37]. Au/Ag alloy nanocomposites displayed a detection range of 0.15–40.00 mg mL⁻¹ to the response of human Immunoglobulin G protein (IgG), which was covering a higher range than those obtained by AuNPs with the same particle size (0.30–20.00 g mL⁻¹). Due to phenomenon of alloying, the large shifts in resonance wavelength were shown to be widely affected by the increase in thickness of the sensing membrane, high dielectric constant of Au/Ag NPs, and electromagnetic coupling between Au/Ag alloy nanocomposites and Au film.

In [38], the authors investigated the effectiveness of biotinylated Ag/Au core-shell nanoplates as enhancers in SPR biosensing of streptavidin protein. They affirm that binding can be monitored by measuring the change in the SPR angle when streptavidin adsorbs on the sensing surface of biotinylated Ag/Au nanoplates.

Recently, an enhanced hydrogen sensing has been demonstrated on a single palladium nanoparticle placed with a variable distance d near a tip region of gold antenna [39]. It was evident that the detection sensitivity of plasmonic gas sensors is of decisive importance when gap regions between NPs are typically small. Later, distinct morphologies of Au/Pd core-shell BNPs are made vulnerable to different facets that display diverse surface atomic arrangements and surface electronic distributions; consequently leading to different adjustable hydrogen sensing properties [40]. Exposing Au/Pd NPs to hydrogen gas leads to the diffusion of atomic hydrogen into the shell layer of Pd thus forming PdH. This gives rise to a change in the RI of the Pd shell, and the absorption spectrum of such NPs detected this change. In this study, particles with larger sizes or thicker Pd shells result in large spectral shifts upon hydrogen absorption. As well, they indicate that the H₂ uptake trajectory depends on the shape of the nanocrystal. LSPR sensing was also developed as an effective way for monitoring different processes including enzymatic activity of oxidation of glucose [41], detection of heavy metal ions such as Hg [42], and colorimetric detection probes of cyanide ions [43].

1.2.4 SERS Enhancement features

SERS enables the identification of vibrational modes of molecules adsorbed on a surface of MNPs with intensified electric fields and amplified Raman signals [44–47]. The enormous outstanding sensitivity of SERS over Raman spectroscopy emerged from two-enhancement mechanisms, namely electromagnetic and chemical enhancements. Electromagnetic enhancement (EM), which arises from the presence of SPR on the surface, can drastically increase the E-field intensity near the NPs by an EF up to 10^7 . Whereas, chemical enhancement involves charge transfer between chemisorbed species and metal surface with SERS enhancement of factor 10^2 . E-field enhancements will not homogeneously occur over the entire metal substrate surface, but will be centered at specific sites called «hotspots». Many experts seek for building such hotspots from NPs with sharp features, roughened surfaces, and high number of inter or intra-particle nanogaps [48,49].

BNPs, used as SERS substrates, can display an extraordinary SERS enhancement that can allow the detection of trace concentrations of chemical and biological molecules [50]. In pursuit of this goal, many efforts were made to fabricate large-scale SERS-active substrates with high density of hotspots yielding huge enhancement. Several studies, for instance, have drawn the attention to the higher EF ascribed to BNPs when compared to monometallic NPs [51,52]. Yong et al. provided the reasons behind observing the stronger SERS signal of Au@Ag core-shell films for rhodamine 6G (R6G) than those from pure Au, Ag and Ag@Au core-shell films [53]. Yong's assumptions were fully justified and endorsed by plausible deductions when he attributed the enhancement to the electronic ligand effect in BNPs and localized electric field enhancement. Figure 5 represents SERS spectra of R6G on the monolayers of Au, Ag, Au@Ag and Ag@Au NPs excited at 532 nm with the observed Raman bands at 1650, 1575, 1538, 1365 and 1190 cm^{-1} , which can be attributed to $\nu(\text{C}-\text{C})$ stretching vibrations of R6G molecules as mentioned in the literature.

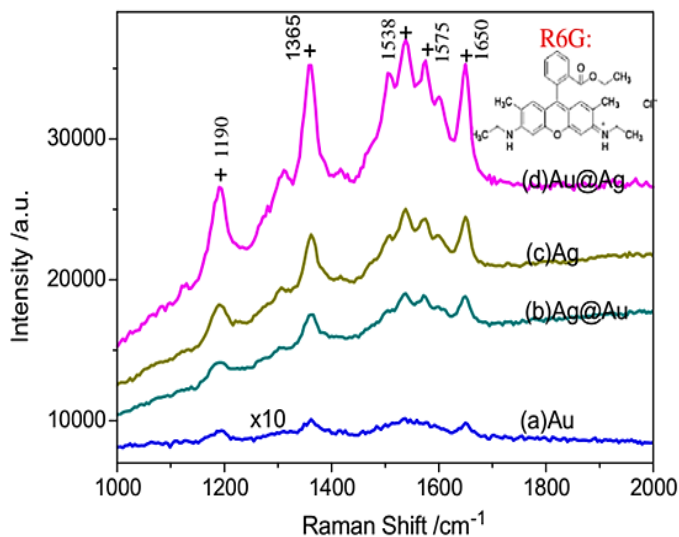


Figure 5. SERS spectra of R6G adsorbed onto (a) Au monolayer; (b) Ag@Au monolayer; (c) Ag monolayer; and (d) Au@Ag monolayer. Adapted from [53]

One of the major drawbacks to adopting a monometallic Pd nanosystem is the weakness of their SERS response. The incorporation of a second MNP such as Ag into Pd can be geared towards enhancing the SERS activity of PdNPs by borrowing the Raman enhancement from the coinage metal (Ag). Whereas, highly branched concave Au/Pd bimetallic nanocrystals, prepared by seed-mediated growth (SMG) in aqueous solution at RT, exhibited a striking SERS enhancement signals at remarkably low concentrations, mainly due to the existence of a high number of intra- and interparticle gaps, tips, and edges that serve as hotspots for amplifying the EM field [54].

Jianlei Shen et al. reported a DNA-mediated method for fabricating Ag/Au nanomushrooms with interior nanogaps and concluded that SERS intensities of these nanomushrooms rely on the area of the nanogap between the gold head and the silver cap [55]. As can be seen from Figure 6, SERS spectral results reveal that SERS intensities from nanomushrooms with interior nanogaps were approximately 30 times greater than the signal from the corresponding nanostructures without nanogaps. Nanomushrooms with interior nanogaps displayed the highest maintainable SERS activity, the best remarkable long-term stability, and the strongest EF.

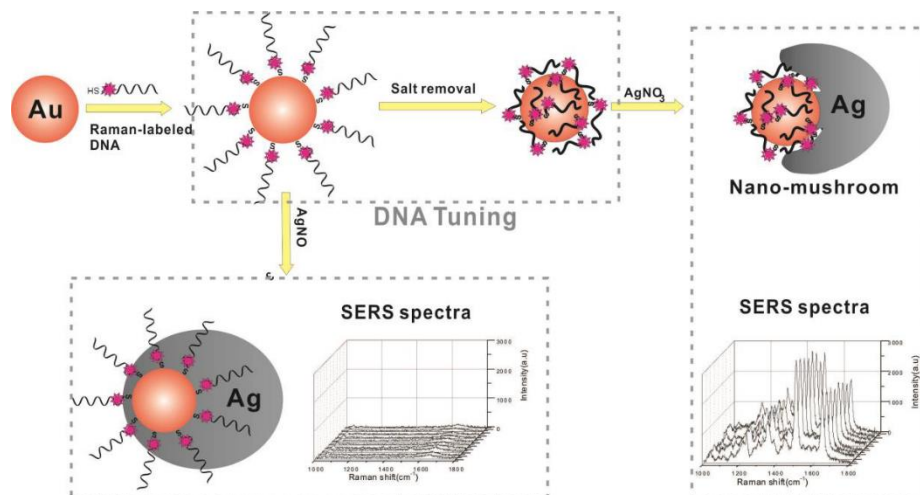


Figure 6. Schematic representation of the controllable synthesis of nanomushrooms and their application in multiplex DNA detection. AuNPs modified with Raman-labeled DNA were used for the oriented growth of silver on their surfaces. Nano-mushrooms with interior gaps were formed in the absence of NaCl; these nanomushrooms generated strong SERS signals. Interestingly, anisotropic Au/Ag nanostructures without interior gaps that showed very weak SERS signals were synthesized in the same reaction solutions if the NaCl in the AuNP–DNA solution was not removed. Adapted from [55]

1.2.5 Solar photothermal conversion properties

Table 1. Solar photothermal conversion performance of different particles prepared using a sodium citrate thermal reduction method. Adapted from [61]

Fluids	Equilibrium temperature change/°C	Solar photothermal conversion efficiency/%	Specific absorption rate/kW·mL
A: Au	57.63 ± 0.34	37.81 ± 0.92	19.83 ± 0.51
B: Au/Ag = 4/6 (Bimetallic NPs)	59.32 ± 0.22	41.37 ± 0.71	21.70 ± 0.42
C: Ag	50.76 ± 0.27	23.35 ± 0.63	12.25 ± 0.35
D: Au/Ag = 4/6 (Blended NPs)	54.59 ± 0.40	31.41 ± 0.93	16.47 ± 0.51
E: H ₂ O	39.66 ± 0.42	-	-

To further understand the importance of BNPs, an additional application was postulated in enhancing photothermal conversion efficiency in solar applications [15]. In the photothermal conversion process, metal nanostructures as Au and Ag can serve as systems that efficiently convert radiated energy into heat upon absorbing light [56–60]. These applications are made

possible through electron-phonon and phonon-phonon interactions generated through the transfer of the kinetic energy of oscillating electrons into the particle lattice. Meijie Chen et al. have reported a facile synthesis of Au/Ag BNPs by a sodium citrate thermal reduction method [61]. Table 1 details the calculated solar photothermal conversion performances of different particles. Experimental results, based on calculation models and descriptions of the energy absorbed per unit volume of NP and time, have assured that Au/Ag BNPs exhibited a higher solar photothermal conversion efficiency and a higher specific absorption rate than pure Au and AgNPs.

1.3 Significant properties of monometals influencing the final bimetallic nanostructures (alloy or core-shell or heterostructure)

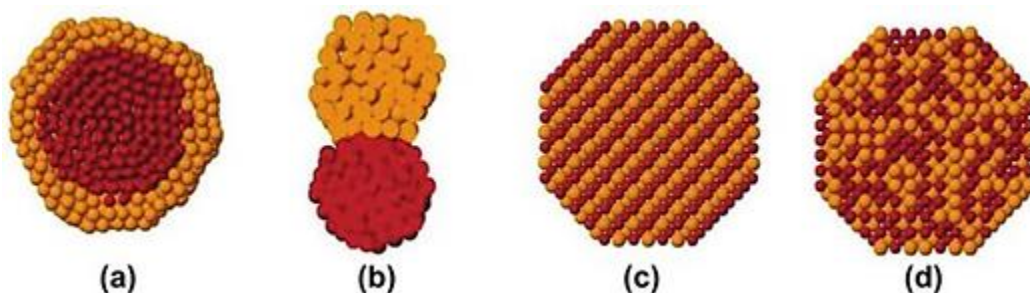


Figure 7. Illustration of a possible mixing pattern in a bimetallic alloy system. (a) the core-shell structure; and (b) heterostructure belong to a phase-separated alloy. Solid-solution alloys include (c) an ordered alloy with long-range order; and (d) random alloys with short-range order. Adapted from [62]

When more than one metal exists in a specific composition of NPs, several factors could be of prime importance in logically speculating the final structuring of BNPs [13]. We note from Figure 7 that there are different mixing patterns for bimetallic systems [62]. Plasmonic noble metals such as Ag (1.246 J.m^{-2}) and Au (1.506 J.m^{-2}) are characterized by their lowest surface energies in comparison to other metals such as Pt (2.489 J.m^{-2}), Pd (2.003 J.m^{-2}), Ru (3.043 J.m^{-2}), and Rh (2.659 J.m^{-2}) [63–65]. When mixed with Pt, Pd, Ru, and Rh, metals with lower surface energies as Ag and Au possess the susceptibility to migrate to the surface of BNPs. Nevertheless, in case of

supporting the surface with surfactants or facet-specific capping agents, the surface will preferentially expose specific composition or specific facet.

On the other hand, the relative strengths of homonuclear and heteronuclear bonds play an important role in alluding to the final structuring of BNPs. In general, stronger heteronuclear (A–B) bonds than homonuclear bonds (A–A and B–B) can lead to alloying/ mixing of metals. However, segregation of metals arises from nanostructures forming stronger homonuclear bonds; thus, tending to be at the center (core) of the cluster. For example, several strengths of bonds were tested for assuming the final atomic ordering of bimetallic nanostructures [66–71]. It was revealed that Au–Au bonding ($D_0 = 215$ and 218 kJ/mol at 0 K and 289 K, respectively) is higher than Au–Pd and Au–Ag thus favoring to typically yield an Au rich core of bimetallic particle, while it is lower than Au–Rh and Au–Ni thus tending to mix with those metals. Also, strengths of silver homonuclear bonding (Ag–Ag) ($D_0 = 159$ and 163 kJ/mol at 0 K and 289 K, respectively) are lower than silver bonding with gold (Ag–Au) and copper (Ag–Cu) thus preferring alloys formation.

To afford the desired final structuring, atomic radius of the two metallic NPs can provide information on the final morphological distributions. Alloyed or core-shell structures could be formed when the atomic radii of two metals are equal. Otherwise, atoms with smaller size have the capability to conquer the more sterically packed core.

Moreover, it is familiar that distinct pairs of metals are susceptible to segregation when their standard potentials are different. Relying on the differences between the reduction potentials of metals, it could be concluded that large differences normally result in a core-shell structure while small differences lead to an alloyed structure [72].

Hybrid nanosystems constituted of Ag and AuNPs devoted special attention of researchers due to their intense and well-defined LSPR bands in the visible range [73]. The crystalline lattice constants of both metals are extremely similar (4.078 Å for Au and 4.086 Å for Ag) [74]. These features supply stable Ag/Au BNPs with crystal structures allowing a high degree of adjustment in the corresponding plasmonic properties [75], in addition to a preferential tendency towards alloy formation. Later, many experts contend, on the other hand, that this evidence is not conclusive by fabricating Ag/Au BNPs adopting a core-shell structure [76].

A complete and reliable interpretation of the optical data of synthesized BNPs is essential for assuring the final structuring of nanostructures. Generally, it is known that Au and AgNPs possess plasmonic absorption bands at approximately 520 and 400 nm, respectively (by taking into consideration the simplest shape: spheres) [77,78]. By mixing the two metals, the appearance of two plasmonic peaks in the absorption spectrum would be expected for a physical mixture of individual Au and AgNPs [61]. However, it is crucial to judge if some mutual interactions seem to exist between both Ag and AuNPs by referring to some experimental means.

By simultaneous (at same time/synchronous) reduction of metallic salts in solution, only one LSPR band is a characteristic for bimetallic alloy nanosystems [79]. In case of alloying, the LSPR spectral positions lie between the positions of those pure Au and pure AgNPs and show absorption bands red-shifted almost linearly with increasing Au content as illustrated in Figure 8(a) [80]. It is worth noting that the absorption intensity of bimetallic systems decreased upon increasing Au content. This could be ascribed to the fact that one monolayer of Au could be adequate for hindering and weakening the Ag plasmon resonance band completely as suggested by Mulvaney et al. [81]

By sequential (successive) reduction of metallic salts, bimetallic core-shell structures with an absorption band blue shifted from the core metal and red shifted from the shell metal could be fabricated [82]. As stated in Figure 8(b) [80], the disappearance of LSPR absorption band of previously formed monometallic particles, used as a core, and the formation of LSPR band of the second metal in the spectra of the same colloid can validate the occurrence of a new plasmonic metal shell.

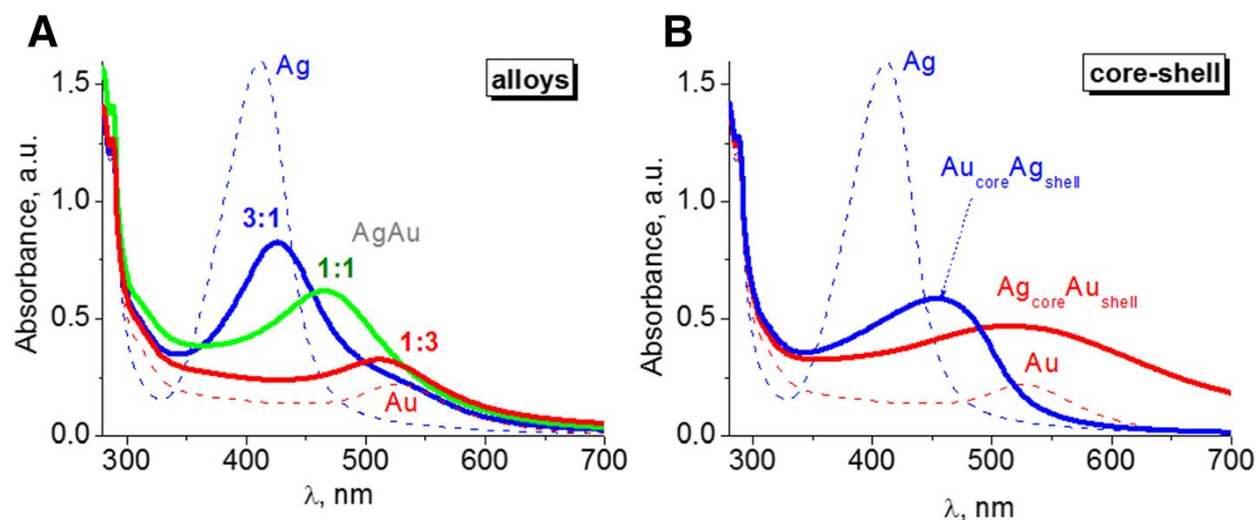


Figure 8. Optical spectra of colloidal solutions of bimetallic NPs of alloy type with different metal molar ratios (a); and core-shell type with different topology (b). Adapted from [80]

1.4 Synthetic Approaches for controlled morphologies of bimetallic nanostructures

Optimizing the functionality and the application performances of BNPs are heavily dependent on the synthetic methods used, which have further strengthened the confidence in advancing the synthetic approaches that can allow their preferential formation [4,12,83–86]. However, a grand challenge still resides in the construction of controlled shapes of BNPs due to the different kinetic and thermodynamic properties of different metals that made them complicated in ensuring synchronous nucleation and growth [1]. To date, the most solution-based synthetic approaches used for shape-selective growth of BNPs are: co-reduction, template-directed growth via galvanic replacement reactions (GRR), and SMG methods [10]. Figure 9 shows the basic synthetic pathways that were successfully used for the fabrication of different types of BNPs. In the first route (Figure 9A), dendritic nanostructures [87–92] or alloyed nanocrystals [93–97] can be manufactured. In the latter two routes (Figure 9B and C), porous hollow [98–102] and core-shell [103–106] bimetallic nanostructures are created respectively. Each synthetic approach has its own conditions for developing such types of bimetallic nanostructures. It is noteworthy that some synthetic strategies require the combination of two or more of these three basic routes at the same time.

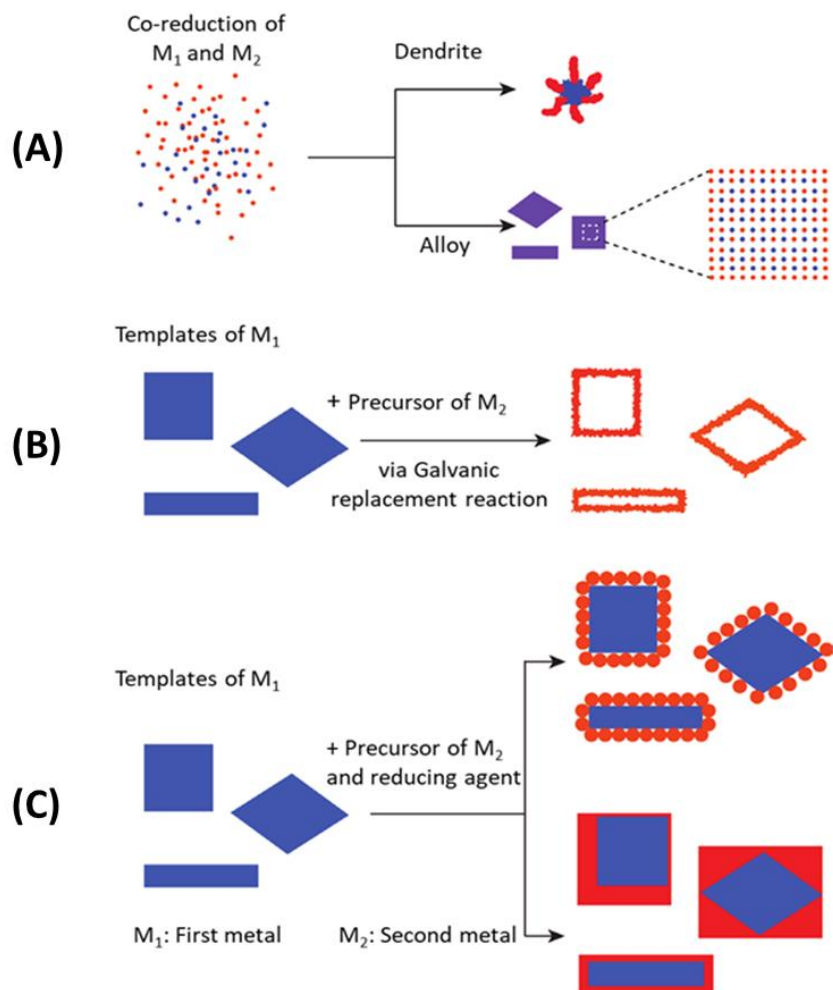


Figure 9. Synthetic approaches for bimetallic nanostructures with controlled shapes. (A) Co-reduction method to form dendritic core-shells or alloyed nanocrystals with polyhedral shapes. (B) Galvanic replacement reaction method to form porous hollow bimetallic nanostructures. (C) Seeded growth for the formation of core-shell nanostructures. Depending on the amount of the precursor and the deposition mode of the second metal, it may form a conformal thin layer coating, thick shell, or nanoparticle array on the surface of the first metal. Adapted from [5]

1.4.1 Lithographic Fabrication (EBL, NSL, NIL)

Unlike solution synthetic methods, lithography has been widely implemented in the fabrication of nanostructures with precise control over the size, shape, nanoscale gaps, and organization of nano-objects on the surface [107,108]. Moreover, the synthesis of uniform reproducible SERS-active substrates, yielding strong SERS signals, has been easily conducted using lithographic techniques [109,110]. Conventional lithographic techniques such as electron beam lithography (EBL) employ

polymeric resists to fabricate masks for deposition or etching of nanostructures with high resolution. A substrate coated with a thin layer of resist, mainly made of a polymer as PMMA, will be exposed to a scanned electron beam over specific regions according to a programmed pattern. Exposing the positive resist (i.e. PMMA) to an electron beam devastated its structuring by breaking it down. These resist exposed areas will be subsequently removed by a chemical development process through an immersion with solvents such as MIBK, TMAH, etc. Afterwards, metals such as Ag or Au can be deposited onto the substrates followed by a step to remove the remaining resist and the metal covering it (lift-off); thus leaving behind an ordered array of Ag or Au nanostructures patterned with high resolution [111].

Their attempts to do BNPs, usually with low throughput productivity, are cumbersome and financially unfeasible [112]. In fact, there is an obstacle in patterning features only a few nanometers apart (below 10 nm) [113]. For this reason, sometimes a high resolution is challenged to define the nanogaps, that maximize the intensity of hotspots, between plasmonic nanostructures. The use of adhesion layers can severely damp plasmonic resonances [114], in addition to a possibility for the perturbation of the uniformity of NPs arrays and their shapes, if a restricted damage to the resist as well as ineffective lift-off at such small sizes could eventuate [113]. It is important to note that this approach is well-suited to generate periodic arrays of NPs with gap sizes limited to 50 nm [115]. Inevitably, non-conventional lithographic techniques such as Nanosphere Lithography (NSL) and Nanoimprint Lithography (NIL) have been developed to mitigate the serious shortcomings recognized by EBL, in an aim to promote a saving in both time and cost and to enhance the productivity.

NSL comprises the self-assembly of colloidal spheres into hexagonally close-packed arrays on surface of substrates. Nanohole arrays can be obtained with this NSL mask from the electrochemical deposition of a metal layer in the interstitial voids created by the mask [116–118]. However, there were some discrepancies regarding this technique since it does not allow the control of the hole diameter and have limited range for the depth of the nanoholes.

NIL is a major breakthrough in nanopatterning because it can produce high resolution structures over a large-area with a high throughput and at low cost [119]. NIL is a three-stage processing route that is applied for the creation of periodic arrays of complex metal nanostructures as Au@Ag structures and Au@AgPd structures [120]. Figure 10 summarizes the proceeding steps followed

for the nanofabrication by nanoimprint lithographic technique. In the initial stage of the process, the deposited resist, acting as target sites for formation of BNPs, will be imprinted and exposed to a reactive ion etch (RIE) thus creating an array of openings on the surface. Prior to imprintation, the polymeric resist was spin-coated and baked on a stationary substrate at elevated temperature and pressure. Imprintation will consequently form cylindrical holes without reaching the bottom of substrate surfaces. As soon as these steps have been carried out, metals will be deposited through the openings and the remaining resist followed by a lift-off procedure for the removal of the resist and a heat treatment. This permits the formation of an array of circular Au disks which are further undergoing a dewetting process to allow their diversion into weakly faceted structures with a near-hemispherical geometry of smaller diameter than the initial Au discs. Subsequently, the resulting Au seeds arrays at the center of each target site are subjected to wet-chemistry solution protocols and can be readily transformed into progressively more sophisticated nanostructures (BNPs: core-shell, core-void-nanoshell, and core-void-nanoframe nanostructures). These protocols are adapted from one of the many seed-mediated fabrication methods that have been designed to generate colloidal nanostructures [120]. However, their claims seem somewhat exaggerated since the usage of NIL stamps can ultimately restrict the density of the nanostructures produced, and show damage over time by disrupting the produced arrays. Such an inappropriate assumption for the temperature used in template dewetting process can lead to grave consequences with regard to control over nanostructures' center-to-center distances and shapes [120].

Taken together, these results suggest that lithographic techniques are still treated as complicated methods due to the multisteps required for developing templates with arrays of nanoscale patterns. Also, its tough conditions make it difficult to replicate.

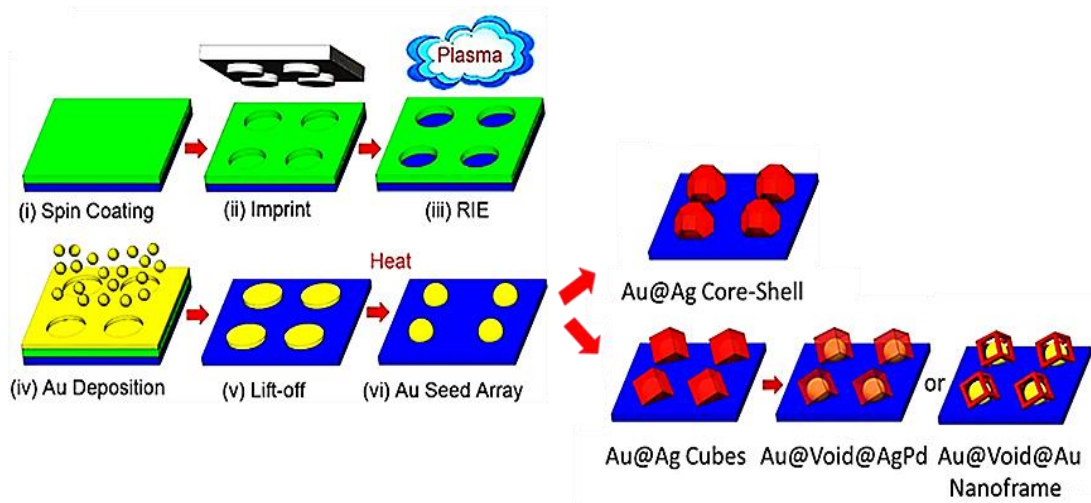


Figure 10. Schematic view showing the formation of periodic arrays of Au nanostructures using NIL followed by templated dewetting, and transformation of Au seed arrays into different structures of BNPs using solution-based syntheses adapted from one of the many seed-mediated protocols that have been devised to generate colloidal nanostructures. Adapted from [120]

1.4.2 DNA-mediated synthesis

DNA mediated synthesis represents an innovative approach for the synthesis of BNPs. This technique provides a higher potential for improving the performance of BNPs by achieving a high degree of control over their shapes, interparticle gaps, and their surface properties [113]. DNA, which is a useful molecule for assembly, has many interesting features including its availability and well-understood interactions [121]. As an easily adaptable material, it has regularly arranged functional groups and well-developed chemistries for different specific modifications [122,123]. For instance, in accordance with [124], distinct morphologies of core-shell Pd/Au BNPs can be modulated by varying the DNA sequences as highlighted in Figure 11. The synthesis was accomplished by co-reduction of Au and Pd precursors on simple Pd nanocubic seeds in the presence of homo-oligomers containing 10 deoxy-ribonucleotides of thymine (T10), adenine (A10), cytosine (C10), and guanine (G10). The different stages as well as the phenomena that are likely to intervene during the growth of Pd/Au BNPs were described accurately [124]. The formation of these nanostructures proceeds through an island-like nucleation of metals on the Pd cube which eventually becomes an epitaxial shell. DNA sequences were highly influential in determining how the incoming metal atoms will undergo deposition and diffusion on the Pd

nanocubic seed. Controlling BNPs morphology through varying DNA binding affinities shifted the morphology into different complex assembly schemes. This indicated that interaction of DNA molecules with two metals is a dynamic process that depends heavily on the sequence of DNA and the identity of metals. The binding of DNA to Pd seed directs the particles growth to the desired shapes by lowering surface energy in a sequence dependent matter. The extent of lowering surface energy can be explained by the differences in binding affinity and coverage density of DNA to Pd nanocubic seed. In summary, A10 mediated particles can significantly lower the surface energy thereby forming rhombicuboctahedron. In contrast, T10 mediated particles lowers the surface energy the least leading to the formation of satellite core-frame bimetallic nanostructures. Additionally, when A10 interacts with gold precursor, it enables the preferential formation of smaller nano-crystallites before its aggregation and deposition on Pd nanocubic seed [125]. While G10 promotes the formation of secondary structure that passivate the surface of seed.

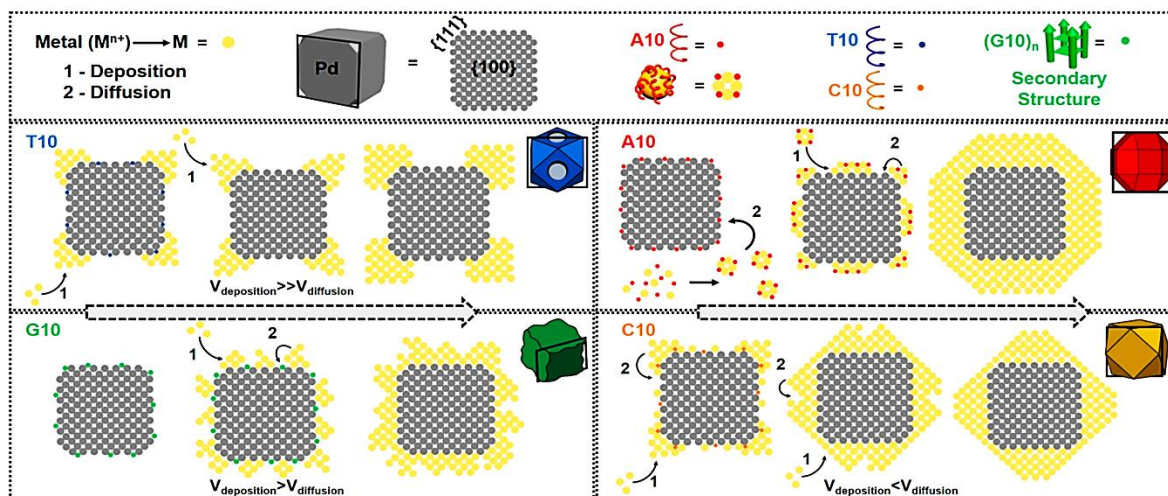


Figure 11. Proposed Mechanism of Growth of different morphological features of Pd/Au Bimetallic Nanostructures Influenced by Different Sequences of DNA. Adapted from [124]

Within the framework of this criteria, experts developed this methodology using a ~ 75 nm concave palladium cube seed as the core [126]. The aim of this study is to examine whether DNA molecules with different sequences could still exert an influence on the surface of seeds enclosed by high-energy sites. There were some significant differences between DNA-mediated growth of the Au shell onto a simple cubic core and concave cubic core as far as influence of DNA is concerned.

This occurred due to the different interactions observed between the DNA molecules and different seeds, which show different properties. Presumably, DNA in presence of simple cubic core triggers a remarkable effect from the beginning of growth of NPs. In fact, contrary to what was previously observed, the initial growth was heavily dictated by the surface energy of the seed when concave cubic core is employed [126].

Bimetallic plasmonic nanosensors consisting of gold nanorods (AuNRs) and palladium satellite nanocrystals with short interparticle spacings were also assembled with the aid of DNA linkers [127].

Other works focused on functionalizing graphene (GR) with single-stranded DNA to enable the growth of PtAu BNPs nanosensors with high densities and dispersions [128]. Integrating GR-based hybrids with DNA molecules prevents the inevitable aggregation of GR sheets, and directs the growth of BNPs with uniform distribution and high dispersion efficiency on GR. This integration leads to an improvement in creating a biosensor that determine glucose at a low applied potential with wide linear range, low detection limit, good selectivity, stability, and reproducibility [128].

J. Brinz et al. presented a gap-tailored construction of Au/Ag core-shell nanoparticle dimers using triangular DNA origami substrates. They combine DNA origami technique with SERS to provide high EF for the detection of single dye molecules (TAMRA and Cy3) [129].

The shortcomings of DNA-programmed assemblies include its difficulty in controlling the location of DNA molecules on surface of NPs. DNA molecules, used for bridging adjacent NPs, could interfere in the SERS detection of adsorbed molecular species and prevent other molecules from entering the gap region [113].

1.4.3 Seed-mediated Growth (SMG)

SMG was viewed as the most used solution-based synthetic approach for shape-selective growth of BNPs. Findings regarding this approach have led to precise manipulation of resulting nanostructures in terms of sizes, aspect ratios, and shapes when managing the growth rates of different crystallographic facets [130]. There is a vast amount of literature on synthesis of core-shell [9,76,131–134] and BNPs heterostructures [105,135,136] using this approach.

Seeded growth was effective in producing Au/Ag core-shell NPs with distinct controllable polyhedral shapes. Continuous epitaxial growth of Ag shells on spherical gold seeds yielded the formation of adjustable Au/Ag spheres, cuboctahedrons, and cubes over a large scale [137].

By tuning the concentration of the capping agent, the amount of reductant, or the rate of injection of the Pd precursor solution, Au/Pd core-shell NPs with a number of morphologies, including octahedra, rectangular bars, cubes, and dendrites were prepared [138]. These shapes were initiated by implementing a kinetic control that enables the manipulation of the rate at which atoms are generated and added to the surface of a growing seed. Figure 12 shows a schematic illustration of the morphology change with the increase in reaction rate. When the reaction rate was very low, octahedral and concave octahedral profiles mainly enclosed by $\{111\}$ facets were attained. In this case, the growth was located in the thermodynamically controlled regime where Pd atoms could migrate along the nanocrystal surface to minimize the total surface energy. A higher reaction rate generated the formation of cubes and rectangular bars enclosed by $\{100\}$ facets with higher surface energies. By increasing the reaction rate beyond the thermodynamically controlled regime, anisotropic overgrowth would emerge owing to a faster rate of atomic addition than that of adatom diffusion on the surface. Accordingly, concave cubes or branched morphologies might reveal in the final products.

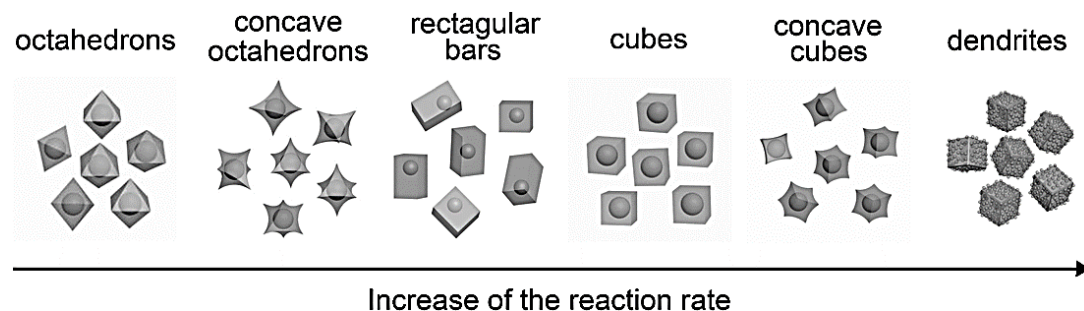


Figure 12. Schematic illustration of the evolution of morphology associated with the Au/Pd core-shell nanocrystals as a function of reaction rate. Adapted from [138]

Yanyun Ma et al. demonstrated the synthesis of Au/Ag core-shell nanocubes with controllable edge lengths in the range of 13.4-50 nm by employing spherical single-crystalline Au-CTAC seeds

(~ 11 nm in size) [139]. In order to identify the key factors of this synthesis and to provide a proposal for synthetic mechanism, Yanyun Ma et al. carried out a parametric study dealing with the influence of different parameters on the structure of BNPs during the addition of AgNO_3 , ascorbic acid, and CTAC into an aqueous suspension containing the Au seed [139]. The thickness of the Ag shells was reliably controlled from 1.2 to 20 nm by varying the ratio of AgNO_3 precursor to Au seeds. The size of the resultant Au/Ag core-shell nanocubes was varied from 13 to 50 nm depending on either the amount of AgNO_3 or the amount of Au seeds added into the reaction solution. Growth of BNPs with different capping agents (CTAB or CTAC) exhibits different impacts on both size and shape of the resultant core-shell nanocrystals. Successful size and shape control on BNPs with high yields has been reported using CTAC instead of CTAB. CTAB leads to evolution of single-crystalline Au seeds into twinned structures due to its weaker oxidative etching power relative to CTAC. Moreover, upon the addition of AgNO_3 solution, the growth step in presence of CTAB leads to the formation of a large quantity of insoluble AgBr precipitate.

By adjusting kinetic and thermodynamic factors, it is possible to optimize the overgrowth process of deposited metals to achieve the desired well-defined morphologies of BNPs [140]. It is worthwhile noting that the choice of reducing agents is of decisive importance in controlling the overgrowth mode in a seeded-growth process [141]. Through this approach, Pd/Au BNPs with distinct crystal growth processes, structures, and morphologies were developed [141]. Byungkwon Lim stated that Pd nanocubes, prepared in an aqueous solution with average edge length of ~ 10 nm, were used as seeds for the growth of HAuCl_4 in presence of two different reducing agents i.e. L-ascorbic acid and citric acid [141]. Introduction of L-ascorbic acid led to the formation of core-shell structure with a conformal overgrowth of Au on Pd, whereas with citric acid it led to formation of Pd-Au dimers adopting a heterostructure form with a localized overgrowth. The marked observation to emerge from the transition from multiple-site to single-site growth was that citric acid can stabilize the {111} facets of the deposited Au particles, thus promoting their growth into a decahedral or platelike structure whose surfaces are enclosed by {111} facets.

SUSAN E. HABAS et al. reported that the degree of lattice mismatch between two metals can also have a strong effect in directing the overgrowth of secondary metals onto well-faceted seeds [142]. In this synthesis, highly faceted cubic Pt seeds, acting as nucleation centers for overgrowth of secondary metal, were exploited in the presence of two different metals i.e. lattice-matched Pd and

lattice-mismatched Au. When there is a close lattice mismatch $\sim 0.77\%$ between seeding (Pt) and deposited metal (Pd), conformal epitaxial growth ensues and results in the formation of Pt/Pd core-shell bimetallic nanocubes. Pt/Pd core-shell nanocubes evolve into Pt/Pd core-shell cuboctahedra and octahedra respectively through an addition of increasing amounts of NO_2 which altered the growth rates along the $\langle 100 \rangle$ and $\langle 111 \rangle$ directions. This study confirmed that defined structure of Pt seed has a direct influence on the controlled overgrowth of Pd from the epitaxial interface. In other words, when growing a different material on well-faceted seeds, the control over nucleation and growth of the secondary structure can be achieved by using the defined seed morphology. Conversely, large differences in lattice mismatch $\sim 4.08\%$ between Pt and Au give rise to a heterostructure showing an anisotropic overgrowth of Au nanorods with a single partially embedded Pt cube at the perimeter.

In order to develop a deep knowledge about the growth mechanism, Feng-Ru Fan et al. rationally designed three binary metallic core-shell nanocrystals i.e. Au/Pd nanocubes, Au/Ag nanocubes, and Au/Pt nanospheres using Au octahedron seeds with two typical growth modes [143]. Mainly, the growth of M2 on the surface of M1 follows three different growth modes: Frank-van der Merwe (FM), layered growth; Volmer-Weber (VW), island growth; and Stranski – Krastanov (SK), first layered growth and later island growth [144]. As demonstrated in Figure 13, the growth of heterogeneous metal shells on the gold core follows a conformal epitaxial growth for both Au/Pd and Au/Ag nanocubes, and a heterogeneous nucleation and island growth for Au/Pt nanospheres. To acquire an epitaxial layered growth of heterogeneous core-shell nanocrystals (F-M mode), several requirements should be met: (i) lattice constants of two metals should be comparable and the lattice mismatch between the two metals should be small enough ($< 5\%$) so that not much lattice strain is introduced when the second metal (M2) is growing on the surface of the first metal (M1); (ii) the electronegativity of the shell metal is lower than the core metal in order to avoid any galvanic displacement reaction and to easily wet the surface of the core by reserving the template of the first metal for the deposition of the second metal; (iii) the bond energy between metal atoms of the shell should be smaller than that between the shell atoms and substrate atoms. Otherwise, a so-called VW growth mode takes place, causing the formation of “islands” of M2 on the M1 nanocrystal surface. Consequently, it is surprising that conformal epitaxial growth mode is applicable to Au/Pd nanocrystals with a large lattice mismatch (4.71%) but not to the Au/Pt one with relatively small lattice mismatch (3.80%). That's why other factors should be taken into

consideration. Higher Pt–Pt bond energy is mainly the factor which is responsible for the differences of growth modes between Pt and other two metals (Pd and Au) [143].

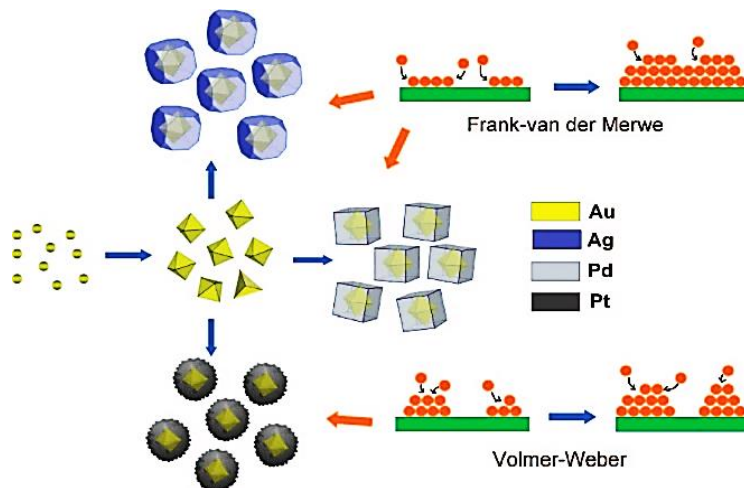


Figure 13. Schematic illustration of two typical growth modes of heterogeneous structure for binary metal core-shell nanoparticles. Adapted from [143]

1.4.4 Copolymer-mediated self-assembly

Assembling nanoscale components into ordered, isotropic, and anisotropic structures is considered as an attractive strategy for creating advanced nanomaterials with a widespread field of applications in catalysis, optoelectronics, sensing, nanomedicine, and bioimaging [145]. Among the synthetic methods of self-assembled BNPs, the use of amphiphilic di-block copolymers incorporated within colloidal NPs has been previously conducted for manufacturing multifunctional nanostructures [145–149]. Copolymer matrix was used as a structure-directing agent for inorganic components and for adjusting the self-assembly into thermodynamically highly stable micro-phase domains with precisely controlled sizes, shapes, and interparticle gap distances [145].

Block copolymer poly(styrene-block-4-vinylpyridine) (PS-*b*-P4VP) spherical micelles, with polar P4VP heads constituting the core and PS tails forming the shell, were employed as efficient building blocks for designing and encapsulating homogeneous Au/Ag alloyed arrays with well-controlled structural properties [150]. Both Au & Ag metallic salts were added to the copolymer solution, with different atomic ratios and different ordering of addition, in presence of hydrazine

monohydrate as reducing agent. BNPs were subsequently diffused into the functional P4VP core of micelles at the end of the synthesis. Convenient block copolymer chain lengths, mainly choice II, were selected in order to prevent the swelling, bursting, and coalescence of micelle cores (refer to Figure 14). This choice enabled the fabrication of stable and spherical NPs with well organization and narrow size distribution. Such an inappropriate order of depositing metallic salts (first Au, then Ag) also leads to serious consequences with regard to formation of insoluble AgCl precipitate, prior to addition of hydrazine. This also hinders the possibility of obtaining high quantities of AuAg alloys [150].

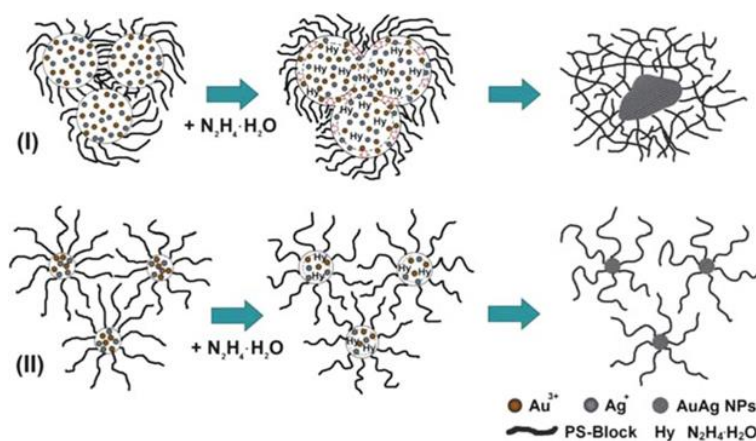


Figure 14. Schematic illustration of the formation of AuAg NPs inside BCPs: (I) PS(145)-PVP(32); and (II) PS(854)-PVP(38). Adapted from [150]

Both blocks of di-block copolymer (PS and P4VP) are totally inconsistent with each other due to their different solubilities and affinities [145]. When several requirements met, such as presence of toluene (selective solvent for PS block) and high polymer concentration, spherical micelles with two different types, either star-like or crew-cut micelles, will be spontaneously formed [145]. However, it has been observed that block copolymer amphiphiles can be assembled into vesicles and other morphologies with remarkable different properties as mentioned in Figure 15.

Controlling micelle's morphology through adding a co-solvent (i.e. water) shifted the morphology from micelles into rods and rings (1D nanostructures) as well as vesicles (2D nanostructures) by selectively swelling the micelle's P4VP core. This indicated that micelle's morphology can be adjusted by varying the degree of swelling of the metal loaded P4VP block, thus providing an important role in stabilizing NPs in solution as well as tuning their diameter, dimensions, and distances when deposited onto solid substrates. The ultimate morphology is also determined by the degree of polymerization and the relative composition of the different blocks [145].

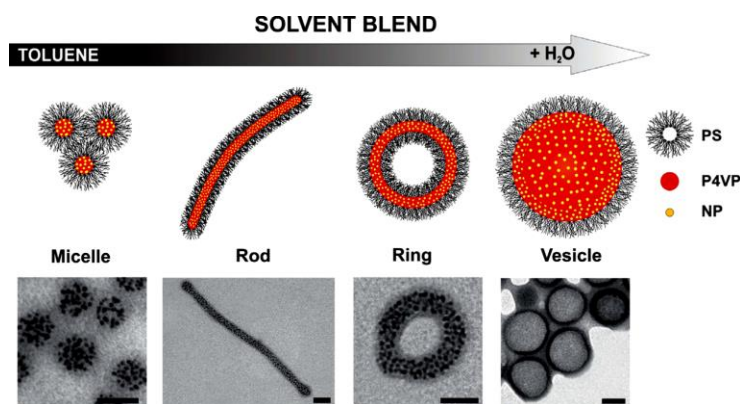


Figure 15. Controlling the micelle morphology through the addition of a co-solvent (H_2O), which selectively swells the micelle's core (P4VP). The morphology is shifted from spherical micelles to rods (or cylinders) and rings as well as vesicles. The TEM micrographs show each of the morphologies separately, where the nanoparticles appear as dark spots in the polymer matrix. The scale bar in the micrographs is 50 nm. Adapted from [145]

Preliminary work in this field focused primarily on co-encapsulation of different types of NPs in the hydrophobic core of the block copolymer micelles [151]. Later, Sunita Sanwaria et al. have confirmed that one type of nanoparticle could be formed in core and the other NP driven to the shell of block copolymer micelles [151]. As can be seen in Figure 16, PS-b-P4VP block copolymer micelles, acting as nanoreactors for fabricating multifunctional core-shell nanofibers, were self-assembled and elongated into a cylindrical shape. PS-coated AgNPs (Nanoparticle 1) were directly combined with cylindrical PS domains of block copolymer. Then, a selective solvent for P4VP was added to the encased Ag-PS-b-P4VP to generate swelling of the P4VP matrix, disintegration, and release of isolated cylindrical domains in the form of nanofibers. The presence of the isolated nanofibers with Ag-loaded-PS core and P4VP shell, enables the immediate contact and interaction

of Au (Nanoparticle 2) with the reactive P4VP shell and protects the encapsulated particles in the core [151].

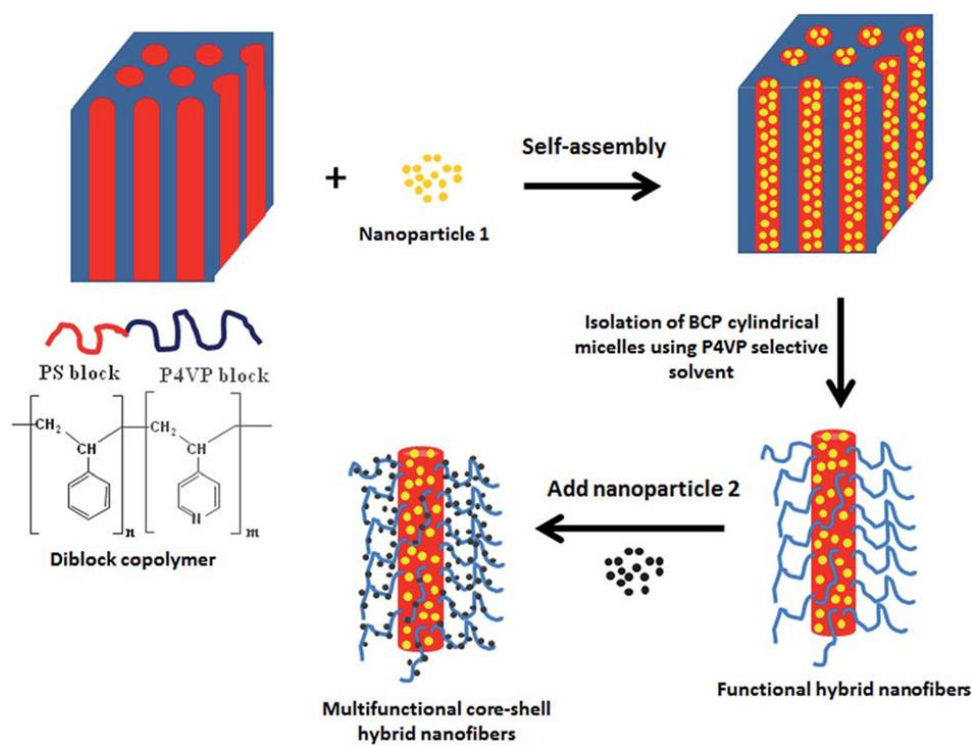


Figure 16. Schematic illustration for the preparation of multifunctional core-shell nanofibers functionalized with two different types of nanoparticles loaded in the core and in the shell from self-assembled block copolymer template via selective solvent approach. Adapted from [151]

Block copolymer templated synthesis was also devised for fabricating Au/Pt [152] and Pd/Pt [153] core-shell structures, arrays of Pt/Ir alloy nanoclusters [154] and Pd/Ag alloy NPs [155].

In particular, major previous efforts and studies were widely concentrating on the fabrication of metallic NPs, using amphiphilic diblock copolymers as templates, via self-assembly approach. Regardless of its great success, most of these methods suffer from a plethora of pitfalls due to the need of many purification steps to obtain purely metallic NPs i.e. selective functionalization of polymer, usage of reducing agents for reduction of metallic salts, and extraction of polymer film via etching or thermal annealing under Ar [156]. It is unfortunate that most of studies have been carried out by fabrication methods that need long processing times and laborious steps.

1.4.5 Other Synthetic Approaches

Table 2 shows a list of different biological, physical, and chemical approaches used for the fabrication of bimetallic nanostructures.

Table 2. List of other synthetic approaches for BNPs

Synthetic Approach	References
Femtosecond Laser Ablation	[157]
Radiolysis	[158,159]
Microemulsions	[160,161]
Biogenic Synthesis	[162,163]
Impregnation method	[164]
Sonochemical Synthesis	[165,166]
Atomic layer deposition	[167]
Solvothermal hot-injection	[77,168]
Sputtering process	[169]
Laser induced dewetting	[170]
Chemical reduction methods	[85,171]
Hydrothermal Synthesis	[25]
Polyol process	[172]
Photodeposition	[173,174]
Galvanic Replacement reactions	[175,176]
Thermal Annealing of metallic films	[50]

1.5 Conclusion

According to the state of art, most studies have tended to focus on solution-based synthetic approaches for shape-selective growth of BNPs. Despite its shortcomings, only lithographic routes have been applied for a direct fabrication of BNPs on surface. The main drawbacks that limit the potential of lithographic technique in manufacturing of large-scale substrates include its high cost, low throughput, and complexity due to its multiple steps and long reaction times. Nevertheless, in comparison to self-assembly methods, lithography is not well-suited for producing controlled nanogaps below 10 nm. Herein, we identify a solution to this dilemma by fabricating BNPs substrates chemically due to the ease of preparation and the stronger Raman enhancements with respect to the physical methods. This thesis is an overview of a preliminary attempt to synthesize

different types of BNPs systems with controlled structural properties on surface via a convenient synthetic chemical route, known as VIPS approach, that requires a marked decrease in the reaction time, and the lack of using any reducing agents and complicated equipment. This innovative approach will be explored in more detail in the next chapters. This strategy has the ability to outperform all previous approaches, by allowing the conducting surface to be responsible for the transfer of electrons to the metallic salts via a simple reduction reaction, and providing an improved control on structural properties. Until now, this methodology has only been applied to monometallic NPs. Within the framework of this criteria, our main target is intended towards fabricating Ag/Au BNPs due to the important traits achieved from this integration. This would be extremely valuable for extending their fundamental properties and applications in plasmonic sensing.

1.6 References

- [1] Zhang, Y.-W., 2018, *Bimetallic Nanostructures: Shape-Controlled Synthesis for Catalysis, Plasmonics, and Sensing Applications*, John Wiley & Sons.
- [2] Ferrando, R., Jellinek, J., and Johnston, R. L., 2008, “Nanoalloys: From Theory to Applications of Alloy Clusters and Nanoparticles,” *Chemical reviews*, **108**(3), pp. 845–910.
- [3] Zaleska-Medynska, A., Marchelek, M., Diak, M., and Grabowska, E., 2016, “Noble Metal-Based Bimetallic Nanoparticles: The Effect of the Structure on the Optical, Catalytic and Photocatalytic Properties,” *Advances in colloid and interface science*, **229**, pp. 80–107.
- [4] Srinoi, P., Chen, Y.-T., Vittur, V., Marquez, M. D., and Lee, T. R., 2018, “Bimetallic Nanoparticles: Enhanced Magnetic and Optical Properties for Emerging Biological Applications,” *Applied Sciences*, **8**(7), p. 1106.
- [5] Zhang, W., and Lu, X., 2013, “Morphology Control of Bimetallic Nanostructures for Electrochemical Catalysts,” *Nanotechnology Reviews*, **2**(5), pp. 487–514.
- [6] Wang, C., Hou, Y., Kim, J., and Sun, S., 2007, “A General Strategy for Synthesizing FePt Nanowires and Nanorods,” *Angewandte Chemie*, **119**(33), pp. 6449–6451.
- [7] Wang, D., Zhao, P., and Li, Y., 2011, “General Preparation for Pt-Based Alloy Nanoporous Nanoparticles as Potential Nanocatalysts,” *Scientific reports*, **1**(1), pp. 1–5.
- [8] Zeng, J., Zhu, C., Tao, J., Jin, M., Zhang, H., Li, Z.-Y., Zhu, Y., and Xia, Y., 2012, “Controlling the Nucleation and Growth of Silver on Palladium Nanocubes by Manipulating the Reaction Kinetics,” *Angewandte Chemie*, **124**(10), pp. 2404–2408.
- [9] Kim, D., Lee, Y. W., Lee, S. B., and Han, S. W., 2012, “Convex Polyhedral Au@Pd Core–Shell Nanocrystals with High-Index Facets,” *Angewandte Chemie International Edition*, **51**(1), pp. 159–163.
- [10] Gu, J., Zhang, Y.-W., and Tao, F. F., 2012, “Shape Control of Bimetallic Nanocatalysts through Well-Designed Colloidal Chemistry Approaches,” *Chemical Society Reviews*, **41**(24), pp. 8050–8065.
- [11] Akinsiku, A. A., Dare, E. O., Ajani, O. O., Ayo-Ajayi, J., Ademosun, O. T., and Ajayi, S. O., 2018, “Room Temperature Phytosynthesis of Ag/Co Bimetallic Nanoparticles Using Aqueous Leaf Extract of *Canna Indica*,” *IOP Conference Series: Earth and Environmental Science*, IOP Publishing, p. 012019.

- [12] Sharma, G., Kumar, A., Sharma, S., Naushad, M., Dwivedi, R. P., AlOthman, Z. A., and Mola, G. T., 2019, "Novel Development of Nanoparticles to Bimetallic Nanoparticles and Their Composites: A Review," *Journal of King Saud University-Science*, **31**(2), pp. 257–269.
- [13] Chen, S., Wang, L., Dong, X., Liu, X., Zhou, J., Yang, J., and Zha, L., 2016, "Fabrication of Monodispersed Au@ Ag Bimetallic Nanorod-Loaded Nanofibrous Membrane with Fast Thermo-Responsiveness and Its Use as a Smart Free-Standing SERS Substrate," *RSC advances*, **6**(54), pp. 48479–48488.
- [14] Zhang, Y., Shoaib, A., Li, J., Ji, M., Liu, J., Xu, M., Tong, B., Zhang, J., and Wei, Q., 2016, "Plasmon Enhanced Photoelectrochemical Sensing of Mercury (II) Ions in Human Serum Based on Au@ Ag Nanorods Modified TiO₂ Nanosheets Film," *Biosensors and Bioelectronics*, **79**, pp. 866–873.
- [15] Carrillo-Torres, R. C., García-Soto, M. J., Morales-Chávez, S. D., Garibay-Escobar, A., Hernández-Paredes, J., Guzman, R., Barboza-Flores, M., and Álvarez-Ramos, M. E., 2016, "Hollow Au–Ag Bimetallic Nanoparticles with High Photothermal Stability," *RSC advances*, **6**(47), pp. 41304–41312.
- [16] Cui, L., Wang, A., Wu, D.-Y., Ren, B., and Tian, Z.-Q., 2008, "Shaping and Shelling Pt and Pd Nanoparticles for Ultraviolet Laser Excited Surface-Enhanced Raman Scattering," *The Journal of Physical Chemistry C*, **112**(45), pp. 17618–17624.
- [17] Sun, Y., Wiley, B., Li, Z.-Y., and Xia, Y., 2004, "Synthesis and Optical Properties of Nanorattles and Multiple-Walled Nanoshells/Nanotubes Made of Metal Alloys," *Journal of the American Chemical Society*, **126**(30), pp. 9399–9406.
- [18] Xu, J. B., Zhao, T. S., and Liang, Z. X., 2008, "Synthesis of Active Platinum- Silver Alloy Electrocatalyst toward the Formic Acid Oxidation Reaction," *The Journal of Physical Chemistry C*, **112**(44), pp. 17362–17367.
- [19] Remita, H., Khatouri, J., Treguer, M., Amblard, J., and Belloni, J., 1997, "Silver-Palladium Alloyed Clusters Synthesized by Radiolysis," *Zeitschrift für Physik D Atoms, Molecules and Clusters*, **40**(1), pp. 127–130.
- [20] Sun, Y., and Xia, Y., 2004, "Mechanistic Study on the Replacement Reaction between Silver Nanostructures and Chloroauric Acid in Aqueous Medium," *Journal of the American Chemical Society*, **126**(12), pp. 3892–3901.

- [21] Skrabalak, S. E., Au, L., Li, X., and Xia, Y., 2007, “Facile Synthesis of Ag Nanocubes and Au Nanocages,” *Nature protocols*, **2**(9), pp. 2182–2190.
- [22] Kim, D., Resasco, J., Yu, Y., Asiri, A. M., and Yang, P., 2014, “Synergistic Geometric and Electronic Effects for Electrochemical Reduction of Carbon Dioxide Using Gold–Copper Bimetallic Nanoparticles,” *Nature communications*, **5**(1), pp. 1–8.
- [23] Xu, D., Bliznakov, S., Liu, Z., Fang, J., and Dimitrov, N., 2010, “Composition-Dependent Electrocatalytic Activity of Pt-Cu Nanocube Catalysts for Formic Acid Oxidation,” *Angewandte Chemie*, **122**(7), pp. 1304–1307.
- [24] Kim, J.-S., Kim, H.-K., Kim, S.-H., Kim, I., Yu, T., Han, G.-H., Lee, K.-Y., Lee, J.-C., and Ahn, J.-P., 2019, “Catalytically Active Au Layers Grown on Pd Nanoparticles for Direct Synthesis of H₂O₂: Lattice Strain and Charge-Transfer Perspective Analyses,” *ACS nano*, **13**(4), pp. 4761–4770.
- [25] Yin, A.-X., Min, X.-Q., Zhang, Y.-W., and Yan, C.-H., 2011, “Shape-Selective Synthesis and Facet-Dependent Enhanced Electrocatalytic Activity and Durability of Monodisperse Sub-10 Nm Pt- Pd Tetrahedrons and Cubes,” *Journal of the American Chemical Society*, **133**(11), pp. 3816–3819.
- [26] Jiang, F., Li, R., Cai, J., Xu, W., Cao, A., Chen, D., Zhang, X., Wang, C., and Shu, C., 2015, “Ultrasmall Pd/Au Bimetallic Nanocrystals Embedded in Hydrogen-Bonded Supramolecular Structures: Facile Synthesis and Catalytic Activities in the Reduction of 4-Nitrophenol,” *Journal of Materials Chemistry A*, **3**(38), pp. 19433–19438.
- [27] Arora, N., Mehta, A., Mishra, A., and Basu, S., 2018, “4-Nitrophenol Reduction Catalysed by Au-Ag Bimetallic Nanoparticles Supported on LDH: Homogeneous vs. Heterogeneous Catalysis,” *Applied Clay Science*, **151**, pp. 1–9.
- [28] Pergolese, B., Bigotto, A., Muniz-Miranda, M., and Sbrana, G., 2005, “Gold/Palladium and Silver/Palladium Colloids as Novel Metallic Substrates for Surface-Enhanced Raman Scattering,” *Applied spectroscopy*, **59**(2), pp. 194–199.
- [29] Muniz-Miranda, M., Caporali, S., Marsili, P., and Giorgetti, E., 2015, “Fabrication and Characterization of Ag/Pd Colloidal Nanoparticles as Stable Platforms for SERS and Catalytic Applications,” *Materials Chemistry and Physics*, **167**, pp. 188–193.

- [30] Muniz-Miranda, M., Gellini, C., Canton, P., Marsili, P., and Giorgetti, E., 2014, “SERS and Catalytically Active Ag/Pd Nanoparticles Obtained by Combining Laser Ablation and Galvanic Replacement,” *Journal of alloys and compounds*, **615**, pp. S352–S356.
- [31] Tan, D., Zhang, J., Shi, J., Li, S., Zhang, B., Tan, X., Zhang, F., Liu, L., Shao, D., and Han, B., 2018, “Photocatalytic CO₂ Transformation to CH₄ by Ag/Pd Bimetals Supported on N-Doped TiO₂ Nanosheet,” *ACS applied materials & interfaces*, **10**(29), pp. 24516–24522.
- [32] Idakiev, V., Ilieva, L., Andreeva, D., Blin, J.-L., Gigot, L., and Su, B.-L., 2003, “Complete Benzene Oxidation over Gold-Vanadia Catalysts Supported on Nanostructured Mesoporous Titania and Zirconia,” *Applied Catalysis A: General*, **243**(1), pp. 25–39.
- [33] Hosseini, M., Barakat, T., Cousin, R., Aboukais, A., Su, B.-L., De Weireld, G., and Siffert, S., 2012, “Catalytic Performance of Core–Shell and Alloy Pd–Au Nanoparticles for Total Oxidation of VOC: The Effect of Metal Deposition,” *Applied Catalysis B: Environmental*, **111**, pp. 218–224.
- [34] Lodewijks, K., Van Roy, W., Borghs, G., Lagae, L., and Van Dorpe, P., 2012, “Boosting the Figure-of-Merit of LSPR-Based Refractive Index Sensing by Phase-Sensitive Measurements,” *Nano letters*, **12**(3), pp. 1655–1659.
- [35] Weng, Y.-C., and Hsiao, Y.-L., 2011, “Comparison of Pt and Ni Foil Electrodes for Amperometric Sensing of Ascorbic Acid,” *Journal of electroanalytical chemistry*, **651**(2), pp. 160–165.
- [36] Huang, Y., Miao, Y.-E., Ji, S., Tjiu, W. W., and Liu, T., 2014, “Electrospun Carbon Nanofibers Decorated with Ag–Pt Bimetallic Nanoparticles for Selective Detection of Dopamine,” *ACS applied materials & interfaces*, **6**(15), pp. 12449–12456.
- [37] Wang, J., Song, D., Wang, L., Zhang, H., Zhang, H., and Sun, Y., 2011, “Design and Performances of Immunoassay Based on SPR Biosensor with Au/Ag Alloy Nanocomposites,” *Sensors and Actuators B: Chemical*, **157**(2), pp. 547–553.
- [38] Gao, C., Lu, Z., Liu, Y., Zhang, Q., Chi, M., Cheng, Q., and Yin, Y., 2012, “Highly Stable Silver Nanoplates for Surface Plasmon Resonance Biosensing,” *Angewandte Chemie International Edition*, **51**(23), pp. 5629–5633.
- [39] Liu, N., Tang, M. L., Hentschel, M., Giessen, H., and Alivisatos, A. P., 2011, “Nanoantenna-Enhanced Gas Sensing in a Single Tailored Nanofocus,” *Nature materials*, **10**(8), pp. 631–636.

- [40] Chiu, C.-Y., and Huang, M. H., 2013, "Polyhedral Au–Pd Core–Shell Nanocrystals as Highly Spectrally Responsive and Reusable Hydrogen Sensors in Aqueous Solution," *Angewandte Chemie*, **125**(48), pp. 12941–12945.
- [41] He, H., Xu, X., Wu, H., and Jin, Y., 2012, "Enzymatic Plasmonic Engineering of Ag/Au Bimetallic Nanoshells and Their Use for Sensitive Optical Glucose Sensing," *Advanced Materials*, **24**(13), pp. 1736–1740.
- [42] Gong, J., Zhou, T., Song, D., Zhang, L., and Hu, X., 2010, "Stripping Voltammetric Detection of Mercury (II) Based on a Bimetallic Au- Pt Inorganic- Organic Hybrid Nanocomposite Modified Glassy Carbon Electrode," *Analytical chemistry*, **82**(2), pp. 567–573.
- [43] Zeng, J., Cao, Y., Chen, J., Wang, X., Yu, J., Yu, B., Yan, Z., and Chen, X., 2014, "Au@Ag Core/Shell Nanoparticles as Colorimetric Probes for Cyanide Sensing," *Nanoscale*, **6**(17), pp. 9939–9943.
- [44] Muniz-Miranda, M., 2015, "Application of the SERS Spectroscopy to the Study of Catalytic Reactions by Means of Mono and Bimetallic Nanoparticles," *Journal of Analytical & Bioanalytical Techniques*, **6**(6), p. 1.
- [45] Sivanesan, A., Witkowska, E., Adamkiewicz, W., Dziewit, \Lukasz, Kamińska, A., and Waluk, J., 2014, "Nanostructured Silver–Gold Bimetallic SERS Substrates for Selective Identification of Bacteria in Human Blood," *Analyst*, **139**(5), pp. 1037–1043.
- [46] Xie, W., and Schlücker, S., 2018, "Surface-Enhanced Raman Spectroscopic Detection of Molecular Chemo-and Plasmo-Catalysis on Noble Metal Nanoparticles," *Chemical Communications*, **54**(19), pp. 2326–2336.
- [47] Sharma, B., Frontiera, R. R., Henry, A.-I., Ringe, E., and Van Duyne, R. P., 2012, "SERS: Materials, Applications, and the Future," *Materials today*, **15**(1–2), pp. 16–25.
- [48] Wang, H., Li, K. B., Xu, C., Xu, S. C., and Li, G. H., 2019, "Large-Scale Solvothermal Synthesis of Ag Nanocubes with High SERS Activity," *Journal of Alloys and Compounds*, **772**, pp. 150–156.
- [49] Hasna, K., Lakshmi, K., Jayaraj, M. K. E., Kumar, K. R., and Matham, M. V., 2016, "Development of High-Sensitive, Reproducible Colloidal Surface-Enhanced Raman Spectroscopy Active Substrate Using Silver Nanocubes for Potential Biosensing Applications," *Journal of Nanophotonics*, **10**(2), p. 026020.

- [50] Khaywah, M. Y., Jradi, S., Louarn, G., Lacroute, Y., Toufaily, J., Hamieh, T., and Adam, P.-M., 2015, "Ultrastable, Uniform, Reproducible, and Highly Sensitive Bimetallic Nanoparticles as Reliable Large Scale SERS Substrates," *The Journal of Physical Chemistry C*, **119**(46), pp. 26091–26100.
- [51] Li, J., Liu, J., Yang, Y., and Qin, D., 2015, "Bifunctional Ag@Pd-Ag Nanocubes for Highly Sensitive Monitoring of Catalytic Reactions by Surface-Enhanced Raman Spectroscopy," *Journal of the American Chemical Society*, **137**(22), pp. 7039–7042.
- [52] Liu, K., Bai, Y., Zhang, L., Yang, Z., Fan, Q., Zheng, H., Yin, Y., and Gao, C., 2016, "Porous Au–Ag Nanospheres with High-Density and Highly Accessible Hotspots for SERS Analysis," *Nano letters*, **16**(6), pp. 3675–3681.
- [53] Yang, Y., Shi, J., Kawamura, G., and Nogami, M., 2008, "Preparation of Au–Ag, Ag–Au Core–Shell Bimetallic Nanoparticles for Surface-Enhanced Raman Scattering," *Scripta Materialia*, **58**(10), pp. 862–865.
- [54] Zhang, L.-F., Zhong, S.-L., and Xu, A.-W., 2013, "Highly Branched Concave Au/Pd Bimetallic Nanocrystals with Superior Electrocatalytic Activity and Highly Efficient SERS Enhancement," *Angewandte Chemie International Edition*, **52**(2), pp. 645–649.
- [55] Shen, J., Su, J., Yan, J., Zhao, B., Wang, D., Wang, S., Li, K., Liu, M., He, Y., and Mathur, S., 2015, "Bimetallic Nano-Mushrooms with DNA-Mediated Interior Nanogaps for High-Efficiency SERS Signal Amplification," *Nano Research*, **8**(3), pp. 731–742.
- [56] Rashidi-Huyeh, M., and Palpant, B., 2004, "Thermal Response of Nanocomposite Materials under Pulsed Laser Excitation," *Journal of applied physics*, **96**(8), pp. 4475–4482.
- [57] Roper, D. K., Ahn, W., and Hoepfner, M., 2007, "Microscale Heat Transfer Transduced by Surface Plasmon Resonant Gold Nanoparticles," *The Journal of Physical Chemistry C*, **111**(9), pp. 3636–3641.
- [58] Hu, M., and Hartland, G. V., 2002, "Heat Dissipation for Au Particles in Aqueous Solution: Relaxation Time versus Size," *The Journal of Physical Chemistry B*, **106**(28), pp. 7029–7033.
- [59] Zeng, N., and Murphy, A. B., 2009, "Heat Generation by Optically and Thermally Interacting Aggregates of Gold Nanoparticles under Illumination," *Nanotechnology*, **20**(37), p. 375702.

- [60] Jain, P. K., Lee, K. S., El-Sayed, I. H., and El-Sayed, M. A., 2006, “Calculated Absorption and Scattering Properties of Gold Nanoparticles of Different Size, Shape, and Composition: Applications in Biological Imaging and Biomedicine,” *The journal of physical chemistry B*, **110**(14), pp. 7238–7248.
- [61] Chen, M., He, Y., and Zhu, J., 2017, “Preparation of Au–Ag Bimetallic Nanoparticles for Enhanced Solar Photothermal Conversion,” *International Journal of Heat and Mass Transfer*, **114**, pp. 1098–1104.
- [62] Wu, D., Kusada, K., and Kitagawa, H., 2016, “Recent Progress in the Structure Control of Pd–Ru Bimetallic Nanomaterials,” *Science and Technology of advanced Materials*, **17**(1), pp. 583–596.
- [63] Tyson, W. R., and Miller, W. A., 1977, “Surface Free Energies of Solid Metals: Estimation from Liquid Surface Tension Measurements,” *Surface Science*, **62**(1), pp. 267–276.
- [64] De Boer, F. R., Mattens, W., Boom, R., Miedema, A. R., and Niessen, A. K., 1988, “Cohesion in Metals. Transition Metal Alloys.”
- [65] Lide, D. R., 2004, *CRC Handbook of Chemistry and Physics*, CRC press.
- [66] Cottrell, T. L., 1958, *The Strengths of Chemical Bonds*, Butterworths Scientific Publications.
- [67] Wilkinson, P. G., 1963, “Diatomic Molecules of Astrophysical Interest: Ionization Potentials and Dissociation Energies,” *The Astrophysical Journal*, **138**, p. 778.
- [68] Darwent, B. deB, 1970, “Bond Dissociation Energies in Simple Molecules.”
- [69] Benson, S. W., 1965, “III-Bond Energies,” *Journal of Chemical Education*, **42**(9), p. 502.
- [70] Kerr, J. A., 1966, “Bond Dissociation Energies by Kinetic Methods,” *Chemical reviews*, **66**(5), pp. 465–500.
- [71] Ackerman, M., Stafford, F. E., and Drowart, J., 1960, “Mass Spectrometric Determination of the Dissociation Energies of the Molecules Ag–Au, AgCu, and AuCu,” *The Journal of Chemical Physics*, **33**(6), pp. 1784–1789.
- [72] Tojo, C., and Vila-Romeu, N., 2014, “Kinetic Study on the Formation of Bimetallic Core-Shell Nanoparticles via Microemulsions,” *Materials*, **7**(11), pp. 7513–7532.
- [73] Kariuki, N. N., Luo, J., Maye, M. M., Hassan, S. A., Menard, T., Naslund, H. R., Lin, Y., Wang, C., Engelhard, M. H., and Zhong, C.-J., 2004, “Composition-Controlled Synthesis of Bimetallic Gold- Silver Nanoparticles,” *Langmuir*, **20**(25), pp. 11240–11246.

- [74] Rodríguez-González, B., Burrows, A., Watanabe, M., Kiely, C. J., and Marzán, L. M. L., 2005, “Multishell Bimetallic AuAg Nanoparticles: Synthesis, Structure and Optical Properties,” *Journal of Materials Chemistry*, **15**(17), pp. 1755–1759.
- [75] Ni, Y., Kan, C., He, L., Zhu, X., Jiang, M., and Shi, D., 2019, “Alloyed Au-Ag Nanorods with Desired Plasmonic Properties and Stability in Harsh Environments,” *Photonics Research*, **7**(5), pp. 558–565.
- [76] Srnová-Šloufová, I., Lednický, F., Gemperle, A., and Gemperlová, J., 2000, “Core-Shell (Ag) Au Bimetallic Nanoparticles: Analysis of Transmission Electron Microscopy Images,” *Langmuir*, **16**(25), pp. 9928–9935.
- [77] Wang, C., Peng, S., Chan, R., and Sun, S., 2009, “Synthesis of AuAg Alloy Nanoparticles from Core/Shell-Structured Ag/Au,” *small*, **5**(5), pp. 567–570.
- [78] Mallin, M. P., and Murphy, C. J., 2002, “Solution-Phase Synthesis of Sub-10 Nm Au-Ag Alloy Nanoparticles,” *Nano Letters*, **2**(11), pp. 1235–1237.
- [79] Chen, D.-H., and Chen, C.-J., 2002, “Formation and Characterization of Au–Ag Bimetallic Nanoparticles in Water-in-Oil Microemulsions,” *Journal of Materials Chemistry*, **12**(5), pp. 1557–1562.
- [80] Shmarakov, I., Mukha, I., Vityuk, N., Borschovetska, V., Zhyschynska, N., Grodzyuk, G., and Eremenko, A., 2017, “Antitumor Activity of Alloy and Core-Shell-Type Bimetallic Ag-Au Nanoparticles,” *Nanoscale research letters*, **12**(1), pp. 1–10.
- [81] Mulvaney, P., Giersig, M., and Henglein, A., 1993, “Electrochemistry of Multilayer Colloids: Preparation and Absorption Spectrum of Gold-Coated Silver Particles,” *The Journal of Physical Chemistry*, **97**(27), pp. 7061–7064.
- [82] Bhoi, V. I., Kumar, S., and Murthy, C. N., 2016, “Cyclodextrin Encapsulated Monometallic and Inverted Core–Shell Bimetallic Nanoparticles as Efficient Free Radical Scavengers,” *New Journal of Chemistry*, **40**(2), pp. 1396–1402.
- [83] Yaseen, T., Pu, H., and Sun, D.-W., 2019, “Fabrication of Silver-Coated Gold Nanoparticles to Simultaneously Detect Multi-Class Insecticide Residues in Peach with SERS Technique,” *Talanta*, **196**, pp. 537–545.
- [84] Zhang, L., Xie, Z., and Gong, J., 2016, “Shape-Controlled Synthesis of Au–Pd Bimetallic Nanocrystals for Catalytic Applications,” *Chemical Society Reviews*, **45**(14), pp. 3916–3934.

- [85] Li, S., Wei, T., Tang, M., Chai, F., Qu, F., and Wang, C., 2018, “Facile Synthesis of Bimetallic Ag-Cu Nanoparticles for Colorimetric Detection of Mercury Ion and Catalysis,” *Sensors and Actuators B: Chemical*, **255**, pp. 1471–1481.
- [86] Nasrabadi, H. T., Abbasi, E., Davaran, S., Kouhi, M., and Akbarzadeh, A., 2016, “Bimetallic Nanoparticles: Preparation, Properties, and Biomedical Applications,” *Artificial cells, nanomedicine, and biotechnology*, **44**(1), pp. 376–380.
- [87] Lim, B., Jiang, M., Camargo, P. H., Cho, E. C., Tao, J., Lu, X., Zhu, Y., and Xia, Y., 2009, “Pd-Pt Bimetallic Nanodendrites with High Activity for Oxygen Reduction,” *science*, **324**(5932), pp. 1302–1305.
- [88] Lim, B., Jiang, M., Yu, T., Camargo, P. H., and Xia, Y., 2010, “Nucleation and Growth Mechanisms for Pd-Pt Bimetallic Nanodendrites and Their Electrocatalytic Properties,” *Nano Research*, **3**(2), pp. 69–80.
- [89] Peng, Z., and Yang, H., 2009, “Synthesis and Oxygen Reduction Electrocatalytic Property of Pt-on-Pd Bimetallic Heteronanostructures,” *Journal of the American Chemical Society*, **131**(22), pp. 7542–7543.
- [90] Wang, L., Nemoto, Y., and Yamauchi, Y., 2011, “Direct Synthesis of Spatially-Controlled Pt-on-Pd Bimetallic Nanodendrites with Superior Electrocatalytic Activity,” *Journal of the American Chemical Society*, **133**(25), pp. 9674–9677.
- [91] Ataee-Esfahani, H., Wang, L., Nemoto, Y., and Yamauchi, Y., 2010, “Synthesis of Bimetallic Au@ Pt Nanoparticles with Au Core and Nanostructured Pt Shell toward Highly Active Electrocatalysts,” *Chemistry of Materials*, **22**(23), pp. 6310–6318.
- [92] Ksar, F., Ramos, L., Keita, B., Nadjo, L., Beaunier, P., and Remita, H., 2009, “Bimetallic Palladium- Gold Nanostructures: Application in Ethanol Oxidation,” *Chemistry of Materials*, **21**(15), pp. 3677–3683.
- [93] Yuan, Q., Zhou, Z., Zhuang, J., and Wang, X., 2010, “Pd–Pt Random Alloy Nanocubes with Tunable Compositions and Their Enhanced Electrocatalytic Activities,” *Chemical communications*, **46**(9), pp. 1491–1493.
- [94] Zhang, H., Jin, M., Wang, J., Li, W., Camargo, P. H., Kim, M. J., Yang, D., Xie, Z., and Xia, Y., 2011, “Synthesis of Pd- Pt Bimetallic Nanocrystals with a Concave Structure through a Bromide-Induced Galvanic Replacement Reaction,” *Journal of the American Chemical Society*, **133**(15), pp. 6078–6089.

- [95] Lee, Y. W., Kim, M., Kang, S. W., and Han, S. W., 2011, “Polyhedral Bimetallic Alloy Nanocrystals Exclusively Bound by {110} Facets: Au–Pd Rhombic Dodecahedra,” *Angewandte Chemie International Edition*, **50**(15), pp. 3466–3470.
- [96] Hong, J. W., Kim, M., Kim, Y., and Han, S. W., 2012, “Tris octahedral Au–Pd Alloy Nanocrystals with High-Index Facets and Their Excellent Catalytic Performance,” *Chemistry—A European Journal*, **18**(52), pp. 16626–16630.
- [97] Tsuji, M., Takemura, K., Shiraishi, C., Uto, K., Yoshida, Y., and Daio, T., 2013, “Synthesis of Cubic Pd–Ag Random Alloy Nanocrystal in an Aqueous Solution in the Presence of CTAB,” *Materials Letters*, **95**, pp. 201–204.
- [98] Zhang, W., Yang, J., and Lu, X., 2012, “Tailoring Galvanic Replacement Reaction for the Preparation of Pt/Ag Bimetallic Hollow Nanostructures with Controlled Number of Voids,” *ACS nano*, **6**(8), pp. 7397–7405.
- [99] Zhang, L., Zhang, J., Jiang, Z., Xie, S., Jin, M., Han, X., Kuang, Q., Xie, Z., and Zheng, L., 2011, “Facile Syntheses and Electrocatalytic Properties of Porous Pd and Its Alloy Nanospheres,” *Journal of Materials Chemistry*, **21**(26), pp. 9620–9625.
- [100] Zhang, H., Jin, M., Liu, H., Wang, J., Kim, M. J., Yang, D., Xie, Z., Liu, J., and Xia, Y., 2011, “Facile Synthesis of Pd–Pt Alloy Nanocages and Their Enhanced Performance for Preferential Oxidation of CO in Excess Hydrogen,” *Acs Nano*, **5**(10), pp. 8212–8222.
- [101] Wu, K.-J., Gao, Y., and Torrente-Murciano, L., 2018, “Continuous Synthesis of Hollow Silver–Palladium Nanoparticles for Catalytic Applications,” *Faraday discussions*, **208**, pp. 427–441.
- [102] Li, J., Sun, X., and Qin, D., 2016, “Ag-Enriched Ag–Pd Bimetallic Nanoframes and Their Catalytic Properties,” *ChemNanoMat*, **2**(6), pp. 494–499.
- [103] Xie, S., Lu, N., Xie, Z., Wang, J., Kim, M. J., and Xia, Y., 2012, “Synthesis of Pd–Rh Core–Frame Concave Nanocubes and Their Conversion to Rh Cubic Nanoframes by Selective Etching of the Pd Cores,” *Angewandte Chemie International Edition*, **51**(41), pp. 10266–10270.
- [104] Zhu, C., Zeng, J., Tao, J., Johnson, M. C., Schmidt-Krey, I., Blubaugh, L., Zhu, Y., Gu, Z., and Xia, Y., 2012, “Kinetically Controlled Overgrowth of Ag or Au on Pd Nanocrystal Seeds: From Hybrid Dimers to Nonconcentric and Concentric Bimetallic Nanocrystals,” *Journal of the American Chemical Society*, **134**(38), pp. 15822–15831.

- [105] Lu, C.-L., Prasad, K. S., Wu, H.-L., Ho, J. A., and Huang, M. H., 2010, “Au Nanocube-Directed Fabrication of Au- Pd Core- Shell Nanocrystals with Tetrahedral, Concave Octahedral, and Octahedral Structures and Their Electrocatalytic Activity,” *Journal of the American Chemical Society*, **132**(41), pp. 14546–14553.
- [106] Yu, Y., Zhang, Q., Liu, B., and Lee, J. Y., 2010, “Synthesis of Nanocrystals with Variable High-Index Pd Facets through the Controlled Heteroepitaxial Growth of Trisoctahedral Au Templates,” *Journal of the American Chemical Society*, **132**(51), pp. 18258–18265.
- [107] Wang, L., Xiong, W., Nishijima, Y., Yokota, Y., Ueno, K., Misawa, H., Qiu, J., and Bi, G., 2011, “Spectral Properties of Nanoengineered Ag/Au Bilayer Rods Fabricated by Electron Beam Lithography,” *Applied optics*, **50**(28), pp. 5600–5605.
- [108] Zhang, W., Rahmani, M., Niu, W., Ravaine, S., Hong, M., and Lu, X., 2015, “Tuning Interior Nanogaps of Double-Shelled Au/Ag Nanoboxes for Surface-Enhanced Raman Scattering,” *Scientific reports*, **5**(1), pp. 1–6.
- [109] Jin, L., She, G., Li, J., Xia, J., Wang, X., Mu, L., and Shi, W., 2016, “A Facile Fabrication of Ag-Au-Ag Nanostructures with Nanogaps for Intensified Surface-Enhanced Raman Scattering,” *Applied Surface Science*, **389**, pp. 67–72.
- [110] Yuan, K., Zheng, J., Yang, D., Jurado Sanchez, B., Liu, X., Guo, X., Liu, C., Dina, N. E., Jian, J., and Bao, Z., 2018, “Self-Assembly of Au@ Ag Nanoparticles on Mussel Shell to Form Large-Scale 3D Supercrystals as Natural SERS Substrates for the Detection of Pathogenic Bacteria,” *ACS omega*, **3**(3), pp. 2855–2864.
- [111] Khaywah, M. Y., 2014, “New Ultrasensitive Bimetallic Substrates for Surface Enhanced Raman Scattering,” PhD Thesis, Troyes.
- [112] Ito, T., and Okazaki, S., 2000, “Pushing the Limits of Lithography,” *Nature*, **406**(6799), pp. 1027–1031.
- [113] Rycenga, M., Cobley, C. M., Zeng, J., Li, W., Moran, C. H., Zhang, Q., Qin, D., and Xia, Y., 2011, “Controlling the Synthesis and Assembly of Silver Nanostructures for Plasmonic Applications,” *Chemical reviews*, **111**(6), pp. 3669–3712.
- [114] Siegfried, T., Ekinici, Y., Martin, O. J., and Sigg, H., 2013, “Engineering Metal Adhesion Layers That Do Not Deteriorate Plasmon Resonances,” *ACS nano*, **7**(3), pp. 2751–2757.

- [115] De Jesus, M. A., Giesfeldt, K. S., Oran, J. M., Abu-Hatab, N. A., Lavrik, N. V., and Sepaniak, M. J., 2005, "Nanofabrication of Densely Packed Metal–Polymer Arrays for Surface-Enhanced Raman Spectrometry," *Applied spectroscopy*, **59**(12), pp. 1501–1508.
- [116] Haynes, C. L., and Van Duyne, R. P., 2001, "Nanosphere Lithography: A Versatile Nanofabrication Tool for Studies of Size-Dependent Nanoparticle Optics," *The Journal of Physical Chemistry B*, **105**(24), pp. 5599–5611.
- [117] Murray-Méthot, M.-P., Ratel, M., and Masson, J.-F., 2010, "Optical Properties of Au, Ag, and Bimetallic Au on Ag Nanohole Arrays," *The Journal of Physical Chemistry C*, **114**(18), pp. 8268–8275.
- [118] Hulteen, J. C., and Van Duyne, R. P., 1995, "Nanosphere Lithography: A Materials General Fabrication Process for Periodic Particle Array Surfaces," *Journal of Vacuum Science & Technology A: Vacuum, Surfaces, and Films*, **13**(3), pp. 1553–1558.
- [119] Guo, L. J., 2007, "Nanoimprint Lithography: Methods and Material Requirements," *Advanced materials*, **19**(4), pp. 495–513.
- [120] Menumerov, E., Golze, S. D., Hughes, R. A., and Neretina, S., 2018, "Arrays of Highly Complex Noble Metal Nanostructures Using Nanoimprint Lithography in Combination with Liquid-Phase Epitaxy," *Nanoscale*, **10**(38), pp. 18186–18194.
- [121] Xu, S., Li, L., Du, Z., Tang, L., Wang, Y., Wang, T., and Li, J., 2009, "A Netlike DNA-Templated Au Nanoconjugate as the Matrix of the Direct Electrochemistry of Horseradish Peroxidase," *Electrochemistry communications*, **11**(2), pp. 327–330.
- [122] Fang, C., Fan, Y., Kong, J. M., Zhang, G. J., Linn, L., and Rafeah, S., 2007, "DNA-Templated Preparation of Palladium Nanoparticles and Their Application," *Sensors and Actuators B: Chemical*, **126**(2), pp. 684–690.
- [123] Chen, S.-M., and Chen, S.-V., 2003, "The Bioelectrocatalytic Properties of Cytochrome C by Direct Electrochemistry on DNA Film Modified Electrode," *Electrochimica acta*, **48**(5), pp. 513–529.
- [124] Satyavolu, N. S. R., Tan, L. H., and Lu, Y., 2016, "DNA-Mediated Morphological Control of Pd–Au Bimetallic Nanoparticles," *Journal of the American Chemical Society*, **138**(50), pp. 16542–16548.

- [125] Thomas, A. C., 2012, “Blue Emitting Gold Nanoclusters Templated by Poly-Cytosine DNA at Low PH and Poly-Adenine DNA at Neutral PH,” *Chemical Communications*, **48**(54), pp. 6845–6847.
- [126] Satyavolu, N. S. R., Pishvaresfahani, N., Tan, L. H., and Lu, Y., 2018, “DNA-Encoded Morphological Evolution of Bimetallic Pd@ Au Core-Shell Nanoparticles from a High-Indexed Core.,” *Nano research*, **11**(9), p. 4549.
- [127] Li, N., Tittl, A., Yue, S., Giessen, H., Song, C., Ding, B., and Liu, N., 2014, “DNA-Assembled Bimetallic Plasmonic Nanosensors,” *Light: Science & Applications*, **3**(12), pp. e226–e226.
- [128] Leng, J., Wang, W.-M., Lu, L.-M., Bai, L., and Qiu, X.-L., 2014, “DNA-Templated Synthesis of PtAu Bimetallic Nanoparticle/Graphene Nanocomposites and Their Application in Glucose Biosensor,” *Nanoscale research letters*, **9**(1), pp. 1–8.
- [129] Prinz, J., Heck, C., Ellerik, L., Merk, V., and Bald, I., 2016, “DNA Origami Based Au–Ag-Core–Shell Nanoparticle Dimers with Single-Molecule SERS Sensitivity,” *Nanoscale*, **8**(10), pp. 5612–5620.
- [130] Niu, W., Zhang, L., and Xu, G., 2013, “Seed-Mediated Growth of Noble Metal Nanocrystals: Crystal Growth and Shape Control,” *Nanoscale*, **5**(8), pp. 3172–3181.
- [131] Jiang, M., Lim, B., Tao, J., Camargo, P. H., Ma, C., Zhu, Y., and Xia, Y., 2010, “Epitaxial Overgrowth of Platinum on Palladium Nanocrystals,” *Nanoscale*, **2**(11), pp. 2406–2411.
- [132] Wang, F., Sun, L.-D., Feng, W., Chen, H., Yeung, M. H., Wang, J., and Yan, C.-H., 2010, “Heteroepitaxial Growth of Core–Shell and Core–Multishell Nanocrystals Composed of Palladium and Gold,” *Small*, **6**(22), pp. 2566–2575.
- [133] Wang, F., Li, C., Sun, L.-D., Wu, H., Ming, T., Wang, J., Yu, J. C., and Yan, C.-H., 2011, “Heteroepitaxial Growth of High-Index-Faceted Palladium Nanoshells and Their Catalytic Performance,” *Journal of the American Chemical Society*, **133**(4), pp. 1106–1111.
- [134] Jin, M., Zhang, H., Wang, J., Zhong, X., Lu, N., Li, Z., Xie, Z., Kim, M. J., and Xia, Y., 2012, “Copper Can Still Be Epitaxially Deposited on Palladium Nanocrystals to Generate Core–Shell Nanocubes despite Their Large Lattice Mismatch,” *ACS nano*, **6**(3), pp. 2566–2573.

- [135] Zhang, H., Li, W., Jin, M., Zeng, J., Yu, T., Yang, D., and Xia, Y., 2011, “Controlling the Morphology of Rhodium Nanocrystals by Manipulating the Growth Kinetics with a Syringe Pump,” *Nano letters*, **11**(2), pp. 898–903.
- [136] Yang, C.-W., Chanda, K., Lin, P.-H., Wang, Y.-N., Liao, C.-W., and Huang, M. H., 2011, “Fabrication of Au–Pd Core–Shell Heterostructures with Systematic Shape Evolution Using Octahedral Nanocrystal Cores and Their Catalytic Activity,” *Journal of the American Chemical Society*, **133**(49), pp. 19993–20000.
- [137] Park, G., Seo, D., Jung, J., Ryu, S., and Song, H., 2011, “Shape Evolution and Gram-Scale Synthesis of Gold@ Silver Core–Shell Nanopolyhedrons,” *The Journal of Physical Chemistry C*, **115**(19), pp. 9417–9423.
- [138] Li, J., Zheng, Y., Zeng, J., and Xia, Y., 2012, “Controlling the Size and Morphology of Au@ Pd Core–Shell Nanocrystals by Manipulating the Kinetics of Seeded Growth,” *Chemistry—A European Journal*, **18**(26), pp. 8150–8156.
- [139] Ma, Y., Li, W., Cho, E. C., Li, Z., Yu, T., Zeng, J., Xie, Z., and Xia, Y., 2010, “Au@ Ag Core- Shell Nanocubes with Finely Tuned and Well-Controlled Sizes, Shell Thicknesses, and Optical Properties,” *ACS nano*, **4**(11), pp. 6725–6734.
- [140] Wang, D., and Li, Y., 2011, “Bimetallic Nanocrystals: Liquid-Phase Synthesis and Catalytic Applications,” *Advanced Materials*, **23**(9), pp. 1044–1060.
- [141] Lim, B., Kobayashi, H., Yu, T., Wang, J., Kim, M. J., Li, Z.-Y., Rycenga, M., and Xia, Y., 2010, “Synthesis of Pd- Au Bimetallic Nanocrystals via Controlled Overgrowth,” *Journal of the American Chemical Society*, **132**(8), pp. 2506–2507.
- [142] Habas, S. E., Lee, H., Radmilovic, V., Somorjai, G. A., and Yang, P., 2007, “Shaping Binary Metal Nanocrystals through Epitaxial Seeded Growth,” *Nature materials*, **6**(9), pp. 692–697.
- [143] Fan, F.-R., Liu, D.-Y., Wu, Y.-F., Duan, S., Xie, Z.-X., Jiang, Z.-Y., and Tian, Z.-Q., 2008, “Epitaxial Growth of Heterogeneous Metal Nanocrystals: From Gold Nano-Octahedra to Palladium and Silver Nanocubes,” *Journal of the American Chemical Society*, **130**(22), pp. 6949–6951.
- [144] Bauer, E., and van der Merwe, J. H., 1986, “Structure and Growth of Crystalline Superlattices: From Monolayer to Superlattice,” *Physical review b*, **33**(6), p. 3657.
- [145] Fahmi, A., Pietsch, T., Mendoza, C., and Cheval, N., 2009, “Functional Hybrid Materials,” *Materials today*, **12**(5), pp. 44–50.

- [146] Lee, J. Y., Lee, J., Jang, Y. J., Lee, J., Jang, Y. H., Kochuveedu, S. T., Lee, S. S., and Kim, D. H., 2011, "Plasmonic Nano-Necklace Arrays via Reconstruction of Diblock Copolymer Inverse Micelle Nanotemplates," *Soft Matter*, **7**(1), pp. 57–60.
- [147] Aizawa, M., and Buriak, J. M., 2007, "Block Copolymer Templated Chemistry for the Formation of Metallic Nanoparticle Arrays on Semiconductor Surfaces," *Chemistry of Materials*, **19**(21), pp. 5090–5101.
- [148] Tercjak, A., Gutierrez, J., Ocando, C. J., Peponi, L., and Mondragon, I., 2009, "Thermoresponsive Inorganic/Organic Hybrids Based on Conductive TiO₂ Nanoparticles Embedded in Poly (Styrene-*b*-Ethylene Oxide) Block Copolymer Dispersed Liquid Crystals," *Acta materialia*, **57**(15), pp. 4624–4631.
- [149] Hood, M. A., Mari, M., and Muñoz-Espí, R., 2014, "Synthetic Strategies in the Preparation of Polymer/Inorganic Hybrid Nanoparticles," *Materials*, **7**(5), pp. 4057–4087.
- [150] Menezes, W. G., Zielasek, V., Dzhardimalieva, G. I., Pomogailo, S. I., Thiel, K., Wöhrle, D., Hartwig, A., and Bäumer, M., 2012, "Synthesis of Stable AuAg Bimetallic Nanoparticles Encapsulated by Diblock Copolymer Micelles," *Nanoscale*, **4**(5), pp. 1658–1664.
- [151] Sanwaria, S., Singh, S., Horechyy, A., Formanek, P., Stamm, M., Srivastava, R., and Nandan, B., 2015, "Multifunctional Core–Shell Polymer–Inorganic Hybrid Nanofibers Prepared via Block Copolymer Self-Assembly," *RSC advances*, **5**(109), pp. 89861–89868.
- [152] Ataee-Esfahani, H., Wang, L., and Yamauchi, Y., 2010, "Block Copolymer Assisted Synthesis of Bimetallic Colloids with Au Core and Nanodendritic Pt Shell," *Chemical communications*, **46**(21), pp. 3684–3686.
- [153] Shim, K., Lin, J., Park, M.-S., Shahabuddin, M., Yamauchi, Y., Hossain, M. S. A., and Kim, J. H., 2019, "Tunable Porosity in Bimetallic Core-Shell Structured Palladium-Platinum Nanoparticles for Electrocatalysts," *Scripta Materialia*, **158**, pp. 38–41.
- [154] Taylor, A. K., Perez, D. S., Zhang, X., Pilapil, B. K., Engelhard, M. H., Gates, B. D., and Rider, D. A., 2017, "Block Copolymer Templated Synthesis of PtIr Bimetallic Nanocatalysts for the Formic Acid Oxidation Reaction," *Journal of Materials Chemistry A*, **5**(40), pp. 21514–21527.

- [155] Ehret, E., Beyou, E., Mamontov, G. V., Bugrova, T. A., Prakash, S., Aouine, M., Domenichini, B., and Aires, F. C. S., 2015, “Bimetallic PdAg Nanoparticle Arrays from Monolayer Films of Diblock Copolymer Micelles,” *Nanoscale*, **7**(31), pp. 13239–13248.
- [156] Khanafer, M., Issa, A., Akil, S., Hamieh, T., Adam, P.-M., and Jradi, S., 2016, “A General Strategy to Incorporate a Wide Range of Metallic Salts into Ring-like Organized Nanostructures via Polymer Self-Assembly,” *RSC advances*, **6**(105), pp. 102843–102852.
- [157] Sree Satya Bharati, M., Byram, C., and Soma, V. R., 2018, “Femtosecond Laser Fabricated Ag@ Au and Cu@ Au Alloy Nanoparticles for Surface Enhanced Raman Spectroscopy Based Trace Explosives Detection,” *Frontiers in Physics*, **6**, p. 28.
- [158] Wang, C.-L., Hsao, B.-J., Lai, S.-F., Chen, W.-C., Chen, H.-H., Chen, Y.-Y., Chien, C.-C., Cai, X., Kempson, I. M., and Hwu, Y., 2011, “One-Pot Synthesis of AuPt Alloyed Nanoparticles by Intense x-Ray Irradiation,” *Nanotechnology*, **22**(6), p. 065605.
- [159] Hai, Z., Kolli, N. E., Chen, J., and Remita, H., 2014, “Radiolytic Synthesis of Au–Cu Bimetallic Nanoparticles Supported on TiO₂: Application in Photocatalysis,” *New Journal of Chemistry*, **38**(11), pp. 5279–5286.
- [160] Heshmatpour, F., Abazari, R., and Balalaie, S., 2012, “Preparation of Monometallic (Pd, Ag) and Bimetallic (Pd/Ag, Pd/Ni, Pd/Cu) Nanoparticles via Reversed Micelles and Their Use in the Heck Reaction,” *Tetrahedron*, **68**(14), pp. 3001–3011.
- [161] Zielińska-Jurek, A., Kowalska, E., Sobczak, J. W., Lisowski, W., Ohtani, B., and Zaleska, A., 2011, “Preparation and Characterization of Monometallic (Au) and Bimetallic (Ag/Au) Modified-Titania Photocatalysts Activated by Visible Light,” *Applied Catalysis B: Environmental*, **101**(3–4), pp. 504–514.
- [162] Sivamaruthi, B. S., Ramkumar, V. S., Archunan, G., Chaiyasut, C., and Suganthi, N., 2019, “Biogenic Synthesis of Silver Palladium Bimetallic Nanoparticles from Fruit Extract of Terminalia Chebula—In Vitro Evaluation of Anticancer and Antimicrobial Activity,” *Journal of Drug Delivery Science and Technology*, **51**, pp. 139–151.
- [163] Abbasi, B. H., Zaka, M., Hashmi, S. S., and Khan, Z., 2018, “Biogenic Synthesis of Au, Ag and Au–Ag Alloy Nanoparticles Using Cannabis Sativa Leaf Extract,” *IET Nanobiotechnology*, **12**(3), pp. 277–284.

- [164] Tsai, C.-H., Xu, M., Kunal, P., and Trewyn, B. G., 2018, “Aerobic Oxidative Esterification of Primary Alcohols over Pd-Au Bimetallic Catalysts Supported on Mesoporous Silica Nanoparticles,” *Catalysis Today*, **306**, pp. 81–88.
- [165] Mizukoshi, Y., Fujimoto, T., Nagata, Y., Oshima, R., and Maeda, Y., 2000, “Characterization and Catalytic Activity of Core-Shell Structured Gold/Palladium Bimetallic Nanoparticles Synthesized by the Sonochemical Method,” *The Journal of Physical Chemistry B*, **104**(25), pp. 6028–6032.
- [166] Neppolian, B., Wang, C., and Ashokkumar, M., 2014, “Sonochemically Synthesized Mono and Bimetallic Au–Ag Reduced Graphene Oxide Based Nanocomposites with Enhanced Catalytic Activity,” *Ultrasonics sonochemistry*, **21**(6), pp. 1948–1953.
- [167] Weber, M. J., Mackus, A. J., Verheijen, M. A., van der Marel, C., and Kessels, W. M., 2012, “Supported Core/Shell Bimetallic Nanoparticles Synthesis by Atomic Layer Deposition,” *Chemistry of Materials*, **24**(15), pp. 2973–2977.
- [168] Vykoukal, V., Bursik, J., Roupčova, P., Cullen, D. A., and Pinkas, J., 2019, “Solvothermal Hot Injection Synthesis of Core-Shell AgNi Nanoparticles,” *Journal of Alloys and Compounds*, **770**, pp. 377–385.
- [169] Kim, Y.-T., Schilling, J., Schweizer, S. L., and Wehrspohn, R. B., 2017, “High Density Ag Nanobranches Decorated with Sputtered Au Nanoparticles for Surface-Enhanced Raman Spectroscopy,” *Applied Surface Science*, **410**, pp. 525–529.
- [170] Oh, Y., Lee, J., and Lee, M., 2018, “Fabrication of Ag-Au Bimetallic Nanoparticles by Laser-Induced Dewetting of Bilayer Films,” *Applied Surface Science*, **434**, pp. 1293–1299.
- [171] Zhang, T., Li, L., Ye, Z., Yang, Q., Tian, Y., and Guo, X., 2018, “Preparation and Characterization of Ag–Pd Bimetallic Nano-Catalysts in Thermosensitive Microgel Nano-Reactor,” *RSC advances*, **8**(33), pp. 18252–18259.
- [172] Bundli, S., Dhak, P., Jensen, M., Gunnæs, A. E., Nguyen, P. D., Fjellvåg, H., and Sjøaastad, A. O., 2019, “Controlled Alloying of Pt-Rh Nanoparticles by the Polyol Approach,” *Journal of Alloys and Compounds*, **779**, pp. 879–885.
- [173] Kowalska, E., Janczarek, M., Rosa, L., Juodkazytis, S., and Ohtani, B., 2014, “Mono-and Bi-Metallic Plasmonic Photocatalysts for Degradation of Organic Compounds under UV and Visible Light Irradiation,” *Catalysis Today*, **230**, pp. 131–137.

- [174] Tanaka, A., Fuku, K., Nishi, T., Hashimoto, K., and Kominami, H., 2013, “Functionalization of Au/TiO₂ Plasmonic Photocatalysts with Pd by Formation of a Core–Shell Structure for Effective Dechlorination of Chlorobenzene under Irradiation of Visible Light,” *The Journal of Physical Chemistry C*, **117**(33), pp. 16983–16989.
- [175] Lei, H., Li, X., Sun, C., Zeng, J., Siwal, S. S., and Zhang, Q., 2019, “Galvanic Replacement–Mediated Synthesis of Ni-Supported Pd Nanoparticles with Strong Metal–Support Interaction for Methanol Electro-Oxidation,” *Small*, **15**(11), p. 1804722.
- [176] Jing, H., and Wang, H., 2015, “Structural Evolution of Ag–Pd Bimetallic Nanoparticles through Controlled Galvanic Replacement: Effects of Mild Reducing Agents,” *Chemistry of Materials*, **27**(6), pp. 2172–2180.

Chapter 2: Self-Assembled Ag Nanocomposites into Ultra-Sensitive and Reproducible Large-Area SERS-Active Opaque Substrates

2.1 Introduction

SERS, which integrates high levels of sensitivity with spectroscopic precision, provides huge enhancements to Raman signals of trace detection levels of chemical and biological molecules adsorbed on metal surfaces [1–3]. The measured Raman signal enhancement in SERS shows impressive EF, up to 14–15 orders of magnitude, thus enabling the ultrasensitive identification of even single molecules [4,5].

The ultrasensitivity of metallic-nanoparticle-based SERS substrates is usually linked to the high number of hotspots formed within the small interspaced gaps between the constituent nanostructures [6]. Moreover, the enhancement of the SERS signal is highly dependent on the plasmonic resonance frequency of synthesized NPs [7]. Generally, as a prerequisite for a maximum intensity SERS signal, there must be a close match between the wavelength (λ) of the plasmon resonance peak of the NPs and the Raman excitation wavelength [7]. Therefore, from an application standpoint, it is crucial to manipulate the interparticle spacings between metallic nanostructures and extract their optical properties.

Recently, a growing body of literature has extensively studied and evaluated several self-assembly approaches in SERS studies [8–10]. Currently, different techniques are being used to arrange self-assembled AgNPs over a large area, thanks to polymers [11–15], block copolymers [16–18], dendrimers [19], proteins [20], and DNA molecules [21,22] acting as matrices for inducing ordering and anisotropic orientation on surfaces, and for controlling the number of constituent particles and their separation. [23–26].

To overcome the serious shortcomings—including uniformity and unsatisfactory reproducibility—in SERS performance, as recognized by the self-assembly approaches [26–29], it is essential to establish a rational and facile method for the fabrication of AgNPs substrates with controllable nanogaps. Additionally, it is highly desirable to enhance the quality of synthesized nanostructures by producing free-standing, flexible, and large-scale SERS substrates with uniform,

stable, reproducible, and highly sensitive SERS signals. In fact, as far as we know, there are still no exhaustive studies applied to synthesize AgNPs via a surface-based strategy.

Herein, in order to reach this ultimate goal, we fabricated AgNPs on a surface via a convenient chemical synthetic route known as VIPS. This highly versatile and unprecedented approach was developed recently by our laboratory team for the fabrication of precisely shaped AuNPs embedded in a PMMA layer [30]. VIPS is considered to be a powerful and simple route because it provides excellent control of the structural properties of NPs. It offers compelling evidence for producing efficient SERS platforms with controlled size, shape, and interparticle gap distances. The success of this approach is obvious in fabricating nanostructures without demanding long processing times, tedious steps, high overheads, high temperatures, or the use of toxic chemicals, reducing agents, and surfactants. Moreover, there is no need for either functionalizing the surface or etching of polymer film. Nevertheless, the VIPS approach is well suited for producing controlled nanogaps below 10 nm.

To accomplish this approach, layers of AgNO₃/PMMA dispersions were deposited on a conducting Si wafer in order to allow the spontaneous formation of large-area SERS-active substrates of AgNPs. To be precise, we carried out a parametric study dealing with the influence of different experimental parameters on the optical and structural properties of AgNPs, such as concentration of Ag precursor and spin-coating speeds. Studies were executed under the conditions described in the Experimental section. Changes in the morphological features of the substrates were identified via SEM characterizations. The optical properties of synthesized AgNPs substrates were monitored through micro-extinction and ellipsometric optical measurements. Ultimately, we assured the effectiveness of AgNPs substrates in SERS applications by using trans-1,2,4-(bipyridyl) ethylene (BPE) as the Raman probe molecule.

2.1.1 Fabrication of AgNPs By Different Self-Assembly Approaches (Copolymer/Polymer/DNA-templated synthesis)

Won Joon Cho et al. [23] have fabricated an ultrahigh density array of self-assembled Ag nanoclusters based on the use of amphiphilic diblock copolymer (PS-b-P4VP). The highly sensitive SERS-active and reproducible nanostructures thus obtained by this approach, in particular, sub-10 nm Ag nanoclusters, showed a significant enhancement of the Raman signal of crystal violet (CV) molecules by an EF exceeding 10⁸. The interparticle spacings between the

neighboring Ag nanoclusters were modulated by varying the ratios of both blocks of copolymer. The success of this synthesis critically depends on several steps such as the: utilization of high temperatures, reduction of metallic salts using a reducing agent, and finally complete removal of block copolymer thin film.

As reported by Amir Fahmi et al. [24], 3D periodic Ag nanostructures in bulk have been successfully generated with controlled size and shape distributions via self-assembly approach by using copolymer (PS-*b*-P4VP). After nanostructuring of the copolymer and solvent evaporation, the inorganic AgNPs were found attached to functional block of the di-block copolymer (i.e. P4VP), thus showing particular organizations into four different 3D morphologies, according to variation of physicochemical parameters such as molecular weight of polymers, volume fraction of one of the blocks or solution conditions. Moreover, monolayers of particle-loaded 2D nanostructures in form of thin honeycomb Ag metallic films have been also performed [24].

Weidong Ruan et al. approach has relied on a surface-guided assembly of AgNPs in the form of rings due to an electrostatic interaction between positively poly (diallyldimethylammonium chloride) (PDDA) polyelectrolytes and negatively charged Ag colloids [25]. Unfortunately, polystyrene (PS) spheres, acting as templates for preparing absorbing active sites on surface, are often needed and selectively removed at the end of synthetic process. Their approach requires the incorporation of different strategies to develop arrays of nanoscale patterns on substrate surfaces.

To promote the formation of interconnected Ag networks, Kai-Ling Liang's group developed an ultimate construction of self-assembled silver fern-like superstructures in poly (vinylalcohol) (PVA) nanocomposite film, which serves as a reducing agent and stabilizer during the film annealing process [26]. This method suffers from a plethora of pitfalls due to the requirement of high temperatures during thermal reduction process. Thus, it offers extremely hard controls on structural properties of synthesized AgNPs. The overall quality and uniformity of AgNPs are both poor due to a lack of homogeneity and reproducibility. As a result of their tendency to agglomerate, the SERS performance of such AgNPs will be unsatisfactory.

By an oil-water interfacial self-assembly, tunable distinct Ag morphologies have been self-assembled from Ag nanooctahedra, stabilized with a hydrophilic polymer poly (vinylpyrrolidone) (PVP), upon a ligand exchange with alkyl thiols of increasing chain lengths [27]. Sensing platforms over a large area were developed from this single anisotropic NP, where hotspots are

highly spreaded over the entire edge length of the assembled nanostructures. However, their attempts to synthesize AgNPs with distinct morphologies are laborious and financially unfeasible. Also, it is plausible that its harsh conditions make it difficult to replicate SERS-active substrates with large number of hotspots.

In addition, DNA molecules have been employed in directing the synthesis of self-assembled Ag nanostructures. Using triangular DNA origami scaffolds with four single strands, Ag dimers ~ 60 nm in diameter, and with an interparticle gap of 3 nm, have been assembled onto silicon substrates [28]. Well-ordered AgNPs ~ 20 nm with controlled gap distances have been also achieved in accordance with DNA-origami directed self-assembly [29]. By frequently performing this synthetic method, center-to center distances between adjacent AgNPs were precisely tuned from 94 to 29 nm. Potential limitations of processes involving the use of DNA molecular linkers have been clearly recognized [5]. DNA molecules, used for bridging Ag adjacent NPs, could interfere in the SERS detection of adsorbed molecular species and prevent other molecules from entering the gap region [5].

2.2 Experimental Part

2.2.1 Synthetic Approach

The experimental procedure bears a close resemblance to the one proposed previously by our group [30–33]. The main principle of this technique relies on the self-assembly of thin-layer PMMA (Sigma-Aldrich, Kappelweg 1, Schn., Germany) into nanoholes, which are used as synthesis reactors for MNPs. More details about this synthesis and mechanism are given in our previous papers [30–33]. Specifically, we aimed to extend the self-assembly approach to a large variety of MNPs with different structural properties. As a brief summary, the strategy was based on a nanophase separation between two thermodynamically incompatible solutions. Upon depositing the mixture by spin-coating on conductive substrates, a thermodynamic instability was prevalent. Here, N-doped silicon substrate was used to allow spontaneous reduction of the silver precursor. Silicon plays a crucial role in promoting electrons to Ag^+ and then producing AgNPs, which prevents the use of any external reducing agent, so that our samples are obtained by a one-shot procedure. This arises due to the fact that metallic salts are strongly dissolved in alcohol, which is a non-solvent of PMMA. Consequently, two different sizes of micelles containing M^{n+} , ethanol, and acetone were distributed on the substrate surface. These micelles exploded after the

evaporation of the solvents, thus leading to the formation of PMMA nanoholes containing two different average diameters of metallic salts due to the complete fitting of NPs into nanoholes. Accordingly, the AgNO₃/PMMA dispersion was fabricated by mixing two incompatible solutions, i.e., PMMA/acetone (C = 30 g/L) and AgNO₃/ethanol. Afterwards, a clean silicon wafer was coated with a monolayer of silver solution in order to shield the formation of monodisperse AgNPs on the surface. Drops of silver solution with different concentrations (10, 20, 30, and 40 mM) were spread onto the silicon substrates at different spinning speeds: 3000, 5000, and 7000 rpm. All of the samples were carefully prepared using the following spin-coating parameters: (time: 30 seconds (s), acceleration: 3000 rpm/s). Generally, to obtain a homogeneous layer, we must choose an acceleration value lower than the speed. Otherwise, we cannot easily reproduce the same thickness for samples prepared using the same conditions. Next, these samples were replicated under stable conditions to check their reproducibility. Figure 17 illustrates the scheme for the fabrication of AgNPs inside PMMA nanoholes via a surface-based strategy.

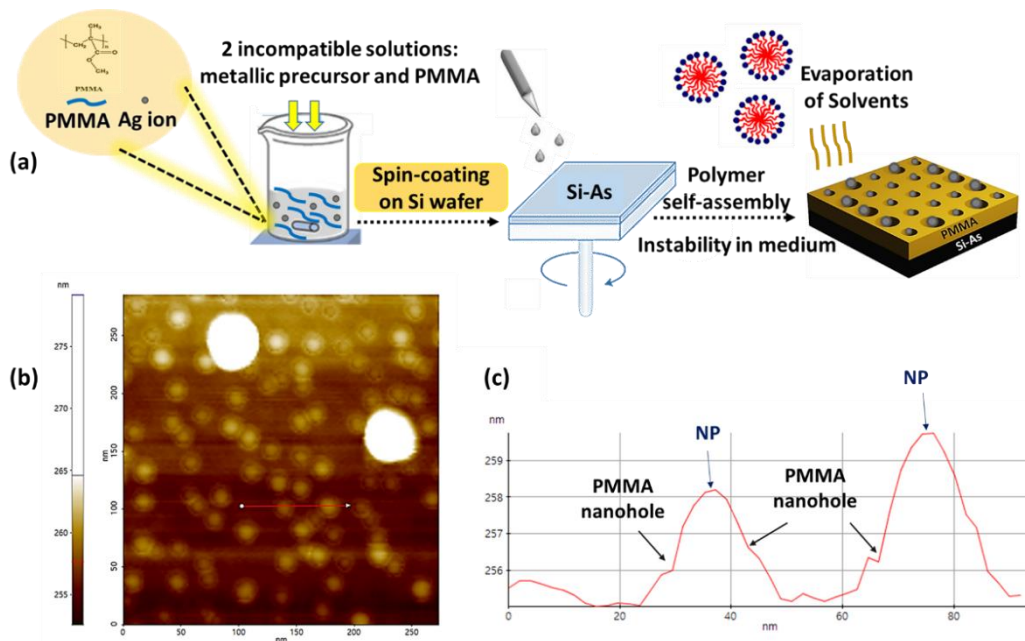


Figure 17. (a) Schematic representation of the VIPS approach, showing the growth of two different diameters of AgNPs into PMMA nanoholes attached with; (b) an AFM image; and (c) its corresponding line-scan profile.

2.2.2 Polymer/Silver Solutions Preparation

Briefly, as mentioned in Figure 18, PMMA/acetone dispersion was sequentially added into AgNO_3 /ethanol solution. In a separate flask, different quantities of silver precursor (mg) were dissolved in 1 mL ethanol upon stirring for 30 min. After dissolving, 0.5 mL of acetone was added in order to obtain a one phase mixture. Afterwards, 1.5 mL of PMMA/acetone dispersion was injected into the above mixture under vigorous stirring for 30 min at RT. Actually, acetone is a good solvent for PMMA since it masks the agglomeration of its chains within the mixture while modulating its interaction with the non-solvent/ metallic salt. PMMA/acetone solution was prepared by dissolution of 0.75 g of PMMA with 25 mL acetone, which is heated under agitation for 24 hours (h) at 40°C to dissolve the PMMA.

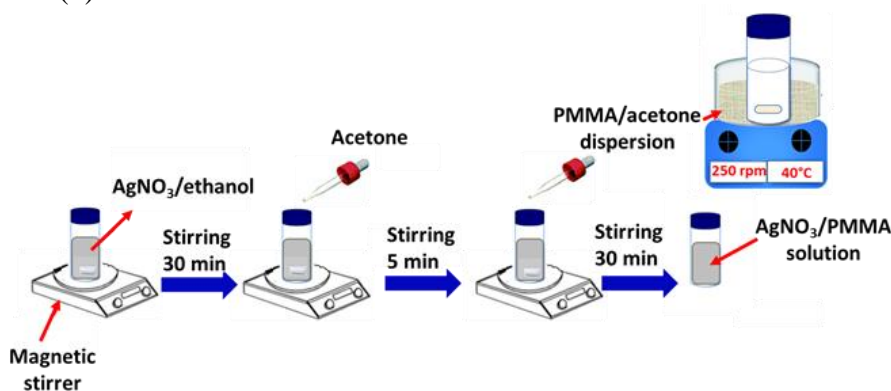


Figure 18. Schematic view showing steps for formation of Ag^+ /PMMA solutions

2.3 Results and Discussions

2.3.1 Adjusting the Optical and Structural Properties of AgNPs

In particular, the promising functions of AgNPs as nanosensors can be optimized through the adjustment of diverse factors, including the concentration of the metal precursor, or the spin-coating speed. This section focuses on the experimental parameters influencing the size distributions, shape, and density of NPs on the surface, the thickness and sizes of the PMMA nanoholes, and the gap distances between the constituent AgNPs. Here, to achieve the best SERS performances, we sought the experimental conditions that would produce an ultrahigh yield of AgNPs with precisely controlled sizes and small gap distances. It is widely known that the strength of the SERS signal of the adsorbed molecules is highly promoted, as the NPs are denser on the substrate, with small interspaced gaps [34].

2.3.1.1 Impact of Spin-Coating Speed

To further understand the role of spin-coating speed in controlling the structural properties of AgNPs, a set of substrates was fabricated at different speeds, while keeping all other experimental parameters unaltered. Adjusting spin-coating speed is one of the main parameters that can control the density, size distribution, growth rate of formation, and gap distances between NPs. In general, 40 mM was considered to be a critical concentration of silver precursor, since it yields a surface full of high density AgNPs. It is relevant to note that the maximum concentration reached with Ag precursor was 40 mM. Increasing the concentration of Ag/ethanol beyond this value caused the formation of PMMA aggregates inside the solution. Thus, it can be conceivably hypothesized that repulsive interactions between both Ag and PMMA solutions should be modulated to be relatively weak in order to prevent the phase separation of the whole dispersions.

As illustrated in Figure 19, SEM images reveal that polydispersity in size and shape decreases with increasing speed. The increase in speed noticeably evolved the morphology of AgNPs from high-index faceted random shapes into nearly isotropic spherical shapes with a high homogeneity over the whole surface. It is noteworthy that we did not aim to produce only spherical NPs, since SERS enhancement is greater with anisotropic nanostructures. To be precise, we wanted to prepare AgNPs using the VIPS strategy that we had mainly developed for gold before now. In a future work, we aim to produce other morphologies. This study requires much more experimentation and investigation of the synthetic method. The most striking observation at 7000 rpm is that all small AgNPs, with an average diameter of about 16 nm, are nearly uniform, monodisperse, spherical, highly dispersed, and organized on the substrate surface with very small interparticle separation distances. Moreover, large AgNPs of average diameter ~ 74 nm display regular nanoscale patterning features, with gap sizes only a few nanometers apart (< 10 nm). Both size regimes of AgNPs exhibit narrow size distributions, with an exquisite control over the size.

The findings at 7000 rpm can lead to important implications for SERS applications. The synthesized substrates, with a high density of hotspots, can be exploited as efficient nanostructures for yielding strong SERS signals from single molecules. In addition, they can be easily scaled for large-scale production due to the greater proportion of different controlled diameters of AgNPs on the surface. Impressively, SERS applications can be readily tuned at variable optical ranges.

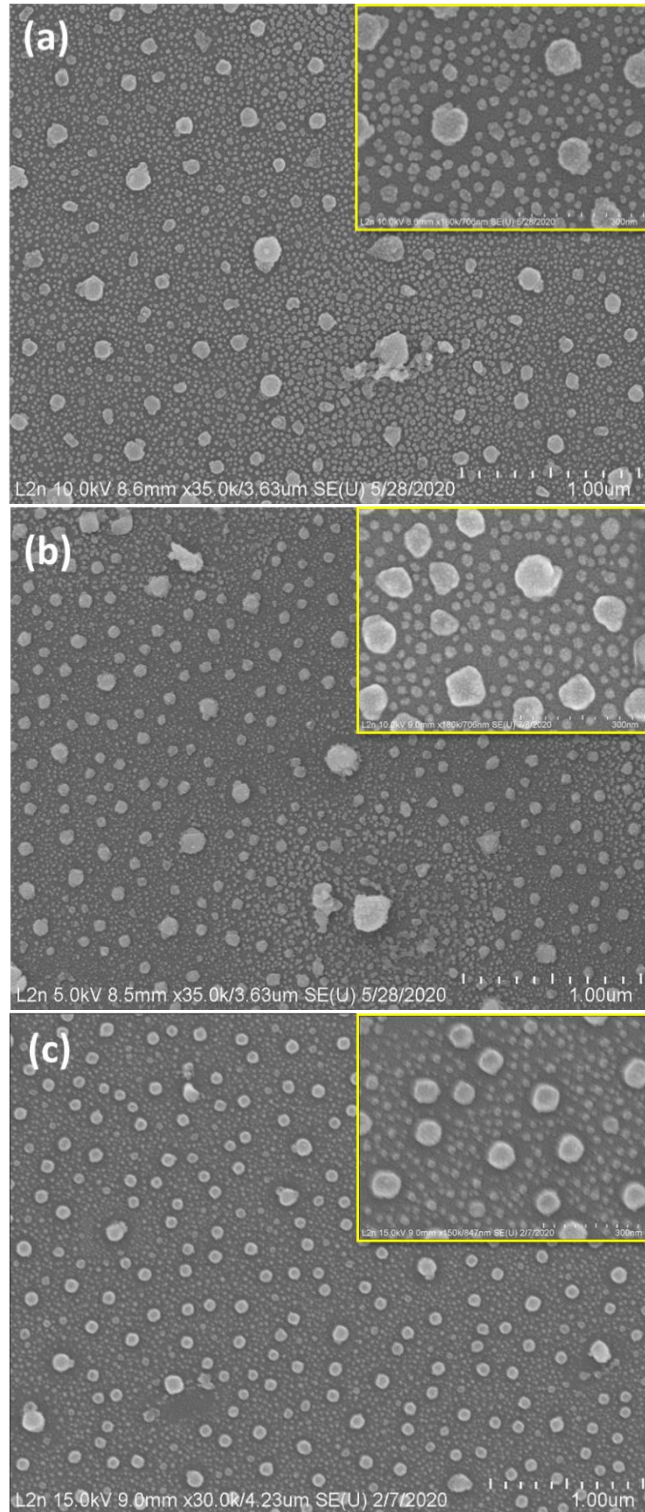


Figure 19. SEM images of 40 mM Ag/PMMA samples fabricated at different spin-coating speeds: (a) 3000; (b) 5000; and (c) 7000 rpm. All insets are the corresponding magnified SEM images at 300 nm.

To further investigate the average diameter of AgNPs at different speeds, size distribution measurements were performed according to SEM images (Figure 54 in Annex). Average diameter changes are presented in Figure 20. Mainly, two different average diameters of AgNPs dominate the entire surfaces at all speeds. By increasing the spin-coating speed from 3000 to 7000 rpm, the diameter of both AgNPs decreases slightly, and then approaches a constant value when exceeding a speed of 5000 rpm.

Spin-coating speed plays an important role in the structuring mechanism, and has a direct influence on the size and distribution of PMMA nanoholes as well as the organization of MNPs inside the holes. In the initial stage of the process, during the deposition of the mixture on the substrate surface, different solvents will start to evaporate according to their volatility and compatibility with the rest of the mixture. This would be the origin of a nanophase separation, which is manifested by the appearance of micelles whose size is dependent on spin-coating speed. At higher spin-coating speeds, the micelles burst rapidly, leaving behind PMMA nanoholes with narrow size distributions. It can be reasonably assumed that these micelles have insufficient time to coalesce into larger micelles; as a consequence, small NPs are obtained, with high density.

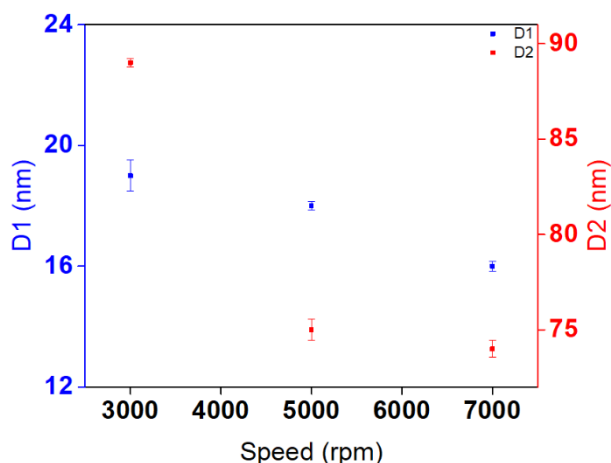


Figure 20. Average diameters (D1 and D2) of AgNPs with their correlated error bars versus spin-coating speed.

The optical characteristics of AgNPs assembled into a PMMA matrix are highlighted in Figure 21. Using a micro-extinction optical microscope, we were unable to clearly observe well-defined and

standard plasmonic peaks for AgNPs. This is not particularly surprising, given the fact that determining absorption and extinction cross-sections from a reflection spectrum is highly complicated. The foremost cause of this difficulty is due to the deposition of nanostructures on solid, opaque substrates. It is essential to consider that substrates supporting nanostructures can have significant effects on the nanostructures' LSPR and near-field distributions [35]. The combination of the halogen lamp's spectral signature with the corresponding plasmonic bands of the nanostructures is also evidence of the difficulty of collecting optical responses using this setup. Another possible explanation is that the PMMA/acetone surface layer is rough, nanoporous, non-continuous, and anti-reflective [36,37]. The reflection from the porosity of the PMMA nanoholes contributes greatly to the responses of the AgNPs. To date, no suitable method has been detected for removing the PMMA from the surface layer without any disturbance to the structuring. Several trials for removing the PMMA were initiated in order to promote the development of well-defined optical properties of AgNPs using a micro-extinction setup. Unfortunately, all of our attempts failed, since removing the PMMA layer impedes the availability of AgNPs in high quantities on the surface.

The existence of PMMA plays a vital role in the synthetic mechanism. The PMMA layer, acting as a coating support for the NPs, can protect AgNPs from extraneous chemical and physical changes by reducing their reactivity. In a previous paper by our group [23], the SERS EF was totally diminished upon removing the PMMA, thus indicating its importance in fulfilling high SERS nanofocusing and enhancement due to its hydrophobic properties. Crucially, PMMA acts as a stabilizing agent to prevent aggregation in samples. In addition, it controls the size and shape of NPs, the kinetics of growth, and the diffusion of atoms.

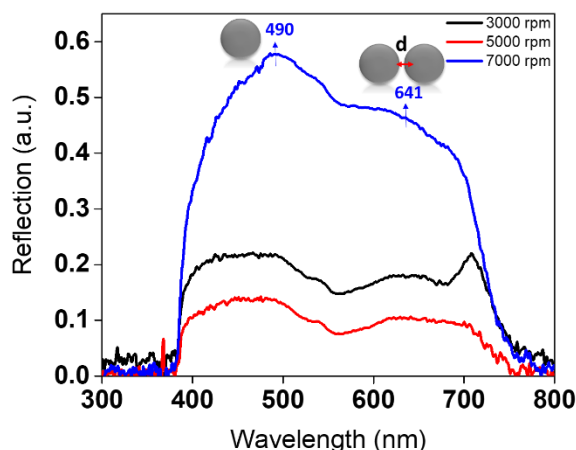


Figure 21. Reflection spectrum of AgNPs/PMMA nanocomposites prepared with different spin-coating speeds. The spectra were extracted using a bright-field optical microscope.

As shown in Figure 21, the intensity of the peaks shows a remarkable increase at high spin-coating speeds, with an enhancement in magnitude. Two optical modes appear at all speeds: one corresponds to the optical response of individual, large AgNPs, and the other to a coupling phenomenon between two closely separated large AgNPs. More details on the attribution of peaks can be found in the “Impact of Concentration of Ag Precursor” section. Thickness-dependent reflected optical spectra of AgNPs are demonstrated from these measurements. As the thickness of the PMMA layer increases, the reflection from AgNPs decreases. In order to acquire evident plasmonic peaks from samples, the layers should be thin enough for the light to penetrate through. This is why it was difficult to detect the optical response clearly at lower speeds—i.e., 3000 and 5000 rpm—due to their high thicknesses, anisotropic geometrical features, and polydispersity, as highlighted in Figures 19 and 22. A clear trend in controlling the thickness of the PMMA is mentioned in Figure 22. The thickness of the resultant PMMA film is tuned from 143 to 112 nm by varying the spin-coating speed, and a thinner layer of PMMA is reproduced well for the substrate prepared at 7000 rpm. Note that a scratch was made in our samples in order to expose the Si wafer and achieve an accurate measurement of the depth of the holes. This was done by means of an AFM technique to predict the overall thickness of the PMMA.

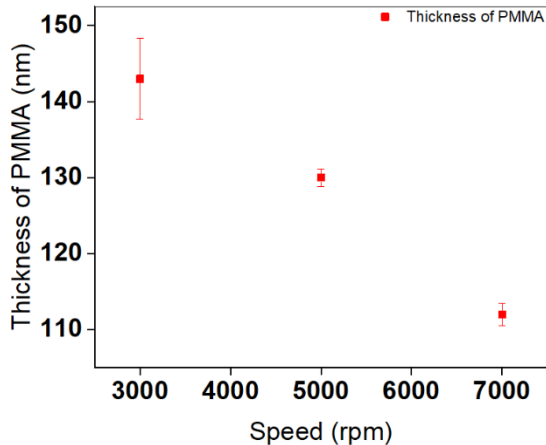


Figure 22. The influence of spin-coating speeds on the thickness of deposited PMMA layers when metal is introduced. Error bars are also displayed in this plot. Measurements of thickness values are extracted using an AFM technique via a line-scratching method.

Taken as a whole, speed significantly affects the thickness of the PMMA nanoholes, as well as the shape and monodispersity of the synthesized substrates. However, no noteworthy differences were found in the number of assembled AgNPs, their average diameters, or their gap distances. For this reason, further experimental investigations are needed in order to estimate significant differences in the structural and optical properties of AgNPs, as illustrated in the next section. The prospect of engineering the structural properties of Ag nanostructures and manipulating their plasmonic properties through spectral shifts serves as a major aim for developing good nanosensors in a broad spectral range.

2.3.1.2 Impact of Concentration of Ag Precursor

To adequately emphasize the effect of concentration, four samples were prepared using the same spin-coating speed: 7000 rpm. Returning to the discussions posed concerning the effects of speed, it is now possible to state that 7000 rpm is a suitable speed for fabricating thin metallic/PMMA layers with homogeneous shape and size distributions of MNPs. The concentration of AgNO₃/ethanol varied from 10 to 40 mM. Figure 23 presents the SEM images of the corresponding AgNP monolayers deposited onto the Si substrates at various concentrations. These images provide a visual analysis of the differences in the structural properties of the AgNP substrates. Few

particles exist at low concentrations (10 and 20 mM), whereas an excessive number of closely separated particles is dominant at high concentrations (30 and 40 mM). Most of the particles at low concentrations are individually isolated from one another with high distances. On the other hand, at higher concentrations, the increase in the density of NPs leads to a decrease in interparticle separation distances. This study further considers the feasibility of producing AgNPs with interparticle spacings of less than 10 nm.

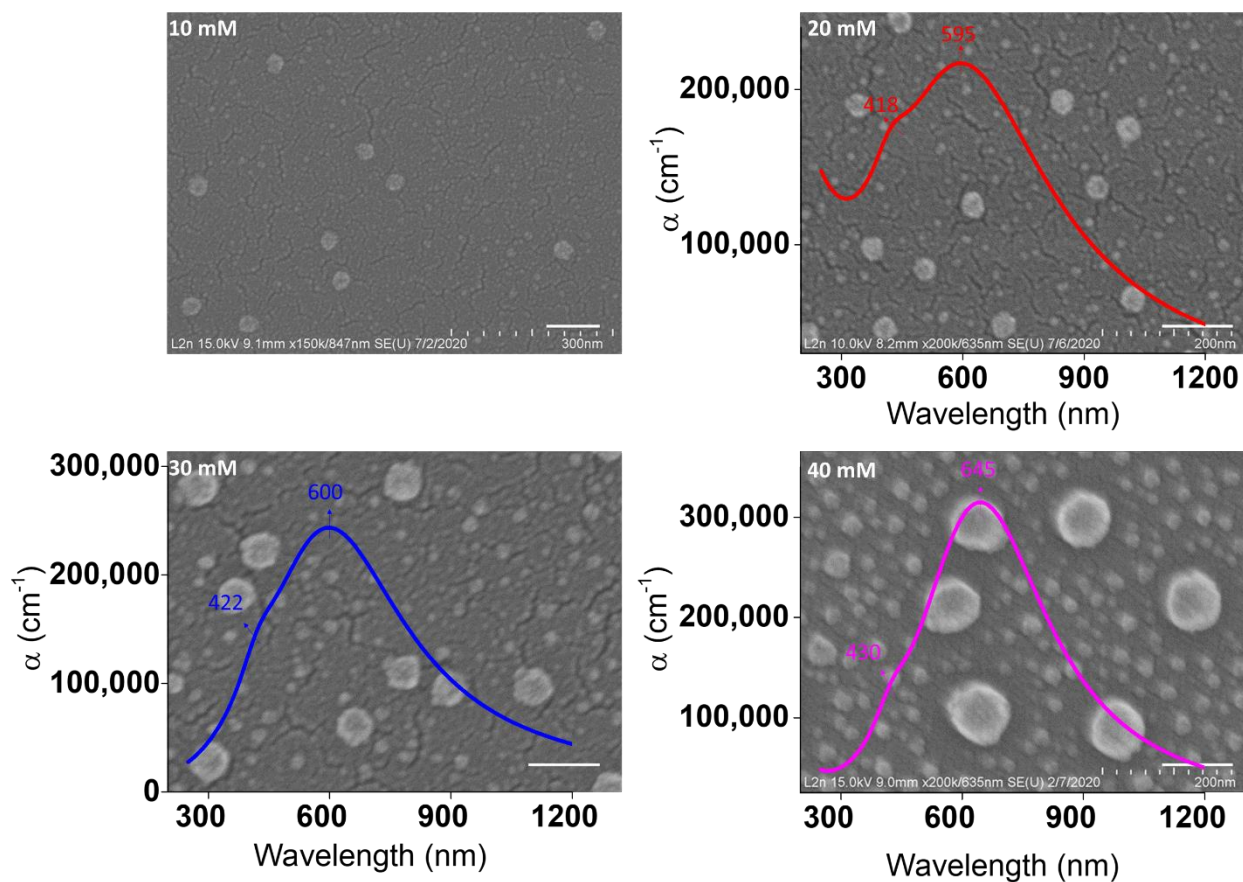


Figure 23. SEM images of Ag samples obtained by varying the concentration of Ag precursor. The scale bar is 100 nm. The insets show the absorption coefficient (α) of AgNPs/PMMA pre-synthesized substrates at each concentration.

Figure 24 confirms that the AFM findings are consistent with previous SEM observations. The AFM technique clearly shows its potential in distinguishing small AgNPs at low concentrations (10 and 20 mM) due to the small radius of curvature used for the tip (< 5 nm).

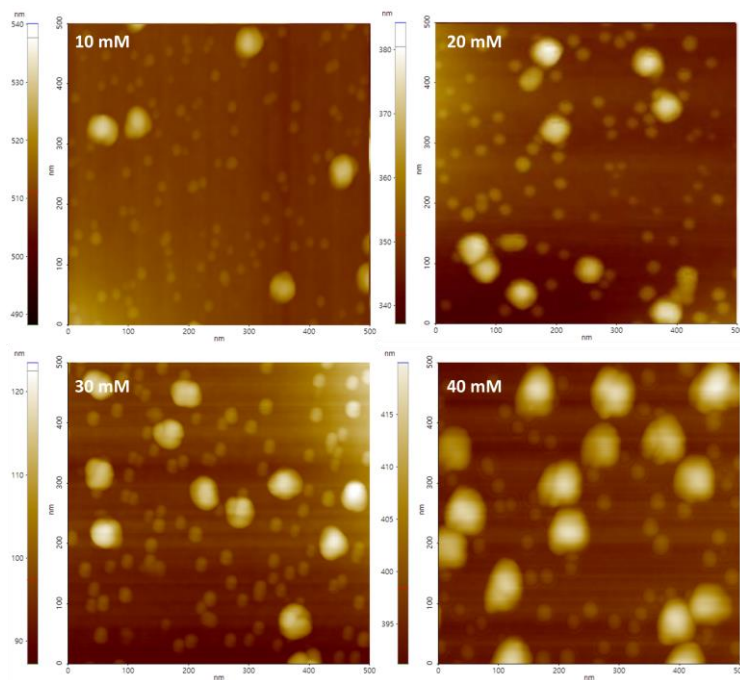


Figure 24. Two-dimensional tapping mode AFM images (500×500 nm) for Ag samples prepared at different concentrations.

The average diameters characterizing the assembled AgNPs are summarized in Table 3. Average diameters are calculated from size distribution histograms at all concentrations (Figure 55 in annex). Typically, two different average diameters of AgNPs are dominant at each substrate surface. By increasing the concentration of Ag, the average diameters of AgNPs increase, and reach their highest at 40 mM. This happened because, in some regions, the resulting small AgNPs participate in a subsequent coalescence and growth into larger spheres.

Table 3. Average diameters of AgNPs (D1 and D2) at different concentrations.

Concentration of Ag (mM)	D1 (nm)	D2 (nm)
10	<7	31
20	7	27–33
30	7–13	43–47
40	12–22	80

Changing the concentration of Ag precursor can primarily affect the particles' quality, and their efficiency of self-assembly. When the concentration is too low, thermodynamic instability will be caused, and the self-assembly will be restricted at the early stage due to the aggregation of PMMA particles. Consequently, it is important to reach the optimal Ag concentration in order to preserve the self-assembly in medium. This can be achieved by using a concentration beyond 20 mM, which leads to the auto-organization of AgNPs on the surface, with well-ordered assembly and good dispersibility.

The optical properties of the synthesized substrates were analyzed through micro-extinction (in reflection mode) and ellipsometric optical measurements. Figure 25 demonstrates the reflection spectra for AgNPs/PMMA at different concentrations. Herein, the change in the structural features of AgNPs confirms that the optical properties can be tuned by varying the concentration. The most conspicuous observation to emerge from the spectroscopic data was the ability of this technique to give such an optical response on monolayers of NPs on the surface. The spectrum of 10 mM AgNPs shows a peak at 453 nm. Similarly, the spectra of 20 and 30 mM AgNPs result in a slight red-shift to 461 and 473 nm, respectively. This slight red-shift is related to changes in the sizes of AgNPs from 31 to 47 nm. With a further increase in the concentration of Ag precursor to 40 mM, the position of this peak is continuously red-shifted into 490 nm. The position of the peak at ~ 490 nm is mainly attributed to the optical response of 80 nm AgNPs. As outlined in the literature review, the extinction spectra of 50 nm AgNPs dispersed in water showed a resonance peak at ~ 430 nm [38]. Changing the medium near the NPs' surface from water to PMMA should induce a ~ 30 nm shift in the optical properties, due to an increase in the RI of the surrounding medium. Increasing the size of AgNPs to 80 nm should also exhibit a continuous red-shift of ~ 30 nm [39].

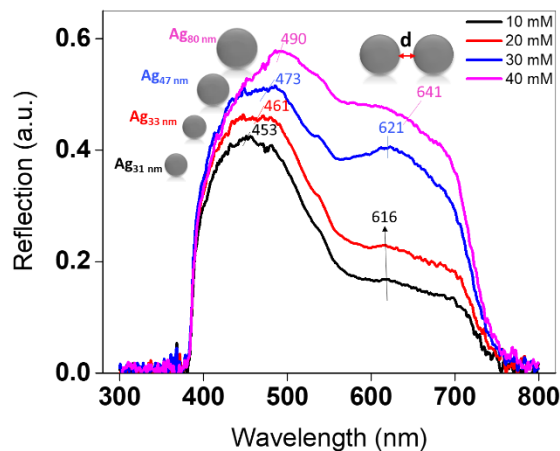


Figure 25. Spectral evolution of reflection of AgNPs/PMMA nanocomposites upon varying the concentration of Ag precursor.

Otherwise, a pronounced change in plasmonic properties was observed when considerably increasing the concentration of Ag precursor to 30 and 40 mM, where the additional second peak appeared clearly. This peak was red-shifted from 616 to 641 nm as the concentration of Ag precursor increased from 10 to 40 mM. This peak refers to a coupling phenomenon, and its position is highly influenced by the gap distances separating the AgNPs. The two reasons for not observing a clear response of the second peak at low concentrations are that (1) there are not enough NPs viewed by the microscope objectives on the excited surface, and (2) the AgNPs are separated by large gaps. It is expected that the number of resonance peaks increases as the symmetry of the structure decreases. As clarified in Figure 19, the VIPS approach enables the fabrication of AgNPs in a nearly isotropic environment, thus impeding the possibility of polarizing electrons in more than one way. Furthermore, enlarging metal nanostructures caused only slight shifts of plasmonic properties, as stated by Paramelle et al. [39]. The plasmonic peak could only be tuned to ~ 500 nm, even if the size of the AgNPs reached 100 nm [39]. Thus, at 40 mM, this remarkable red-shift to 641 nm is due to the existence of a large number of hotspots that yield a high EM between closely separated 80 nm AgNPs.

Based on discrete dipole approximation (DDA) theoretical simulations, the extinction optical response of 80 nm nanosphere dimers, suspended in water with 10 nm gap distances, should induce

a peak at ~ 560 nm [40]. The extent of this red-shift is maximized as the nanostructures become incredibly close to one another (< 10 nm) [5]. With further decrease in gap distances and increase in the RI of the surrounding medium, when AgNPs dispersed in PMMA approach the surface of the Si substrate, the peak will be dramatically red-shifted to 600 nm and beyond. Figure 25 also indicates that the scattering intensity increased as the concentration of AgNPs changed from 10 to 40 mM. This can be regarded as an indicator of an increase in the density of the NPs on the surface of the substrate. It is relevant to note that the micro-extinction optical technique is not suitable for nanostructures with dimensions of less than ~ 30 nm. Ordinarily, for small particles with a size of < 30 nm, absorption has ascendancy over scattering, thus making it complicated in detecting an optical response directly [41].

Recently, it was investigated that ellipsometry can be used for interpreting the optical spectra of the assemblies of anisotropic gold nanocubes (AuNC) on opaque substrate surfaces [30,33]. Ellipsometric theoretical calculations, based on physical modelling, were performed on AgNPs samples in order to acquire a deep knowledge about their optical features. The model proposed previously by Rana et al. was improved by adding a third oscillator for NPs. This model system was chosen because it assumes that the mixture is composed of three materials (inclusions and host) playing asymmetric roles. Furthermore, we selected it in order to consider the spherical inclusions, with high volume fractions and high interactions between one another. For a detailed review of the technique and model used, see our previous papers [30,33]. (details are also presented in Appendix-B)

As noted in Figure 26, experimental ellipsometric angles (Ψ and Δ) are characterized by a marked red-shift in positions as concentration is increased. However, a slight shift in Δ angles occurs, thus denoting that the thickness of the substrates is slightly shifted. The Δ angle is usually more sensitive to the thickness of the composite layer than the Ψ angle. The broadness and shift of the Ψ angle with increased concentration is widely affected by the increase in the ratio of the number of AgNPs to their corresponding thickness. As expected, there are some discrepancies in the sample prepared at 10 mM. The ellipsometric angles at 10 mM lie between the ones prepared at 20 and 30 mM. This apparent lack of correlation can be justified by the high nonuniformity of the sample over the area of the excitation beam. A closer inspection for this sample at high magnification reveals that its surfaces are full of PMMA aggregates in different regions. This lack

of agreement could also be linked to the low volume fraction of AgNPs on the excited surface. Therefore, a low number of photons will be collected when exciting the weakly interacting plasmonic NPs with the matrix layer. The high surface roughness of the sample prepared at 10 mM could have influenced the results obtained. As is well known, ellipsometric measurements and modelling are extremely hard to conduct when light scattering by surface roughness reduces the reflected light intensity severely.

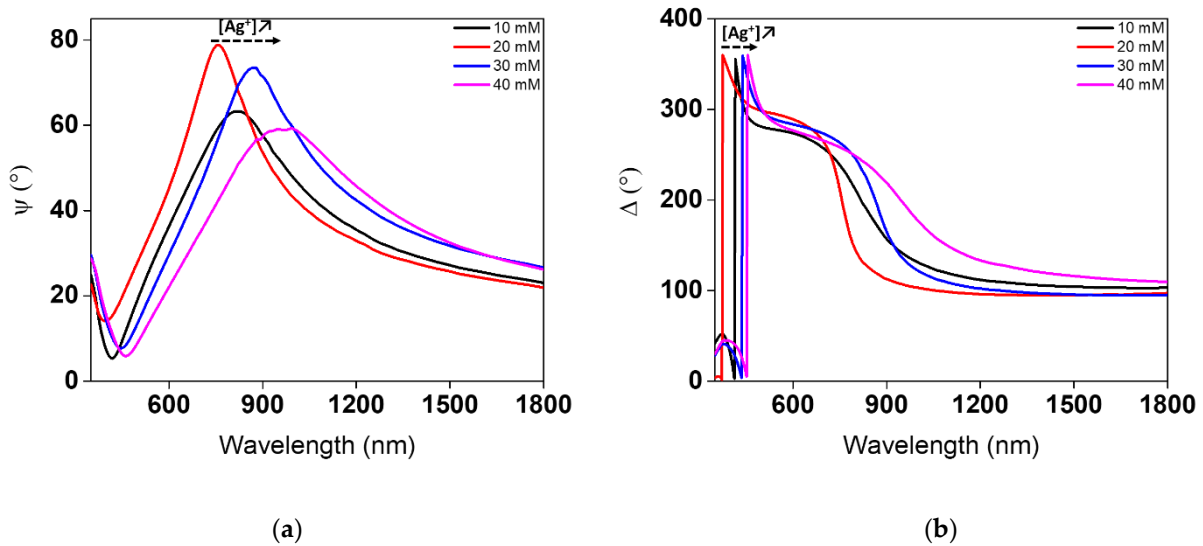


Figure 26. Variations of experimental ellipsometric angles (a) Ψ and (b) Δ in AgNPs/PMMA film/c-Si structures, as functions of the concentration of the Ag precursor.

In Figure 51 in annex, to some extent, the experimental pseudo-dielectric functions of AgNPs/PMMA film/c-Si structures match fairly well with the fitted ones, and further emphasize the validity of our model. Slight disagreement is evident in some regions, since size distribution is not counted in our modelling. In our view, modelling pseudo-dielectric functions represents a good initial step toward determining the absorption coefficient (α) of Ag/PMMA samples, as mentioned in the insets of Figure 23. The dielectric functions (ϵ_r and ϵ_i), refractive index (n), and extinction coefficient (k) can be found in the Annex (Figure 52 and 53). The insets in Figure 23 reveal that two plasmonic bands are observed at each concentration, and their maximum is highly red-shifted when increasing the concentration.

The maximum wavelength λ_{max} of the first plasmonic band is progressively red-shifted from 418 to 430 nm with increasing concentration. The observed shift can be interpreted as being a result of the increase in size of AgNPs from 7 to 22 nm. These peaks are also visible in the Mie calculations, and have been assigned to the optical responses of small AgNPs through quantitative analysis based on calculations of Mie extinction cross-sections [42,43].

Further shifts in the λ_{max} of the second plasmonic band, from 595 to 645 nm, with preferential increase in intensity, are related to the coupling between AgNPs that are affected by the RI of PMMA. The increase in intensity is associated with the huge number of AgNPs that exist on the substrate surface. It is apparent from Figure 25 that the relative positions of the LSPR bands of the second peak are in good agreement with the ellipsometric results.

Theoretical spectra calculated using Mie theory (Equation 2) for a homogeneous nanosphere are outlined in Figure 27, in order to determine the sum of the scattering and absorption cross-sections of spherical NPs. Simulations were carried out on single AgNPs, of different sizes, dispersed in a highly porous PMMA. Theoretical simulations of AgNPs at a fixed RI of PMMA ~ 1.25 , with the radius varying from 7 to 50 nm, predict a red-shift of the LSPR wavelength of major dipolar peaks with an increased extinction efficiency. In general, large nanostructures eventually lead to the appearance of multiple SP modes other than the dipole modes.

$$\sigma_{ext} = 3V \varepsilon_m^{\frac{3}{2}} \frac{\omega}{c} \frac{3 \varepsilon_{iNP}}{(\varepsilon_{rNP} + 2 \varepsilon_m)^2 + \varepsilon_{iNP}^2} \quad (2)$$

where c is the speed of light, V is the volume of the particle, ω is the frequency, ε_m is the dielectric function of the matrix, ε_{iNP} and ε_{rNP} are respectively the imaginary part and the real part of the dielectric function of the nanoparticle.

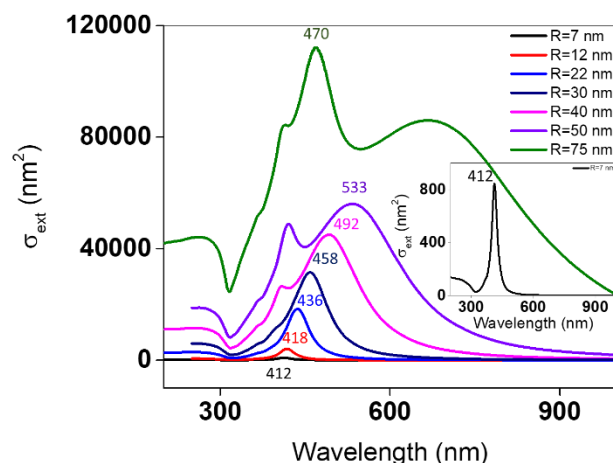


Figure 27. Mie theory calculations for the extinction cross-sections of different sizes of AgNPs suspended in a highly porous PMMA.

The characteristic peaks for ~ 30 nm AgNPs at 20 mM are too close to distinguish between experimental results (453–461 nm) and theoretical simulation spectra (458 nm). For $R = 47$ nm at 30 mM, it is expected theoretically to have a dipolar peak between 492–533 nm. However, μ_{ext} results display a peak at 473 nm. This difference is due to the fact that in Mie simulations the information is derived from only one homogeneous nanosphere. AgNPs with $R = 75$ nm exhibit a dipolar peak at 470 nm. This value correlates favorably with μ_{ext} results (~ 490 nm), and further supports our previous findings. Presumably, some differences between simulations and μ_{ext} results are likely due to ensemble averaging effects over many different sizes.

The micro-extinction technique is remarkably insensitive to the detection of small NPs ($R < 30$ nm) and quadrupolar modes of large NPs ($R > 30$ nm), whereas ellipsometry is sensitive to the most abundant network of NPs over all the surface.

Contrary to Mie simulations at fixed RI of PMMA, a micro-extinction setup can figure out the slight variations in the thickness and RI of PMMA as experimental parameters vary. Moreover, in μ_{ext} optical microscopy, the focal spot of an optical beam is analyzing a micrometric zone of NPs that represent many NPs. Taking that into account, our results should be validated by using two complementary techniques to get an overall optical response of all sizes of Ag samples. In this

regard, a significant correlation was recognized between both experimental (μext) and theoretical (ellipsometric and Mie simulations, respectively) data.

2.3.2 SERS Analysis

First, we studied the effect of spin-coating speed on the sensing properties of the obtained substrates. The results in Figure 28 show an enhancement of the SERS signal with increasing speed. To be precise, no major difference is observed between 3000 and 5000 rpm, which correlates strongly with the results shown in Figures 19–21. Below 7000 rpm, the samples revealed quite similar structural properties. The enhancement increase shown at higher speeds is attributed to the presence of higher numbers of NPs on the substrate surface (Figure 19), which is related to closely separated nano-objects. As a result, more hotspots might exist at higher speeds, allowing for better SERS enhancement. To go further in the evaluation of the sensing features, we then performed SERS for the samples shown in Figure 23. Here, we showed a change in the structural and optical properties of AgNPs when silver precursor concentration was varied.

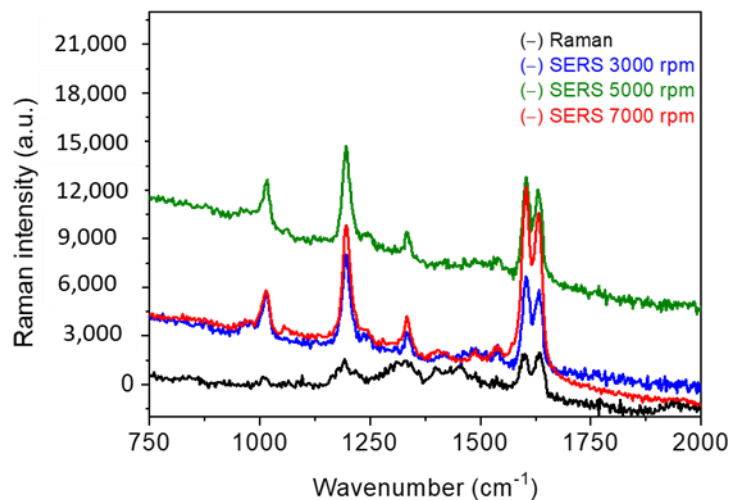


Figure 28. The Raman and SERS spectra of BPE at 10^{-5} M. Raman measurements were obtained with 10^{-2} M of BPE. Spectra were obtained at $P = 5$ mW over 5 s. Each curve is an average of 10 spectra collected from different positions on the substrate. All spectra were shifted vertically for the observation in all figures.

Similarly, Figure 29 also highlights noticeable results by showing an enhancement of the SERS signal with increasing precursor concentration. According to Figure 23, the number of AgNPs

increases with Ag precursor concentration. Moreover, the second plasmon peak—which is linked to coupling—shifted from ~ 600 nm (10 mM) to 645 nm (40 mM). This latter figure is quite close to the excitation wavelength (633 nm) used for the experiments. This feature ($\lambda_{\text{excitation}} - \lambda_{\text{max}} = 0$) is crucial, and plays a major role in enhancing the Raman intensity. For this reason, we might obtain a higher SERS EF for AgNPs prepared with larger precursor amounts. It is noteworthy that, in this section, we were able to obtain a SERS signal using a 1 s acquisition time. Therefore, we tried to decrease the BPE concentration to 10^{-10} M, and it was possible to obtain a SERS signal at this concentration value. To be in the same experimental conditions in Raman and SERS, which is crucial for any EF calculation, we performed measurements of both signals for 5 s. Based on literature [31,32] using the same type of PMMA nanocomposites for SERS, we related the high sensitivity of the samples to the repulsive interaction that exists between PMMA and NPs. Thus, by pushing the BPE, PMMA consequently directs it onto the NPs' surface. As a result, the target molecules will be concentrated in the SERS focal volume, which highly increases the SERS intensity.

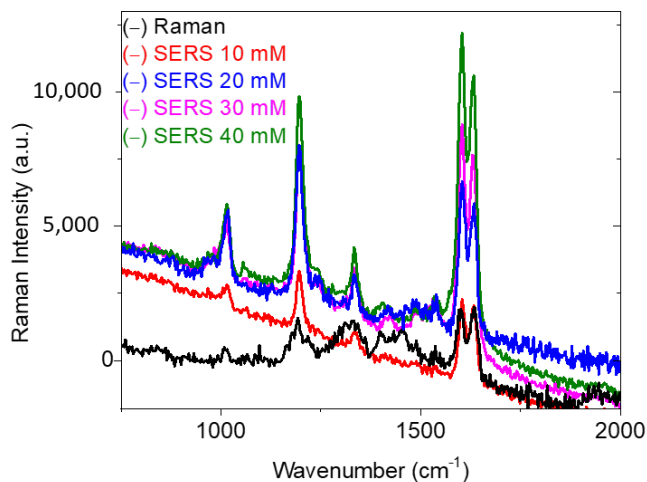


Figure 29. The Raman and SERS spectra of BPE at 10^{-10} M for AgNPs prepared with different silver precursor concentrations. Raman measurements were obtained with 10^{-2} M of BPE. Spectra were obtained at $P = 5$ mW over 5 s. Each curve is an average of 10 spectra collected from different positions on the substrate.

Precisely, BPE molecules adsorb to the MNPs through the nitrogen groups, which makes pyridine derivatives very good candidates for SERS measurements. Thus, since the interaction takes place on nitrogen, which has more affinity for the metal than for PMMA, the BPE will be self-driven towards the plasmons. This finding has been reported in our previous studies [31–33].

Then, we employed the peak at 1605 cm^{-1} to estimate the EF through the following equation:

$$EF = (I_{SERS} \times N_{normal}) / (I_{normal} \times N_{SERS}) \quad (3)$$

where I_{SERS} and I_{normal} are the intensities of the same band for the SERS and normal Raman spectra, respectively. N_{SERS} is the number of molecules probed in SERS, and N_{normal} is the number of molecules excited in classical Raman. EF corresponds to the SERS intensity of one molecule divided by the Raman intensity of one molecule without the SERS substrate, and can be seen as an absolute EF of the scattering cross-section of the test molecule. EF calculation requires the excitation and collection volumes in the solution to be known. Knowing the probe molecule concentration, the N_{normal} can then be estimated. N_{SERS} can be obtained from knowledge of the active surface area of the substrate that is being probed, the footprint of an adsorbed molecule, and the surface coverage.

The focal volume of our Raman system is 11 fl. The SERS confocal volume (SCV) corresponds to 1.5×10^{-3} fl, considering the size of our NPs. SCV was calculated using the following equation:

$$SCV = S \times h \quad (4)$$

where S and h are the excited surface and height, respectively.

$$S = \pi r^2, \quad (5)$$

and h corresponds to beam penetration depth, where r is the beam radius, and is calculated based on the excitation wavelength value (632.8 nm). Then, S is multiplied by the percentage of surface coverage by the NPs. Finally, we multiply S by the number of NPs determined after calculation of the surface of one NP, based on SEM images.

These volumes allow the detection of 3×10^7 molecules in Raman, and 5 molecules in SERS, for a concentration of 10^{-10} M. At 1605 cm^{-1} , I_{SERS} and I_{normal} correspond to 12,000 and 2,100, respectively. From there, we obtained EF 3×10^{10} for the 10 mM sample, while 10^{13} , 5×10^{14} , and 10^{15} were determined for 20, 30, and 40 mM, respectively. The obtained high values of EF can be

attributed to the hydrophobic features of the PMMA layer embedded with the AgNPs. This finding was reported and discussed in detail in our previous studies [30–33]. Indeed, at high BPE concentrations, multiple layers of molecules could be detected. Therefore, decreasing the concentration might decrease the amount of BPE adsorbed on the AgNPs. Furthermore, it can be expected that we tend toward the presence of one layer of molecules close to the NPs' surface, which causes the Raman exaltation and then leads to this increase in the EF.

2.4 Conclusion

We have obtained comprehensive results demonstrating the value of the VIPS approach in conducting efficient SERS platforms (detection of five molecules) with controlled structural and sensing properties. The significance of our work lies in fabricating large-scale SERS-active opaque substrates, with high density of hotspots, yielding huge enhancements. Better surface roughness and overall bulk flatness, homogeneity of refractive index, and absence of secondary back reflection make silicon and opaque substrates greater for optical characterizations and applications. Correlating the structural properties of AgNPs with SERS enhancements has shown an enormous benefit in advancing both the perception of the fundamental mechanisms of SERS effects, and the strategies used to control the assembled NPs for efficient sensing applications.

This study could further provide the framework for triggering the formation of advanced, multifunctional hybrid materials such as Ag/Au organized inside PMMA nanoholes. This could conceivably lead to promising sensing features.

2.5 References

- [1] Zhang, Q., Lee, Y. H., Phang, I. Y., Lee, C. K., and Ling, X. Y., 2014, “Hierarchical 3D SERS Substrates Fabricated by Integrating Photolithographic Microstructures and Self-Assembly of Silver Nanoparticles,” *Small*, **10**(13), pp. 2703–2711.
- [2] Rycenga, M., Camargo, P. H., Li, W., Moran, C. H., and Xia, Y., 2010, “Understanding the SERS Effects of Single Silver Nanoparticles and Their Dimers, One at a Time,” *The journal of physical chemistry letters*, **1**(4), pp. 696–703.
- [3] Sharma, B., Frontiera, R. R., Henry, A.-I., Ringe, E., and Van Duyne, R. P., 2012, “SERS: Materials, Applications, and the Future,” *Materials today*, **15**(1–2), pp. 16–25.
- [4] Wang, L., Sun, Y., and Li, Z., 2015, “Dependence of Raman Intensity on the Surface Coverage of Silver Nanocubes in SERS Active Monolayers,” *Applied Surface Science*, **325**, pp. 242–250.
- [5] Rycenga, M., Cobley, C. M., Zeng, J., Li, W., Moran, C. H., Zhang, Q., Qin, D., and Xia, Y., 2011, “Controlling the Synthesis and Assembly of Silver Nanostructures for Plasmonic Applications,” *Chemical reviews*, **111**(6), pp. 3669–3712.
- [6] Hasna, K., Lakshmi, K., Jayaraj, M. K. E., Kumar, K. R., and Matham, M. V., 2016, “Development of High-Sensitive, Reproducible Colloidal Surface-Enhanced Raman Spectroscopy Active Substrate Using Silver Nanocubes for Potential Biosensing Applications,” *Journal of Nanophotonics*, **10**(2), p. 026020.
- [7] Khanafer, M., Izquierdo-Lorenzo, I., Akil, S., Louarn, G., Toufaily, J., Hamieh, T., Adam, P.-M., and Jradi, S., 2016, “Silver Nanoparticle Rings of Controllable Size: Multi-Wavelength SERS Response and High Enhancement of Three Pyridine Derivatives,” *ChemistrySelect*, **1**(6), pp. 1201–1206.
- [8] Cao, Q., Yuan, K., Yu, J., Delaunay, J.-J., and Che, R., 2017, “Ultrafast Self-Assembly of Silver Nanostructures on Carbon-Coated Copper Grids for Surface-Enhanced Raman Scattering Detection of Trace Melamine,” *Journal of colloid and interface science*, **490**, pp. 23–28.
- [9] Babich, E. S., Gangrskaja, E. S., Reduto, I. V., Béal, J., Redkov, A. V., Maurer, T., and Lipovskii, A. A., 2019, “Self-Assembled Silver Nanoparticles in Glass Microstructured by Poling for SERS Application,” *Current Applied Physics*, **19**(10), pp. 1088–1095.

- [10] Chen, J., Guo, L., Qiu, B., Lin, Z., and Wang, T., 2018, “Application of Ordered Nanoparticle Self-Assemblies in Surface-Enhanced Spectroscopy,” *Materials Chemistry Frontiers*, **2**(5), pp. 835–860.
- [11] Zeng, J., Jia, H., An, J., Han, X., Xu, W., Zhao, B., and Ozaki, Y., 2008, “Preparation and SERS Study of Triangular Silver Nanoparticle Self-Assembled Films,” *Journal of Raman Spectroscopy: An International Journal for Original Work in all Aspects of Raman Spectroscopy, Including Higher Order Processes, and also Brillouin and Rayleigh Scattering*, **39**(11), pp. 1673–1678.
- [12] Wei, H., Li, J., Wang, Y., and Wang, E., 2007, “Silver Nanoparticles Coated with Adenine: Preparation, Self-Assembly and Application in Surface-Enhanced Raman Scattering,” *Nanotechnology*, **18**(17), p. 175610.
- [13] Zhu, L., Dai, H., Zhang, S., Hu, D., Zhou, Q., Zou, M., Adkins, J., and Zheng, J., 2019, “Enhanced Surface-Enhanced Raman Scattering (SERS) Sensitivity by the Self-Assembly of Silver Nanoparticles (Ag NPs) Laminated on Polydimethylsiloxane (PDMS),” *Analytical Letters*, **52**(18), pp. 2868–2882.
- [14] Manojkumar, K., Mecerreyes, D., Taton, D., Gnanou, Y., and Vijayakrishna, K., 2017, “Self-Assembly of Poly (Ionic Liquid)(PIL)-Based Amphiphilic Homopolymers into Vesicles and Supramolecular Structures with Dyes and Silver Nanoparticles,” *Polymer Chemistry*, **8**(22), pp. 3497–3503.
- [15] Detsri, E., and Popanyasak, J., 2015, “Fabrication of Silver Nanoparticles/Polyaniline Composite Thin Films Using Layer-by-Layer Self-Assembly Technique for Ammonia Sensing,” *Colloids and Surfaces A: Physicochemical and Engineering Aspects*, **467**, pp. 57–65.
- [16] Zhang, Y., Filipczak, P., He, G., Nowaczyk, G., Witczak, L., Raj, W., Kozanecki, M., Matyjaszewski, K., and Pietrasik, J., 2017, “Synthesis and Characterization of Ag NPs Templated via Polymerization Induced Self-Assembly,” *Polymer*, **129**, pp. 144–150.
- [17] Sakai, T., Ishihara, A., and Alexandridis, P., 2015, “Block Copolymer-Mediated Synthesis of Silver Nanoparticles from Silver Ions in Aqueous Media,” *Colloids and Surfaces A: Physicochemical and Engineering Aspects*, **487**, pp. 84–91.

- [18] Park, J. T., Koh, J. H., Lee, K. J., Seo, J. A., Min, B. R., and Kim, J. H., 2008, "Formation of Silver Nanoparticles Created in Situ in an Amphiphilic Block Copolymer Film," *Journal of applied polymer science*, **110**(4), pp. 2352–2357.
- [19] Lataifeh, A., and Kraatz, H.-B., 2019, "Self-Assembly of Silver Nanoparticles-Low Generation Peptide Dendrimer Conjugates into Poly-L-Lysine," *Materials Letters*, **254**, pp. 353–356.
- [20] Kahraman, M., Sur, I., and Culha, M., 2010, "Label-Free Detection of Proteins from Self-Assembled Protein-Silver Nanoparticle Structures Using Surface-Enhanced Raman Scattering," *Analytical chemistry*, **82**(18), pp. 7596–7602.
- [21] Zheng, Y., Li, Y., and Deng, Z., 2012, "Silver Nanoparticle–DNA Bionanoconjugates Bearing a Discrete Number of DNA Ligands," *Chemical Communications*, **48**(49), pp. 6160–6162.
- [22] Wei, G., Wang, L., Liu, Z., Song, Y., Sun, L., Yang, T., and Li, Z., 2005, "DNA-Network-Templated Self-Assembly of Silver Nanoparticles and Their Application in Surface-Enhanced Raman Scattering," *The Journal of Physical Chemistry B*, **109**(50), pp. 23941–23947.
- [23] Cho, W. J., Kim, Y., and Kim, J. K., 2012, "Ultrahigh-Density Array of Silver Nanoclusters for SERS Substrate with High Sensitivity and Excellent Reproducibility," *ACS nano*, **6**(1), pp. 249–255.
- [24] Fahmi, A., Pietsch, T., Mendoza, C., and Cheval, N., 2009, "Functional Hybrid Materials," *Materials today*, **12**(5), pp. 44–50.
- [25] Ruan, W., Wang, C., Ji, N., Lu, Z., Zhou, T., Zhao, B., and Lombardi, J. R., 2008, "Surface-Guided Self-Assembly of Silver Nanoparticles on Edges of Heterogeneous Surfaces," *Langmuir*, **24**(16), pp. 8417–8420.
- [26] Liang, K.-L., Wang, Y.-C., Lin, W.-L., and Lin, J.-J., 2014, "Polymer-Assisted Self-Assembly of Silver Nanoparticles into Interconnected Morphology and Enhanced Surface Electric Conductivity," *RSC Advances*, **4**(29), pp. 15098–15103.
- [27] Lee, Y. H., Shi, W., Lee, H. K., Jiang, R., Phang, I. Y., Cui, Y., Isa, L., Yang, Y., Wang, J., and Li, S., 2015, "Nanoscale Surface Chemistry Directs the Tunable Assembly of Silver Octahedra into Three Two-Dimensional Plasmonic Superlattices," *Nature communications*, **6**(1), pp. 1–7.

- [28] Heck, C., Kanehira, Y., Kneipp, J., and Bald, I., 2019, “Amorphous Carbon Generation as a Photocatalytic Reaction on DNA-Assembled Gold and Silver Nanostructures,” *Molecules*, **24**(12), p. 2324.
- [29] Pal, S., Deng, Z., Ding, B., Yan, H., and Liu, Y., 2010, “DNA-Origami-Directed Self-Assembly of Discrete Silver-Nanoparticle Architectures,” *Angewandte Chemie*, **122**(15), pp. 2760–2764.
- [30] Omar, R., Naciri, A. E., Jradi, S., Battie, Y., Toufaily, J., Mortada, H., and Akil, S., 2017, “One-Step Synthesis of a Monolayer of Monodisperse Gold Nanocubes for SERS Substrates,” *Journal of Materials Chemistry C*, **5**(41), pp. 10813–10821.
- [31] Akil-Jradi, S., Jradi, S., Plain, J., Adam, P.-M., Bijeon, J.-L., Royer, P., and Bachelot, R., 2012, “Micro/Nanoporous Polymer Chips as Templates for Highly Sensitive SERS Sensors,” *RSC advances*, **2**(20), pp. 7837–7842.
- [32] Khanafer, M., Issa, A., Akil, S., Hamieh, T., Adam, P.-M., and Jradi, S., 2016, “A General Strategy to Incorporate a Wide Range of Metallic Salts into Ring-like Organized Nanostructures via Polymer Self-Assembly,” *RSC advances*, **6**(105), pp. 102843–102852.
- [33] Omar, R., Naciri, A. E., Fahes, A., Jradi, S., Issa, A., Kuznetsov, D., Shur, V., Zelenovskiy, P., Battie, Y., and Akil, S., 2020, “Precise Control of the Size and Gap between Gold Nanocubes by Surface-Based Synthesis for High SERS Performance,” *Soft matter*, **16**(7), pp. 1857–1865.
- [34] Kundu, S., and Nithiyantham, U., 2013, “In Situ Formation of Curcumin Stabilized Shape-Selective Ag Nanostructures in Aqueous Solution and Their Pronounced SERS Activity,” *Rsc Advances*, **3**(47), pp. 25278–25290.
- [35] Gómez, D. E., Davis, T. J., and Funston, A. M., 2014, “Plasmonics by Design: Design Principles to Structure–Function Relationships with Assemblies of Metal Nanoparticles,” *Journal of Materials Chemistry C*, **2**(17), pp. 3077–3087.
- [36] Meier, T., and Solares, S. D., 2016, “Rhodamine-Doped Nanoporous Polymer Films as High-Performance Anti-Reflection Coatings and Optical Filters,” *Nanoscale*, **8**(40), pp. 17675–17685.
- [37] Paul, P., Pfeiffer, K., and Szeghalmi, A., 2020, “Antireflection Coating on PMMA Substrates by Atomic Layer Deposition,” *Coatings*, **10**(1), p. 64.

- [38] Praveena, V. D., 2017, “Synthesis and Characterisation of an Eco Friendly Nano Silver Complexed Chitosan Biopolymer Thin Films for Removal of Water Pollutants.”
- [39] Paramelle, D., Sadovoy, A., Gorelik, S., Free, P., Hobley, J., and Fernig, D. G., 2014, “A Rapid Method to Estimate the Concentration of Citrate Capped Silver Nanoparticles from UV-Visible Light Spectra,” *Analyst*, **139**(19), pp. 4855–4861.
- [40] Hooshmand, N., and El-Sayed, M. A., 2019, “Collective Multipole Oscillations Direct the Plasmonic Coupling at the Nanojunction Interfaces,” *Proceedings of the National Academy of Sciences*, **116**(39), pp. 19299–19304.
- [41] Gonzalez, A. L., Reyes-Esqueda, J. A., and Noguez, C., 2008, “Optical Properties of Elongated Noble Metal Nanoparticles,” *The Journal of Physical Chemistry C*, **112**(19), pp. 7356–7362.
- [42] Majic, M., and Le Ru, E. C., 2020, “Numerically Stable Formulation of Mie Theory for an Emitter Close to a Sphere,” *Applied optics*, **59**(5), pp. 1293–1300.
- [43] Amirjani, A., Firouzi, F., and Haghshenas, D. F., 2020, “Predicting the Size of Silver Nanoparticles from Their Optical Properties,” *Plasmonics*, **15**(4), pp. 1077–1082.

Chapter 3: A Novel Surface-Based Strategy For selective overgrowth of Ag nanostructures on Au nanocrystals

3.1 Introduction

Functional hybrid materials, consisting of two incorporated MNPs, were fabricated for the purpose of generating new desirable properties and functionalities, as reported in Chapter 1 [1,2]. The extraordinary features of bimetallic nanomaterials have been employed in several applications such as SERS [3–5], LSPR sensors [6,7], catalysis [8], and photothermal conversion [9]. The combination of both AuNPs and AgNPs in a bimetallic system appears as a beneficial approach for merging the advantages of both Ag optical enhancing properties and Au chemical surface properties [10,11]. This relevance is based on the fact that AgNPs provide higher enhancements in Raman intensities when compared to other metals such as Au and Pd. Otherwise, AuNPs are usually more desired than AgNPs due to their stability, biocompatibility, and resistance to oxidation.

For several years great effort has been devoted to the fabrication of different bimetallic nanostructures, including Ag/Au [12], Au/Pd [13,14], Au/Pt [15], Ag/Pd [16], Ag/Pt [17], and Pt/Pd [18], with well-controlled morphologies and well-defined structures. Different types of BNPs, specifically: alloys, core-shell, and heterostructures, have been explored through several approaches such as lithography [19], laser ablation [20], SMG [21,22], GRR [23], microemulsions [24], chemical co-reduction [25], copolymer-mediated self-assembly [26], DNA-mediated synthesis [27,28], biological synthesis [29], and many other methods [30]. SMG has been identified as being the most used approach for preparing BNPs [2]. In this route, the overgrowth mode of the deposited metal on different side facets of the performed nuclei is highly influenced by both the kinetic and thermodynamic parameters. The kinetic adjustment can be achieved by using proper stabilizing and reducing agents that expose specific crystal planes. For instance, the presence of different reducing agents (CTAC, L-ascorbic acid, hydrazine) has particularly allowed the development of four distinct morphologies of core-shell/alloy AuPd BNPs (octahedrons, rhombic dodecahedron, nanodendrites) [31–33]. The results in [33] have suggested that high reduction rates promoted the simultaneous reduction of precursors by forming thermodynamically unfavored structure.

The nucleation and growth of Ag on one, three, and six of the equivalent {100} faces on a Pd seed has been achieved by simply manipulating the rate at which different amounts of AgNO₃ precursor were added [34]. This effectively produced bimetallic nanocrystals with three structures: hybrid dimers, eccentric nanobars, and core-shell nanocrystals [34].

The way of interaction between the secondary metal and the performed seed is widely affected by the reduction rates of metal ions, surface free energies, metal bond energies, and lattice mismatches [2]. Additionally, the structure, shape, size, and amount of seed NPs significantly control the growth mechanism and final morphologies of BNPs [35]. Jae Hee Song et al. have mentioned that Ag preferentially undergoes an anisotropic overgrowth onto {111} and {100} facets of the electrochemically synthesized Au nanorod seeds, thus leading to dumbbell-like bimetallic nanostructures [36]. The {110} facets of Au nanorod seeds were less attainable for an Ag overgrowth because of their stronger interactions with the cationic surfactants [36]. The morphology of Pt/Au heterostructures with a different number of heterojunctions, evolving from pear to peanut to clover-like structures, has been modulated by varying the sizes of Pt seeds from 3 to 7 nm respectively [37]. The morphology control was driven by a thermodynamic equilibrium between the Au coherence energy, the particle surface energy, and the Pt/Au heterogeneous interfacial energy. During the synthesis, the concentration of precursors, reaction temperature, pH, and growth time are also main factors for controlling the anisotropic shapes of inorganic NPs [38,39].

Even though the efficiency of controlling the structural properties of bimetallic nanostructures has been improved in recent years, most improvements have been achieved by solution-based protocols. However, to the best of our knowledge, rare studies have addressed the issue of fabricating BNPs with a high degree of reproducibility in terms of composition and yield of controlled morphological structures. Also, the SERS performance of such protocols is disappointing due to the lack of homogeneity and reproducibility. This is probably a result of the tendency of colloidal NPs to agglomerate when deposited on substrate surfaces.

Nonetheless, it is possible to further ameliorate the efficiency by an innovative surface-based strategy. With this goal, we developed a new nanofabrication method (VIPS) to obtain reproducible, large-scale, and structure-controlled bimetallic nanomaterials on a surface relevant for applications in the fields of SERS and plasmon detection. VIPS approach deals with studying

the self-assembly and control of nano-objects assisted by polymer nanostructuring (PMMA) [40]. The originality of this method is linked to the spontaneous reduction of the metallic precursor when depositing the M^+ /PMMA dispersion onto a conductive substrate. Also, its importance lies in its simplicity of manufacturing, the ability for structuring at RT, the possibility for controlling the structural properties of nanostructures, and the capability to firmly attach the nanostructures to the surface of the substrate without any functionalization or removal of polymer films. To date, this approach has been limited to monometallic nanoparticles such as Ag and Au [41,42]. Ag nanorings and nanospheres, dispersed in PMMA thin layer, have emerged using the VIPS process [42,43]. Recently, this method has represented its potential in fabricating precisely shaped Au nanostructures with different well-controlled morphologies, including nanocubes, nanorectangles, nanohexagons, and nanoprisms [44]. These monometallic systems have been successfully used as reliable SERS-active substrates with high ultra-sensitivity, stability, and reproducibility over a large scale.

The present study aims to develop an effective and economical strategy for designing two distinct structures of BNPs, mainly core-shell and heterostructures. Herein, the efficiency and sensitivity of bimetallic substrates were examined by SERS technique. Then, the influence of structural parameters on the sensitivity of fabricated BNPs as SERS nanosensors was demonstrated. To go further, the optical properties of BNPs were determined using micro-extinction measurements. The structural features of bimetallic substrates were identified by SEM characterizations. The overall BNPs properties were modulated by varying the concentrations of Au precursors, Ag/Au molar ratios, and spin-coating speeds. The purity of samples was checked by chemical characterization using energy dispersive X-ray spectroscopy (EDX). A possible explanation of the synthetic mechanism is proposed. The formation of bimetallic nanostructures with controlled morphologies follows the steps outlined in the mechanistic study.

3.2 Experimental Part

3.2.1 Fabrication of bimetallic substrates

The chemical reagents used in this synthesis were silver nitrate ($AgNO_3$, VWR International bv, Leuven, Belgium), sodium tetrachloroaurate (III) dihydrate ($NaAuCl_4 \cdot 2H_2O$, Sigma-Aldrich, Steinheim, Germany), and poly (methyl methacrylate) (PMMA, Sigma-Aldrich, Kappelweg 1, Schnelldorf, Germany). All of these chemicals and materials were used as received without further

purification. The solvents used throughout the whole experiments were ethanol (VWR International S.A.S., Fontenay-sous-Bois, France) as solvent of precursor molecules, and acetone (CARLO ERBA S.A.S.) as a good solvent of PMMA. Arsenic-doped silicon substrates (Si-As), that were used for coating the metallic salts/polymer dispersions, were purchased from Silicon materials society (100 orientation, ~ 525 ohm resistivity). For thin films deposition, Si wafers were cut into substrates of 2×2 cm sizes based on the dimensions of the used spin-coating machine chamber (PolosSPIN150i/200i infinite). Then, Si-As (2 × 2 cm sizes) substrates were subjected to a cleaning process by a sonication in a mixture of soap, water, acetone, and isopropanol for 30 min to remove all the anchored impurities. Generally, spin-coating machines can use a range of substrate surfaces that can be increased or decreased depending on the desired applications and usage.

The procedure used to prepare AgNO₃/PMMA solution is described in Chapter 2 (Section 2.2.2). NaAuCl₄/PMMA solution is prepared similarly, but with a change in the type of precursor molecule. Briefly, the NaAuCl₄/PMMA mixture with precise proportions was kept with a continuous stirring for 30 min under RT conditions. A subsequent addition of an acetone solvent (co-solvent), known to be a very good solvent for PMMA and also miscible with the other solvents in the mixture, was needed to adjust the interactions and eliminate the phase separation to obtain a thermodynamically stable mixture.

Our steps proceed in the same way as indicated in [42]. To fabricate bimetallic nanostructures, two different M⁺/PMMA layers were deposited subsequently on a conducting Si wafer by spin-coating at different experimental parameters (spin-coating speed: 3000, 5000, 7000, &10000 rpm, acceleration: 3000 rpm/s, and time: 30 s). Si wafers were then coated with 100 μL drop of AgNO₃/PMMA solution as a first layer followed by NaAuCl₄/PMMA as a second layer. The time delay between the two deposited layers is 10 min. Applying a coating of a different material such as Au can protect the Ag layer from extraneous chemical and physical changes and eliminate its reactivity. The concentration of AgNO₃/PMMA dispersion was fixed in all the experiments at 40 mM. The NaAuCl₄/PMMA solutions were prepared in different concentrations in order to obtain proportional ratios of Ag and Au ($R = C_{Ag}/C_{Au}$): 0.4, 0.5, 0.6 & 2. The ratios represent the respective coating of concentrations of 100, 80, 60, and 20 mM of NaAuCl₄/PMMA layers to 40 mM of AgNO₃/PMMA layer.

3.3 Results and Discussions

3.3.1 Influence of Ag/Au molar ratio

3.3.1.1 Structural properties

Upon spin-coating on silicon, a PMMA thin layer embedded with Ag^+ (at AgNO_3 concentration of 40 mM), was directly coated by Au^{3+} /PMMA dispersion in order to produce BNPs. Then, aiming to modulate the BNPs features, we prepared different substrates with various Au precursor concentration at fixed Ag concentration (Ag/Au ratios were: 0.4, 0.5, 0.6, and 2). The influence of Au concentration was studied by carrying out the samples at a spin-coating speed of 7000 rpm. This speed has been chosen as a suitable condition for fabricating homogeneous shape and size distributions of MNPs according to our previous studies [44]. The precise position and shape of plasmon bands are also sensitive to the layer thickness and polydispersity. By ellipsometry technique, the layer thickness of such sample was estimated to be ~ 220 nm. All samples had approximately the same thickness because we prepared all the substrates using the same spin coating speed (7000 rpm). One can see in Figure 30(a) heterostructures including silver nanospheres (AgNS) and AuNC when the synthesis is carried out at a low concentration of Au i.e. 20 mM. In this case, the two metals prefer to nucleate and grow individually by sharing a mixed interface. At this sample, we noted an inconsistency with Rana et al. results where 20 mM Au^{3+} /PMMA monolayer on Si-As substrate only directs the growth of gold nanospheres (AuNS) instead of AuNC [41]. Introducing a second metal as Ag^+ ions to the reaction system has brought about changes in both the nucleation and growth stages of nanostructures, and accelerated the reaction kinetics since nanocubes formation requires high synthetic process energy. As a result, different growth of NPs ensues, thus giving rise to structural properties not necessarily corresponding to its case when deposited on a conductive substrate as one layer i.e. as a monometal layer.

A major proportion of eccentric core-shell bimetallic nanostructures is dominated at moderate concentrations of Au i.e. 60 mM (Figure 30(b)). Herein, the shell does not completely encapsulate the core. Speed effect study provides further evidence for this interesting structure, as stated in Figure 33.

In Figure 30(c) and (d), the low Ag/Au ratios enable the formation of a high number of anisotropic AuNC and Au nanorectangles (AuNR) over the whole surface. At this condition, the reaction

proceeds rapidly in a way that a minor quantity of Au atoms takes part in the buildup of bimetallic nanostructures. An excess of Au^{3+} kinetically favors the production of anisotropic AuNC and AuNR. The mixture contains all the conditions that promote its fast kinetics of growth including the high volatility of solvents (ethanol and acetone), high concentration of Au precursor (> 60 mM), high spin-coating speed (7000 rpm), and high pH and molecular weight ($M_w = 397.80$ g/mol) of gold precursor molecule ($\text{NaAuCl}_4 \cdot 2\text{H}_2\text{O}$). Some key factors on the shape control of AuNPs are summarized in [44]. Among these parameters, the influence of the non-solvent of metallic salts, PMMA solvents, and the chemical nature of counter ions is cited [44].

Summing up the results, it can be concluded that increasing the concentration of gold precursor additives to extreme values affects highly the nanoparticles aspect ratio, gap distances, and density of AuNPs on the surface.

One of the major drawbacks to adopting two metallic precursors in a reaction system is that the two different metal atoms cannot contribute equally to the metal-metal bond formation due to their different reaction kinetics. Also, the differences in reaction kinetics might stimulate the origination of separate monometallic phases i.e. a physical mixture of two metals.

Therefore, a proper ratio of two metals is necessary to meet both the thermodynamic and kinetic requirements for the growth of bimetallic nanostructures by avoiding a monometallic phase separation and achieving a composition control. This was fulfilled by using Ag/Au ratios ($R_{\text{Ag}/\text{Au}}$) of 2 and 0.6 to fabricate heterostructures and core-shell structures respectively.

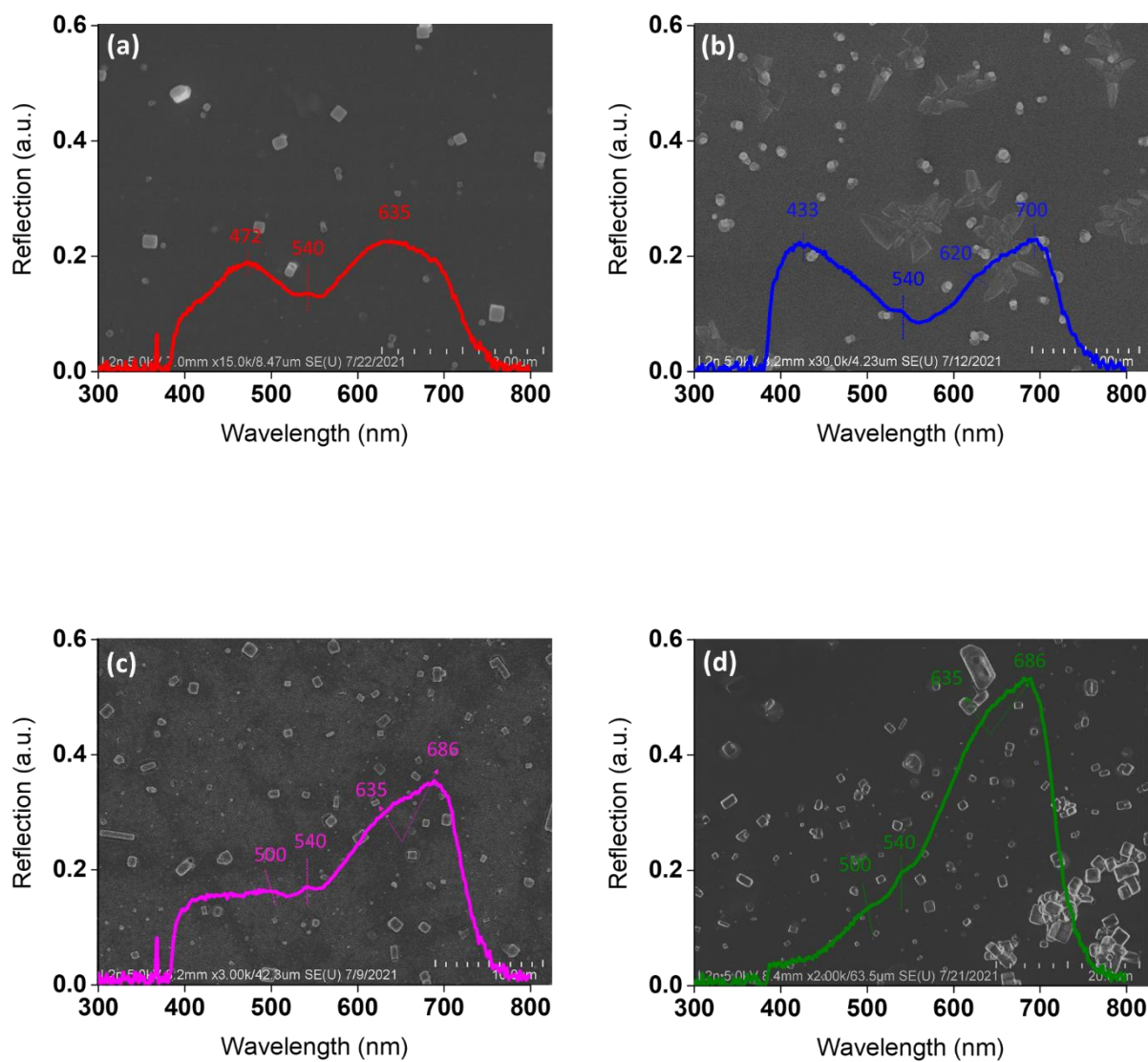


Figure 30. SEM images of bimetallic nanostructures synthesized by deposition of two M^+ /PMMA layers on Arsenide-doped silicon (Si-As) substrate. Different mixing patterns of BNPs obtained with different ratios of Ag/Au: (a) $R_{Ag/Au} = 2$; (b) $R_{Ag/Au} = 0.6$; (c) $R_{Ag/Au} = 0.5$; and (d) $R_{Ag/Au} = 0.4$. Scale bars of SEM images are: (a) 3; (b) 1; (c) 10; and (d) 20 μm . The insets correlate with the reflection optical results taken from BNPs substrates. The reflection spectra were collected by modifying the concentrations of NaAuCl_4 /PMMA-acetone from 20 to 100 mM, whereas the concentration of AgNO_3 /PMMA and the speed were kept constant at 40 mM and 7000 rpm respectively.

3.3.1.2 Optical vs chemical characterizations

Through the use of a micro-extinction setup, we were able to monitor the changes in the optical properties at each ratio. The results are pointed out in the insets of Figure 30.

Indeed, to some extent, a red-shift in the position of AuNPs peaks accompanied by increased intensities are notable with high Au concentrations. The intensity of peaks is proportional to the increase in the number of NPs on the surface.

When the final ratio of Ag/Au is 2, we observe the formation of three bands (~ 472, 540, and 635 nm). The peak at ~ 472 nm confirms the existence of AgNS response. The peak occurring at 635 nm arises from the response of the longitudinal peak of anisotropic AuNC, which are considerably affected by the RI of PMMA. It appears that the measurements are not sensitive to the coupling response of heterostructures.

For bimetallic substrate, which is prepared at ratio Ag/Au ~ 0.6, the appearance of the first three bands (~ 433, 540, and 620 nm) indicates that this system contains a mixing pattern of Au and AgNPs. The fourth peak located at 700 nm is related to the response of the bimetallic core-shell system. However, it is crucial to judge if both Ag and AuNPs exist on the substrate surface. This is confirmed by an EDX mapping study in Figure 31. The line scan reveals that the core/shell nanoparticle is composed of enriched AgNPs and a lower quantity of AuNPs. A quantity of sodium (Na) and chlorine (Cl) is also observed. This is due to a space charge region consisting of a double layer of positive and negative ions around the Au seed [45]. X-ray spectrometry detects elements but it is not capable to differentiate between ionic and non-ionic species.

The spectrum of this system is characterized by a remarkable blue-shift of the plasmon band of Ag from 472 to 433 nm, and a slight blue-shift of Au response from 635 to 620 nm. The combination of a decrease in the size of AgNPs and a change in the shape of AuNPs triggers this blue-shift. More details on the attribution of peaks are given in Section 3.3.2.

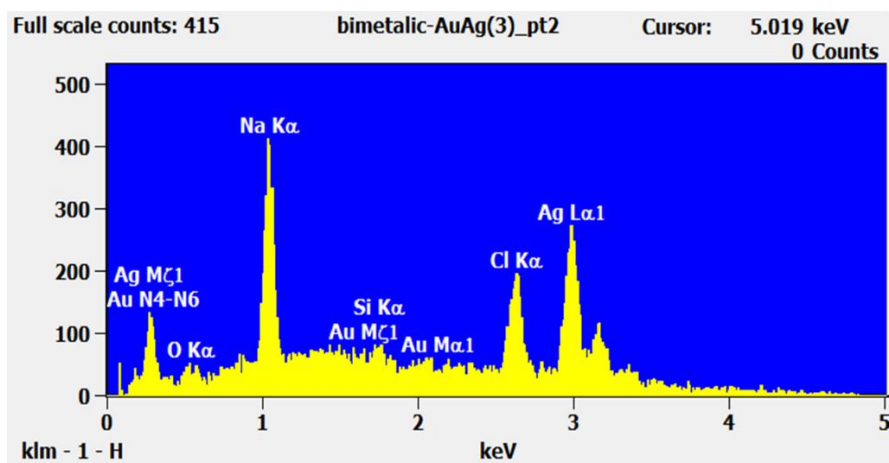


Figure 31. EDX spectrum showing the characteristic X-rays originated from interacting a single core/shell nanoparticle with an electron beam. This spectrum refers to the sample prepared at ratio $R_{Ag/Au} = 0.6$.

The spectral observations are highly dominated by the response of AuNPs at $R_{Ag/Au} = 0.5$ and 0.4 . Here, the contribution from AgNPs is no longer visibly observed in the micro-extinction spectrum. This does not preclude the possibility of having the two regimes of the monometallic counterparts on the substrate surfaces. The optical spectrum exhibits four different peaks at ~ 500 , 540 , 635 , and 686 nm, which indicated that the first band is assigned to Ag response and the latter three bands to Au response. The spectrum of anisotropic Au nanocubes shows a couple of overlapped longitudinal peaks at 635 and 686 nm (i.e. one for single particle and another for coupling effect) beyond the transverse peak near 540 nm. The impressive red shift to ~ 686 nm is explained by the presence of anisotropic cubic-shaped NPs with increased sizes and small gap distances (< 10 nm). The fabricated substrates are also influenced by the high RI of PMMA. According to Boundary Elementary Method (BEM) simulations, the interaction of 65 nm Au–Au isotropic nanocube dimers in air, separated by 10 nm gap distances, gives a peak at 620 nm [41].

All the samples have almost a peak positioned at around 540 nm. This transverse resonance mode shows essentially no shift. This result is in agreement with the response of a single isotropic AuNC of size 65 nm in an air matrix, with rounded edges, calculated by BEM simulations [41].

It is obvious from Figure 30 that the bimetallic systems are immensely low in metal quantity. In our typical synthesis, both Ag and Au metallic precursors are mixed with PMMA solutions, acting

as metallic NPs synthesis reactors. Owing to the presence of two PMMA layers of thickness ≥ 200 nm, a great proportion of NPs is restricted between the PMMA layers, thus preventing its presence in high quantities. In fact, the chemistry of the surface plays an important role in the self-assembly process. The structuring of the bimetallic system is influenced by the repulsive interactions between its constituents, which are totally different from the ones existing on monometallic systems. For instance, in the synthesis of monometallic AuNC and AgNS, the PMMA micelles loaded with both precursors tend to avoid the hydrophilic silicon surface. Therefore, a high quantity of small size micelles is produced leading then to the formation of a high-density substrate. In contrast, when depositing Au/PMMA on Ag/PMMA, the second layer of PMMA micelles embedded with AuNPs will be spread on a hydrophobic surface (PMMA), in relation to lower repulsive interactions between micelles. Therefore, micelles tend to coalesce and lead then to the formation of a lower amount of larger size nanoparticles on the substrate surface.

3.3.1.3 Sensing properties (SERS) :

In order to assess the effectiveness of the substrates produced, the resulting bimetallic nanostructures were then used for the detection of 4,4'-BP. The analytical Raman spectrum of 4,4'-BP has five featured peaks in the range of 900-1600 cm^{-1} [46]. The characteristic vibrational modes are at 980, 1215, 1285, 1493, and 1593 cm^{-1} [46].

Basically, SERS efficiency is maximum for $\lambda_{\text{LSPR}} \sim \lambda_{\text{Raman}}$. For this reason, the samples were excited at 633 nm near to Au response, as highlighted in Figure 32(a).

The adsorption of 4,4'-BP molecules on BNPs surfaces causes modifications and shifts in their well-known vibrational frequencies. The vibrational signatures become centered at 1026, 1085, 1235, 1290, 1513, and 1618 cm^{-1} . The computed and experimental frequencies in the Raman and SERS spectra and assignments of BP are fully justified in the literature [47]. The shifts are clarified by a change in geometric and electronic structures due to the interaction between the lone pairs of the nitrogen atoms of the BP ring and BNPs on the surface [48]. This substantiates the fact that a chemical enhancement is mainly contributing to the enhancement of SERS signals [48]. In general, the SERS of a chemical origin, which cannot exceed 10^2 EF, is attributed to the formation of charge transfer complexes between the target molecule and the metal surface [49].

All vibrational bands on the BP-coated substrates almost have the same positions and broadness when varying the ratios of Ag/Au.

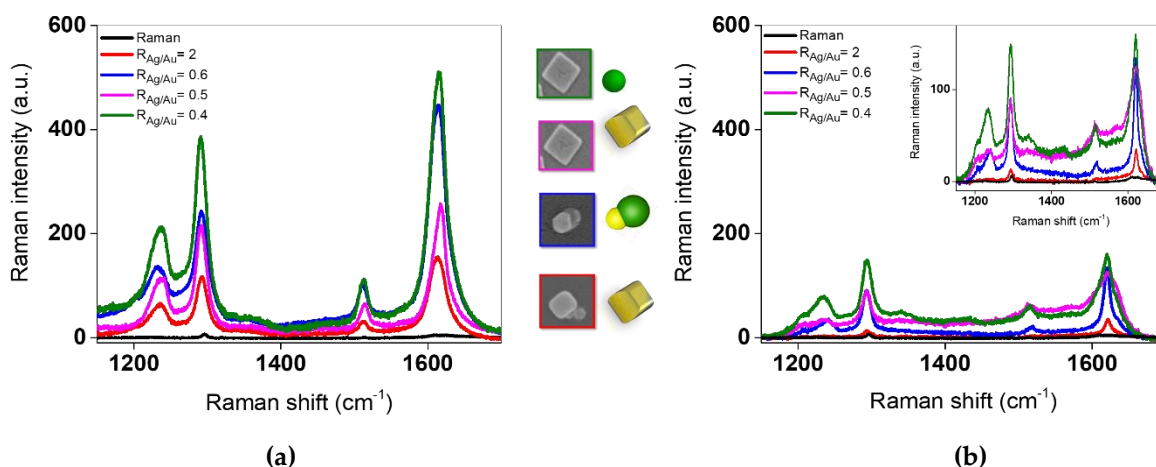


Figure 32. Raman and SERS spectra of BP-coated bimetallic substrates with different compositions recorded at λ excitation of: (a) 633 nm; and (b) 514 nm. Normalization of SERS intensities was performed by Origin software.

The quantity of NPs excited by the laser directly influences the intensity of the SERS signal. At $R_{Ag/Au} = 2$, the density of NPs is conspicuously lower than the other substrates prepared at low ratios of Ag/Au. This results in less intense SERS signals. Herein, the Au nanoparticles generated are cubic-shaped.

BP molecules exposing high-index facets with hexagon shapes on BNPs surface show significantly enhanced SERS sensitivities at $R_{Ag/Au} = 0.6$. Increasing the number of edges, crystallographic facets, corners, and faces is of decisive importance in the SERS sensitivity of NPs. It is evident that, in these anisotropic shapes, more active and multiple crystallographic facets are coherently present, thus the interaction is comparatively preferable with greater opportunity for adsorption of BP molecules on active facets [50]. The surface atoms on high-index facets are high-energy active sites [51]. Electronic effect and localized electric field enhancement between the two metals could also make an additional contribution to such an enhancement of the SERS signal [52]. Although the trend of results between $R_{Ag/Au} = 0.6$ and 0.5 differ, it could nevertheless be argued that synergistic effects between two metals affect the SERS signal.

To build highly sensitive SERS substrates, sharp features of AuNC can have a strong impact on the enhancement of SERS properties. The high electric field, large surface area, and large hot-spot volumes associated with anisotropic nanocube-nanocube contacts at $R_{Ag/Au} = 0.5$ and 0.4 are responsible for the intense SERS signals [50]. At $R_{Ag/Au} = 0.4$, the increase in the number of

efficient hotspots, presented in the gaps, tips, and edges, focuses the electromagnetic field and enhances the amplification of SERS signals.

Additional tests were performed for evaluating the sensitivity of substrates at an excitation wavelength of 514 nm in order to match the plasmonic band of AgNPs this time. Figure 32(b) shows a similar trend in the variations of SERS intensities at different ratios. This provides adequate proof for using the bimetallic substrates as wide-range SERS active substrates. The excitation of the surfaces at 514 nm, where the LSPR of the transverse band of Au \sim 540 nm and the band of Ag at low ratios \sim 500 nm has a significant overlap with the laser, leads to lower sensitive signals with respect to those at 633 nm. This indicates that EM, due to LSPR modes, is important in a wavelength range beyond 600 nm. Commonly, increasing the signal intensity does not always result from tuning the LSPR closer to the excitation wavelength. As can be seen in the insets of Figure 30, the reflection from AgNPs is lower than that of AuNPs and this is certainly due to the low amount of non-anisotropic shapes of AgNPs (i.e. spherical) excited on the surface. The high density of NPs and hotspots regions are essential factors to enhance the sensitivity of the SERS analysis [53].

Given that our findings are based on a very limited number of NPs, the results from such analysis indicate that anisotropic bimetallic substrates are convenient for sensitive BP detection and are potential candidates for SERS-based sensors. In our view, the origins of SERS features heavily relies on three factors: (i) additional chemical effects favored on anisotropic NPs due to the presence of highly reactive facets with higher binding affinities for analytes, (ii) SERS nanofocusing of analytes targeted on metallic regions due to the presence of a hydrophobic PMMA layer [42,54], and (iii) synergistic effects between two MNPs. Our SERS results share a number of similarities with Khaywa et al. findings where thermally-annealed double layers of BNPs are fabricated [55].

3.3.2 Speed Effect Study on the bimetallic sample at $R_{Ag/Au} = 0.6$

Further studies on the bimetallic sample at $R_{Ag/Au} = 0.6$ were required to elucidate its structure. Figure 33(a) reveals the SEM images of Ag/Au core-shell structures obtained at different speeds.

In SMG, the addition of metal ions (as Ag^+), reducing agents, and surfactants behave as driving agents for the growth and control of shapes of NPs. Herein, the surface is passivated with PMMA

to prevent the agglomeration of nanoparticles and then to ensure the stability of the substrates. The concentration of PMMA ($C = 30 \text{ g/L}$) and its molecular weight ($M_w = 350,000 \text{ g/mol}$) is fixed in all the samples. Similarly, the samples were prepared using the same concentration of Ag^+ ions on an identical type of substrate (Si-As). Consequently, the kinetic parameters will only be adjusted by the spin-coating speed, which acts as an alternative driving agent. Spin-coating speeds promote intervention in the distribution rate of growth of Ag^+ ions on Au seeds through adjusting the time between the evaporation of solvents and the assembly of vesicles. The Au seeds will be rapidly approached and covered by Ag atoms at high speeds.

A pronounced change in the optical properties of BNPs, as illustrated in Figure 33(b, c), confirms that the speed of evaporation of solvents is a key parameter that controls its structural properties. Further shifts in plasmon bands were obtained at different speeds with preferential maintenance of the four plasmonic bands. The first peak is red-shifted from 405 to 447 nm in a predictable manner by increasing the spin-coating speed. This is a result of the presence of AgNPs on the surface with increased sizes. The other peaks ($\sim 540, 620, \text{ and } 695\text{-}700 \text{ nm}$) are approximately constant at all speeds. The plasmon resonance peak at 620 nm becomes clearly recognized at high spin-coating speeds i.e. 7000 and 10000 rpm.

The extinction spectra of isotropic AuNPs of 70-nm-diameter hexagons, prepared by a SMG in an aqueous bulk solution, have a plasmon band near 540 nm [56]. A noticeable agreement is evident with our findings. Taking into consideration that the Au nanohexagons (AuNH) are unsymmetrical in structure, an additional peak is observed near 620 nm. The average of single-particle scattering properties of vertically oriented AuNH with lateral sizes $\sim 160 \text{ nm}$, prepared by SMG and deposited on indium tin oxide (ITO) substrates, displays two peaks at ~ 560 and 693 nm [57]. The single-particle scattering spectra were estimated on ~ 50 NPs [57]. It is difficult to reach a red-shift near 700 nm with very low densities and high gap distances of AuNH on the surface, with sizes $\sim 70 \text{ nm}$. This assures that the peak at $\sim 620 \text{ nm}$ is originated from the response of anisotropic AuNH embedded in high RI of PMMA. Using a micro-extinction setup, our measurements have only been conducted on a small area of NPs. Inevitably, the optical properties of single-particle scattering measurements are smaller than the ensemble solution values [58]. Ruibin Jiang et al. concluded that the influence of an internal Au core on plasmonic properties of core-shell nanorods boosts once Ag shell thickness reaches a value lower than 5 nm [59]. At this condition, the core

metal will exert a high impact on its coupling and interaction with the exterior shell. A shell thickness < 5 nm is expected in our fabricated structures. This strengthens the coupling between interior and exterior NPs and makes the Ag shell highly affected by the high RI sensitivity of AuNH and PMMA. This allows the continuous red-shift of the peak into ~ 700 nm. Accordingly, the peaks situated at 695-700 nm and assigned to the coupled core-shell system are quite analogous at all speeds due to the slight variations in the shell thicknesses. Based on the SEM images, with the presence of an unsymmetrical hexagon Au core with constant lateral average size of ~ 70 nm and shape at all speeds, it is worth noting that the shift of optical properties is quite sensitive to the shell thicknesses and unaffected by the core [60]. According to previous assumptions, it is anticipated that the LSPR bands of the core-shell systems are gradually red-shifted owing to the fact that the thicknesses of the shell are decreased [61].

(a)

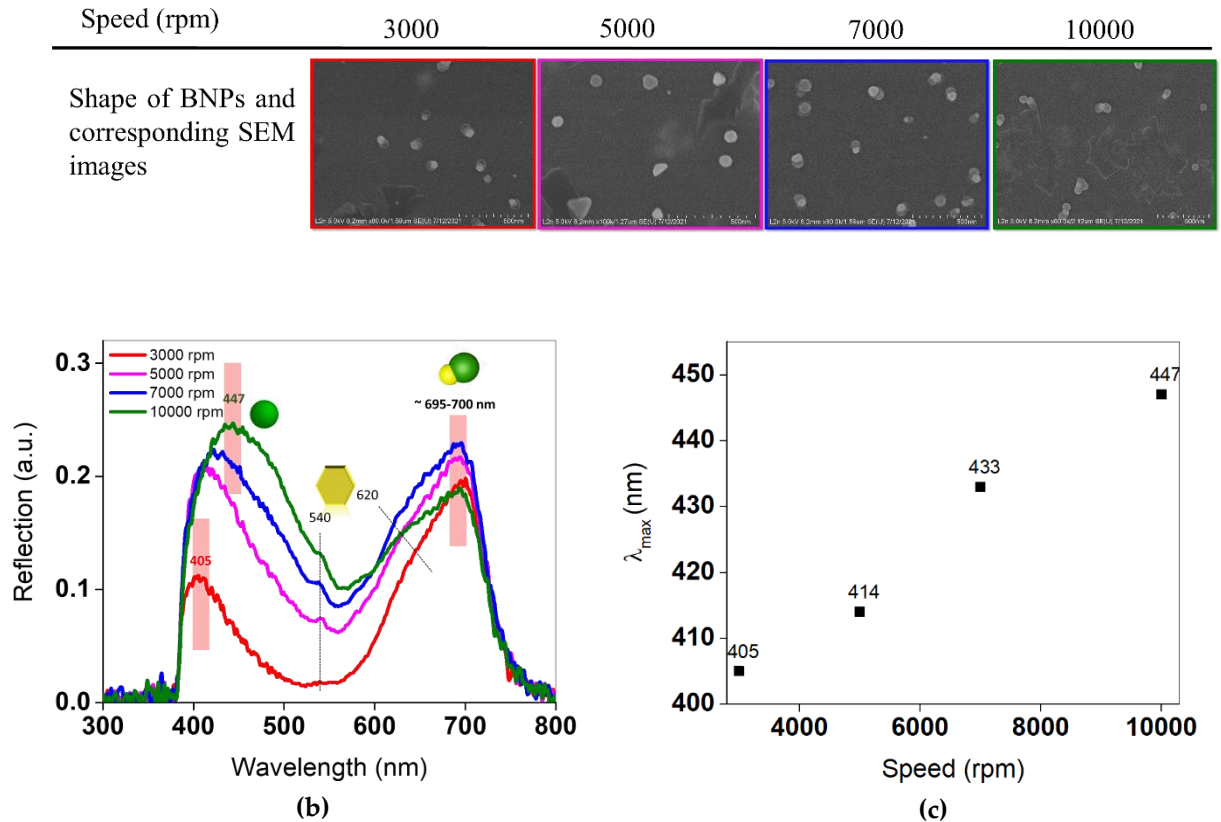


Figure 33. (a) SEM micrographs of Ag/Au core-shell structures obtained by varying spin-coating speed at constant ratio $R_{Ag/Au} = 0.6$; (b) The influence of spin-coating speed on the experimental reflection spectra of BNPs as it approaches a silicon surface; and (c) The variation of the maximum wavelength of the first plasmon band as a function of spin-coating speed.

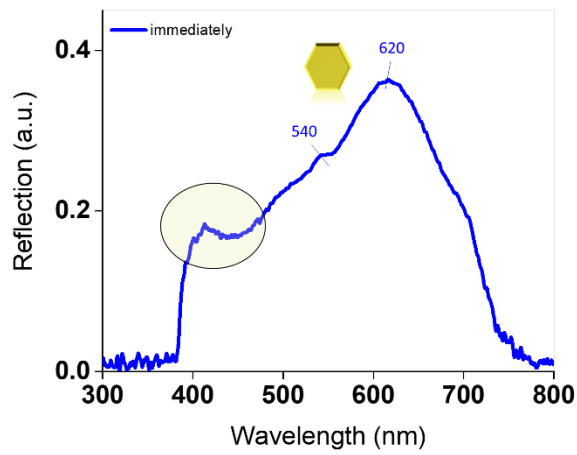
3.3.3 Optical monitoring on $R_{\text{Ag}/\text{Au}} = 0.6$ at 7000 rpm

This study can be considered as time-dependent fabrication and analysis of BNPs, as a first step towards enhancing our understanding of the mechanism of formation of core-shell structures. It is apparent from Figure 34 that the evolution of the reflection spectra differs with time on the same sample.

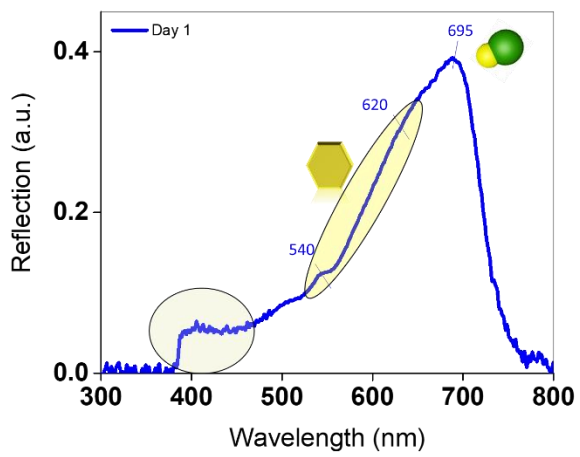
When the substrate is freshly analyzed (Figure 34(a)), the reflection spectra show the presence of two bands at ~ 540 and 620 nm. This proves that the formation of AuNPs starts immediately due to their high rate of growth. Typically, anisotropic geometries yield additional dipole resonances consistent with their shapes, thus giving rise to more than one peak [35]. This is an evidence to support the hypothesis that AuNPs have non-spherical morphologies. The hexagon shape of AuNPs is presented in Figure 33. At the same time, a slow appearance of reflected bands of Ag in the 400 nm region takes place during the synthesis.

Within 6 h (Figure 34(b)), a major new peak exhibits a red-shift to 695 nm, as revealed by the time-dependent reflection spectra. The peaks of AuNPs (~ 540 and 620 nm) were reduced in intensity. This observation emphasizes the upgrowth of a new bimetallic system. The formation time of BNPs ~ 6 h was noticeably accelerated by the presence of Au, but overall it was still slower than that of Au alone. This might be caused by the seeding effect of Au. This also demonstrates the need to overcome a certain time to start the formation of BNPs. Afterwards, the major peak shift becomes slow by moving only to 700 nm. The increased deposition of Ag atoms over time caused the intensity to decrease, thus resulting in large sizes and few numbers of NPs. As the time prolonged, the reflection band of Ag red-shifts and its intensity has considerably increased. This is ascribed to the contribution of the excess of Ag atoms in the growth of AgNPs.

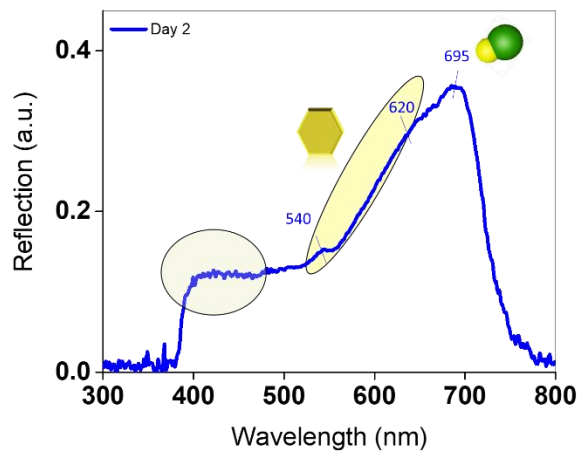
No other time evolution is then observed in the reflection spectra after 1 week of synthesis (Figure 34(g)). This suggests that the sample reaches a stable condition and completes its growth after 1 week. This time is appropriate for the complete consumption of all the precursors.



(a)



(b)



(c)

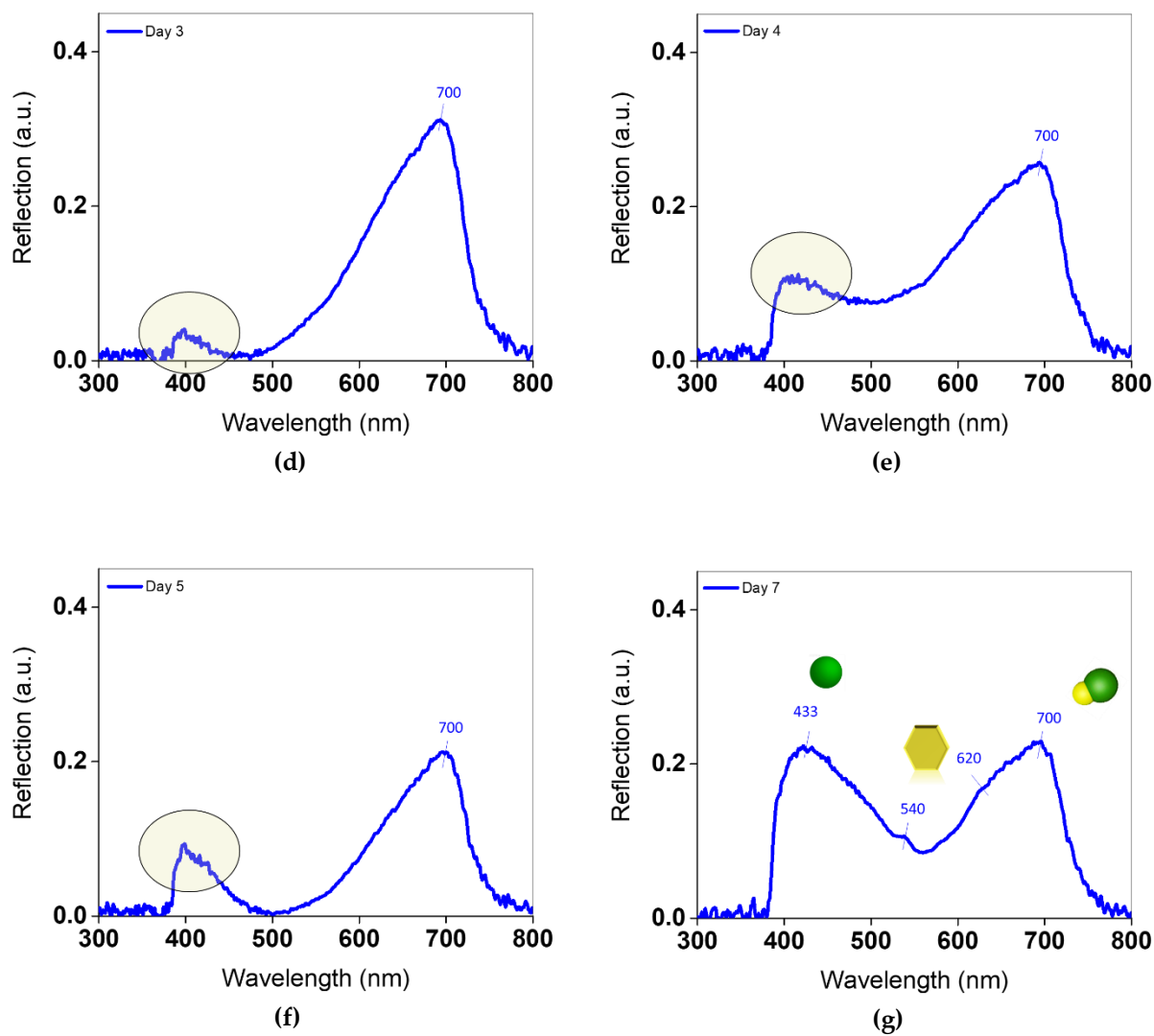


Figure 34. Spectral evolution of reflected bands of Ag/Au/PMMA metallic layers on Si surface at ratio $R= 0.6$ and speed 7000 rpm from (a) fresh substrate to (b) 6h old substrate to (g) 1 week old substrate.

3.3.4 Proposed Mechanism at different Ag/Au ratios

The pathway mechanism for forming BNPs is suggested in Figure 35. The growth of different BNPs structures depends on a combination of several factors including the relative strengths of homonuclear and heteronuclear bonds, surface energies of bulk elements, and its relative atomic sizes [62]. It has been established that the relative bond strengths of Ag and Au metals follow the order where Au-Au bond ($D^0 = 218$ kJ/mol at 289 K) precedes the Ag-Au ($D^0 = 203$ kJ/mol at 289 K) and Ag-Ag ($D^0 = 163$ kJ/mol at 289 K) bonds respectively. This makes new Au atoms favor the deposition on Au surface of NPs rather than Ag surface, while new Ag atoms will be more propositional to accumulate on the Au surface of NPs. The surface energy of Ag (1.25 J.m⁻²) is lower than that of Au (1.5 J.m⁻²) and their atomic sizes ($r = 144$ pm) are comparable. This implies that Ag atoms tend to be placed at the surface of NPs [63].

Generally, the mechanism is based on a seeded growth process on the surface. The reduction of both Ag⁺ and Au³⁺ ions is initiated once the two layers are deposited on the Si-As substrate. The conductivity of this latter and the counter ions (NO₃⁻ and Cl⁻) play a vital role in providing the electrons into the metallic precursors. This widely complicates the understanding of the mechanism since there is no control over the sources of free electrons. To prevent any initiation of alloyed structures, the procedure was made at RT to inhibit any inter-diffusion between Ag and Au atoms. In our synthetic conditions, most of the Ag and Au ions are immediately reduced to atoms before the formation of nuclei due to the high reduction rate of nucleation and growth. This leads to a preferential collision of atoms and nuclei instead of collisions between either atoms or nuclei. The number of nuclei formed from Au (fast nucleation) is higher than Ag nuclei (slow nucleation). The fast nucleation rate of Au is certainly due to its high reduction potential ($E^0 = 1.498$ V) when compared to Ag ($E^0 = 0.7996$ V) [63]. This promotes the further growth of Ag atoms on the formed Ag and Au nuclei via homogeneous and heterogeneous growth respectively. The way of the growth of Ag atoms is affected by the surface energy of the different shapes (cubic or hexagon) of exposed Au seed facets.

A heteroepitaxial overgrowth results from the close match in lattice constants and crystal structures between the seed (Au) and deposited metal (Ag) [64]. It is still possible, however, for the final nanostructure shape to differ from that of the initial seed as the crystal habit is also governed by the growth rate of crystallographic facets.

For heterostructures (Figure 35(a)), the growth follows the VW mode [65]. The deposition of Ag atoms starts to grow on the higher surface energy {110} edges followed by a possible sequential migration into {111} vertices of Au cubic seed and {100} facets by surface diffusion. This is broadly consistent with prior observations in the literature [66–68]. Since deposition occurs at a much faster rate than diffusion, the growth is restricted to the {110} facets of the cubic seed. This leaves the {100} and {111} facets unexposed to any atomic deposition, and forms segregated islands on {110} facets.

At extreme values of Au additives (Figure 35(b)), a high quantity of Au atoms will undergo a homogeneous growth on Au nuclei and form a considerable quantity of anisotropic AuNPs and high aspect ratios. This will not exclude the probability of the presence of minor amounts of BNPs and AgNPs on the surface. The Au cubic seeds simply grew into larger cubes still enclosed by {100} facets. Both deposition and diffusion occur uniformly on all the facets of the cubic seed, ultimately forming high aspect ratios of anisotropic AuNC through a layered growth (FM mode).

The sample with eccentric core-shell BNPs (Figure 35(c)) can be viewed as an intermediate between FM and SK growth modes [65]. Ordinarily, in face-centered cubic (FCC) nanocrystals, the surface free energies of high-index facets of Au decrease in the order of {111}>{100}>{110}[35]. Besides having twin boundaries, the hexagon-shaped AuNP contains {111} and {200} lattice planes [69]. The (111) lattice planes cover a much larger portion of the particle's surface [69]. This facilitates the preferential growth of Ag atoms onto {111} facets of polycrystalline AuNH seed, and promotes the growth into crystals exposing {111} planes rather than uniform coverage at all the facets of AuNH. This observation is supported by previous studies, where new atoms are more exposed to grow along <{111}> directions [69–71]. Eventually, an anisotropic eccentric core-shell structure with enriched Ag in the outer layer is developed since the Ag atoms did not coat the AuNH from all its entire sides.

The findings of the mechanism point towards the idea that Au additives act as: (i) accelerating agents for reduction of Ag and formation of BNPs, (ii) preferential sites for the growth of Ag atoms (nucleation centers-seeding effect).

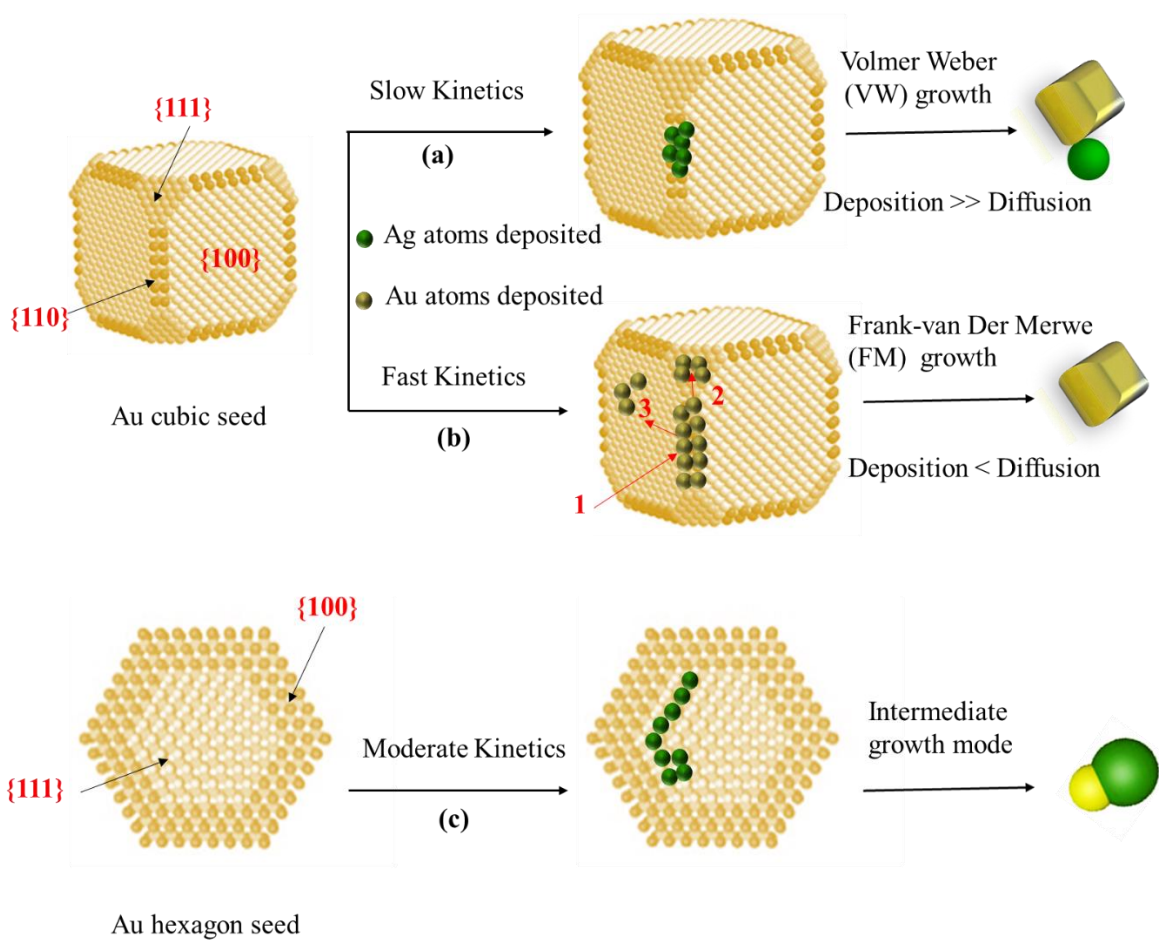


Figure 35. Schematic illustration of the mechanistic framework of BNPs at slow, moderate, and fast regimes of kinetics.

3.4 Conclusion

We demonstrated a rapid surface-based approach for the fabrication of Ag/Au BNPs with tunable dimensions and morphologies. In this synthesis way, the resulted heterostructures were mainly mediated by the repulsive interactions between the two nanometal/PMMA layers and the substrate surface. Precisely, these interaction forces can be controlled by the speed and the Ag/Au molar ratios. As a result, a relatively safe, facile, and cost-effective synthesis was accomplished. Anisotropic growth modes of BNPs have been attained by a site-selective heterogeneous growth of Ag on substrate-based Au seeds. A regime of slow and moderate kinetics has directed the reaction towards a bimetallic heterostructure and core-shell configuration. Fast rates of reaction have induced a physical mixture of nanospheres and anisotropic nanocubes.

The optical properties of BNPs on the opaque surface were successfully predicted and improved using a micro-extinction setup. These advancements are in demand in a field where any change in structural properties can result in huge changes in optical and sensing signatures. Results so far on anisotropic BNPs were promising as SERS sensors promoters. This was derived from a chemical enhancement on the steps, edges, tips, corners, and kinks of the high-indexed facets. Although these results were only validated on very small densities of surfaces, the synergistic effects between two coupled metals still render this sample the high sensitivity. The evaluation of sensors with different wavelengths has illustrated its optical versatility. A comparative SERS study has been done to provide a correlation between anisotropic shapes and sensing properties.

This study provides a framework for synthesizing more complex hybrid nanomaterials with dual functionalities such as Ag/Pd and Au/Pd. By manipulating the morphology in such a precise way, hybrid systems can be exploited in bio-detection, diagnosis, catalysis, and optical applications.

3.5 References

- [1] Ramos, R. M. C. R., and Regulacio, M. D., 2021, “Controllable Synthesis of Bimetallic Nanostructures Using Biogenic Reagents: A Green Perspective,” *ACS omega*, **6**(11), pp. 7212–7228.
- [2] Li, G., Zhang, W., Luo, N., Xue, Z., Hu, Q., Zeng, W., and Xu, J., 2021, “Bimetallic Nanocrystals: Structure, Controllable Synthesis and Applications in Catalysis, Energy and Sensing,” *Nanomaterials*, **11**(8), p. 1926.
- [3] Prakash, O., Sil, S., Verma, T., and Umapathy, S., 2019, “Direct Detection of Bacteria Using Positively Charged Ag/Au Bimetallic Nanoparticles: A Label-Free Surface-Enhanced Raman Scattering Study Coupled with Multivariate Analysis,” *The Journal of Physical Chemistry C*, **124**(1), pp. 861–869.
- [4] Yang, Y., Zhang, Q., Fu, Z.-W., and Qin, D., 2014, “Transformation of Ag Nanocubes into Ag–Au Hollow Nanostructures with Enriched Ag Contents to Improve SERS Activity and Chemical Stability,” *ACS applied materials & interfaces*, **6**(5), pp. 3750–3757.
- [5] Hwang, E. Y., Lee, J. H., and Lim, D. W., 2020, “Anisotropic Bimetallic Core–Satellite–Poly (Aniline) Nanohybrids for Detection of Autoantibodies,” *Macromolecular Rapid Communications*, **41**(20), p. 2000331.
- [6] Dong, P., Lin, Y., Deng, J., and Di, J., 2013, “Ultrathin Gold-Shell Coated Silver Nanoparticles onto a Glass Platform for Improvement of Plasmonic Sensors,” *ACS applied materials & interfaces*, **5**(7), pp. 2392–2399.
- [7] Zhang, C., Yin, A.-X., Jiang, R., Rong, J., Dong, L., Zhao, T., Sun, L.-D., Wang, J., Chen, X., and Yan, C.-H., 2013, “Time–Temperature Indicator for Perishable Products Based on Kinetically Programmable Ag Overgrowth on Au Nanorods,” *ACS nano*, **7**(5), pp. 4561–4568.
- [8] Liu, J., Zheng, Y., Hong, Z., Cai, K., Zhao, F., and Han, H., 2016, “Microbial Synthesis of Highly Dispersed PdAu Alloy for Enhanced Electrocatalysis,” *Science advances*, **2**(9), p. e1600858.
- [9] Zhu, G., Wang, L., Bing, N., Xie, H., and Yu, W., 2019, “Enhancement of Photothermal Conversion Performance Using Nanofluids Based on Bimetallic Ag–Au Alloys in Nitrogen-Doped Graphitic Polyhedrons,” *Energy*, **183**, pp. 747–755.

- [10] Bai, Y., Gao, C., and Yin, Y., 2017, “Fully Alloyed Ag/Au Nanorods with Tunable Surface Plasmon Resonance and High Chemical Stability,” *Nanoscale*, **9**(39), pp. 14875–14880.
- [11] Kang, H., Buchman, J. T., Rodriguez, R. S., Ring, H. L., He, J., Bantz, K. C., and Haynes, C. L., 2018, “Stabilization of Silver and Gold Nanoparticles: Preservation and Improvement of Plasmonic Functionalities,” *Chemical reviews*, **119**(1), pp. 664–699.
- [12] Pham, T. T. H., Vu, X. H., Dien, N. D., Trang, T. T., Van Truong, N., Thanh, T. D., Tan, P. M., and Ca, N. X., 2020, “The Structural Transition of Bimetallic Ag–Au from Core/Shell to Alloy and SERS Application,” *RSC Advances*, **10**(41), pp. 24577–24594.
- [13] Zhang, L., and Zhang, C., 2013, “Dodecahedral Au@ Pd Nanocrystals with High-Index Facets and Excellent Electrocatalytic Activity and Highly Efficient Surface-Enhanced Raman Scattering Enhancement,” *Nanoscale*, **5**(13), pp. 6074–6080.
- [14] Hong, J. W., Lee, Y. W., Kim, M., Kang, S. W., and Han, S. W., 2011, “One-Pot Synthesis and Electrocatalytic Activity of Octapodal Au–Pd Nanoparticles,” *Chemical Communications*, **47**(9), pp. 2553–2555.
- [15] Tan, C., Sun, Y., Zheng, J., Wang, D., Li, Z., Zeng, H., Guo, J., Jing, L., and Jiang, L., 2017, “A Self-Supporting Bimetallic Au@ Pt Core-Shell Nanoparticle Electrocatalyst for the Synergistic Enhancement of Methanol Oxidation,” *Scientific reports*, **7**(1), pp. 1–10.
- [16] da Silva, A. G., Rodrigues, T. S., Haigh, S. J., and Camargo, P. H., 2017, “Galvanic Replacement Reaction: Recent Developments for Engineering Metal Nanostructures towards Catalytic Applications,” *Chemical Communications*, **53**(53), pp. 7135–7148.
- [17] Rodrigues, T. S., da Silva, A. G., Goncalves, M. C., Fajardo, H. V., Balzer, R., Probst, L. F., da Silva, A. H., Assaf, J. M., and Camargo, P. H., 2016, “Catalytic Properties of AgPt Nanoshells as a Function of Size: Larger Outer Diameters Lead to Improved Performances,” *Langmuir*, **32**(36), pp. 9371–9379.
- [18] Yin, A.-X., Min, X.-Q., Zhu, W., Wu, H.-S., Zhang, Y.-W., and Yan, C.-H., 2012, “Multiply Twinned Pt–Pd Nanoicosahedrons as Highly Active Electrocatalysts for Methanol Oxidation,” *Chemical Communications*, **48**(4), pp. 543–545.
- [19] Liusman, C., Li, S., Chen, X., Wei, W., Zhang, H., Schatz, G. C., Boey, F., and Mirkin, C. A., 2010, “Free-Standing Bimetallic Nanorings and Nanoring Arrays Made by on-Wire Lithography,” *ACS nano*, **4**(12), pp. 7676–7682.

- [20] Rybaltovsky, A., Epifanov, E., Khmelenin, D., Shubny, A., Zavorotny, Y., Yusupov, V., and Minaev, N., 2021, “Two Approaches to the Laser-Induced Formation of Au/Ag Bimetallic Nanoparticles in Supercritical Carbon Dioxide,” *Nanomaterials*, **11**(6), p. 1553.
- [21] Qin, Y., Wang, B., Wu, Y., Wang, J., Zong, X., and Yao, W., 2021, “Seed-Mediated Preparation of Ag@ Au Nanoparticles for Highly Sensitive Surface-Enhanced Raman Detection of Fentanyl,” *Crystals*, **11**(7), p. 769.
- [22] Krishnan, S. K., Esparza, R., Flores-Ruiz, F. J., Padilla-Ortega, E., Luna-Bárceñas, G., Sanchez, I. C., and Pal, U., 2018, “Seed-Mediated Growth of Ag@ Au Nanodisks with Improved Chemical Stability and Surface-Enhanced Raman Scattering,” *ACS omega*, **3**(10), pp. 12600–12608.
- [23] Xia, X., Wang, Y., Ruditskiy, A., and Xia, Y., 2013, “25th Anniversary Article: Galvanic Replacement: A Simple and Versatile Route to Hollow Nanostructures with Tunable and Well-Controlled Properties,” *Advanced Materials*, **25**(44), pp. 6313–6333.
- [24] Li, T., Zhou, H., Huang, J., Yin, J., Chen, Z., Liu, D., Zhang, N., and Kuang, Y., 2014, “Facile Preparation of Pd–Au Bimetallic Nanoparticles via in-Situ Self-Assembly in Reverse Microemulsion and Their Electrocatalytic Properties,” *Colloids and Surfaces A: Physicochemical and Engineering Aspects*, **463**, pp. 55–62.
- [25] Gilroy, K. D., Ruditskiy, A., Peng, H.-C., Qin, D., and Xia, Y., 2016, “Bimetallic Nanocrystals: Syntheses, Properties, and Applications,” *Chemical reviews*, **116**(18), pp. 10414–10472.
- [26] Guo, S., Li, J., Dong, S., and Wang, E., 2010, “Three-Dimensional Pt-on-Au Bimetallic Dendritic Nanoparticle: One-Step, High-Yield Synthesis and Its Bifunctional Plasmonic and Catalytic Properties,” *The Journal of Physical Chemistry C*, **114**(36), pp. 15337–15342.
- [27] Lee, J.-H., Kim, G.-H., and Nam, J.-M., 2012, “Directional Synthesis and Assembly of Bimetallic Nanosnowmen with DNA,” *Journal of the American Chemical Society*, **134**(12), pp. 5456–5459.
- [28] Sutter, E., Zhang, B., and Sutter, P., 2020, “DNA-Mediated Three-Dimensional Assembly of Hollow Au–Ag Alloy Nanocages as Plasmonic Crystals,” *ACS Applied Nano Materials*, **3**(8), pp. 8068–8074.

- [29] Sun, L., Yin, Y., Lv, P., Su, W., and Zhang, L., 2018, “Green Controllable Synthesis of Au–Ag Alloy Nanoparticles Using Chinese Wolfberry Fruit Extract and Their Tunable Photocatalytic Activity,” *RSC advances*, **8**(8), pp. 3964–3973.
- [30] Rajeev, R., Datta, R., Varghese, A., Sudhakar, Y. N., and George, L., 2021, “Recent Advances in Bimetallic Based Nanostructures: Synthesis and Electrochemical Sensing Applications,” *Microchemical Journal*, p. 105910.
- [31] Hong, J. W., Kim, D., Lee, Y. W., Kim, M., Kang, S. W., and Han, S. W., 2011, “Atomic-Distribution-Dependent Electrocatalytic Activity of Au–Pd Bimetallic Nanocrystals,” *Angewandte Chemie International Edition*, **50**(38), pp. 8876–8880.
- [32] Lee, Y. W., Kim, M., Kang, S. W., and Han, S. W., 2011, “Polyhedral Bimetallic Alloy Nanocrystals Exclusively Bound by {110} Facets: Au–Pd Rhombic Dodecahedra,” *Angewandte Chemie International Edition*, **50**(15), pp. 3466–3470.
- [33] Lee, Y. W., Kim, M., Kim, Y., Kang, S. W., Lee, J.-H., and Han, S. W., 2010, “Synthesis and Electrocatalytic Activity of Au–Pd Alloy Nanodendrites for Ethanol Oxidation,” *The Journal of Physical Chemistry C*, **114**(17), pp. 7689–7693.
- [34] Zeng, J., Zhu, C., Tao, J., Jin, M., Zhang, H., Li, Z.-Y., Zhu, Y., and Xia, Y., 2012, “Controlling the Nucleation and Growth of Silver on Palladium Nanocubes by Manipulating the Reaction Kinetics,” *Angewandte Chemie*, **124**(10), pp. 2404–2408.
- [35] Motl, N., Smith, A., DeSantis, C., and Skrabalak, S., 2014, “Engineering Plasmonic Metal Colloids through Composition and Structural Design,” *Chemical Society Reviews*, **43**(11), pp. 3823–3834.
- [36] Song, J. H., Kim, F., Kim, D., and Yang, P., 2005, “Crystal Overgrowth on Gold Nanorods: Tuning the Shape, Facet, Aspect Ratio, and Composition of the Nanorods,” *Chemistry–A European Journal*, **11**(3), pp. 910–916.
- [37] Wang, C., Tian, W., Ding, Y., Ma, Y., Wang, Z. L., Markovic, N. M., Stamenkovic, V. R., Daimon, H., and Sun, S., 2010, “Rational Synthesis of Heterostructured Nanoparticles with Morphology Control,” *Journal of the American Chemical Society*, **132**(18), pp. 6524–6529.
- [38] Bastús, N. G., Comenge, J., and Puntès, V., 2011, “Kinetically Controlled Seeded Growth Synthesis of Citrate-Stabilized Gold Nanoparticles of up to 200 Nm: Size Focusing versus Ostwald Ripening,” *Langmuir*, **27**(17), pp. 11098–11105.

- [39] Wu, Z., Yang, S., and Wu, W., 2016, "Shape Control of Inorganic Nanoparticles from Solution," *Nanoscale*, **8**(3), pp. 1237–1259.
- [40] Omar, R., Naciri, A. E., Fahes, A., Jradi, S., Issa, A., Kuznetsov, D., Shur, V., Zelenovskiy, P., Battie, Y., and Akil, S., 2020, "Precise Control of the Size and Gap between Gold Nanocubes by Surface-Based Synthesis for High SERS Performance," *Soft matter*, **16**(7), pp. 1857–1865.
- [41] Omar, R., Naciri, A. E., Jradi, S., Battie, Y., Toufaily, J., Mortada, H., and Akil, S., 2017, "One-Step Synthesis of a Monolayer of Monodisperse Gold Nanocubes for SERS Substrates," *Journal of Materials Chemistry C*, **5**(41), pp. 10813–10821.
- [42] Fahes, A., En Naciri, A., Navvabpour, M., Jradi, S., and Akil, S., 2021, "Self-Assembled Ag Nanocomposites into Ultra-Sensitive and Reproducible Large-Area SERS-Active Opaque Substrates," *Nanomaterials*, **11**(8), p. 2055.
- [43] Khanafer, M., Issa, A., Akil, S., Hamieh, T., Adam, P.-M., and Jradi, S., 2016, "A General Strategy to Incorporate a Wide Range of Metallic Salts into Ring-like Organized Nanostructures via Polymer Self-Assembly," *RSC advances*, **6**(105), pp. 102843–102852.
- [44] Akil, S., Omar, R., Kuznetsov, D., Shur, V., En Naciri, A., and Jradi, S., 2021, "Advanced Large-Scale Nanofabrication Route for Ultrasensitive SERS Platforms Based on Precisely Shaped Gold Nanostructures," *Nanomaterials*, **11**(7), p. 1806.
- [45] Gilroy, K. D., Hughes, R. A., and Neretina, S., 2014, "Kinetically Controlled Nucleation of Silver on Surfactant-Free Gold Seeds," *Journal of the American Chemical Society*, **136**(43), pp. 15337–15345.
- [46] Ma, Y., Wang, S., Li, Z., Hu, W., Jiang, S., Song, X., and Wang, C., 2017, "Theoretical and Experimental Study of Surface-Enhanced Raman Scattering of 4, 4'-Bipyridine Molecule on Graphene," *JOURNAL OF ATOMIC AND MOLECULAR SCIENCES*, **8**(3), pp. 127–130.
- [47] Zhuang, Z., Cheng, J., Wang, X., Zhao, B., Han, X., and Luo, Y., 2007, "Surface-Enhanced Raman Spectroscopy and Density Functional Theory Study on 4, 4'-Bipyridine Molecule," *Spectrochimica Acta Part A: Molecular and Biomolecular Spectroscopy*, **67**(2), pp. 509–516.

- [48] Wu, D.-Y., Li, J.-F., Ren, B., and Tian, Z.-Q., 2008, “Electrochemical Surface-Enhanced Raman Spectroscopy of Nanostructures,” *Chemical Society Reviews*, **37**(5), pp. 1025–1041.
- [49] Chen, L., Gao, Y., Cheng, Y., Su, Y., Wang, Z., Li, Z., and Zhang, R.-Q., 2015, “Strong Core@ Shell Dependence in Surface-Enhanced Raman Scattering of Pyridine on Stable 13-Atom Silver-Caged Bimetallic Clusters,” *The Journal of Physical Chemistry C*, **119**(30), pp. 17429–17437.
- [50] Reguera, J., Langer, J., de Aberasturi, D. J., and Liz-Marzán, L. M., 2020, “Anisotropic Metal Nanoparticles for Surface-Enhanced Raman Scattering,” *Colloidal Synthesis of Plasmonic Nanometals*, pp. 713–754.
- [51] Zhang, L., Zhang, J., Kuang, Q., Xie, S., Jiang, Z., Xie, Z., and Zheng, L., 2011, “Cu²⁺-Assisted Synthesis of Hexoctahedral Au–Pd Alloy Nanocrystals with High-Index Facets,” *Journal of the American Chemical Society*, **133**(43), pp. 17114–17117.
- [52] Wan, M., Zhao, H., Peng, L., Zou, X., Zhao, Y., and Sun, L., 2020, “Loading of Au/Ag Bimetallic Nanoparticles within and Outside of the Flexible SiO₂ Electrospun Nanofibers as Highly Sensitive, Stable, Repeatable Substrates for Versatile and Trace SERS Detection,” *Polymers*, **12**(12), p. 3008.
- [53] Li, K., Liu, G., Zhang, S., Dai, Y., Ghafoor, S., Huang, W., Zu, Z., and Lu, Y., 2019, “A Porous Au–Ag Hybrid Nanoparticle Array with Broadband Absorption and High-Density Hotspots for Stable SERS Analysis,” *Nanoscale*, **11**(19), pp. 9587–9592.
- [54] Akil-Jradi, S., Jradi, S., Plain, J., Adam, P.-M., Bijeon, J.-L., Royer, P., and Bachelot, R., 2012, “Micro/Nanoporous Polymer Chips as Templates for Highly Sensitive SERS Sensors,” *RSC advances*, **2**(20), pp. 7837–7842.
- [55] Khaywah, M. Y., 2014, “New Ultrasensitive Bimetallic Substrates for Surface Enhanced Raman Scattering,” PhD Thesis, Troyes.
- [56] Orendorff, C. J., Sau, T. K., and Murphy, C. J., 2006, “Shape-Dependent Plasmon-Resonant Gold Nanoparticles,” *small*, **2**(5), pp. 636–639.
- [57] Yin, H., Guo, Y., Cui, X., Lu, W., Yang, Z., Yang, B., and Wang, J., 2018, “Plasmonic and Sensing Properties of Vertically Oriented Hexagonal Gold Nanoplates,” *Nanoscale*, **10**(31), pp. 15058–15070.

- [58] Qin, F., Zhao, T., Jiang, R., Jiang, N., Ruan, Q., Wang, J., Sun, L.-D., Yan, C.-H., and Lin, H.-Q., 2016, “Thickness Control Produces Gold Nanoplates with Their Plasmon in the Visible and Near-Infrared Regions,” *Advanced Optical Materials*, **4**(1), pp. 76–85.
- [59] Jiang, R., Chen, H., Shao, L., Li, Q., and Wang, J., 2012, “Unraveling the Evolution and Nature of the Plasmons in (Au Core)–(Ag Shell) Nanorods,” *Advanced Materials*, **24**(35), pp. OP200–OP207.
- [60] Pustovalov, V. K., Astafyeva, L. G., and Fritzsche, W., 2012, “Optical Properties of Core–Shell Gold–Silver and Silver–Gold Nanoparticles for near UV and Visible Radiation Wavelengths,” *Plasmonics*, **7**(3), pp. 469–474.
- [61] Chen, Y., Wu, H., Li, Z., Wang, P., Yang, L., and Fang, Y., 2012, “The Study of Surface Plasmon in Au/Ag Core/Shell Compound Nanoparticles,” *Plasmonics*, **7**(3), pp. 509–513.
- [62] Kinhal, K. V., Bhatt, N., and Pushpavanam, S., 2021, “Unraveling Reaction Pathways for Tuning Bimetallic Nanoparticle Structures: Role of Reactant Addition Sequence,” *Journal of Nanoparticle Research*, **23**(7), pp. 1–17.
- [63] Zaleska-Medynska, A., Marchelek, M., Diak, M., and Grabowska, E., 2016, “Noble Metal-Based Bimetallic Nanoparticles: The Effect of the Structure on the Optical, Catalytic and Photocatalytic Properties,” *Advances in colloid and interface science*, **229**, pp. 80–107.
- [64] Cho, E. C., Camargo, P. H., and Xia, Y., 2010, “Synthesis and Characterization of Noble-Metal Nanostructures Containing Gold Nanorods in the Center,” *Advanced Materials*, **22**(6), pp. 744–748.
- [65] Feng, Y., He, J., Wang, H., Tay, Y. Y., Sun, H., Zhu, L., and Chen, H., 2012, “An Unconventional Role of Ligand in Continuously Tuning of Metal–Metal Interfacial Strain,” *Journal of the American Chemical Society*, **134**(4), pp. 2004–2007.
- [66] Li, J., Sun, X., and Qin, D., 2016, “Ag-Enriched Ag-Pd Bimetallic Nanoframes and Their Catalytic Properties,” *ChemNanoMat*, **2**(6), pp. 494–499.
- [67] Li, J., Liu, J., Yang, Y., and Qin, D., 2015, “Bifunctional Ag@Pd-Ag Nanocubes for Highly Sensitive Monitoring of Catalytic Reactions by Surface-Enhanced Raman Spectroscopy,” *Journal of the American Chemical Society*, **137**(22), pp. 7039–7042.
- [68] Xia, Y., Gilroy, K. D., Peng, H.-C., and Xia, X., 2017, “Seed-Mediated Growth of Colloidal Metal Nanocrystals,” *Angewandte Chemie International Edition*, **56**(1), pp. 60–95.

- [69] Kuo, C.-H., Chiang, T.-F., Chen, L.-J., and Huang, M. H., 2004, "Synthesis of Highly Faceted Pentagonal-and Hexagonal-Shaped Gold Nanoparticles with Controlled Sizes by Sodium Dodecyl Sulfate," *Langmuir*, **20**(18), pp. 7820–7824.
- [70] Gai, P. L., and Harmer, M. A., 2002, "Surface Atomic Defect Structures and Growth of Gold Nanorods," *Nano Letters*, **2**(7), pp. 771–774.
- [71] Sun, Y., Gates, B., Mayers, B., and Xia, Y., 2002, "Crystalline Silver Nanowires by Soft Solution Processing," *Nano letters*, **2**(2), pp. 165–168.

Chapter 4: Synthetic design of shape-controlled Ag/Au oligomers via silver-assisted growth strategy

4.1 Introduction

It has become increasingly important to control the shape of nanostructures, as many of their physiochemical properties are highly shape-dependent [1,2]. Although fairly empirical, nanocrystal shape control remains a challenging problem for integrated nanomaterial systems [3]. Several effective synthetic strategies have been developed over the past years to facilitate the creation of bimetallic nanostructures with a variety of structures and components [4–7]. Plenty of related works are cited in both Chapters 1 and 3. Zero-dimensional 0D (tetrahedrons, octahedrons, cubes, icosahedrons, rhombic dodecahedrons ...) [8,9], 1D (rods, wires..) [10,11], 2D (triangular and hexagonal plates) [12], and many derivative bimetallic structures (core-frame, nanoboxes and nanocages) [13,14] are reported in the literature. Table 4 represents a summary of shape-controlled bimetallic nanostructures, including alloys, core–shells, and heterostructures, that have been successfully synthesized through colloidal routes of continuous growth, crystallites coalescence, seeded growth, and GRR [15].

The method of creating AgNPs coupled with AuNPs would be extremely valuable for extending their fundamental properties and applications in plasmonic sensing [16,17]. In this case, with AgNPs brought close to adjacent AuNPs, a drastically intensified E-fields within extremely small regions will drive the E-field enhancement to extreme values. Thus, BNPs will act as efficient SERS platforms for detection of an important single molecules [16,17]. However, the nominal SERS performances of colloidal dispersions are distinct from the substrate-supported colloids and the nanostructured substrates in the dry state.







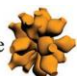


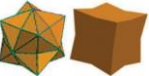
A reliable and quantitative colloidal SERS probe must consider several key aspects related to analyte adsorption, signal stability, and colloidal stability in order to achieve a combination of efficiency and robustness [18–20]. To succeed in doing this, the colloidal SERS sensing probes must meet several requirements: (a) Sensors should be designed to promote an ultra-sensitive quantitative adsorption of analytes and enhance their characteristic signals, (b) The SERS signal yield should be effective so that the detection limit can be increased, (c) SERS measurement conditions should be long-term stable, homogeneous, reliable, and reproducible.

In Chapter 3, we have achieved the formation of heterostructures, eccentric core-shells, and physical mixtures of two metals on surfaces by varying the concentration of Au^{3+} . Herein, we aimed to investigate the influence of Ag^+ concentration on the synthetic products and sensing characteristics. The objective was to accurately elucidate the real structure and the pathway of synthesis of Ag/Au BNPs through the analysis of samples taken at several time intervals during the synthesis. In this chapter, we provide a comprehensive view of the synthesis of BNPs by VIPS method as well as the mechanism of action based on their unique optical properties. A description of how diverse factors interact to produce these unique traits is also discussed. Finally, the applications of BNPs in SERS are presented.

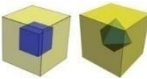
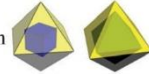
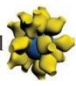



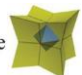
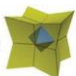

To the best of our knowledge, shape-sensitive SERS performances of BNPs have been scarcely investigated [32]. Understanding the promotion effect in sensing applications as well as building a correlation between structural properties of BNPs and SERS performance will give us powerful insights into the rational design of robust bimetallic sensors in future. Even with our achievements in precisely controlling the morphology and structure of BNPs on surface and establishing their formation mechanisms, there are still several significant challenges to overcome. It is worthy to note that the studied substrates were not the most suitable for SERS since we only focused on the influence of structure and morphology of BNPs on sensitivity. In all samples, the BNPs were low in densities and separated by large gap distances. Despite this, the results successfully prove that the adsorption of the analyte on nanostructured substrate surfaces instantaneously occurs with no retardation effects by detecting 4,4'-BP in about 1 s, which is considered as an ultra-rapid measurement time response. Also, the results achieved were satisfactory and above expectations. The limit of detection (LOD) $\sim 10^{-5}$ M for such an ultrasensitive probe may be lower compared to that of other ultrasensitive probe designs, but it is still in the order of magnitude expected for the conditions of our fabricated substrates. Because of the high colloidal stability provided by the PMMA matrix stabilization, SERS does not form active aggregates. Aggregation without control might provide a quick route to boosting SERS signal strength, but fails to predictably and reproducibly stabilize the signal. Further studies on the current topic are therefore recommended in order to enhance the quality of bimetallic sensors. As a preliminary attempt, the SERS results are promising and should be validated by optimization of synthetic conditions to attain full covered bimetallic surfaces.

Table 4. A summary of (a) alloyed; (b) core-shell; and (c) heterostructures bimetallic systems with well-defined shapes synthesized by four colloidal routes, and lists of their geometric structures and key factors of shape control. Adapted from [15]



(a) alloyed

Bimetallic nanostructures	Synthetic route	Key factors in the synthetic process	Synthetic cases
Cube 	Continuous growth	Capping agents strongly bind on {100} facets	Pt-M ^{7,8,10,11,40}
Tetrahedron  Octahedron 	Continuous growth	Capping agents strongly bind on {111} facets	Pt-M ^{8,10,11,38}
Icosahedron 	Continuous growth	Slow reduction rate; capping agents strongly bind on {111} facets	Pt-Pd ¹²
Rod 	Continuous growth	Surfactant-formed templates	Pt-Fe ¹³ , Pt-Cu ⁴⁴
Multi-pod 	Continuous growth	Facet-specific oxidative etching	Au-Pt ¹⁹
Dendritic structure 	Crystallites coalescence	Rapid reduction; polymer-formed templates	Pt-Pd, ⁴⁵ Au-Pd ³⁶
Wires 	Crystallites coalescence	Facet-oriented attachment of crystallites	Au-Ag, ¹⁴ Pt-Ag ¹⁵
Hollow structure 	Galvanic replacement reaction	Kirkendall effect	Pt-Pd ^{20,21}
Concave structure 	Galvanic replacement reaction	Underpotential deposition	Au-Pd, ⁴⁶ Pt-Cu ²³

(b) core-shell

Bimetallic nanostructures	Synthetic route	Key factors in the synthetic process	Synthetic cases
Cube 	Seeded growth	Capping agents strongly bind on {100} facets	Pt@Pd, ⁹ Au@Pd ^{25,47}
Octahedron 	Seeded growth	Capping agents strongly bind on {111} facets	Pt@Pd, ⁹ Pd@Pt ⁴⁸
Core-dendritic shell 	Crystallites coalescence	Rapid reduction; polymer-formed templates	Pd@Pt, ⁴⁸ Pd@Rh, ⁴⁹ Au@Pd@Pt ¹⁷
Tetrahexahedron  Tris-octahedron 	Seeded growth	Template-directed epitaxial deposition	Au@Pd ^{50,51}
Tetrahexahedron  Concave cube 	Seeded growth	Large lattice mismatch; oxidative etching promoted Ostwald ripening	Au@Pd ^{41,42}
Concave cube  Concave octahedron 	Seeded growth	Growth rate control on different facets	Pt@Rh, ²² Au@Pd ⁴¹

(c) heterostructures

Bimetallic nanostructures	Synthetic route	Key factors in the synthetic process	Synthetic cases
Binary structure 	Seeded growth	Island growth caused by large lattice mismatch or rapid reduction	Au-Pt, ⁹ Pt-Pd ³²
Multi-pod 	Galvanic replacement reaction	Facet-specific galvanic replacement reaction	Pd-Pt ¹⁸

4.2 Results and Discussions

4.2.1 SEM Images & Optical Characteristics:

First, it is worthy to note that we performed all experiments (synthesis and characterizations) according to the experimental section given in Chapter 3. Two sets of substrates were conducted to determine the effect of concentration of $\text{AgNO}_3/\text{PMMA}$ on the composition and morphology of BNPs. The structure of BNPs was readily tuned by controlling the Ag/Au molar ratio as shown in the previous chapter but here we fix the Au concentration precursor (60 mM) and we vary the Ag one from substrate to another. Figure 36 reveals that Ag concentration change greatly influences the kinetics of growth of BNPs into specific structures and shapes. The morphology of bimetallic system evolves from inter-connected hetero-oligomers to eccentric core/shell bimetallic nanostructures when Ag/Au ratio increases from 0.3 to 0.6. To better visualize these structures, the zoom-in portion of the images are given in insets of Figure 36. Figure 36(a) shows a structure of oligomer chains of different kinds of metals. EDX result demonstrates the presence of both Ag and Au on the substrate surfaces, as indicated in Figure 37. The electron beam was focused on one aggregate particle for the purpose of identifying the elements in individual particles. When the particles are sufficiently large, the electron beam can be focused on a specific region of the particle surface area or center to investigate its regional composition. This often reveals non-uniformity in the real composition of the particles. Consequently, both Ag and Au showed similar intensities regardless of Au's higher concentrations. The MNPs fuse together along different directions by forming metallic bonds at the interfacial sites to grow into chains. The particles grow into chains through a combination of a direct nucleation and growth onto the seed particles and OAP. The monitoring of spectral profiles with time in Figure 38 provides a detailed understanding of the mechanism of formation of inter-connected hetero-oligomers at low $R_{\text{Ag}/\text{Au}} = 0.3$. At high $R_{\text{Ag}/\text{Au}} = 0.6$, in Figure 36(b), the fast reaction kinetics allows the Ag atoms to readily approach the Au seeds by rapidly growing on its multiple sites. Consequently, an eccentric core-shell configuration is produced.

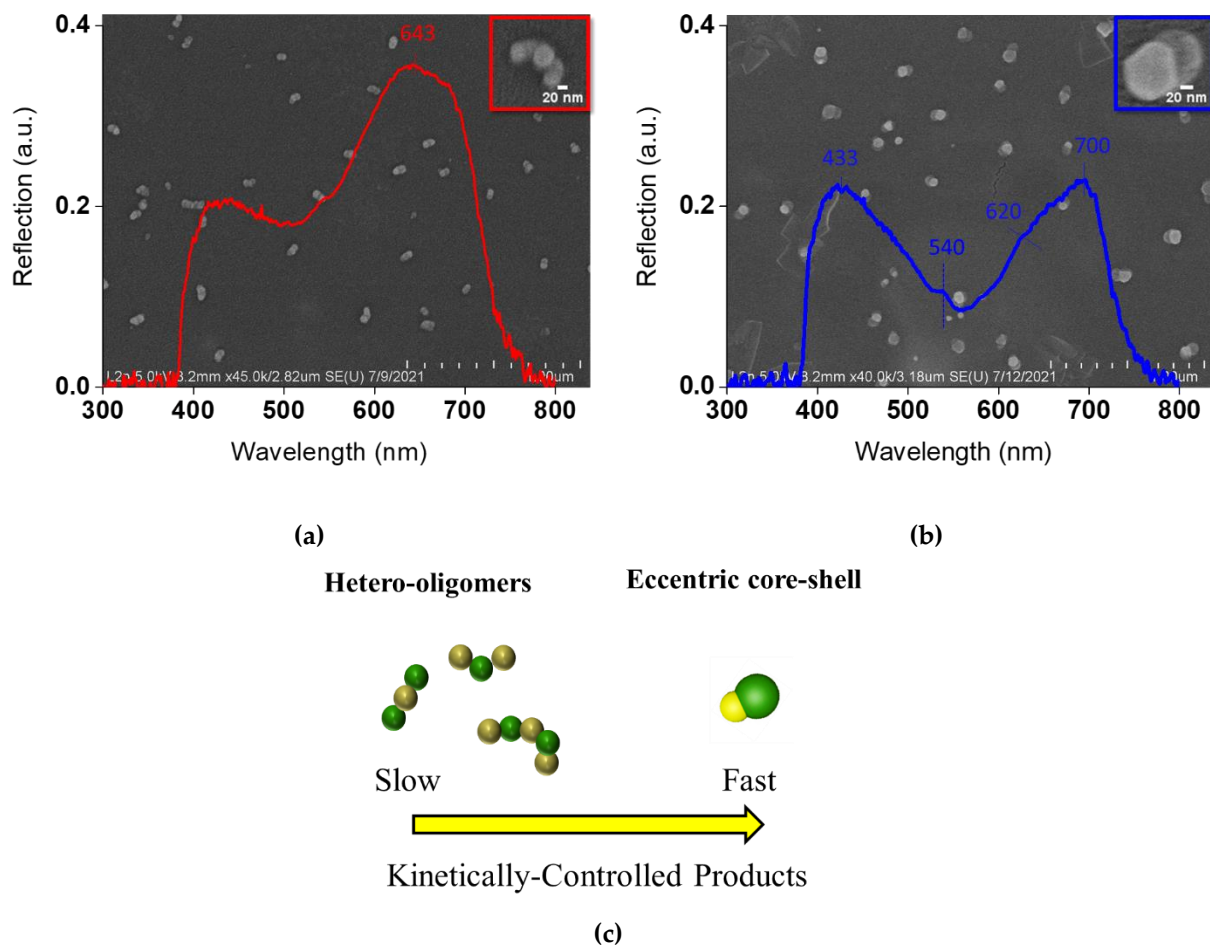


Figure 37. Representative SEM images of synthesized Ag/Au bimetallic nanostructures, demonstrating that diverse morphologies and configurations are made possible by deposition of different concentrations of Ag^+ /PMMA on Si-As substrates: (a) hetero-oligomers at low ratios of $R_{\text{Ag}/\text{Au}} = 0.3$; and (b) eccentric core-shell structures at high ratios of $R_{\text{Ag}/\text{Au}} = 0.6$. The scale bar of SEM images is $1 \mu\text{m}$. The insets show the corresponding optical spectra changes and a cross-sectional SEM image of each bimetallic nanostructure, revealing its structure and profile. (c) Schematic illustration of the kinetically-controlled bimetallic nanostructures produced by simply altering the rate of reaction and concentration of Ag^+ /PMMA precursor.

Ag^+ ions can control the SMG of the AuNPs through surface passivation, and can access a different set of high-index particle shapes [21–24]. Controlling the concentration of Ag cationic additives has directed the growth of AuNPs into four different morphologies including octahedra, rhombic dodecahedra, truncated ditetragonal prisms, and concave cubes [25]. The UPD of Ag onto an existing Au surface facets, a process which involves the reduction of Ag^+ ions on Au surface rather than in bulk by reducing agents, has been suggested as the cause of these shape-directing properties [26]. The deposition of Ag on higher energy surface facets of Au impedes the further deposition of Au on that same facets and stabilizes it, causing it to slowdown in growth and be retained in the final nanoparticle structure. Consequently, a monolayer or submonolayer of Ag forms on Au particles due to Ag UPD [27]. For this reason, the Ag^+ concentration on surfaces of Au particles is considered as an important factor in controlling AuNPs anisotropic growth.

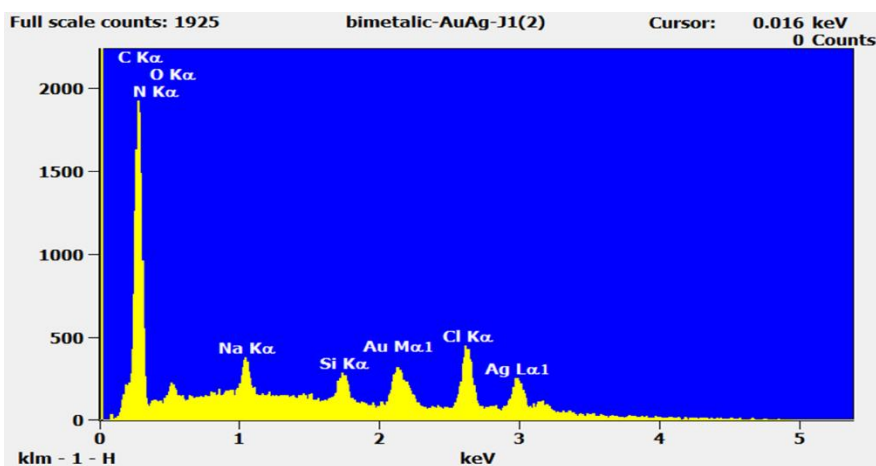


Figure 38. EDX spectrum showing the characteristic X-rays originated from interacting a single hetero-oligomer nanoparticle with an electron beam. This spectrum refers to the sample prepared at ratio $R_{\text{Ag}/\text{Au}} = 0.3$.

In Ag-assisted SMG synthetic methods, higher Ag^+ ions concentrations in the reaction solution allow more Ag^+ ions to be available for rapid coverage of more open Au surfaces and more stabilization of higher-energy facets, thereby inhibiting Au displacement of Ag. In contrast, at low concentration of Ag^+ ions, Au deposition occurs more frequently on particle surfaces and the reaction conditions prefer the displacement of Ag by Au. The preference for Au to form on open surfaces is due to the inability of Ag to completely cover these surfaces at such low concentrations. Therefore, the initially formed Ag on high energy facets will be more likely to be displaced. Ag

then redeposits and reaches a lower-energy facet where it can attain complete and uniform coverage and therefore better prevent Au deposition [27]. This confirms why AuNPs tend to have ill-defined facets at low Ag^+ concentrations, whereas more exotic structures with high index facets were often found at high concentrations of Ag^+ .

An optical analysis was carried out on the two substrate-based bimetallic nanostructures, as highlighted in the insets of Figure 36. Hetero-oligomers exhibit only a single broad LSPR band at 643 nm, but the anisotropy of eccentric core-shell structures gives rise to four LSPR bands, corresponding to the response of AgNPs (~ 433 nm), transverse axis and longitudinal axis of AuNH (~ 540 and 620 nm), and the coupling response of core-shell system (~ 700 nm) respectively. The optical properties of the core metal (Au) can be clearly seen since the shell does not surround the core in a continuous layer, as clarified in Chapter 3.

4.2.2 Optical Monitoring and Proposed Mechanism

To confirm the suggested mechanism, Figure 38 summarizes the evolution of plasmon bands with time. The synthesis can be divided into four stages: Formation of (a) monomers of AuNPs, (b) Au dimers, (c) Ag-Au hetero-dimers, and (d) Ag/Au hetero-oligomers with rounded corners and edges.

Initially, at Day 1, the sample exhibits one plasmonic band at 530 nm which corresponds to a response of AuNS monomers dispersed in a PMMA matrix (size ~ 20 nm).

The position of this characteristic band changes completely with time. Notably, with increasing the reaction time (Day 2), the peak gradually broadens and red-shifts towards longer wavelengths ~ 610 nm, and becomes more enhanced in intensity. The peak, assigned by an arrow at 530 nm, is overlapped with the new band formed at 610 nm. Dimerization of AuNPs with a decrease in interparticle separation distances induces the broadness of spectrum and the large shift.

A DDA method was previously performed to evaluate the effects of interparticle spacings on the extinction and near-field properties of Au–Au, Ag–Ag, and Au–Ag nanosphere homo and hetero-dimers [28]. Dimers were analyzed under z-polarization incidence in an ambient medium of RI near 1.33 [28]. The extinction spectra of single dimer of AuNS with size ~ 20 nm and interparticle space $d=5$ nm showed a peak at ~ 580 nm. Changing the local environment of NPs (i.e. PMMA medium with RI ~ 1.5) and the presence of an underlying Si-As substrate of different permittivity

compared to the rest of NPs can have unusual effects on the position of LSPR band. This justifies the red-shift of the major peak into ~ 610 nm. An additional weakly enhanced Ag peak at ~ 407 nm is also formed at Day 2.

Furthermore, at Day 3, we noticed new plasmon bands centered at 450 and 590 nm, which could be attributed to the formation of Ag-Au spherical hetero-dimers, suggesting that the interaction between the two metals can take place if the reaction is prolonged beyond 48 h. The peak position of Au-Ag hetero-dimer at 450 nm is due to AgNPs, and the other at 590 nm is due to AuNPs. Both MNPs are affected by the RI of the other metal. The maximum intensity decreases as the interaction between hetero-dimers occur. Based on a DDA simulation of different sizes of Au-Ag hetero-dimers in RI ~ 1.33 , there are two consistent extinction peaks sensitive to interparticle gap distances [28]. A dimer structure composed of Ag-Au hetero-dimer nanospheres with the radius of $R = 20$ nm and the interparticle separation distance of $g = 5$ nm displays two extinction peaks near 420 and 550 nm [28]. The most significant factor behind the shift in the LSPR position of hetero-dimers is the change in the surrounding environment, which impacts the local RI experienced by the NPs.

At Day 5, a new LSPR band ~ 643 nm is formed and intensified. However, the larger shift is most likely due to increased interactions between the two MNPs on surface. Changes in the structure of the bimetallic system lead to a red-shift of the coupled mode and increased scattering contributions. The broadness of this peak is clarified by the high formation of aggregated BNPs. The number of junctions per nanoparticle (NP) increases with the time, thus resulting in a continuous red-shift of the band. The shape of aggregates resembles a chain-like configuration and the aggregation process follows a step-growth mode [29]. To this end, all the monomers and oligomers have a similar tendency towards aggregation. Due to the slow kinetics, the incoming Ag monomers favor to spontaneously aggregate with the Au monomers. As NPs aggregate and reaction proceeds, their monomers will be consumed, resulting in dimers, then trimers, which further aggregate to sequentially form oligomers. According to current research, OAP might occur as a result of collisions of aligned nanocrystals or rotation of misaligned NPs in contact towards low-energy interface configurations [30]. OAP primarily forms hetero-oligomers at dispersed or agglomerated conditions through successive collisions or direct contact at specific directions. Precisely, the particles are continuously rotated and interacted with each other until they achieve the perfect

lattice match. When particles are close enough to each other, there can be a sudden jump between them which causes a type of contact and, consequently, a type of lateral atom-by-atom addition.

Similar spectral features for this sample were observed after 5 days of synthesis. The emergence of same peaks highlights the stability of this sample.

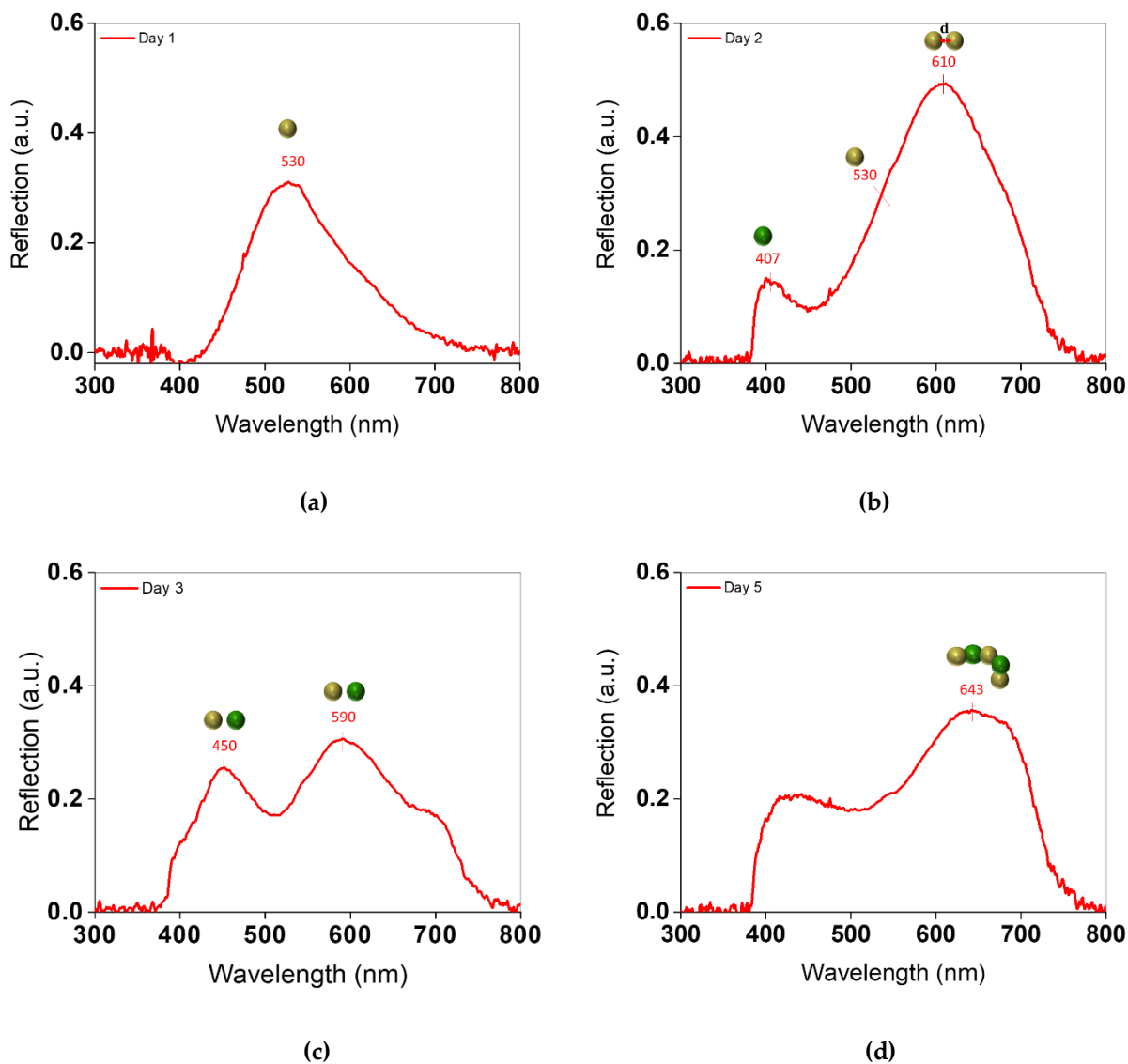


Figure 39. The reflected plasmon band positions measured as a function of synthesis time for the sample prepared at low ratio $R_{Ag/Au} = 0.3$. Monitoring of spectral profiles identifies the mechanism involved in the formation of hetero-oligomers on substrate-based platforms.

4.2.3 SERS features

The SERS spectra were captured on both bimetallic substrates, coated with equal concentrations of 4,4'-BP. Figure 39 shows that the average SERS spectra of 4,4'-BP on the bimetallic eccentric core-shell surface shows a higher signal intensity than for the hetero-oligomers surface at both excitation wavelengths i.e. 514 and 633 nm. The details of SERS measurements are previously mentioned in Chapter 3. Figure 40 also represents the measured SERS signals from different probe sites, which were randomly selected on BNPs substrate surfaces covered with 4,4'-BP. The most important feature in the design of BNPs by VIPS approach is the use of a PMMA matrix not only to confine the particles, increment their stability and avoid their aggregation under operation conditions, but also to enhance their SERS sensitivity.

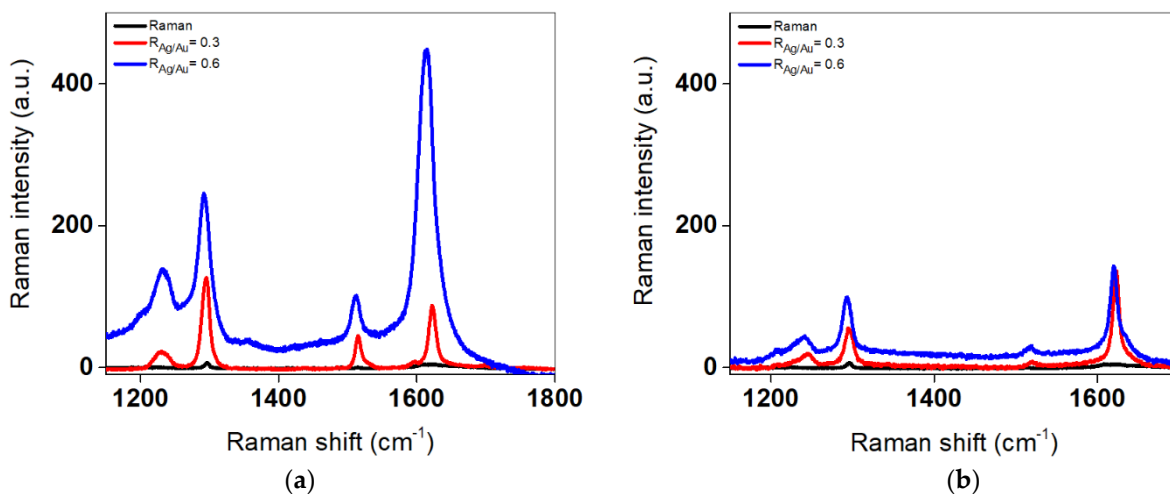


Figure 40. Raman and SERS spectra on the hetero-oligomers and eccentric core-shell bimetallic nanostructures at different excitation wavelengths: (a) 633 nm; and (b) 514 nm. Each spectrum is an average of at least 3 regions which were acquired from randomly selected spots on the samples.

The SERS results of both substrates cannot be compared in terms of density of BNPs and number of exterior hotspots.

Herein, the morphology of bimetallic nanostructures has a direct effect on its SERS sensitivity. Eccentric core-shell BNPs have special electronic effects at their interfaces that facilitate the vigorous adsorption of analytes onto the BNPs surface, which ultimately increase SERS efficiency. The selective growth of AgNPs on the tips of AuNH creates interior plasmonic hotspots where the electromagnetic field is greatly enhanced [31], allowing the eccentric core-shell structures to exhibit greatly improved SERS performance. Well-designed nanosensors with defined anisotropic facets tend to have increased surface coverage, which further enhances its active surface sites. These enhanced sensing properties can be ascribed to the presence of sharp corners and edges in the high-index faceted hexagon Au-core of the shield-like Au-Ag core-shell structure, in relation with concentrated hot-spots in the nanoparticle's tips. The inefficient SERS sensitivity at low ratios is attributed to the ill-defined irregular shapes of BNPs oligomers and its round effect at the corners. It is worth pointing out that the enrichment of Ag atoms in eccentric core-shell BNPs helps to improve its SERS effect.

Tailoring a close match of LSPR relative to the laser excitation wavelength ($\Delta\lambda = 633 - 620 = 13$ nm) generates a high SERS sensitivity with eccentric core-shell BNPs. The hetero-oligomers show the weakest SERS peak, although their LSPR peak ~ 643 nm overlapped the most with the 633 nm excitation. This weak correlation reflects the high sensitivity of eccentric core-shell BNPs due to the accumulation of high number of intrinsic hotspots created at its sharp corners. In contrast, with excitation at 520 nm, away from the LSPR peak ~ 643 nm, the SERS efficiency of the Ag/Au hetero-oligomers was greatly reduced.

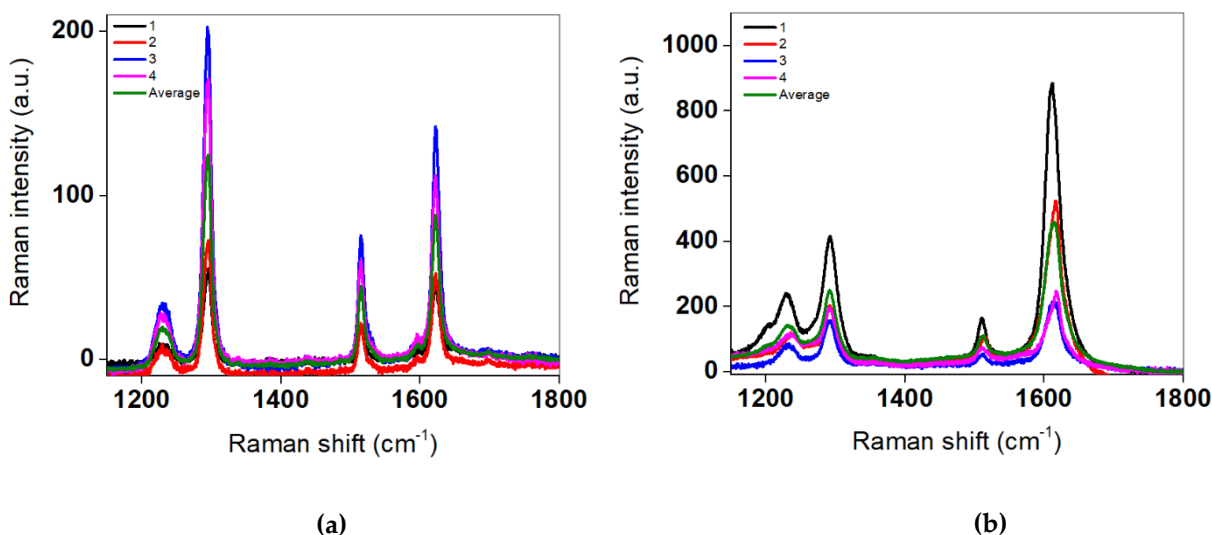


Figure 41. SERS spectra collected from 4 randomly selected points on (a) hetero-oligomers; and (b) eccentric core-shell substrate surfaces.

4.3 Conclusion

This study has demonstrated a general one-pot strategy to elaborate Ag/Au hetero-oligomers and eccentric core-shell nanostructures. According to our results, Ag/Au molar ratio plays the most significant role in directly affecting the reaction mechanism and the resulting products. Increased Ag concentrations effectively deposited the Ag atoms on the AuNH seeds in a core-shell configuration. In contrast, synthesis at lower Ag/Au ratio yielded aggregated spherical hetero-oligomers. Seed-mediated synthesis of Au nanostructures commonly uses cationic additives that have shape-directing effects, such as Ag⁺ ions. Anisotropic hexagon AuNPs form when Ag⁺/PMMA concentration is high, while its lowest concentration promotes the growth of quasi-isotropic AuNPs on surfaces. As a result, at high ratios $R_{\text{Ag}/\text{Au}} = 0.6$, the presence of high-energy facets on Au allows incoming Ag atoms to deposit therein at a much faster rate than on other seemingly isotropic surfaces. If the ratio is low, the remaining Ag ions that don't contribute to Au growth will be quite low, restricting the coating of Ag on Au seeds and making it likely only to form spherical AgNPs that are strongly thermodynamically favored. Spherical AuNPs do not have the desired facets that allow the adsorption of Ag atoms. Consequently, this sample will undergo a step-growth mode and OAP to complete its growth into hetero-oligomers.

4.4 References

- [1] Dong, D., Shi, Q., Sikdar, D., Zhao, Y., Liu, Y., Fu, R., Premaratne, M., and Cheng, W., 2019, "Site-Specific Ag Coating on Concave Au Nanoarrows by Controlling the Surfactant Concentration," *Nanoscale Horizons*, **4**(4), pp. 940–946.
- [2] Stolle, H. L. K. S., Kluitmann, J. J., Csáki, A., Köhler, J. M., and Fritzsche, W., 2021, "Shape-Dependent Catalytic Activity of Gold and Bimetallic Nanoparticles in the Reduction of Methylene Blue by Sodium Borohydride," *Catalysts*, **11**(12), p. 1442.
- [3] Ali, S., Sharma, A. S., Ahmad, W., Zareef, M., Hassan, M. M., Viswadevarayalu, A., Jiao, T., Li, H., and Chen, Q., 2021, "Noble Metals Based Bimetallic and Trimetallic Nanoparticles: Controlled Synthesis, Antimicrobial and Anticancer Applications," *Critical reviews in analytical chemistry*, **51**(5), pp. 454–481.
- [4] Kumar-Krishnan, S., Estevez-González, M., Pérez, R., Esparza, R., and Meyyappan, M., 2017, "A General Seed-Mediated Approach to the Synthesis of AgM (M= Au, Pt, and Pd) Core–Shell Nanoplates and Their SERS Properties," *RSC advances*, **7**(44), pp. 27170–27176.
- [5] Khan, M., Al-Hamoud, K., Liaqat, Z., Shaik, M. R., Adil, S. F., Kuniyil, M., Alkhatlan, H. Z., Al-Warthan, A., Siddiqui, M. R. H., and Mondeshki, M., 2020, "Synthesis of Au, Ag, and Au–Ag Bimetallic Nanoparticles Using *Pulicaria Undulata* Extract and Their Catalytic Activity for the Reduction of 4-Nitrophenol," *Nanomaterials*, **10**(9), p. 1885.
- [6] Rodríguez, R. C., Troiani, H., Moya, S. E., Bruno, M. M., and Angelomé, P. C., 2020, "Bimetallic Ag–Au Nanoparticles Inside Mesoporous Titania Thin Films: Synthesis by Photoreduction and Galvanic Replacement, and Catalytic Activity," *European Journal of Inorganic Chemistry*, **2020**(6), pp. 568–574.
- [7] Kaur, V., Tanwar, S., Kaur, G., and Sen, T., 2021, "DNA-Origami-Based Assembly of Au@Ag Nanostar Dimer Nanoantennas for Label-Free Sensing of Pyocyanin," *ChemPhysChem*, **22**(2), pp. 160–167.
- [8] Zhang, J., Dong, Y., Liu, Q., Zhou, M., Mi, G., and Du, X., 2019, "Hierarchically Alloyed Pd–Cu Microarchitecture with Tunable Shapes: Morphological Engineering, and Catalysis for Hydrogen Evolution Reaction of Ammonia Borane," *International Journal of Hydrogen Energy*, **44**(57), pp. 30226–30236.

- [9] Zhang, J., Yang, H., Fang, J., and Zou, S., 2010, “Synthesis and Oxygen Reduction Activity of Shape-Controlled Pt₃Ni Nanopolyhedra,” *Nano letters*, **10**(2), pp. 638–644.
- [10] Liao, H.-G., Cui, L., Whitlam, S., and Zheng, H., 2012, “Real-Time Imaging of Pt₃Fe Nanorod Growth in Solution,” *science*, **336**(6084), pp. 1011–1014.
- [11] Xia, B. Y., Wu, H. B., Li, N., Yan, Y., Lou, X. W., and Wang, X., 2015, “One-Pot Synthesis of Pt–Co Alloy Nanowire Assemblies with Tunable Composition and Enhanced Electrocatalytic Properties,” *Angewandte chemie international edition*, **54**(12), pp. 3797–3801.
- [12] Hu, C., Mu, X., Fan, J., Ma, H., Zhao, X., Chen, G., Zhou, Z., and Zheng, N., 2016, “Interfacial Effects in PdAg Bimetallic Nanosheets for Selective Dehydrogenation of Formic Acid,” *ChemNanoMat*, **2**(1), pp. 28–32.
- [13] Chen, Y., Yang, Y., Fu, G., Xu, L., Sun, D., Lee, J.-M., and Tang, Y., 2018, “Core–Shell CuPd@ Pd Tetrahedra with Concave Structures and Pd-Enriched Surface Boost Formic Acid Oxidation,” *Journal of Materials Chemistry A*, **6**(23), pp. 10632–10638.
- [14] Yin, S., Xu, Y., Liu, S., Yu, H., Wang, Z., Li, X., Wang, L., and Wang, H., 2020, “Binary Nonmetal S and P-Co-Doping into Mesoporous PtPd Nanocages Boosts Oxygen Reduction Electrocatalysis,” *Nanoscale*, **12**(27), pp. 14863–14869.
- [15] Gu, J., Zhang, Y.-W., and Tao, F. F., 2012, “Shape Control of Bimetallic Nanocatalysts through Well-Designed Colloidal Chemistry Approaches,” *Chemical Society Reviews*, **41**(24), pp. 8050–8065.
- [16] Hooshmand, N., 2017, “Plasmonic Field Distribution of Homo-and Hetero Dimeric Ag and Au Nanoparticles,” *NANOPLASMONICS*, p. 141.
- [17] William, R. V., Das, G. M., Dantham, V. R., and Laha, R., 2019, “Enhancement of Single Molecule Raman Scattering Using Sprouted Potato Shaped Bimetallic Nanoparticles,” *Scientific reports*, **9**(1), pp. 1–12.
- [18] Höller, R. P., Jahn, I. J., Cialla-May, D., Chanana, M., Popp, J., Fery, A., and Kuttner, C., 2020, “Biomacromolecular-Assembled Nanoclusters: Key Aspects for Robust Colloidal SERS Sensing,” *ACS Applied Materials & Interfaces*, **12**(51), pp. 57302–57313.
- [19] Jahn, I. J., Žukovskaja, O., Zheng, X.-S., Weber, K., Bocklitz, T. W., Cialla-May, D., and Popp, J., 2017, “Surface-Enhanced Raman Spectroscopy and Microfluidic Platforms: Challenges, Solutions and Potential Applications,” *Analyst*, **142**(7), pp. 1022–1047.

- [20] Zong, C., Xu, M., Xu, L.-J., Wei, T., Ma, X., Zheng, X.-S., Hu, R., and Ren, B., 2018, “Surface-Enhanced Raman Spectroscopy for Bioanalysis: Reliability and Challenges,” *Chemical reviews*, **118**(10), pp. 4946–4980.
- [21] Ahmed, W., Glass, C., and van Ruitenbeek, J. M., 2014, “Facile Synthesis of Gold Nanoworms with a Tunable Length and Aspect Ratio through Oriented Attachment of Nanoparticles,” *Nanoscale*, **6**(21), pp. 13222–13227.
- [22] Wang, Y., Zeng, Y., Fu, W., Zhang, P., Li, L., Ye, C., Yu, L., Zhu, X., and Zhao, S., 2018, “Seed-Mediated Growth of Au@ Ag Core-Shell Nanorods for the Detection of Ellagic Acid in Whitening Cosmetics,” *Analytica chimica acta*, **1002**, pp. 97–104.
- [23] Hinman, J. G., Stork, A. J., Varnell, J. A., Gewirth, A. A., and Murphy, C. J., 2016, “Seed Mediated Growth of Gold Nanorods: Towards Nanorod Matryoshkas,” *Faraday discussions*, **191**, pp. 9–33.
- [24] Liu, M., and Guyot-Sionnest, P., 2005, “Mechanism of Silver (I)-Assisted Growth of Gold Nanorods and Bipyramids,” *The Journal of Physical Chemistry B*, **109**(47), pp. 22192–22200.
- [25] Personick, M. L., Langille, M. R., Zhang, J., and Mirkin, C. A., 2011, “Shape Control of Gold Nanoparticles by Silver Underpotential Deposition,” *Nano letters*, **11**(8), pp. 3394–3398.
- [26] Tran, T. T., and Lu, X., 2011, “Synergistic Effect of Ag and Pd Ions on Shape-Selective Growth of Polyhedral Au Nanocrystals with High-Index Facets,” *The Journal of Physical Chemistry C*, **115**(9), pp. 3638–3645.
- [27] Langille, M. R., Personick, M. L., Zhang, J., and Mirkin, C. A., 2012, “Defining Rules for the Shape Evolution of Gold Nanoparticles,” *Journal of the American Chemical Society*, **134**(35), pp. 14542–14554.
- [28] Luo, D., Shi, B., Zhu, Q., Qian, L., Qin, Y., and Xie, J., 2020, “Optical Properties of Au–Ag Nanosphere Dimer: Influence of Interparticle Spacing,” *Optics Communications*, **458**, p. 124746.
- [29] Wang, Y., He, J., Liu, C., Chong, W. H., and Chen, H., 2015, “Thermodynamics versus Kinetics in Nanosynthesis,” *Angewandte Chemie International Edition*, **54**(7), pp. 2022–2051.

- [30] Lee, E. J., Ribeiro, C., Longo, E., and Leite, E. R., 2005, "Oriented Attachment: An Effective Mechanism in the Formation of Anisotropic Nanocrystals," *The Journal of Physical Chemistry B*, **109**(44), pp. 20842–20846.
- [31] Yang, X. Q., Lu, Y., Liu, Y., Wang, J., Shao, L., and Wang, J. F., "Heterostructures Built through Site-Selective Deposition on Anisotropic Plasmonic Metal Nanocrystals and Their Applications," *Small Structures*, p. 2100101.
- [32] Akil, S., Omar, R., Kuznetsov, D., Shur, V., En Naciri, A., and Jradi, S., 2021, "Advanced Large-Scale Nanofabrication Route for Ultrasensitive SERS Platforms Based on Precisely Shaped Gold Nanostructures," *Nanomaterials*, **11**(7), p. 1806.

Summary, Conclusions, Perspectives, and Supplementary Information

Conclusions

This dissertation investigated that VIPS approach, an innovative surface-based strategy, can be applied to the synthesis of bimetallic nanostructures with different configurations. This surface approach holds wide appeal because it is convenient, rapid, and inexpensive. Given the multitude of methods available for fabricating BNPs, most previous research has predominantly focused on solution-based techniques. **Chapter 1** summarizes a substantial amount of work performed on BNPs synthesis.

Chapter 2 describes a novel, one-shot strategy to fabricate ultrasensitive SERS sensors based on Ag/PMMA nanocomposites. Upon spin coating of a dispersion of PMMA and silver precursor on N-doped silicon substrate, closely separated AgNPs were self-assembled into uniform nanospheres. As a result, a thin hydrophobic PMMA layer embedded with AgNPs was obtained on the whole silicon substrate. Consequently, a large-scale, reproducible SERS platform was produced through a rapid, simple, low-cost, and high-throughput technology. In addition, reproducible SERS features and high SERS EF were determined ($EF \sim 10^{15}$). This finding matches the highest EF reported in literature to date (10^{14}) for silver aggregates. The potential and novelty of this synthesis is that no reducing agent or copolymer was used, nor was any preliminary functionalization of the surface carried out. In addition, the AgNPs were fabricated directly on the substrate's surface; consequently, there was no need for polymer etching. Then, the synthetic method was successfully applied to prepare opaque SERS platforms. Opaque surfaces are needed in photonic devices because of the absence of secondary back reflection, which makes optical analysis and applications easier.

In **Chapter 3**, we report an innovative facile polymer-templated synthesis of Ag/Au BNPs on large surface. By controlling the reaction kinetics, the BNPs have been successfully prepared with a variety of structures: heterostructures, eccentric core-shells, and physical mixtures of two metals. The amount and initial shape of the Au seeds structures determined the final architectures of bimetallic nanostructures. The underlying synthesis mechanism of BNPs was regulated by a SMG

on the surface. The newly formed Ag atoms were directed to selectively nucleate and then epitaxially grow on specific facets of a cubic/hexagonal Au seeds. Comprehensive results demonstrating an optical response of two M⁺/PMMA layers on opaque surfaces by micro-extinction measurements were obtained. Sensors based on anisotropic bimetallic substrates were ideal for sensitive 4,4'-BP detection. The polymer surface-induced accumulation of high electric fields on nanoscale sensing volumes of anisotropic core/shell BNPs allowed more analyte molecules to access their high-index facets. This sample possessed a high SERS sensitivity despite only being validated on very small densities of surfaces; thanks to the synergistic effects between the two coupled metals. The present findings suggest that a surfactant-free synthesis can be used as a powerful mean of defining growth strategies based on silicon substrate platforms.

Chapter 4 Two distinct bimetallic nanostructures, namely, hetero-oligomers and eccentric core-shells were obtained under low and high Ag⁺/PMMA concentrations, respectively. The Ag concentration-dependent, facet-specific passivation, and presence/absence of anisotropic facets were the main factors responsible for controlling the structures of final products. Based on an understanding of the role of Ag⁺ ions in controlling the shape of anisotropic AuNPs, we can apply tailored concentrations of Ag⁺ to design NPs with desired anisotropic surface facets to allow site-specific Ag coatings on AuNPs. The morphology differences of both substrate samples resulted in discrete plasmonic and sensing features. In SERS studies, we showed that the site-selective deposition of Ag on anisotropic AuNH delivers more advantages than the hetero-oligomers nanostructures counterparts.

As a summary, there still exist many opportunities in the development of various bimetallic nanostructures with site-selective nanomaterial deposition on plasmonic NPs and the exploration of their applications. The improved preparation technique (VIPS) and the deepened understanding of the mechanisms in the growth and performance/property enhancement of such nanostructures will greatly extend their applications in sensing, biomedicine, and plasmonic photocatalysis.

Perspectives

The aim of this thesis was to fabricate multifunctional bimetallic nanomaterials as an important step towards advanced SERS applications. Lot of studies were conducted for optimizing the experimental conditions that can allow the elaboration of the suitable bimetallic nanomaterial. However, we still need to perform more trials to conduct full covered bimetallic surfaces. In order to develop sensitive bimetallic nanostructures more suitable for SERS, the following aspects could be further explored:

- Because this is conspicuously a surface mechanism, conductivity of substrates plays a vital role in the synthetic mechanism. The substrate conductivity shows a major role in the spontaneous reduction of metallic salts and formation of MNPs. Generally, ITO-coated glass substrates are more conductive than Si-As. Relying on the differences between the electrical conductivities of both substrates, high density of BNPs can be obtained by making a deposition on ITO substrates.
- These problems can also be overcome if bimetallic compounds are adopted as single-source molecular precursors. This could be effective in producing BNPs easily owing it to the presence of one PMMA layer instead of two. This could promote the interaction between the two MNPs and allow their presence on surfaces with high quantities.
- Figure 41 reveals that BNPs still exist even after removing the PMMA, which is confirmed by the decrease of reflection intensity without having any null response. The PMMA was extracted from the second layer of hetero-oligomers bimetallic sample after 5 days of synthesis. The bimetallic sample was rinsed with MIBK solvent for 1 min. Interestingly, BNPs retain the same band forms despite the absence of polymer matrix, demonstrating their excellent adhesion to the substrate. This indicates that a stabilizer is unnecessary here, as opposed to colloidal synthesis. It is extremely important to have this property, since removal of this stabilizer could disrupt the morphology of nanostructures, and that would be an inconvenience in most synthesis methods.

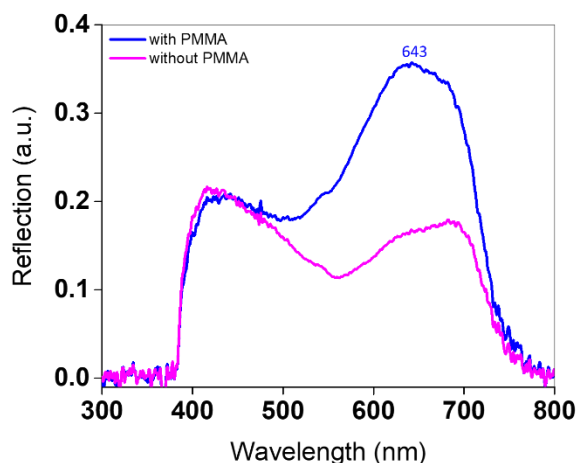
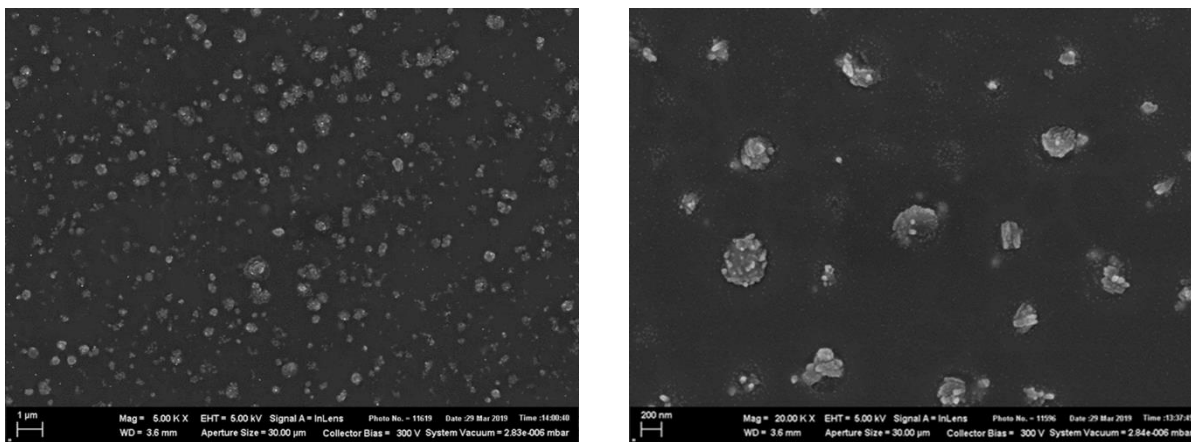


Figure 42. Reflection optical spectra of hetero-oligomers bimetallic sample before and after rinsing of second PMMA layer

- VIPS approach can be extended to formation of alloys, as shown in Figure 42. This was achieved by using PMMA dissolved in MIBK instead of acetone, heating the sample at 100°C for 30 min, adopting $\text{HAuCl}_4 \cdot 3\text{H}_2\text{O}$ as gold precursor molecule, and using 20 mM as a concentration of both $\text{AgNO}_3/\text{PMMA}$ and $\text{HAuCl}_4 \cdot 3\text{H}_2\text{O}$ precursors. The sample was spin-coated at a speed of 10000 rpm. We propose that further research should be undertaken in the following area. This study is deferred to a future work. Choosing 60 mM and 40 mM as an optimal concentration for gold and silver solutions respectively can allow the better correlation of the plasmonic optical responses to structural parameters and can lead to more encouraging results. As a result of the high densities and small intra- and interparticle distances between the corn-flakes NPs, which induce hot spots to accumulate in the confocal volume of measurement, a high SERS EF could be obtained. Such a high sensitivity could be particularly effective in detecting rare and dangerous chemicals in biomedicine, safety, and environmental pollution.



(a)

(b)

Figure 43. SEM images showing a bimetallic system that could demonstrates an alloyed structure.

- The design of plasmonic Ag/Au bimetallic systems requires the creation of improved modelling methods capable of predicting their unique optical properties. However, the dielectric functions of these novel systems (core/shell, heterostructures, and hetero-oligomers) on surfaces are not yet entirely known. For this reason, we proposed to measure the dielectric functions of BNPs by spectroscopic ellipsometry followed by estimating the percentage of elements in bimetallic system by X-ray photoelectron spectroscopy (XPS). The dielectric function can then be introduced into a modified Mie theory in order to simulate the extinction optical responses of a set of BNPs with different stoichiometric distributions. The development of a correlation between experimental (Micro-extinction Setup) and theoretical (Ellipsometry Technique) optical studies will enable further advancements in the study of bimetallic nanostructures.
- Future work should consider examining other bimetallic systems (i.e. Au/Pd, Ag/Pd ...) as this could lead to interesting discoveries and unique dual and multi-component nanomaterials.

Appendix-A (related to Chapters 3 and 4)

Preliminary Studies to fabricate BNPs

Mixing two metallic precursors in solution

The first attempts made to make BNPs from mixing two different metallic precursors were not successful. This study was initiated in order to enable the formation of BNPs on substrate surfaces

and not in solution. A required amount of NaAuCl_4 and AgNO_3 precursors were added to the mixture solution, containing solvents and PMMA solution, to obtain different desired molar ratios of Ag/Au : 0.2, 0.25, 0.3, 0.4, 0.5, 0.6, 1. Mixing together the metallic precursors solutions and PMMA solution in precise proportions creates rapidly a thermodynamic unstable mixture with a phase separation. In Figure 43, the color of the Ag/Au bimetallic nanofluid changed from brown orange (A) to yellow (G) to colorless (H) after adding PMMA solution. The color changes may be attributed to the small amount of Ag^+ in the mixture which served as an additive to tune the growth process of AuNPs. Usually, AgNO_3 has two roles in the field of NPs synthesis in solutions. It behaves as a driving agent for growth and control of shapes of NPs, and as a reducing agent for generation of atoms instead of ions. For this reason, the amount of silver solution was smaller compared to gold solution. Unfortunately, it fails to take into account that silver precursor makes reduction for gold ions present in the solution, thus leading to presence of NPs inside the solution. But, our work seeks to address how to form BNPs on surface rather in solution.

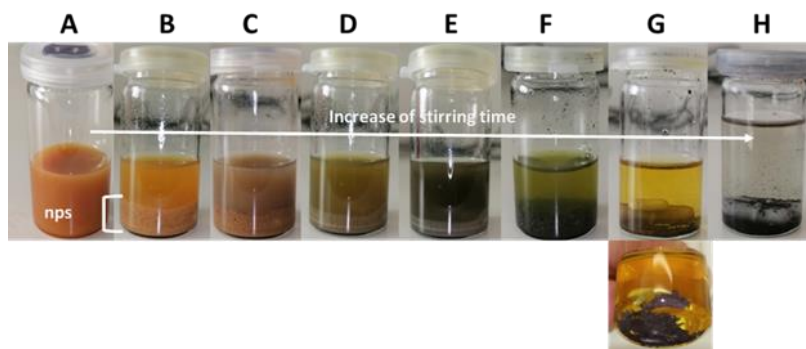


Figure 44. Photograph of the Au–Ag bimetallic nanofluids prepared using different molar ratios of Au to Ag precursors.

Removing PMMA from first Ag^+/PMMA layer followed by subsequent deposition of $\text{Au}^{3+}/\text{PMMA}$ as second layer

Removing PMMA from first layer was done using different methods. We intended to remove PMMA from the first layer and preserve it in the second layer to maintain the hydrophobicity of surface, which is crucial for SERS. Unfortunately, the methods fail to eliminate the PMMA without affecting the NPs.

The substrate sample was subjected to a PMMA extraction by rinsing the first Ag⁺/PMMA layer with MIBK solvent for 1 min. MIBK, which is a good solvent for PMMA, removed the majority of the AgNPs products (Figure 44(b)). As indicated in Chapter 2, AgNPs were completely localized and fitted inside the PMMA nanoholes.

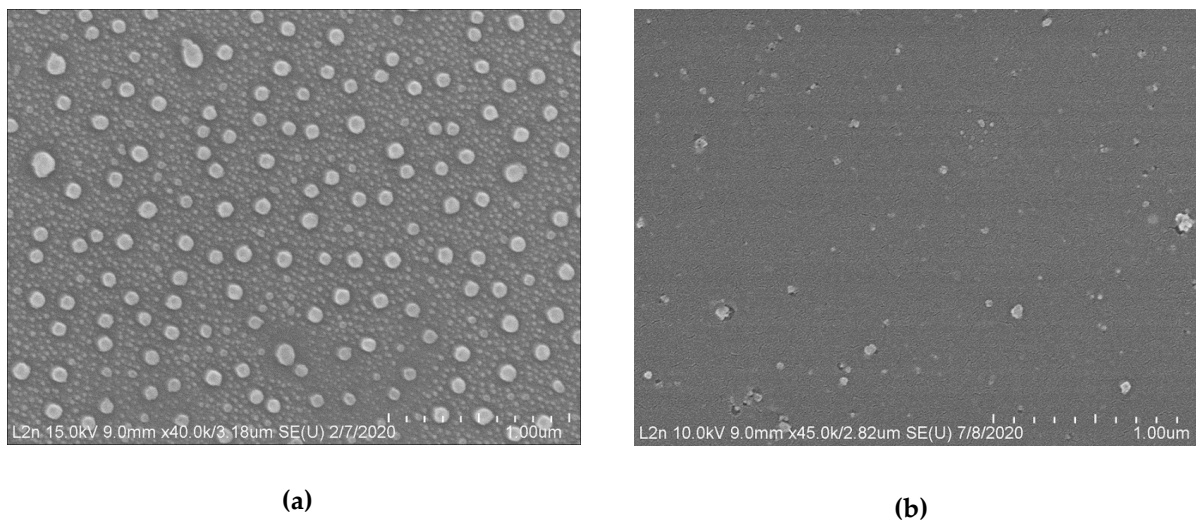


Figure 45. SEM images of (a) Ag(40)/PMMA without rinsing; and (b) Ag(40)/PMMA after rinsing with MIBK for 1 min

Disjunctive Deposition of two metallic layers

As highlighted in Figure 45, the disjunctive deposition of 60 mM NaAuCl₄/PMMA-acetone as a second layer on 40 mM AgNO₃/PMMA-acetone using 7000 rpm as a spin-coating speed shows that a physical mixture of Ag and AuNPs are existed on the conductive substrate. The time delay between the two deposited metallic layers was 1 week. AuNRs with tunable aspect ratios were achieved by VIPS approach on surfaces. This result is promising because the high aspect ratios of Au nanorods can easily tune the plasmonic peaks into the NIR regions. In NIR regions, where absorbance of light by biological tissues is at its minimum, these geometrical shapes of AuNPs are set to become a vital factor in biomedical imaging, SERS biosensors, and localized photothermal therapy applications [1]. This result paves the way toward more comprehensive surface manufacturing and opens perspectives in the synthesis of Au nanorods on surfaces. Despite this, it was not our main objective in the meantime. It was our intention to focus on synthesis of bimetallic nanostructures.

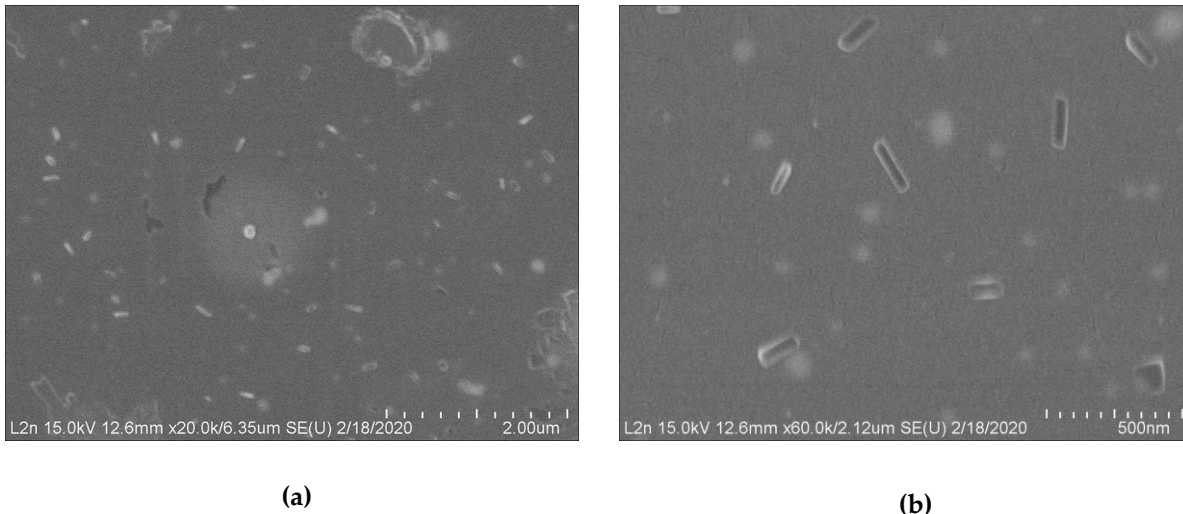


Figure 46. SEM images of Ag(40)-Au(60) bimetallic sample synthesized by disjunctive deposition of the two layers with a time delay of 1 week

Successive Deposition of two metallic layers

The way of synthesis of bimetallic sample (Figure 46) is practically the same as the one mentioned in Chapter 3. The time delay between the two deposited layers was 10 min. We concluded that using this strategy allowed the formation of bimetallic nanostructures. The PMMA layer overlaid on top of the underlying layer was an ~ exact duplicate. Hence, the two metals were able to interact with one another and organize into specific configurations. Figure 46 reveals the profile of the two PMMA layers when taking the SEM image without any metallization.

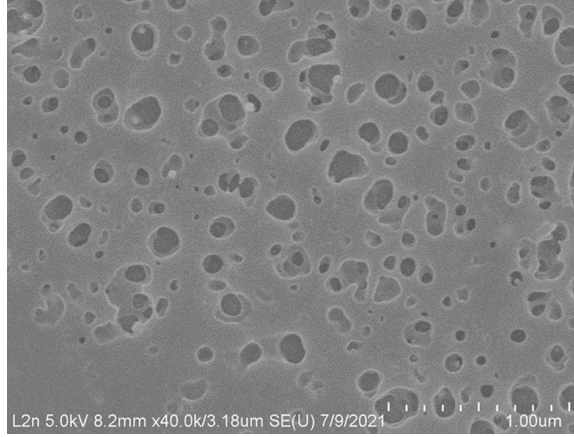


Figure 47. SEM image showing the arrangement of the two PMMA layers after a successive deposition with time delay of 10 min

Appendix-B (related to Chapter 2)

Principle of Ellipsometry

Ellipsometry is an optical analysis technique based on the change in polarization of light during reflection on a flat surface. A rectilinear polarized light wave, sent to a sample, transforms into an elliptical one after reflection (refer to Figure 47). Ellipsometry analyzes the properties of elliptically polarized light by determining directly the ellipsometric angles Ψ and Δ , which corresponds to the amplitude ratio and phase difference of the ratio of p- and s-polarized reflectivities respectively [2,3]. In the reflection mode, Ψ and Δ are defined by the basic equations (6) and (7):

$$\rho = \frac{r_p}{r_s} = \tan\Psi e^{i\Delta} \quad 0^\circ \leq \Delta \leq 360^\circ, \quad (6)$$

$$\tan\Psi = \frac{|r_p|}{|r_s|} \text{ and } \Delta = \delta_p - \delta_s \quad 0^\circ \leq \Psi \leq 90^\circ, \quad (7)$$

where r_p and r_s are the Fresnel amplitude reflection coefficients for the polarization parallel (p) and perpendicular (s) to the plane of incidence; δ_p and δ_s are the phases of r_p and r_s .

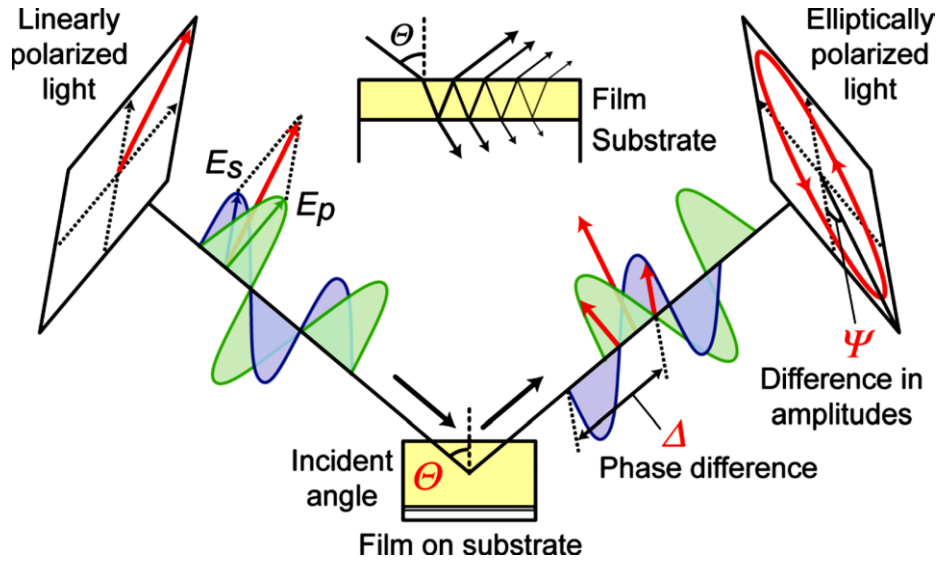


Figure 48. Schematic illustration of spectroscopic ellipsometry principle. Adapted from [2].

Ellipsometric Data Analysis

The values of the ellipsometric parameters (Ψ and Δ) significantly depend on the optical constants (refractive index (n) and extinction coefficient (k)), thickness of film, wavelength of light, and incident angle [4].

In order to extract the effective optical properties of metallic/PMMA films and thickness of films, a suitable model is required. Ellipsometry analysis is performed by fitting the experimental spectra using an optical model. Figure 50 reveals the summary of data analysis procedure in spectroscopic ellipsometry. The main optical parameters determined after modelling and minimizing the χ^2 error function between the experimental and the calculated ellipsometric data are: real (ϵ_r) and imaginary (ϵ_i) parts of the dielectric function (Equation 10 and 11), refractive index (n) (Equation 12), extinction coefficient (k) (Equation 13), and the absorption coefficient (α) (Equation 14). By exploiting equation 8, the fit quality is given by the value of χ^2 according to Levenberg–Marquardt algorithm [5].

$$\chi^2 = \frac{1}{2N-M} \sum_{i=1}^N [(\Psi_i^{model} - \Psi_i^{exp})^2 + (\Delta_i^{model} - \Delta_i^{exp})^2] \quad (8)$$

where N denotes the number of data collected versus wavelength λ , M is an abbreviation of the number of model parameters, and the superscripts model and exp refer to modelled and experimental values respectively.

Ellipsometry Technique

The instrument employed was UVISEL phase-modulated ellipsometer of Horiba which provides an accurate measurement over wide spectral ranges from 190 to 2100 nm. The design of this setup is geared towards achieving a high sensitivity for characterizing thin film thicknesses and optical constants. The system is fully integrated with Xe lamp source attached to a polarizer, photoelastic modulator, analyzer, and a detection system comprising a monochromator and two detectors. The two detectors used are a photomultiplier for UV-VIS and an InGaAs photodiode for NIR applications. The configuration of the UVISEL phase modulated ellipsometer is shown in the Figure 48 below [6].

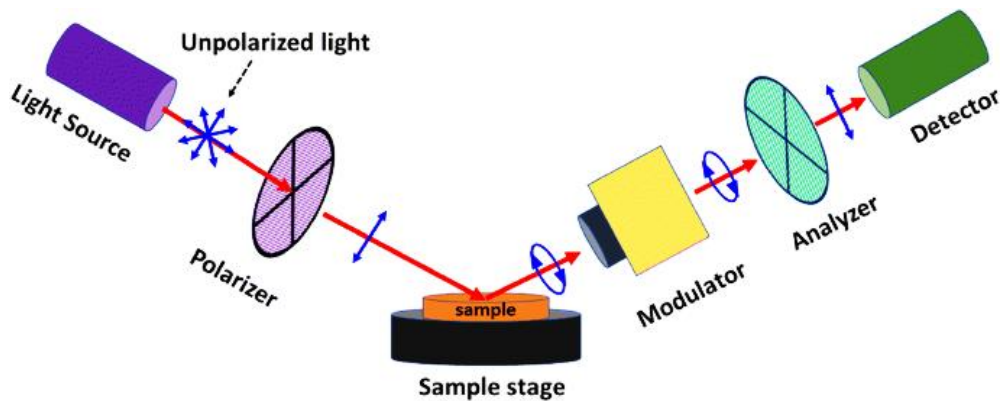


Figure 49. Configuration of the UVISEL phase modulated ellipsometer used for measurements. Adapted from [6]

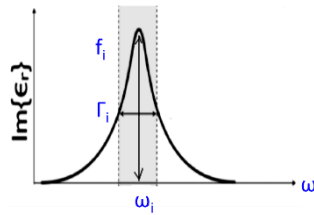
Modelling

Many theoretical approaches, such as classical effective medium approximation theory (EMT), were widely used for detecting the optical properties of nanostructures embedded in a host medium. EMT, including Maxwell-Garnet (MG) and Bruggeman theories, takes into consideration the dielectric constants and volume fractions of each constituent. Indeed, conventional EMT is not specifically designed to shapes other than spherical and spheroidal ones. Bruggeman theory

assumes that the mixture is composed of two isotropic and homogeneous materials with identical roles. MG theory has not dealt with structures containing particles dispersed in a non-continuous and porous medium of another compound. This theory is appropriate for two materials (inclusions and host) with unsymmetrical roles. The most fundamental approximation in MG theory is that the size of spherical NPs (inclusions) is much smaller than wavelength of light. Unfortunately, it neglects the presence of high volume fractions of spherical inclusions with strong coupling effects [7,8]. The first set of analyses confirmed that EMT theory cannot be successfully used in modelling the samples. To overcome the difficulty, it is necessary to adopt a model that is fully compliant with our sample's conditions.

Modelling was accomplished by using three classical Lorentz oscillators that consider AgNPs and PMMA film as a one homogeneous layer. Two oscillators are used for AgNPs and the remaining one for PMMA film. The well-known values of the optical constants of silicon were kept fixed while proceeding with the modelling. Lorentz model (mentioned in Figure 49) is described by the Lorentz dispersion equation [5], as stated in equation 9:

$$\epsilon(\omega) = \epsilon_{\infty} + \omega_p^2 \sum_{i=1}^N \frac{\omega_i^2 f_i}{\omega_{0,i}^2 - \omega^2 + j \omega \Gamma_i} \quad (9)$$



where f_i represents the strength of oscillator; for the i^{th} oscillator ω_i is the resonance frequency; Γ_i stands for the broadening coefficient; ϵ_∞ represents the contribution of the optical transitions at higher energies; ϵ is the composite effective dielectric function. The i index identifies the number of optical transitions.

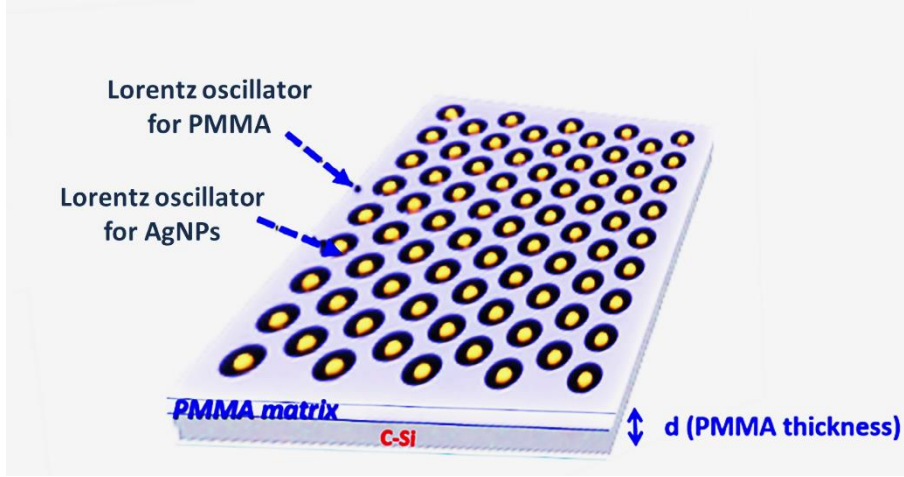


Figure 50. Physical model constructed for a thin MNPs/PMMA film formed on a substrate surface.

According to Lorentz dispersion law, the calculations of optical parameters of MNPs/PMMA film can be expressed as:

$$\epsilon_r = n^2 - k^2 \quad (10)$$

$$\epsilon_i = 2nk \quad (11)$$

$$n = \sqrt{\frac{1}{2} (\sqrt{\epsilon_r^2 + \epsilon_i^2} + \epsilon_r)} \quad (12)$$

$$k = \sqrt{\frac{1}{2} (\sqrt{\epsilon_r^2 + \epsilon_i^2} - \epsilon_r)} \quad (13)$$

$$\alpha = \frac{4\pi k}{\lambda} \quad (14)$$

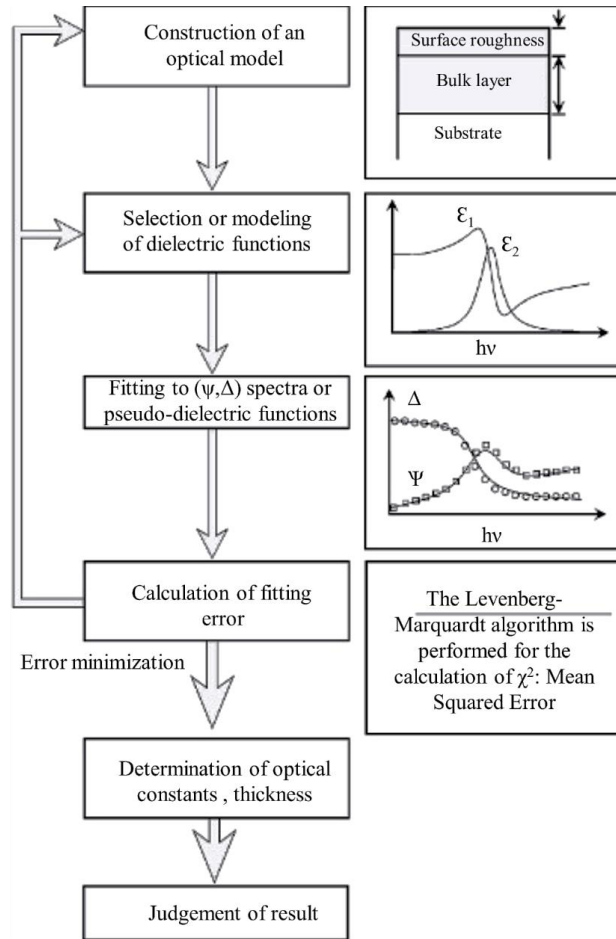


Figure 51. Flowchart of the data analysis procedure in spectroscopic ellipsometry. Adapted from [5].

Fitting the Experimental Measurements & Extraction of Optical Constants

To provide the best fit of pseudo-dielectric functions spectral data, we construct a model with three classical Lorentz oscillators, two for AgNPs and the other for PMMA film. Such findings are depicted in Figure 51. The solid and dotted lines show fitted and experimental results respectively. The pseudo-dielectric function represents a dielectric function obtained directly from the measured values psi and delta. Figure 52 and 53 shows the variations of the optical constants (ϵ_i and ϵ_r , n and k) of AgNPs loaded in PMMA holes when changing the concentration of Ag precursor. The dielectric functions (ϵ_i and ϵ_r) are commonly dependent on the number and structural properties

of particles on surface, and on the effective index of the whole PMMA layer, respectively. ϵ_i in Figure 52 is fully compliant with α spectras (mentioned in Chapter 2).

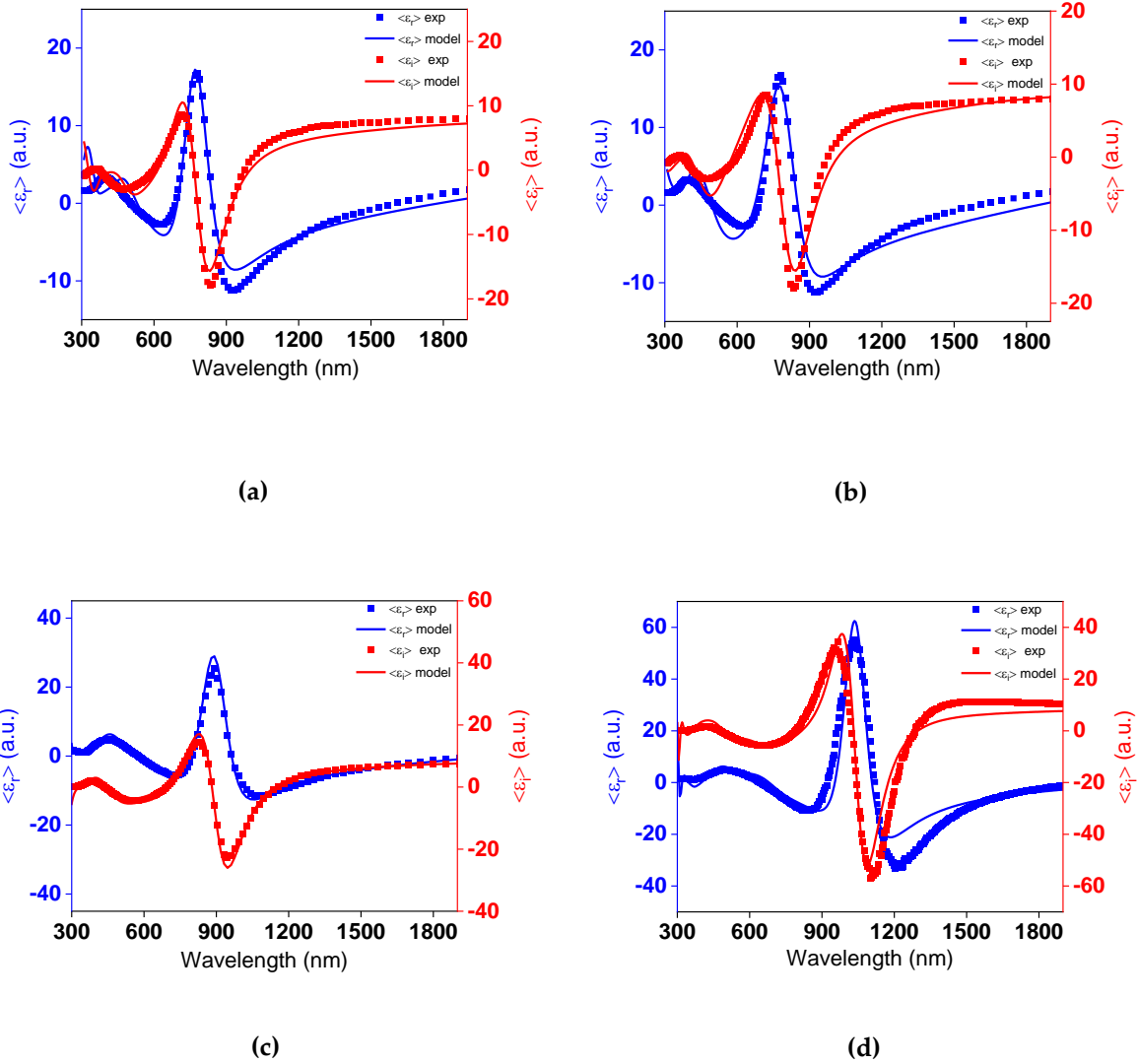


Figure 52. Comparison between experimental and fitted pseudo-imaginary and real dielectric functions (ϵ_i , ϵ_r) of AgNPs/PMMA film/c-Si structures at different concentrations of Ag precursor: (a) 10; (b) 20; (c) 30; and (d) 40 mM.

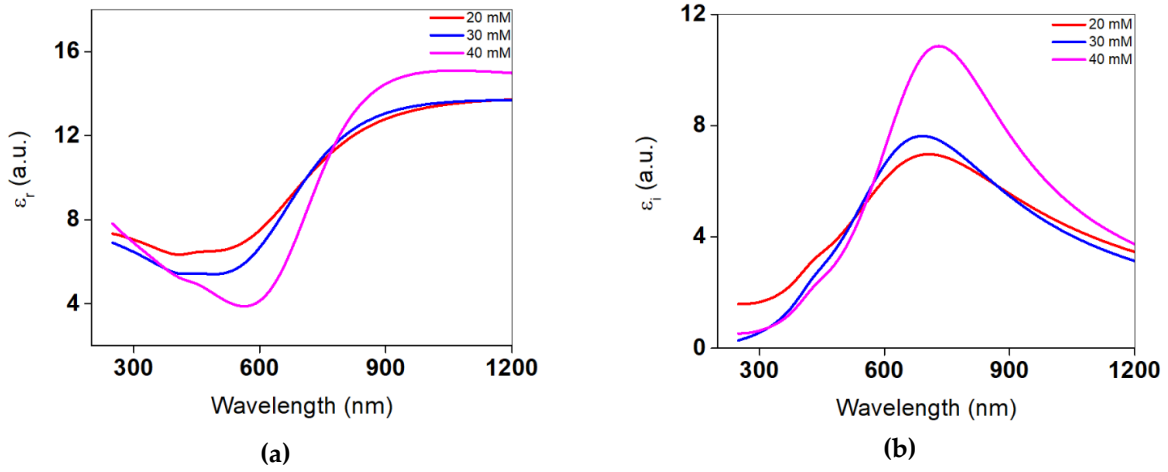


Figure 53. Dielectric functions ((a) ϵ_r and (b) ϵ_i) of Ag/PMMA layers at different concentrations.

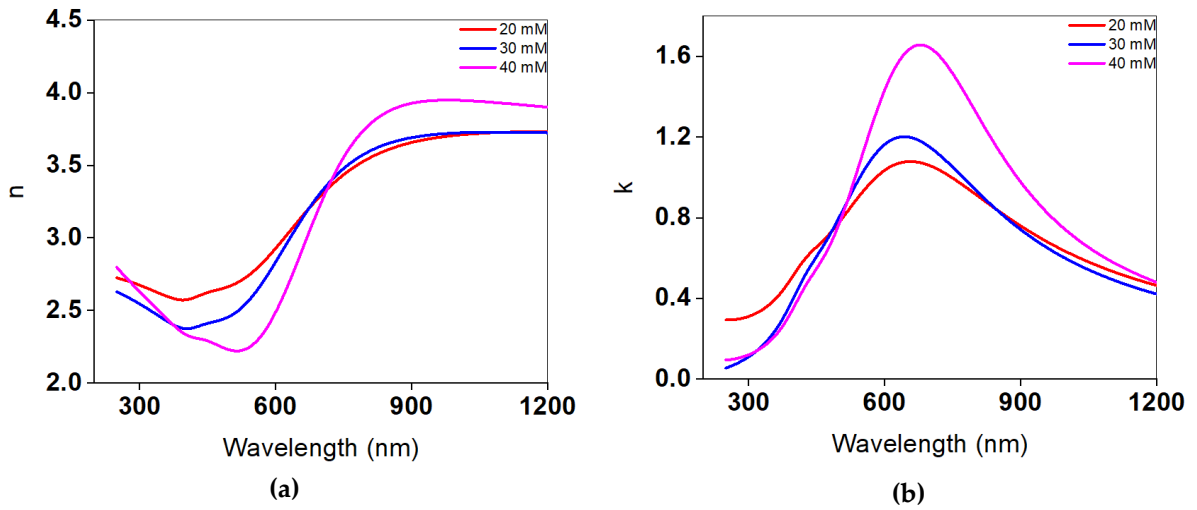
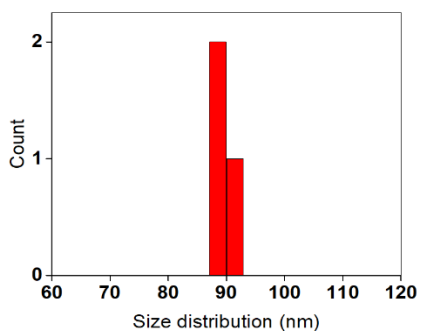


Figure 54. Refractive index ((a) n) and extinction coefficients ((b) k) of AgNPs/PMMA layers at different concentrations.

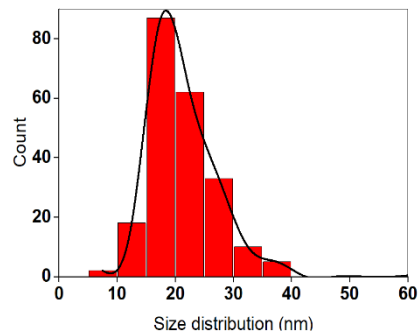
Size Distributions Histograms

Speed Effect Study



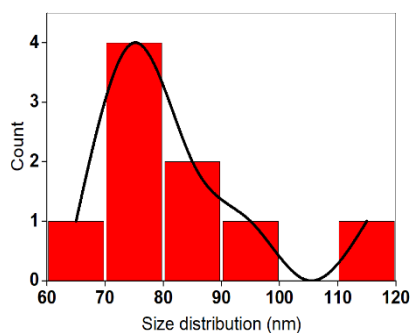
Mean diameter= 89 nm

(a)



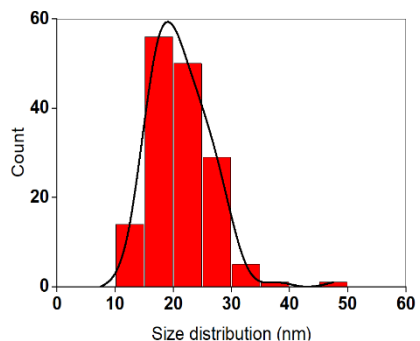
Mean diameter= 19 nm

(b)



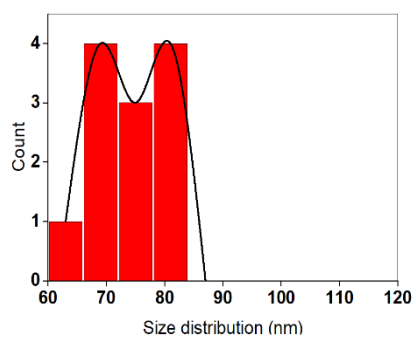
Mean diameter= 75 nm

(c)



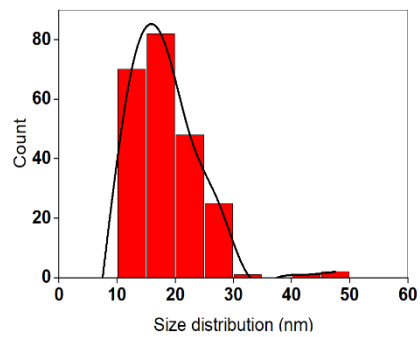
Mean diameter= 17 nm

(d)



Mean diameter= 74 nm

(e)



Mean diameter= 16 nm

(f)

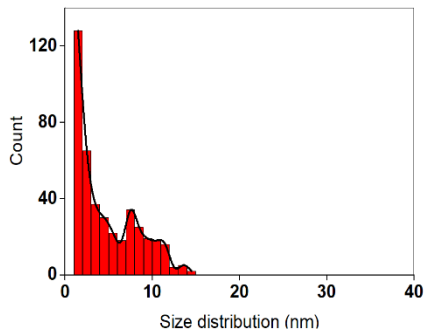
Figure 55. Size distribution histograms for the determination of average diameters (D1 and D2) of AgNPs prepared at different spin-coating speeds: (a,b) 3000; (c,d) 5000; and (e,f) 7000 rpm.

Concentration Effect Study

Difficult to determine from SEM

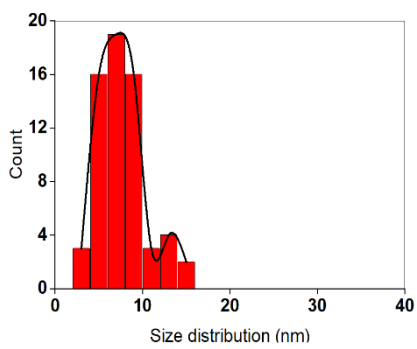
Mean diameter < 7 nm

(a)



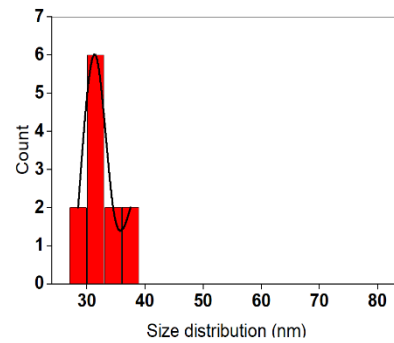
Mean diameter= 7 nm

(c)



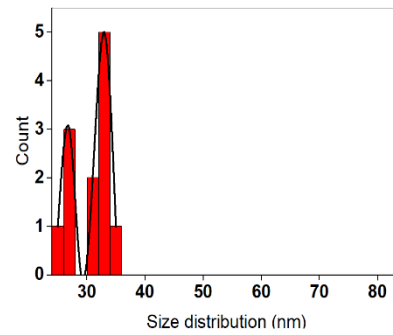
Mean diameter= 7-13 nm

(e)



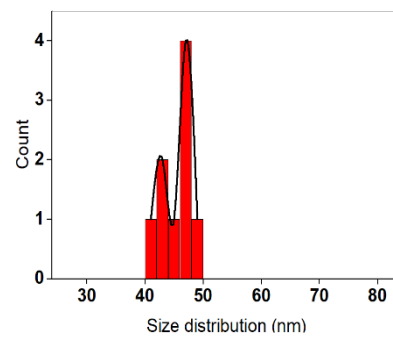
Mean diameter= 31 nm

(b)



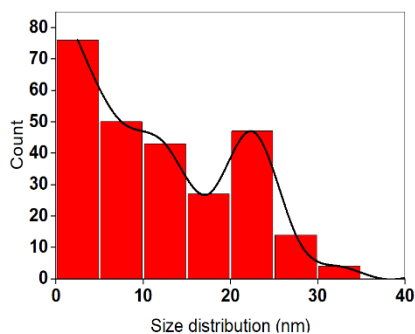
Mean diameter= 27-33 nm

(d)

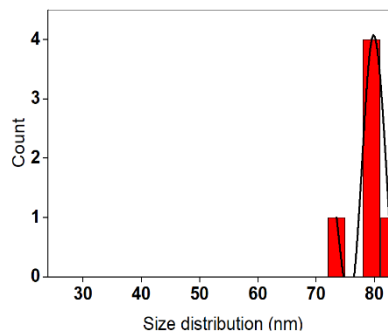


Mean diameter= 43-47 nm

(f)



Mean diameter= 12-22 nm
(g)



Mean diameter= 80 nm
(h)

Figure 56. Size distribution histograms for the determination of average diameters (D1 and D2) of AgNPs prepared at different concentrations of Ag precursor: (a,b) 10; (c,d) 20; (e,f) 30; and (g,h) 40 mM.

Appendix-C

Characterization techniques

Atomic force microscopy (AFM): AFM measurements were performed using a Park Systems NX10 (ParkSystems, Orsay, France) operating in tapping mode. Depending on the analyzed samples, this technique can easily be adapted to suit all requirements. Samples were simply placed on the XY scanner with high orthogonality, and then imaged by using pre-mounted super sharp (SSS-NCHR) probes (nanosensors) with a high mechanical Q factor for high sensitivity. The probes offer unique features, such as: aspect ratio at 200 nm from the tip apex in the order of 4:1, half-cone angle at 200 nm from apex $< 10^\circ$, resonant frequency = 330 kHz, spring constant = 42 N/m, and tip radius of curvature < 5 nm.

Scanning electron microscopy (SEM): The instrument employed in collecting SEM images was a HITACHI SU8030 SEMFEG (Carl Zeiss, Oberkochen, Germany), which was manipulated in a secondary electron imaging mode at an accelerating voltage = 5–15 kV, magnification = 30–250 K, working distance = 8200–9100 μm , and emission current = 7000–15,600 nA. The samples were coated with a 5 nm Pt/Pd metal layer. Coatings of samples with a conductive Pt/Pd layer were done to prevent the charging and improve the secondary electron signal.

Micro-extinction spectra (μext): Measurements were taken using a custom-built BX51 Olympus optical microscope (LORDIL, Nancy, France). The system was fully integrated with SpectraWiz (StellarNet, Tampa, FL, USA) software for recording the optical spectra of samples in the Vis region (400–800 nm). An incident beam from a halogen lamp (size $\sim 10 \mu\text{m}$) was localized at normal incidence onto the substrates during all measurements. In this spatial optical technique, the focal spot of an optical beam is analyzing the reflection from a micrometric zone of NPs. For opaque substrates, this setup was managed in reflection mode in order to extract the percentage reflection at pixel n using the current sample, reference (silicon wafer), and dark datasets:

$$R_n = ((\text{sample}_n - \text{dark}_n)/(\text{ref}_n - \text{dark}_n)) \times 100 \quad (1)$$

where sample, ref, and dark are respective photon energies.

All spectra were acquired using a 10-x objective in a bright-field mode. The spectra were thoroughly checked by mapping the surface of samples in different areas. Average data were acquired for a minimum of 6 regions per sample in order to check their homogeneity and reproducibility.

Ellipsometric measurements: The change in polarized light upon light reflection on a sample was measured using a phase-modulated ellipsometer (UVISEL, HORIBA Jobin Yvon SAS, Longjumeau, France) in the 200–1800 nm spectral range. To ensure a high sensitivity of the measurements, an incidence angle of 70° was chosen. The spot size of the used light beam was typically $1000 \mu\text{m}^2$. This setup directly measures the amplitude ratio (Ψ) and phase difference (Δ) angles between p- and s-polarized light. In general, after measurement of absolute values of psi and delta, construction of an optical model is required for data analysis. From modelling, physical properties including the optical constants, absorption coefficients, and film thicknesses of samples can be extracted. Data analysis and modelling were performed using DeltaPsi2 software from Horiba Scientific.

Surface-enhanced Raman scattering (SERS): For AgNPs samples, SERS measurements were performed on a Dilor Jobin-Yvon Spex instrument (HORIBA Jobin Yvon SAS, Longjumeau, France) from Horiba with a 632.8 nm laser and CCD detection. Both excitation and collection were conducted through a long-distance 50-x. Results were collected on a $10 \mu\text{L}$ BPE droplet deposited on AgNPs substrate. The measurements were made after the evaporation of water from

the drop in order to obtain a higher signal/noise ratio. We used a laser power of 5 mW and an acquisition time of 5 s. It is noteworthy that it was not possible to obtain the same spectra (peaks) in the same measurement conditions (time, laser power, pinhole, etc.) for RAMAN and SERS. Therefore, we increased the concentration of BPE so as to be able to compare between the spectra, and then to calculate an EF. All Raman analyses were performed with 10^{-2} M of BPE. In order to get an idea about the reproducibility of the results, five experiments were conducted at different parts of the same substrate. After the acquisition of several measurements, an average curve was calculated for each substrate SERS signal at a given BPE concentration.

For bimetallic samples, SERS measurements were carried out using a multi-wavelength Raman spectrophotometer equipped with a SPEX TRIAX 550 monochromator and a liquid nitrogen cooled CCD (Spectrum One with CCD 3000 controller, ISA Jobin Yvon – SPEX). For all the SERS and Raman measurements, the probe molecule 4,4'-bipyridine (4,4'-BP) is detected in a liquid medium with a droplet volume of 10 μ L at different excitation wavelengths (514 and 633 nm). The best procedure for this investigation was to execute rapid spectra acquisitions before the drying of the drop. The core problem of the drying process is impeding the uniform stacking of analytes over the substrate surface. This will probably lead to undesirable preferential coatings of analytes on SERS hotspots regions. The SERS signal was collected during an acquisition time of 1 s via a 20-x magnification objective with a numerical aperture (NA) \sim 0.25. The probed area was \sim 30 μ m in diameter and the laser power was 10 mW. An average of at least 3 signals in different regions on the deposited drop was systematically calculated to compare the SERS intensities of the different substrates. The concentration of 4,4'-BP detected in Raman and SERS was 10^{-2} and 10^{-3} M respectively. The same experimental conditions were applied in all the SERS measurements and for all the analyzed substrates.

Energy dispersive X-ray spectroscopy (EDX): Elemental mapping on the fabricated BNPs was achieved using a high resolution EDX unit connected to a field emission scanning electron microscope (SEM-FEG, Carl Zeiss) operated with a beam voltage of 5 kV. When the electron beam is irradiated on the focused NPs region, the elements emit X-rays at characteristic energies, whose intensity increases in proportion to its concentration in the NPs zone.

References

- [1] Meng, L., Zhang, J., Li, H., Zhao, W., and Zhao, T., 2019, "Preparation and Progress in Application of Gold Nanorods," *Journal of Nanomaterials*, **2019**.
- [2] Yokoyama, D., 2011, "Molecular Orientation in Small-Molecule Organic Light-Emitting Diodes," *Journal of Materials Chemistry*, **21**(48), pp. 19187–19202.
- [3] Ahmed, F., Naciri, A. E., Grob, J., Stchakovsky, M., and Johann, L., 2009, "Dielectric Function of ZnTe Nanocrystals by Spectroscopic Ellipsometry," *Nanotechnology*, **20**(30), p. 305702.
- [4] Boulouz, A., Naciri, A. E., Pascal-Delannoy, F., Sorli, B., and Koutti, L., 2009, "Spectroscopic Ellipsometry Study of XPbO–(1- x) TiO₂ Thin Films Elaborated by Mixed Reactive Thermal Co-Evaporation," *Journal of Physics D: Applied Physics*, **42**(24), p. 245304.
- [5] Fujiwara, H., 2007, *Spectroscopic Ellipsometry: Principles and Applications*, John Wiley & Sons.
- [6] Mazumder, M., Ahmed, R., Hasan, M., Lee, S.-J., and Lee, M.-S., 2020, "Spectroscopic Ellipsometry of Asphalt Binder: A Study of Optical Constants," *International Journal of Civil Engineering*, **18**(3), pp. 251–259.
- [7] Keita, A.-S., Naciri, A. E., Delachat, F., Carrada, M., Ferblantier, G., and Slaoui, A., 2010, "Spectroscopic Ellipsometry Investigation of the Optical Properties of Nanostructured Si/SiN_x Films," *Journal of Applied Physics*, **107**(9), p. 093516.
- [8] Battie, Y., Resano-Garcia, A., Chaoui, N., Zhang, Y., and En Naciri, A., 2014, "Extended Maxwell-Garnett-Mie Formulation Applied to Size Dispersion of Metallic Nanoparticles Embedded in Host Liquid Matrix," *The Journal of chemical physics*, **140**(4), p. 044705.

Résumé de la thèse:

Nanostructures bimétalliques Ag/Au auto-assemblées sur une grande surface
pour des plateformes SERS.

Par : Abeer FAHES

Les systèmes bimétalliques hybrides, composés de deux nanostructures métalliques, sont considérés comme une technologie durable en raison de leur capacité à améliorer, rénover et enrichir les propriétés de leurs composants intégrés. La synthèse chimique en solution de nanoparticules bimétalliques plasmoniques (BNPs) avec différentes morphologies a suscité une attention considérable et a été la plus utilisée. Cependant, afin de stabiliser ces BNPs à l'échelle nanométrique, l'étape de fabrication nécessite l'utilisation de plusieurs étapes et de plusieurs composés chimiques tels que les tensioactifs pour contrôler l'énergie de surface. Même si ces BNPs ont été largement impliquées dans de nombreuses applications, il existe toujours un besoin d'alternatif d'élaboration à faible coût, évolutif et applicable directement après fabrication. Jusqu'à présent, aucune étude n'a permis la synthèse de substrats de BNPs directement en surface avec un contrôle précis des tailles et des morphologies des nanoparticules.

Afin de remédier à ces problématiques de synthèse, nous avons développé dans cette thèse une technique reproductible et bien contrôlée, appelée séparation de phase induite par la vaporisation (VIPS) permettant d'auto-assembler des nanoparticules d'or (AuNPs) et d'argent (AgNPs) dans une fine couche de poly(méthacrylate de méthyle, PMMA). Les substrats de Silicium (dopés N) utilisés comme support des nanostructures présentent des propriétés multifonctionnelles telles que réducteurs chimiques du sel métallique, tensioactifs et agents de structuration. Dans le but d'obtenir les plateformes souhaitées, les paramètres expérimentaux de l'approche synthétique ont été optimisés avec précision. Malgré le fait qu'il est difficile d'étudier mécaniquement le processus de croissance des NPs car cette approche de synthèse implique l'intervention d'un grand nombre de composants (substrat de Silicium, PMMA, contre-ions, Ag^+ et Au^{3+}) pouvant coopérer ou entrer en compétition les uns avec les autres, une étude mécanistique large a été établie. Ceci a été réalisé à travers des mesures optiques par micro-extinction des substrats obtenus. Des mesures SERS ont été ensuite effectuées pour évaluer la sensibilité des échantillons en tant que nanocapteurs.

Enfin, la présente thèse offre de nouvelles possibilités pour créer des nanomatériaux hybrides de dimensions et géométries contrôlables sur une grande surface (lab-On-Chip) pour des applications en détection et particulièrement pour le SERS, et pour la photocatalyse.

Le travail de thèse s'articule autour de trois axes majeurs :

- Le développement expérimental d'une technique nouvelle de synthèse de nanostructures composites (métalliques/organiques)
- La généralisation de cette méthode de synthèse à la préparation d'hétérostructures plasmoniques tels que Ag@Au ainsi que sur leurs caractérisations structurales et optiques
- L'utilisation de ces nanocomposites dans la détection de molécules organiques par la technique SERS

La thèse est composée de cinq chapitres dont les objectifs et modes opératoires sont relativement différents

Le chapitre 1 est le chapitre introductif du projet entier de la thèse et il est divisé en deux parties principales. La première partie a souligné l'importance d'incorporer deux nanoparticules métalliques (MNPs) dans un seul système dans plusieurs applications telles que la catalyse, le SERS, les capteurs à base de plasmons de surface localisés (LSPR) et la conversion photothermique. Ces multifonctionnalités découlent des effets synergiques qui se produisent entre les systèmes hybrides, notamment les effets électroniques, les effets bifonctionnels et les effets d'ensemble. La deuxième partie a fourni un aperçu général des approches synthétiques principalement utilisées pour la fabrication de nanostructures bimétalliques avec des caractéristiques morphologiques bien contrôlées. La majorité des études citées dans la littérature reposent sur des protocoles d'élaboration en milieu liquide.

Un procédé de synthèse décrit dans ce projet connu sous le nom de VIPS, utilisé pour la fabrication de nanocubes d'or monodisperses intégrés dans une couche de polymère auto-assemblée en nanotrous, a été réalisé récemment. Cette approche de synthèse simple, rapide et en une seule étape a montré son efficacité dans le contrôle des tailles, des formes des nanoparticules obtenues et des gaps inter-particulaires. De plus, il n'était pas nécessaire d'utiliser un agent réducteur ou un copolymère à blocs pour induire l'auto-assemblage ; il n'y avait donc aucune exigence de

fonctionnalisation de la surface du substrat ou de gravure du film polymère. L'originalité de cette méthode est liée à la réduction spontanée du précurseur métallique lors du dépôt de la dispersion M^+ /PMMA sur un substrat conducteur. Plus précisément, dans les chapitres 2, 3 et 4, nous avons discuté de l'extension du procédé VIPS à une grande variété de sels monométalliques dont l'Argent et aux hétérostructures bimétalliques dont Ag/Au.

Dans le chapitre 2, un récapitulatif des méthodes de synthèse des AgNPs par auto-assemblage au moyen de polymères, de copolymères à blocs et d'acide désoxyribonucléique (DNA) est présenté. Les inconvénients de ces techniques telles que le manque de reproductibilité et d'uniformité dans le SERS ont été également discutées. Ainsi, si l'on veut aller plus loin, et utiliser l'auto-assemblage pour construire des nanomatériaux fonctionnels qui pourraient être compatibles avec les applications SERS, il est nécessaire d'augmenter la stabilité et la performance des nanostructures auto-assemblées.

Ce chapitre décrit ainsi la synthèse de nanocomposites Ag/PMMA en grandes quantités sur un substrat à l'aide de la méthode VIPS déjà évoquée pour former des substrats SERS de grande surface, reproductibles et ultra-sensibles. En utilisant la technique VIPS, un PMMA est auto-assemblé en couche mince nanoperforée dont les trous sont utilisés comme réacteurs de synthèse de nanoparticules. Ce chapitre a également examiné les différents paramètres expérimentaux affectant les propriétés structurales et optiques des AgNPs. Les AgNPs en tant que nanocapteurs, en particulier, ont été optimisés en ajustant un certain nombre de facteurs, notamment la concentration de précurseurs métalliques et la vitesse de dépôt par spin-coating.

La modification de la concentration du précurseur d'Ag a considérablement influencé le résultat de l'auto-assemblage et par conséquent les propriétés finales des nanoparticules obtenues. En dessous d'un seuil de concentration critique, une instabilité thermodynamique a gêné l'auto-assemblage en début de procédé à cause d'une agrégation du PMMA. De plus, une vitesse appropriée a été choisie pour fabriquer une couche de polymère mince et homogène, et pour produire une haute sensibilité de réflexion de la lumière à partir de nanoparticules (NPs), vu qu'on détecte la réponse optique du substrat en réflexion pour les mesures optiques.

L'extraction de ces propriétés optiques était nécessaire pour ajuster la longueur d'onde d'excitation Raman afin qu'elle corresponde étroitement à la bande de résonance plasmonique de surface, condition nécessaire dans les mesures SERS.

Les AgNPs ont été caractérisées optiquement par deux techniques complémentaires: une technique de micro-extinction directe et une technique ellipsométrique indirecte qui nécessite la construction d'un modèle physique.

Un modèle physique révélant le PMMA et les AgNPs comme une seule couche homogène est construit sur la base de trois oscillateurs de Lorentz classiques (un pour le PMMA et deux autres pour les AgNPs). Selon la loi de dispersion de Lorentz, ce modèle génère des données quantitatives satisfaisantes (constantes optiques, épaisseurs et coefficients d'absorption) en impliquant une mesure primaire des angles ellipsométriques expérimentaux bruts (rapport d'amplitude (Ψ) et différence de phase (Δ)) suivie d'un montage correct de ces angles.

Par la suite, l'ensemble de données expérimentales et théoriques ont été comparés aux simulations de Mie pour confirmer les résultats.

La relation entre les dimensions structurelles et les propriétés SERS a été étudiée afin de développer des nanocapteurs capables de détecter de faibles traces de molécules chimiques et biologiques.

Dans cette étude, nous avons montré que des rendements élevés d'AgNPs localisés dans des trous de PMMA peuvent être utilisés comme substrats SERS efficaces et robustes pour détecter des molécules de BPE avec des facteurs d'exaltation (EF) élevés en comparaison avec les valeurs détectées dans la littérature pour la BPE. Les propriétés hydrophobes du PMMA, qui fournissent un mécanisme d'adsorption sélective des molécules de BPE sur les AgNPs, ainsi que des densités élevées des substrats en AgNPs et une différence minime entre les longueurs d'onde LSPR et Raman, sont à l'origine de la sensibilité élevée de ces substrats en SERS.

Les systèmes bimétalliques ont été efficaces pour rénover et enrichir les propriétés de leurs composants intégrés. L'approche VIPS se prêterait bien à une utilisation dans la synthèse de BNPs Ag/Au de morphologies variables. Pour cette raison, les chapitres 3 et 4 ont été consacrés au développement de l'approche VIPS pour l'étendre aux nanomatériaux bimétalliques.

Le chapitre 3 nous a permis d'établir une étude mécanistique de la nucléation et la croissance des systèmes Ag/Au. Précisément, l'adsorption sélective des AgNPs sur des sites spécifiques des graines d'au conduisait à des modes de croissance hautement anisotropes médiée par l'énergie de surface de ces graines. Le résultat était des NPS Ag/Au de morphologies différentes telles que les hétérostructures et les architectures coeur/coque.

Dans le chapitre 4, cette approche a également été utilisée mais pour fabriquer d'autres types de morphologies de BNPs comme les hétéro-oligomères via un mode de croissance par étapes et un processus d'attachement orienté (OAP).

Pour conclure sur les chapitres 3 et 4, l'élaboration des BNPs via la méthode VIPS a montré un changement principal du mécanisme de croissance de ces nanoparticules en comparaison avec les monométalliques. Notamment, le dépôt d'une couche de PMMA dopée en Au^{3+} sur une autre dopée en Ag^+ induit un changement radical de l'auto-assemblage du PMMA de la seconde couche. Par conséquent le mécanisme derrière la formation des BNPs est complètement différent par aux études précédentes faites sur la synthèse des nanométaux par VIPS. De plus, nous avons présenté les différentes techniques de caractérisation utilisées tout au long de ces études qui ont aidé de manière complémentaire à comprendre la composition chimique, les propriétés structurelles, les propriétés optiques et leur sensibilité en SERS. Il s'agit notamment de l'EDX, du SEM et de la spectroscopie μext .

Nous avons également étudié l'influence des conditions expérimentales telles que la vitesse de spin-coating, les concentrations de précurseurs Ag et Au et les rapports molaires Ag/Au sur les propriétés structurelles, optiques et SERS des nanostructures bimétalliques. Le bon rapport ($R_{\text{Ag/Au}}$) entre les deux métaux a joué un rôle clé dans la croissance des nanostructures bimétalliques pour limiter la séparation des phases monométalliques et permettre le contrôle de la composition finale d'un substrat.

La compréhension fondamentale limitée des BNPs sur les surfaces rend encore difficile la compréhension du mécanisme exact qui provoque les interactions hybrides sur les surfaces malgré les progrès dans ce domaine. Pour cette raison, des efforts ont été consacrés à comprendre le rôle de chaque constituant dans le processus de formation des nanostructures en surface. Le travail tout au long des chapitres a tourné autour de l'investigation des mécanismes sous-jacents de la

formation des BNP via une étude thermodynamique/physico-chimique et une étude mécanistique en temps réel.

Les cristaux d'Au formés pendant la synthèse ont agi de deux manières en tant qu'agent de réduction chimique de l'Ag⁺ et qui conduit à la formation de BNP, et en tant qu'agent directeur servant à fournir des sites privilégiés pour la croissance des atomes d'Ag.

Les ions Ag⁺ ont agi comme agents de contrôle de la forme finale des BNP ; en raison d'un dépôt sous-potentiel (UPD), qui est responsable de la stabilisation des différentes facettes cristallographiques des AuNPs. En évaluant ces capteurs à différentes longueurs d'onde d'excitation Raman, nous avons ensuite démontré que les substrats bimétalliques pouvaient servir de substrat actif SERS dans un large domaine spectral.

Le chapitre 5 résume les principales conclusions tirées des quatre chapitres précédents et envisage les possibilités (perspectives) futures de ce travail. En résumé, il existe encore de nombreuses opportunités dans le développement de diverses nanostructures bimétalliques avec dépôt sélectif de nanomatériaux spécifiques (inorganiques/organiques) sur des NP plasmoniques et l'exploration de leurs applications. La technique de synthèse qui consiste en une combinaison VIPS/SMG et la compréhension approfondie des mécanismes de croissance et d'amélioration des performances/propriétés de ces nanostructures étendront considérablement leurs applications dans la détection bio-chimique, la biomédecine et la photocatalyse plasmonique.